Aerospace and Mechanical Engineering Department
Space Structures and Systems Laboratory

A Frequency-domain Approach to Subspace Identification of Nonlinear Systems

Application to Aerospace Structures

Thesis submitted in fulfilment of the requirements for the degree of
Doctor in Engineering Sciences

by

Jean-Philippe Noël, Ir.
Research fellow of the F.R.S. – FNRS

February 2014

Author's contact details

Jean-Philippe NOËL

Space Structures and Systems Laboratory
Aerospace and Mechanical Engineering Department
University of Liège

1, Chemin des chevreuils
4000 Liège, Belgium

Email: JP.Noel@ulg.ac.be
Phone: +32 4 3664854

Members of the Examination Committee

Prof. Jean-Claude GOLINVAL (President of the Committee)
University of Liège (Liège, Belgium)
Email: JC.Golinval@ulg.ac.be

Prof. Gaëtan KERSCHEN (Advisor)
University of Liège (Liège, Belgium)
Email: G.Kerschen@ulg.ac.be

Prof. Lawrence N. VIRGIN
Duke University (Durham, NC)

Prof. David J. EWINS
Imperial College/University of Bristol (London/Bristol, UK)

Prof. Emmanuel FOLTÊTE
FEMTO-ST Institute (Besançon, France)

Prof. Johan SCHOUKENS
Vrije Universiteit Brussel (Brussels, Belgium)

Prof. Greg DIMITRIADIS
University of Liège (Liège, Belgium)

Prof. Pierre ROCHUS
University of Liège (Liège, Belgium)

Abstract

The construction of mathematical models from experimental data is an essential step in the design process of engineering systems. The different tasks involved in this activity, from the measurement and processing of data to the validation of the model, fall into the general field of system identification. In structural dynamics, the theoretical and experimental aspects of linear system identification have been successfully addressed since the early seventies, and mature analytical, computational and testing tools have emerged. Nonlinear system identification of vibrating structures has also enjoyed significant advances during the past few years. However, the common practice in industry is to ignore nonlinearities, arguably because their analysis is still regarded as impractical.

The objective of this doctoral thesis is precisely to progress towards the development of a practical system identification methodology dedicated to real-life nonlinear structures. The first facet of the thesis is to introduce a nonlinear generalisation in the frequency domain of the so-called subspace identification methods. The proposed frequency-domain nonlinear subspace identification (FNSI) approach yields accurate models of large-scale systems comprising strong nonlinearities, closely-spaced modes and high damping. Because it can also estimate a large number of parameters while maintaining an acceptable computational burden, the second facet of this research is to investigate the utilisation of cubic splines as a very flexible means to model complex nonlinearities. Finally, the third facet of the present work is to derive nonlinear models with optimal statistical properties in the presence of measurement noise. This is achieved by embedding the FNSI method into the maximum likelihood identification framework.

The scope of the identification and modelling tools developed in this thesis encompasses nonlinear structural systems originating from the various areas of vibration engineering, including the aerospace, mechanical or civil fields, amongst others. Throughout the dissertation, these tools are illustrated using numerical and experimental structures of increasing complexity, mainly related to aerospace applications.

Acknowledgements

I first have to acknowledge the "Fonds de la Recherche Scientifique – FNRS" for the financial support I received as a Research Fellow through a FRIA grant. Part of my research was also financed by the European Space Agency which is gratefully acknowledged.

Money is not everything, and pursuing doctoral studies is a journey rife with difficulties. I would like to thank those who helped me bring this thesis to fruition during the last three and a half years.

I am particularly thankful to my advisor, Prof. Gaëtan Kerschen, obviously for his guidance, advices and encouragements, but also for his constant stream of new ideas and for the many occasions he gave me to present my research, in particular in international conferences.

I am also grateful to Prof. Stefano Marchesiello at the Politecnico di Torino, Prof. Emmanuel Foltête and Dr. Scott Cogan at the FEMTO-ST Institute in Besançon, and Prof. J. Schoukens at the Vrije Universiteit Brussel for their warm hospitality during my stays in their research groups.

I express my gratitude to Professors Jean-Claude Golinval, Lawrence Virgin, David Ewins, Emmanuel Foltête, Johan Schoukens, Greg Dimitriadis and Pierre Rochus, who accepted to serve on my examination committee.

Je tiens finalement à remercier, en français, ma famille, en particulier mes parents et ma soeur, pour leurs encouragements constants tout au long de mes études universitaires. Je ne peux terminer sans te remercier toi, Louise, pour ton soutien inconditionnel et pour avoir toujours cru en moi.

Contents

Introduction

System identification in structural dynamics aims at building accurate mathematical models from input and output measurements acquired on the real structure. This is a discipline that has evolved considerably during the last decades. Since the early seventies, modal analysis, which is indubitably the most popular approach to performing linear system identification of vibrating structures, has successfully embraced increasingly complex systems in a broad range of application fields. The theory of modal analysis is covered in the comprehensive textbooks by Ewins [23] and Maia and Silva [57], and sophisticated techniques have been developed to implement modal analysis tools, such as the Ibrahim time-domain method [39], the eigensystem realisation algorithm [41], the polyreference least-squares complex frequency-domain method [89] and the subspace deterministic-stochastic algorithm [116]. It is fair to say that modal analysis is today a mature research area, which is applicable to highly damped, geometrically complex structures with high modal density and large modal overlap. The possibility to calculate confidence intervals on modal parameters from noise information is also within reach [17, 96]. Unification of the theoretical development of modal identification algorithms was attempted in Ref. [7], which is another sign of the maturity of this research field.

However, the existence of nonlinear behaviour in modal testing, at least in certain regimes of motion, is a challenge the structural engineer is more and more frequently confronted with. A meaningful example of this reality is the important number of works evidencing nonlinearity in aerospace structures witnessed during the last few years. For instance, nonlinearities arising from the appearance of gaps in the truss supports of the Huygens probe were attested during the modal survey of the Cassini spacecraft [14]. The analysis of in-orbit data of the International Space Station also highlighted that the opening of a pin connection in the assembly of its solar arrays led to severe nonlinearity [50]. Moreover, nonlinearities were reported during the Ground Vibration Test (GVT) of the Airbus A400M, and were attributed to the elastomeric mounts supporting the four turboprop engines of the aircraft [4]. Similarly, GVT data collected on an F-16 fighter revealed that the wing-to-payload mounting interfaces of the aircraft were sources of nonlinearity [79]. This survey shows that the need for appropriate tools to address nonlinear components in the design process of engineering systems is becoming obvious. It is therefore not surprising to notice that the development of system identification techniques applicable to nonlinear systems is currently an active research area in the structural dynamics community.

Nonlinear system identification is a challenging task in view of the wide variety and complexity of nonlinear phenomena. The most salient feature of nonlinear dynamics is the absence of principle of superposition. This implies that any combination of loads applied simultaneously to a nonlinear system does not result in the same response as the sum of the individual responses to each of the loads acting separately. The principle of superposition is the cornerstone of the linear theory of vibrations, and explains why most of the identification methods developed for linear systems break down in the presence of nonlinearity. Another distinct property of nonlinear systems is that their natural frequencies and modes shapes may vary according to the amplitude of excitation. Nonlinear systems may also possess multiple, co-existing stable equilibrium positions with separate domains of attraction, in contrast with the single equilibrium position possible in linear theory. This competing co-existence may lead to sudden transitions, or "jumps", between solutions for small perturbations. Other intriguing behaviours with no linear counterpart nonlinear systems may exhibit include bifurcations, quasiperiodicity and chaos [31, 72, 111].

Besides the complexity of nonlinear phenomena, the other major challenge in nonlinear system identification is that the functional which maps the input onto the output of a nonlinear system is not known beforehand. By way of example, in the case of the well-known Duffing oscillator, this functional comprises a cubic polynomial form of nonlinearity [20], whereas hysteretic damping is one possible type of nonpolynomial nonlinearity. The selection of an adequate nonlinear functional is an additional difficulty compared to linear system identification where the input-output mapping is obviously known.

Significant progress in nonlinear system identification has been enjoyed during the last fifteen years or so [47] and, to date, multi-degree-of-freedom lumped-parameter systems [19, 82] and continuous structures with localised nonlinearities [44, 112] are attainable. The identification of weak nonlinearities in more complex systems has also been addressed in the recent past. For instance, an aircraft-like experimental structure consisting of a wing with two stores suspended by means of nonlinear pylons with hardening characteristics was acurately identified in Ref. [93]. Good results in the nonlinear identification of a complete helicopter with marked softening behaviour of one vibration mode were also obtained in [15], and similarly in the case of the aileron mode of a large transport aircraft in [26].

The identification of structures with complex, and possibly strongly, nonlinear components nevertheless remains a distinct challenge in the current state of the art. In this context, black-box models have received noticeable attention. A black-box model takes advantage of a very flexible mathematical structure to encompass a generally vast class of nonlinear systems, regardless the type and the strength of the nonlinearities [107]. Black-box models were utilised, *e.g.*, to study complicated friction dynamics in Refs. [22, 127]. The price to pay for the flexibility of a black-box model is that it conveys no physical insight into the structure under test. Black-box models also suffer from a rapid growth of the dimensionality of the inverse problem as the number of degrees of freedom and of nonlinearities in the system increases, which may limit their practical usefulness.

Needs in the field and contributions of the thesis

In spite of the recent developments of nonlinear system identification briefly reviewed in this introduction, the common practice in industry is to ignore nonlinearities, arguably because their analysis is still regarded as impractical. There are three key needs that, we believe, should drive the developments in the field to progress towards a practical methodology applicable to real-life structures:

i. an effective methodology of practical utility should be applicable to structures with multiple inputs and outputs, strong nonlinearities, high modal density and high nonproportional damping;

ii. it should also be sufficiently flexible to represent various types of stiffness and damping nonlinearities, while preserving physical insights into the structural behaviour;

iii. it should finally accommodate the presence of noise in the measurement of the inputs and outputs of the structure to guarantee the accuracy of the identified model in experimental conditions.

This doctoral thesis is precisely an attempt to develop a nonlinear system identification methodology satisfying these three needs. Each of them raises important challenges and leads to original contributions throughout the manuscript. The scope of these contributions encompasses nonlinear structural systems originating from the various areas of vibration engineering, including the aerospace, mechanical or civil fields, amongst others. The applications addressed in this dissertation are however related mainly to the aerospace industry, since aircraft and spacecraft structures are known to be regularly prone to nonlinear phenomena, as evidenced at the beginning of this introductory chapter.

The first contribution of the thesis is to develop a nonlinear generalisation in the frequency domain of the so-called subspace identification methods. This development is motivated by the recognised effectiveness of subspace methods as powerful identification tools for linear vibrating systems. The proposed frequency-domain nonlinear subspace identification (FNSI) method is demonstrated using the SmallSat spacecraft, a full-scale satellite structure, based on synthetic data. The SmallSat spacecraft possesses a nonlinear mechanical filtering device with multiple stops. This application is challenging for several reasons, including the number and the nonsmoothness of the nonlinearities, the presence of high nonproportional damping and the important overlaps between modal frequencies.

As most identification approaches in nonlinear structural dynamics, the successful application of the FNSI method is conditional upon an accurate knowledge of the mathematical functionals representing the nonlinearities. The second contribution of the thesis in this context is to investigate the utilisation of cubic splines as a very flexible means to characterise complex nonlinearities in structural systems. Experimental data collected on a nonlinear solar array structure are exploited to this end. The structure consists of two

parallel plates assembled with bolted connections to mimic the dynamics of space solar arrays in folded configuration. This application is challenging because of the existence of impacts between the two plates at high excitation amplitude, and of the activation of complicated nonlinear elastic and dissipative mechanisms within the bolted connections.

The derivation of the FNSI algorithm relies on deterministic arguments, which may result in suboptimal models in the presence of disturbing noise. An alternative approach based on stochastic arguments is to formulate the identification problem through the minimisation of a well-chosen cost function incorporating noise information. The third contribution of this doctoral thesis is to embed the FNSI method into the maximum likelihood framework to identify nonlinear structural models with optimal statistical properties.

Outline of the thesis

Chapter 1 addresses the experimental identification of the SmallSat spacecraft in view of building a computational model with good predictive capabilities. The complete identification procedure, from nonlinearity detection and characterisation to parameter estimation, is carried out based on experimental data collected during a qualification campaign of the spacecraft. The combined use of established analysis techniques brings different perspectives to the observed dynamics. More precisely, the spacecraft is shown to exhibit particularly interesting nonlinear behaviours, including jumps, modal interactions, force relaxation and impact chattering. Specific attention is devoted to nonlinear modal interactions as their experimental evidence in the case of a complex, real-life structure is an important finding of the chapter.

Chapter 2 introduces a new subspace identification method dedicated to nonlinear systems by revisiting existing linear frequency-domain subspace algorithms. An identification theorem is stated and proved, and the consistency of the developed algorithm is investigated in the presence of measurement noise. The proposed FNSI method is illustrated numerically on an academic example, namely a Duffing oscillator. The experimental identification of an electronic circuit emulating the behaviour of a single-degree-of-freedom mechanical system with one nonlinear spring, referred to as the Silverbox benchmark, is finally studied.

Chapter 3 demonstrates the identification capabilities of the FNSI method using the SmallSat spacecraft. To this end, a full-scale finite element model of the structure is built to conduct a series of numerical experiments. The SmallSat identification is challenging for several reasons, including the number and the nonsmoothness of the nonlinearities, the presence of high nonproportional damping and the important overlaps between modal frequencies. The existence of local and global modes of vibration, the great number of instrumented locations, and the selection of the model order are additional difficulties.

Chapter 4 studies the usefulness of cubic splines in modelling the stiffness and damping

nonlinearities of a space solar array structure in stowed configuration. Three experimental data sets collected for increasing force levels are analysed in order to detect nonlinearity based on distortions appearing in frequency response function measurements. Complex behaviours including unilateral impacts and geometrically nonlinear deformations are then successfully identified. Splines are shown to bring superior accuracy with respect to ordinary polynomials with the same number of parameters.

Chapter 5 investigates the possibility of embedding the model parameter estimates generated using the FNSI method into the maximum likelihood identification framework. An introduction to the maximum likelihood cost function is provided, emphasising that it simplifies to a weighted least-squares estimator in the frequency domain. Analytical expressions for the elements of the Jacobian matrix associated with the minimisation of the cost function are also derived. The complete methodology is illustrated on a Duffing oscillator and on the Silverbox benchmark.

Conclusions are finally drawn regarding the contributions this doctoral thesis brings to the field of nonlinear system identification, and guidelines for future research are delineated.

Chapter 1

Experimental identification of the complex dynamics of a strongly nonlinear aerospace structure

Abstract

The present chapter addresses the experimental identification of the SmallSat spacecraft, a strongly nonlinear satellite structure conceived by EADS-Astrium, in view of building a computational model with good predictive capabilities. The complete identification procedure, from nonlinearity detection and characterisation to parameter estimation, is carried out based on experimental data collected during a qualification campaign of the spacecraft. The combined use of established analysis techniques, such as the wavelet transform and the restoring force surface method, brings different perspectives to the observed dynamics. More precisely, the spacecraft is shown to exhibit particularly interesting nonlinear behaviours, including jumps, modal interactions, force relaxation and impact chattering. Specific attention is devoted to nonlinear modal interactions as their experimental evidence in the case of a complex, real-life structure is an important finding of the chapter.

1.1 Introduction

The process of identifying a nonlinear structural model may be viewed as a progression through three successive steps, namely detection, characterisation and parameter estimation. This progression is illustrated in Fig. 1.1, following the ideas in Ref. [47].

1. Detection: *Is there ?*

   Ascertain if nonlinearity exists in the structural behaviour, *e.g.*, yes.

2. Characterisation: *Where ? What ? How ?*

   i. Localise the nonlinearity, *e.g.*, at the joint;

   ii. determine the type of nonlinearity, *e.g.*, Coulomb friction;

   iii. select the functional form of the nonlinearity, *e.g.*, $g(q, \dot{q}) = c\,\mathrm{sign}(\dot{q})$.

3. Parameter estimation: *How much ?*

   Calculate the coefficients of the nonlinear model, *e.g.*, $c = 5.47$.

Figure 1.1: Three-step identification process for nonlinear structural models.

The literature about nonlinearity detection is extensive, and is nicely summarised in the monograph by Worden and Tomlinson [126]. There are various concepts developed for the analysis of linear systems which do not directly apply to nonlinear theory, and may therefore serve in principle as detection tools. The breakdown of the superposition principle is such a concept. It is usually employed in a restricted form, referred to as the homogeneity test. This test amounts to comparing frequency response or ordinary coherence functions measured at different forcing amplitudes in order to reveal potential distortions in specific frequency bands. The homogeneity test is a popular detection tool since almost all commercial spectrum analysers allow the straightforward display of frequency response and ordinary coherence plots. A more elaborated diagnosis method relies on the use of the Hilbert transform, as introduced in Ref. [105]. This method exploits the fact that frequency response functions (FRFs) are invariant under a Hilbert transformation. The use of the subspaces obtained by principal component analysis is another interesting technique to detect nonlinearity because, unlike many approaches, it provides the user with quantitative, and hence objective, detection margins [36]. In Ref. [103], it is similarly shown that well-designed excitation signals may be utilised to reveal the odd and even nature of the nonlinearities, while quantifying their importance in the system response.

Nonlinearity characterisation is the second step of the identification process. It is aimed at localising nonlinearities in the system, determining their type, and selecting appropriate functional forms to represent them. An exhaustive review of the existing techniques

for addressing nonlinearity characterisation is realised in [47]. Characterisation is a challenging task because the physical phenomena that may entail nonlinearity are numerous and may result in plethora of dynamic behaviours, as stressed in the introductory chapter of this thesis. The most common types of nonlinearities encountered in structural systems include geometrical, material, boundary condition, dry friction and hysteresis nonlinearities. Geometrical nonlinearity occurs when the structure undergoes large displacements or deformations, as in the academic case of the pendulum. A specific nonlinear beam test rig with geometrical nonlinearity has often been studied in the technical literature [8, 44, 53, 67]. It was proposed in the framework of the European COST Action F3 [29] and consists of a main cantilever beam whose free end is connected to a thin, short beam clamped on its other side (see Fig. 1.2 (a)). The thin beam can exhibit geometrically nonlinear behaviour due to large displacements compared to its thickness.

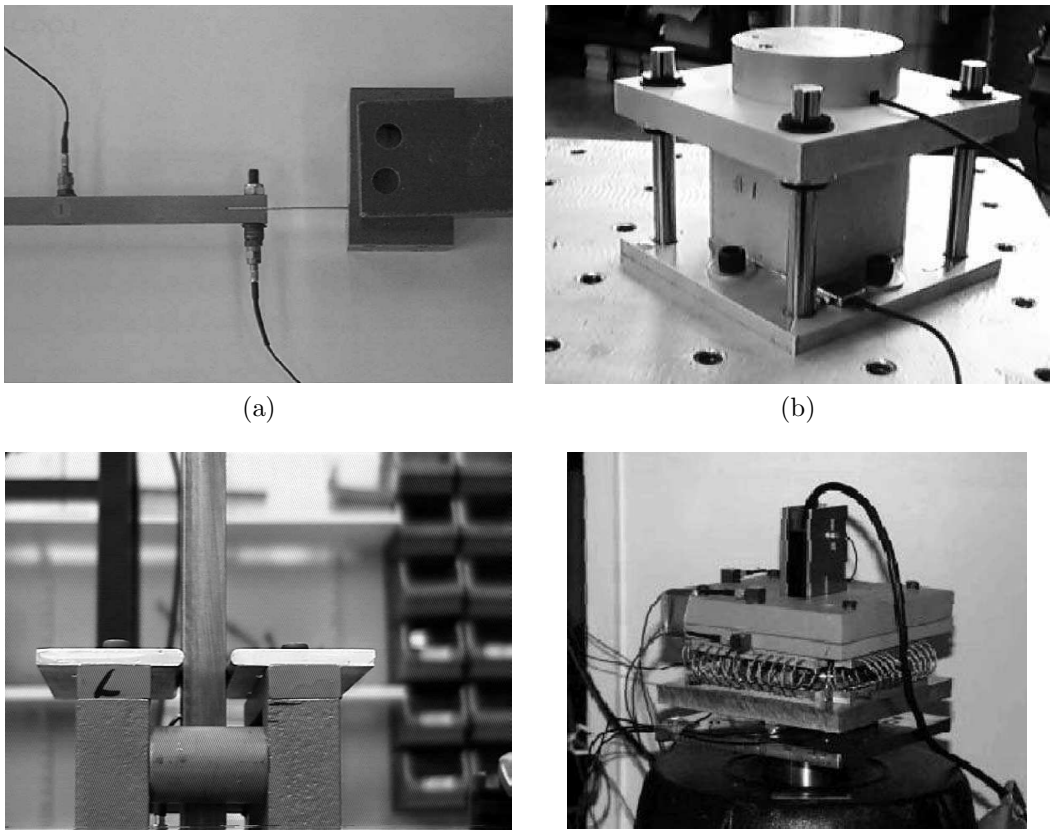

(a) (b)

(c) (d)

Figure 1.2: (a) Cantilever beam connected to a short, thin beam exhibiting geometrically nonlinear behaviour of cubic type; (b) foam-mass system with stress-strain relationship of fifth-order polynomial form; (c) beam with mechanical stops inducing piecewise-linear motion; (d) helical wire rope isolators mounted between a load mass and a base mass and characterised by a softening behaviour due to friction.

Furthermore, nonlinearity may be caused by a nonlinear stress-strain relationship in certain materials. This is usually the case when using rubbers [99] and foams [106] (see Fig. 1.2 (b)). Boundary conditions may also lead to nonlinear behaviour, as a result, for instance, of micro-impacts in loosed joints at the interface between subcomponents [79], or of mechanical stops limiting the amplitude of motion [43] (see Fig. 1.2 (c)). Finally, damping nonlinearity is ubiquitous in engineering structures, the two most representative examples of which are dry friction and hysteretic damping. Numerous experimental studies reported such mechanisms, *e.g.*, in helical wire rope isolators [42] (see Fig. 1.2 (d)), or in assemblies with bolted connections [22].

Parameter estimation is the last step towards the establishment of a nonlinear model with good predictive capabilities. This is arguably the most difficult step in the identification process, but also the one that conveys the most valuable information about the system under test. A large body of methods exists in the technical literature to estimate parameters in nonlinear structural models. One should cite, without being exhaustive but pointing out some of the most established techniques [47], the restoring force surface [60] and nonlinear identification through feedback of the outputs [3] methods which rely on a direct least-squares fitting of the equations of motion, the reverse path methods in the time [69] and frequency domain [98], the nonlinear resonant decay method [94] and its variants [26], the time-domain subspace method [58], and the so-called CONCERTO method [15]. It is eventually worth noting that the three-step progression outlined in Fig. 1.1 is generally referred to as a white-box identification methodology. In white-box identification, the mathematical representation of the nonlinearities is specified in advance based on physics. Assuming the functional form of the nonlinearities may however be a hard requirement to handle in certain circumstances. The recourse to grey- and black-box models may thus be a relevant alternative in such situations, as they largely bypass the complicated step of characterising nonlinearity. This possibility is discussed in more details in Chapter 4 where the usefulness of cubic splines in nonlinear system identification is investigated.

The present chapter addresses the experimental identification of the SmallSat spacecraft, a strongly nonlinear satellite structure conceived by EADS-Astrium. The complete identification procedure, from nonlinearity detection and characterisation to parameter estimation, is carried out based upon experimental data collected during a classical spacecraft qualification campaign. Because such campaigns are constrained by the need to reduce the measurement time, no dedicated tests were performed for the purpose of this study. Typical sine-sweep driven-base data are therefore exploited without the knowledge of the actual input force at the shaker-to-structure interface. The SmallSat spacecraft was equipped with a vibration isolation device with multiple stops, acting as a mechanical filter to mitigate high-frequency disturbances coming from an inertia wheel through the presence of a soft elastomeric interface. An accurate estimation of the clearances and stiffness properties of the nonlinear components is achieved in this chapter in view of building a computational model of the SmallSat with good predictive capabilities.

The contribution of the chapter stems from an unconventional application of established and robust analysis techniques to carry out the three steps of the identification process. The combined use of these techniques also brings different perspectives to the observed dynamics. More precisely, the spacecraft is shown to exhibit particularly interesting nonlinear behaviours, including jumps, modal interactions, force relaxation and chattering during impacts on the mechanical stops. Specific attention is devoted to nonlinear modal interactions as their experimental evidence in the case of a complex, real-life structure is another important contribution of the chapter. In particular, it is found that – potentially dangerous – nonlinear resonances between modes with noncommensurate linear frequencies are possible due to the frequency-energy dependence of nonlinear dynamics. These observations will be compared with numerical predictions obtained by applying continuation algorithms to a finite element model of the satellite structure.

The chapter starts with a detailed introduction to the SmallSat spacecraft structure and its nonlinear vibration isolation device in Section 1.2. Low-level random data are exploited in the form of transmissibility functions to estimate the linear modal properties of the spacecraft. Nonlinearity detection is achieved in Section 1.3 through the visual inspection of the raw sine-sweep time series and phase-plane portraits. Restoring force plots and time-frequency spectra are then analysed in Section 1.4 to gain additional insight towards accurately characterising nonlinear behaviour. Finally, a multi-degree-of-freedom formulation of the restoring force surface method is established in Section 1.5 to estimate the parameters of the nonlinear device.

The content of this chapter was prepared within the framework of the European Space Agency (ESA) Technology Research Programme study "Advancement of Mechanical Verification Methods for Non-linear Spacecraft Structures (NOLISS)" and is entirely reported in Ref. [78]. Experimental data were measured in collaboration with EADS-Astrium and LMS International at Astrium facilities in Stevenage (UK). The author also thanks Astrium SAS for sharing information about the SmallSat spacecraft.

1.2 The SmallSat spacecraft structure

The SmallSat structure was conceived by EADS-Astrium as a low-cost platform for small satellites in low earth orbits [100]. It is a monocoque tube structure which is 1.2 m in height and 1 m in width. It is composed of eight flat faces for equipment mounting purposes, creating an octagon shape, as shown in Fig. 1.3. The octagon is manufactured using carbon-fibre-reinforced plastic by means of a filament winding process. The structure thickness is 4 mm with an additional 0.25-mm-thick skin of Kevlar applied to both the inside and outside surfaces to provide protection against debris. The top floor is an 1-m^2 sandwich aluminium panel, with 25-mm core and 1-mm skins. The interface between the spacecraft and the launch vehicle is achieved via four aluminium brackets located around cut-outs at the base of the structure. The total mass including the interface brackets is around 64 kg.

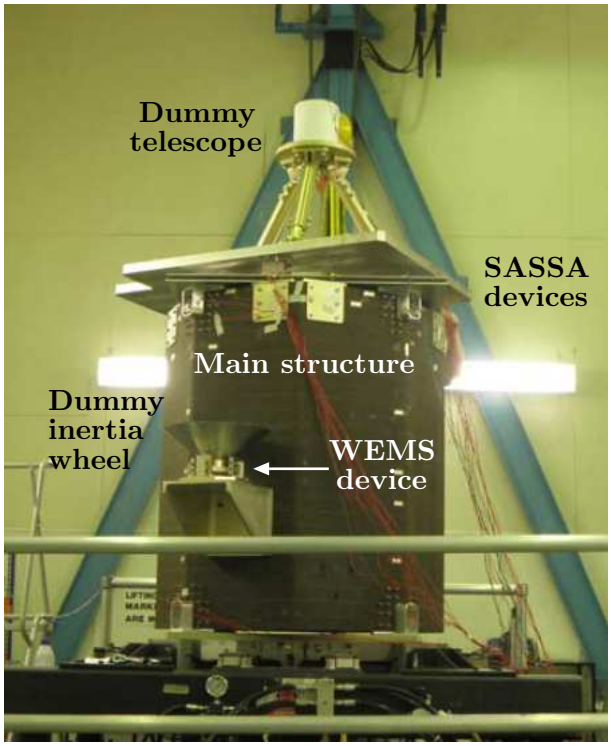

Figure 1.3: SmallSat spacecraft equipped with an inertia wheel supported by the WEMS device and a dummy telescope connected to the main structure by the SASSA isolators.

The spacecraft structure supports a dummy telescope mounted on a baseplate through a tripod; its mass is around 140 kg. The dummy telescope plate is connected to the SmallSat top floor by three shock attenuators, termed shock attenuation systems for spacecraft and adaptor (SASSAs) [13], whose dynamic behaviour may exhibit nonlinearity. Besides, as depicted in Fig. 1.4 (a), a support bracket connects to one of the eight walls the so-called wheel elastomer mounting system (WEMS) device which is loaded with an 8-kg dummy inertia wheel. The WEMS device acts as a mechanical filter which mitigates high-frequency disturbances coming from the inertia wheel through the presence of a soft elastomeric interface between its mobile part, *i.e.* the inertia wheel and a supporting metallic cross, and its fixed part, *i.e.* the bracket and by extension the spacecraft. Moreover, the WEMS incorporates eight mechanical stops, covered with a thin layer of elastomer, and designed to limit the axial and lateral motions of the inertia wheel during launch, which gives rise to strongly nonlinear dynamic phenomena.

Fig. 1.4 (b) presents a simplified, yet relevant, modelling of the WEMS device where the inertia wheel, owing to its important rigidity, is seen as a point mass. The four nonlinear connections (NCs) between the WEMS mobile and fixed parts are labelled NC $1-4$. Each NC possesses a trilinear spring in the axial direction (elastomer in traction/compression plus two stops), a bilinear spring in the radial direction (elastomer in shear plus one stop), and a linear spring in the third direction (elastomer in shear). The stiffness and the damping properties of the WEMS device were estimated during experiments carried

out by EADS-Astrium at subsystem level (see Table 1.1), and will serve as reference values in this study. For confidentiality, stiffness coefficients and clearances are given through adimensionalised quantities.

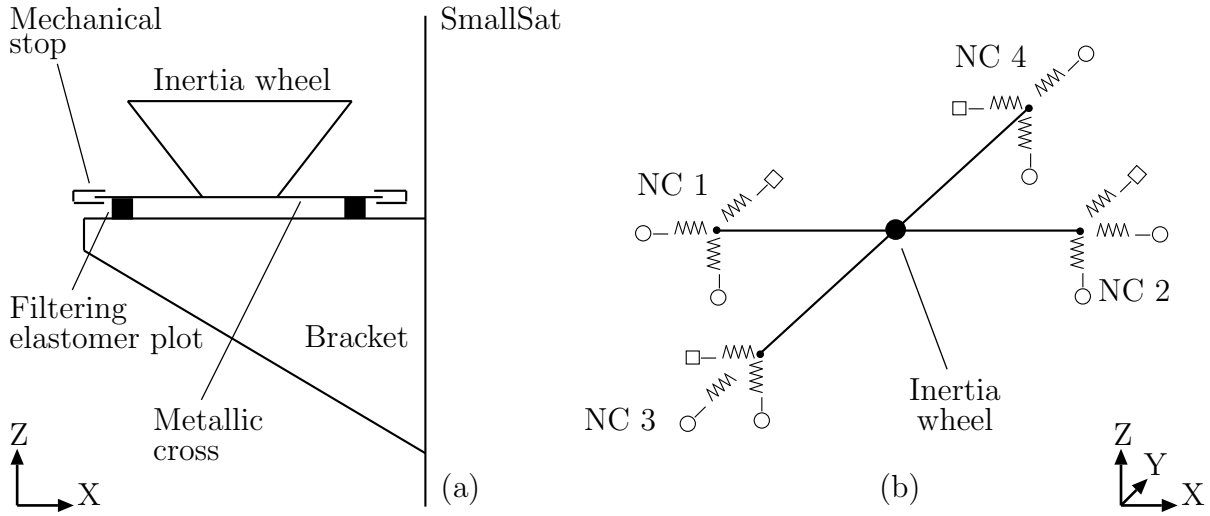

Figure 1.4: WEMS device. (a) Detailed description of the WEMS components; (b) simplified modelling of the WEMS mobile part considering the inertia wheel as a point mass. The linear and nonlinear connections between the WEMS mobile and fixed parts are signalled by squares and circles, respectively. Throughout the thesis, lateral motions of the WEMS device correspond to X- and Y-axis, and axial motion refers to Z-axis.

	Lateral X and Y	Axial Z
Stiffness coefficient of the elastomer plots	2	8
Stiffness coefficient of the mechanical stops	40	100
Clearance	2	1.5
Damping coefficient of the elastomer plots (Ns/m)	37	63

Table 1.1: Reference stiffness and damping properties of the WEMS device estimated during experiments carried out by EADS-Astrium at subsystem level.

Low-level random data were acquired throughout the test campaign, specifically between each qualification run, to monitor the integrity of the structure. This was performed considering axial white-noise excitations filtered in 5 – 100 Hz and driven via a base acceleration of 0.001 g^2/Hz. As they are not prescribed by the space testing standards, high-level random excitations were not applied. The low-level time series are exploited herein to identify the linear modal properties of the spacecraft, utilising transmissibility functions (TFs) as no force measurement was available at the shaker-to-structure interface. The TFs measured on the dummy inertia wheel and telescope in the X, Y and Z directions are plotted in Fig. 1.5 (a – f), given a reference accelerometer located on the shaking table. One remarks that the large bandwidths of the resonance peaks reveal the high damping induced by the elastomeric components in the system. The ordinary coherence functions corresponding to the axial TFs of Fig. 1.5 (e – f) are also depicted in Fig. 1.6 (a – b), respectively. They are both seen to be close to unity for most of the excited frequencies and deteriorate beyond 80 Hz due to poor signal-to-noise ratio (SNR). This proves that the structure can be assumed to behave linearly at this low input level and, in turn, that the analysis of the TFs can yield a reliable identification of its linear modal properties. This analysis is conducted using the frequency-domain identification algorithm derived in Ref. [63]. The resulting estimates of the resonance frequencies and damping ratios of the spacecraft are given in Table 1.2. One notes that the two significant dips observed in Fig 1.6 (a) around 10 and 45 Hz can be attributed to the presence of modes 1, 5 and 6 in the corresponding intervals. The estimated damping ratios also confirm the presence of high damping in the system.

Mode	Frequency (Hz)	Damping ratio (%)
1	8.19	4.36
2	20.18	5.21
3	22.45	6.76
4	34.30	5.03
5	43.16	2.76
6	45.99	3.72
7	55.71	3.66
8	64.60	4.78
9	88.24	2.89

Table 1.2: Linear resonance frequencies and damping ratios estimated using a frequency-domain identification algorithm applied to low-level random data (0.001 g^2/Hz).

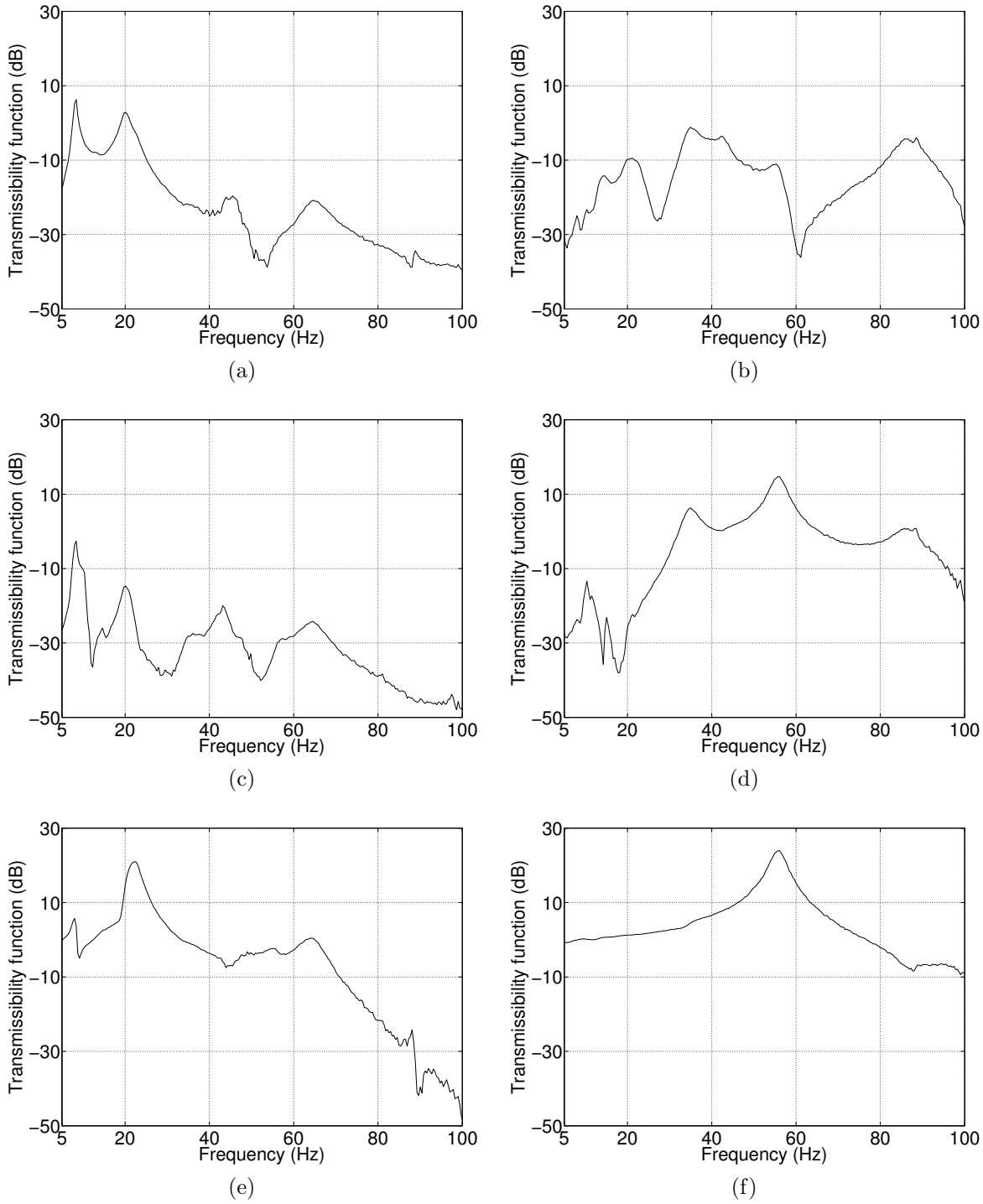

Figure 1.5: Transmissibility functions computed using low-level random data (0.001 g^2/Hz) in the X (first row), Y (second row) and Z (last row) directions. Left column: dummy inertia wheel; right column: dummy telescope.

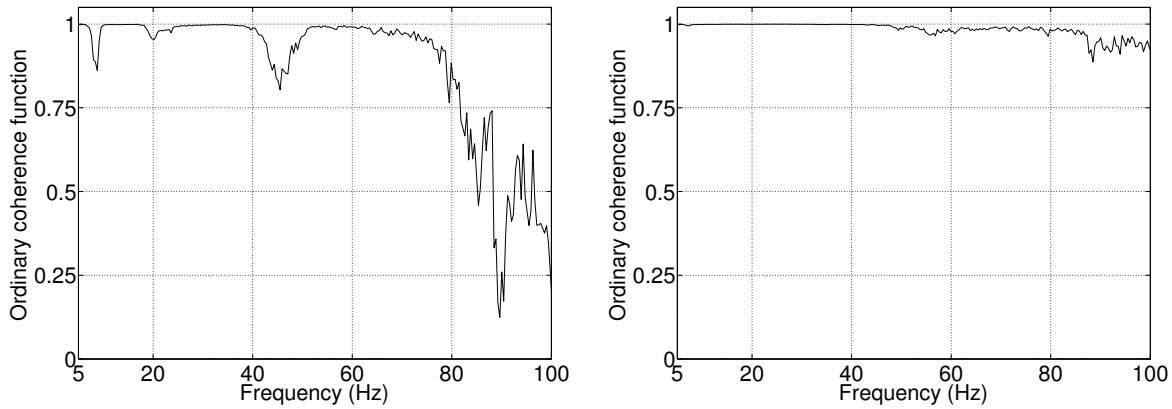

(a) (b)

Figure 1.6: Ordinary coherence functions computed using low-level random data (0.001 g^2/Hz) in the Z direction. (a) Dummy inertia wheel; (b) dummy telescope.

The actual qualification test campaign consisted of swept-sine base excitations applied to the spacecraft for different amplitude levels, sweep rates and directions, as prescribed by the testing standards established by ESA [12]. Two specific data sets measured under 0.6 g and 1 g axial loadings and for positive sweep rates of 2 and 4 octaves per minute, respectively, are exploited in the present chapter for nonlinear system identification. For conciseness, their analysis is focused in the next sections on the frequency range between 5 and 15 Hz, *i.e.*, the vicinity of the first mode of vibration of the structure. The associated spacecraft motion is depicted in Fig. 1.7 through the modal coordinates of the inertia wheel and the telescope in the X, Y and Z directions. This motion consists mainly in a swing oscillation of the inertia wheel around Y-axis.

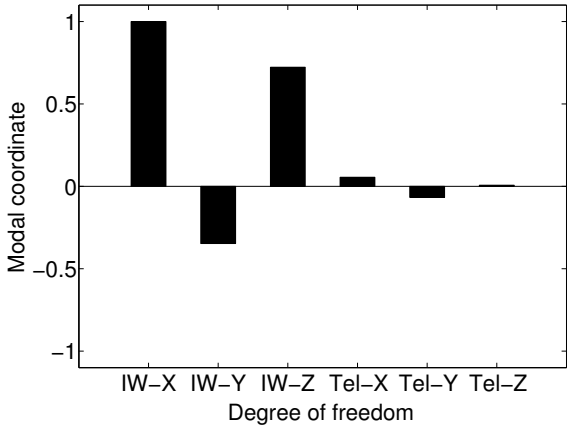

Figure 1.7: First mode of vibration of the spacecraft described through the modal coordinates of the dummy inertia wheel and telescope in the X, Y and Z directions.

1.3 Detection of nonlinearity

Nonlinearity detection is the first step of the identification process in Fig. 1.1, and basically boils down to seeking departures from linear theory predictions. In this regard, stepped- and swept-sine excitations are particularly convenient because, if linear, the structure is known to generate a pure sine wave in output, and distortions may be detected without requiring complicated post-processing. Various other detection tools were listed in the introductory section of the chapter, as the test for homogeneity of frequency response and ordinary coherence functions, or the computation of subspaces based on principal component analysis. However, they generally require high-level random measurements which are not available in this study.

1.3.1 Envelope-based analysis of the raw time series

Nonlinear distortions in response to sine excitations can sometimes be such that a mere visual inspection of the raw time series is sufficient to reveal nonlinear behaviour. To this end, the axial relative displacements across NC 1 measured at 0.6 g and 1 g are plotted in Fig. 1.8 (a – b), respectively, versus sweep frequency. Note that the excitation frequency is an exponential function of time with a rate, which is the derivative of frequency with respect to time, expressed in octaves per minute [12]. Given the knowledge of the sweep rate, this definition enables the conversion from time to sweep frequency throughout the chapter. Note also that the measured accelerations were integrated twice using the trapezium rule and then high-pass filtered to obtain displacement signals [123]. For confidentiality, relative displacements and velocities are adimensionalised in the thesis.

The first observation is the absence of proportionality between the time responses in Fig. 1.8 (a – b). This is especially visible for negative displacements where the maximum amplitude reached at 0.6 g and 1 g is almost unchanged. This violates the principle of superposition, a cornerstone of the linear theory. The location of the resonance in amplitude in the two graphs can also be seen to be shifted towards higher frequencies, from 8.3 to 9 Hz as the level is increased from 0.6 to 1 g. One further remarks the clear skewness and the nonsmoothness of the envelope of oscillations in Fig. 1.8 (b), which exhibits a sudden transition from large to small amplitudes of vibration, referred to as a jump phenomenon. This envelope also presents a significant asymmetry entailing larger amplitudes of motion in positive displacement, and a discontinuity in slope for negative displacements around 7.5 Hz.

By contrast, the envelope of response at 0.6 g shows no important evidence of nonlinear distortions. However, analysing the response in the vicinity of resonance, *i.e.* in the 8.1 – 8.4 Hz interval, as presented in Fig. 1.8 (c), highlights the presence of harmonics in the time series. A similar inspection at 1 g, depicted in Fig. 1.8 (d) in 8.4 – 8.7 Hz, reveals much more significant harmonics and a limitation of the amplitude of motion in negative displacement resulting in the aforementioned asymmetry of the response.

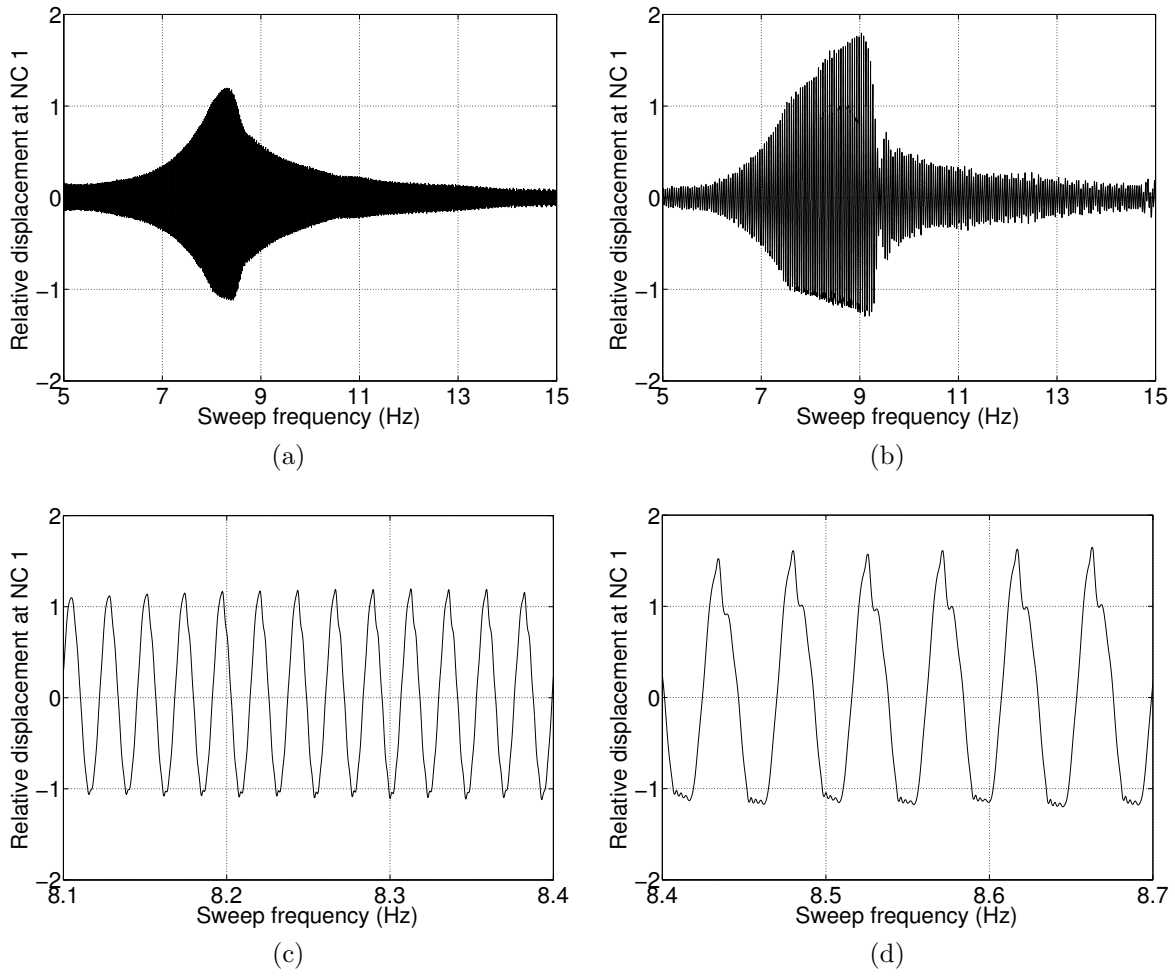

Figure 1.8: Nonlinearity detection at 0.6 g (left column) and 1 g (right column). (a – b) Envelope-based analysis; (c – d) close-up of the displacement signals.

1.3.2 Phase-plane diagram

An under-utilised but useful means of revealing harmonic distortions is a phase-plane diagram, where the system trajectory draws an ellipse in the case of a pure sine wave in output. The relative displacements of Fig. 1.8 (c – d) are plotted versus the corresponding relative velocities to generate phase-plane trajectories in Fig. 1.9 (a – b), respectively. The detection of harmonics at 0.6 g is now straightforward, and the activation of a strongly nonlinear regime of motion is also confirmed at 1 g.

A meaningful representation of the nonlinear jump phenomenon observed in Fig. 1.8 (b) can also be achieved in the phase plane. This phenomenon stems from the intrinsic property of a nonlinear system to possess multiple stable solutions of its equations of motion, with co-existing basins of attraction. This competing co-existence may result in "jumps"

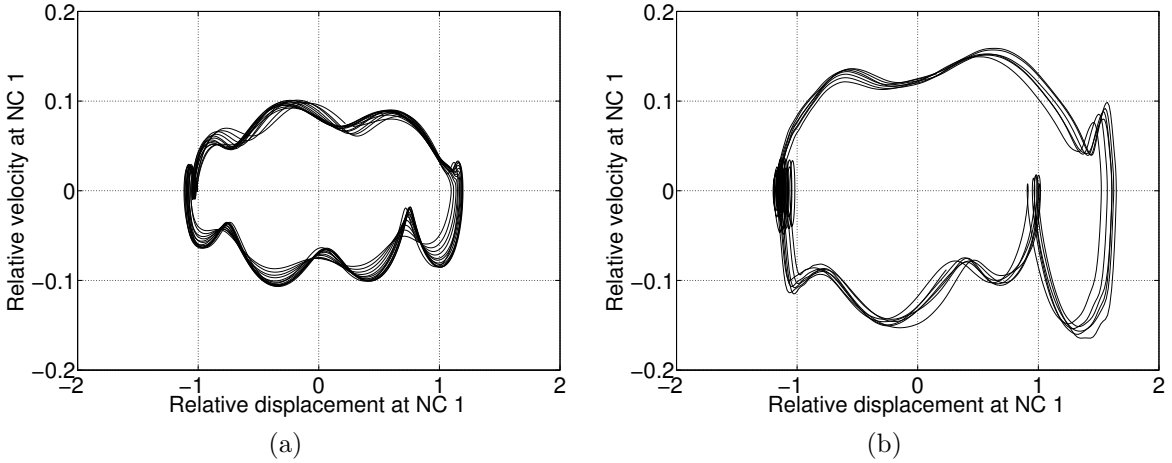

(a)

(b)

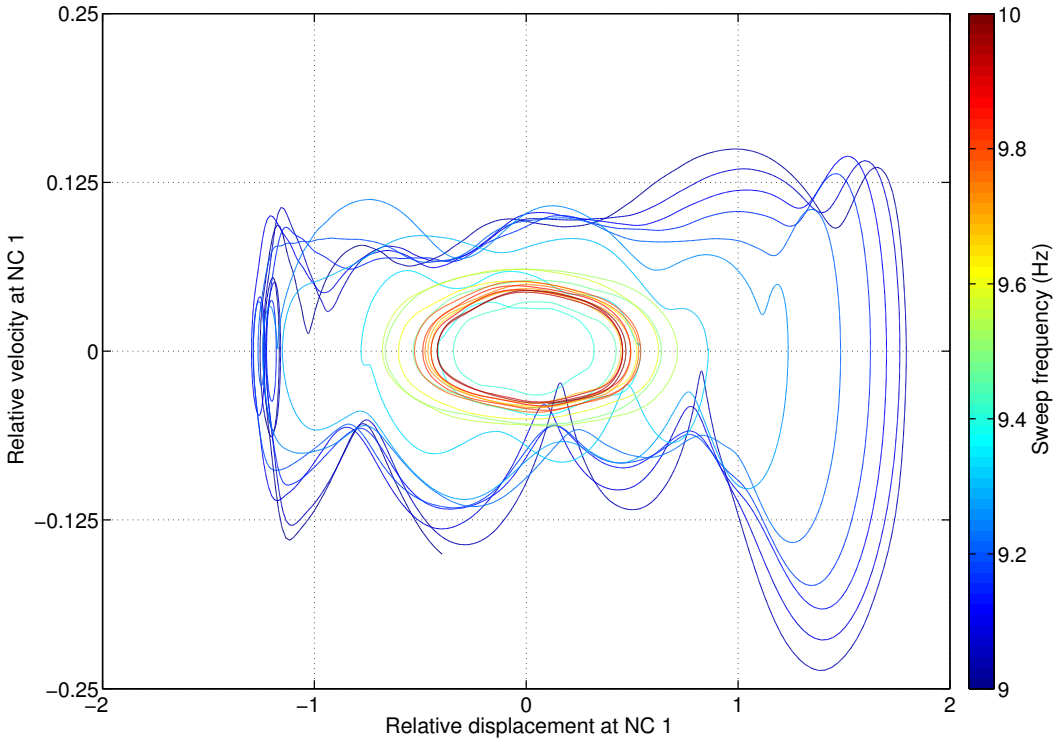

(c)

Figure 1.9: Nonlinearity detection using phase-plane diagrams at (a) 0.6 g and (b) 1 g; (c) representation of the nonlinear jump phenomenon observed in Fig. 1.8 (b) in the phase plane parametrised by the excitation frequency.

between solutions for small perturbations of the system, in particular small variations of the forcing frequency. Fig. 1.9 (c) depicts the phase-plane trajectory corresponding to Fig. 1.8 (b) in the interval from 9 to 10 Hz, and parametrised by the excitation frequency as a colour map. This reveals a sudden transition at 9.4 Hz from a nonlinear to a linear regime of motion, *i.e.*, from a high- to a low-amplitude solution of the equations of motion.

In summary of the nonlinearity detection step, all the results in this section highlight multiple symptoms of the activation of nonlinear dynamics at 1 g, namely the loss of superposition principle, the shift of the resonance frequency, the jump phenomenon, the asymmetry and the discontinuity of the response envelope, and the presence of significant harmonics. The diagnosis is similar at 0.6 g where nonlinear distortions, though being much less significant, were made evident in a distorted phase-plane trajectory.

1.4 Characterisation of nonlinearity

Nonlinearity characterisation is the second step of the identification process in Fig. 1.1, and primarily amounts to selecting appropriate functional forms to represent the nonlinearities in the system. Characterisation is of paramount importance, as the success of the third step of the process, *i.e.* the estimation of model parameters, is conditional upon a precise understanding of the nonlinear mechanisms involved. As pointed out in the introduction of the chapter, it is also a very challenging step because the physical phenomena that may entail nonlinearity are numerous and may result in plethora of dynamic behaviours.

1.4.1 Visual inspection and histogram

Beyond detection, the visual inspection of the time series can help gain insight into nonlinear behaviour. The existence of a discontinuity in the envelope of oscillation in Fig. 1.8 (b) results from the nonsmooth nature of the nonlinearity, and the existence of a clearance in the system. The location of the discontinuity yields a direct estimation of this clearance at around -1. The modification of the slope of the envelope also translates a substantial increase of stiffness, which is confirmed by the shift of the resonance towards higher frequencies in Fig. 1.8 (a – b), and by the amplitude-limiting effect visible in Fig. 1.8 (d). Finally, the asymmetry observed in the response can be explained by the prestress applied to the elastomer plots by gravity, which implies a smaller clearance in the – Z direction.

A particularly meaningful representation of the measured time series for clearance estimation is a histogram. This is plotted in Fig. 1.10 (a – b) for the relative displacements of Fig. 1.8 (a – b), respectively. The accumulation of samples in the left-hand tail of the double-peak-shaped distribution typical of sine waves, which is another manifestation of the asymmetry of the WEMS device, leads to a consistent estimation of the NC 1 negative clearance at 1. Note that a more accurate estimation of the NC 1 and NC 2 clearances

will be realised in Section 1.5.

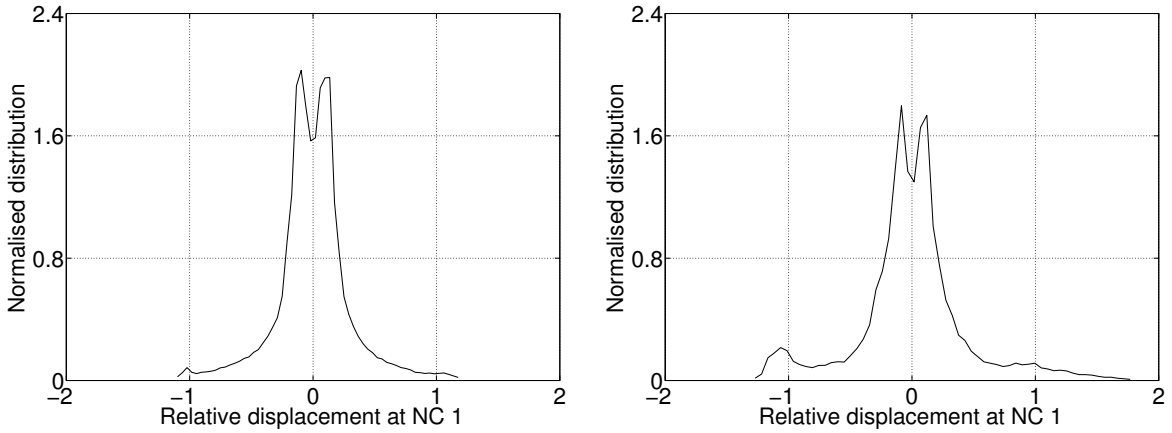

Figure 1.10: Nonlinearity characterisation via histograms of the time series. (a) 0.6 g; (b) 1 g.

1.4.2 Restoring force surface plots

The restoring force surface (RFS) method, first introduced by Masri and Caughey [60] and covered in detail in the textbook [126], serves commonly as a parameter estimation technique, as in Section 1.5 of the present chapter. This section introduces an unconventional use of the RFS method for nonlinearity characterisation purposes, relying exclusively on measured signals. The starting point is Newton's second law of dynamics written for a specific degree of freedom (DOF) located next to a nonlinear structural component, namely

$$\sum_{n=1}^{n_p} m_{i,n}\,\ddot{q}_n + g_i(\mathbf{q},\dot{\mathbf{q}}) = p_i \tag{1.1}$$

where i is the DOF of interest, n_p the number of DOFs in the system, $m_{i,j}$ the mass matrix elements, $\mathbf{q}$, $\dot{\mathbf{q}}$ and $\ddot{\mathbf{q}}$ the displacement, velocity and acceleration vectors, respectively, $\mathbf{g}$ the restoring force vector encompassing elastic and dissipative effects, and $\mathbf{p}$ the external force vector. The key idea of the approach is to discard in Eq. (1.1) all the inertia and restoring force contributions that are not related to the nonlinear component, as they are generally either unknown, *e.g.*, the coupling inertia coefficients, or not measured, *e.g.*, the rotational DOFs. If we denote by j another measured DOF located across the nonlinear connection, Eq. (1.1) is therefore approximated by

$$m_{i,i}\,\ddot{q}_i + g_i(q_i - q_j, \dot{q}_i - \dot{q}_j) \approx p_i. \tag{1.2}$$

If no force is applied to DOF i, a simple rearrangement leads to

$$g_i(q_i - q_j, \dot{q}_i - \dot{q}_j) \approx -m_{i,i}\,\ddot{q}_i. \tag{1.3}$$

Eq. (1.3) shows that the restoring force of the nonlinear connection is approximately proportional to the acceleration at DOF i. Hence, by simply representing the acceleration signal, with a negative sign, measured at one side of the nonlinear connection as a function of the relative displacement and velocity across this connection, the nonlinearities can be conveniently visualised, and an adequate mathematical model for their description can then be selected. This methodology has already been successfully applied to the characterisation of the nonlinearities at the wing tips of the MS-760 Morane Saulnier aircraft [45], and in the wing-to-payload interfaces of an F-16 aircraft [79].

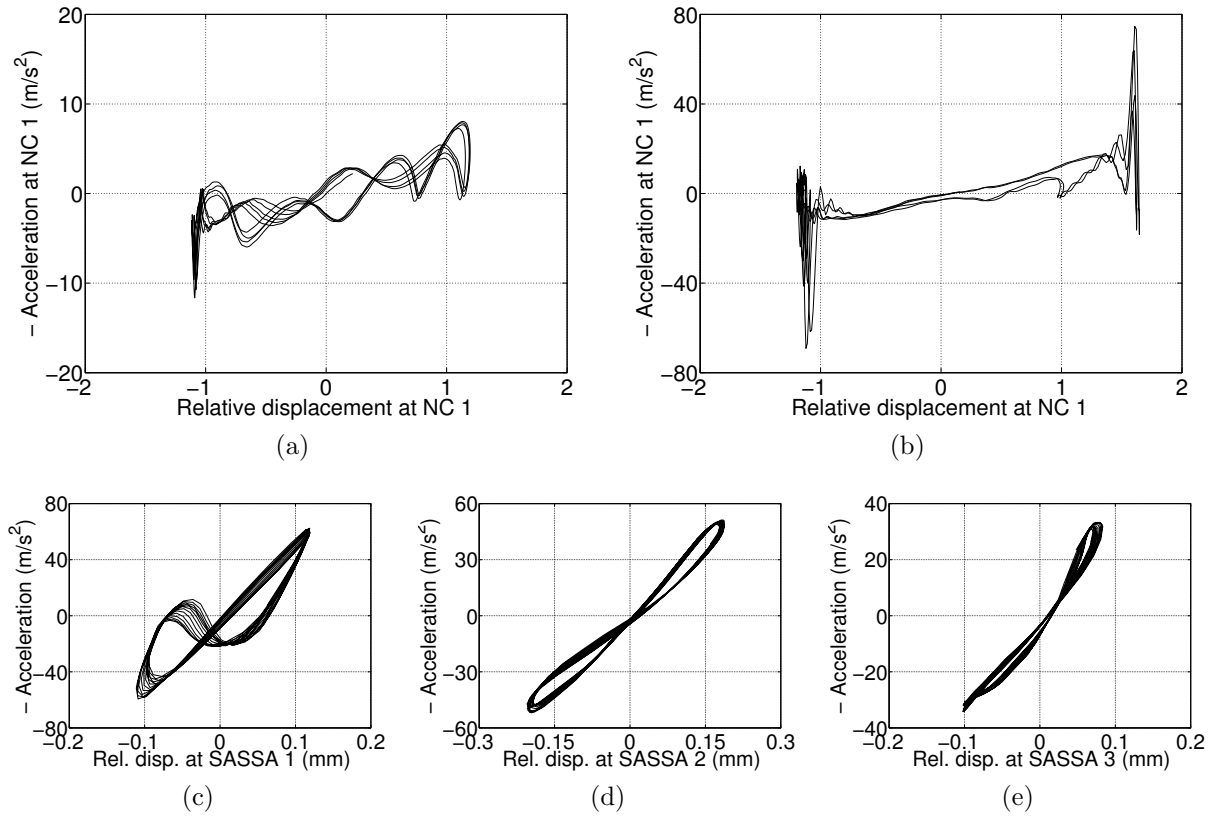

Figure 1.11: Nonlinearity characterisation of the WEMS device (top row) and of the three SASSA isolators (bottom row) using the restoring force surface method. (a) 0.6 g; (b – e) 1 g.

To visualise the elastic nonlinearities of the WEMS device, a cross section along the axis where the velocity is zero of the restoring force surface defined by the triplets $(q_{i,k} - q_{j,k}, \dot{q}_{i,k} - \dot{q}_{j,k}, -\ddot{q}_{i,k})$, where k refers to the k-th sampled instant, can be drawn. Fig. 1.11 (a – b) shows the plots corresponding to NC 1 at 0.6 g and 1 g, respectively. These plots

are particularly useful as they reaffirm the nonsmooth and asymmetric nature of the nonlinearities in the system, and the estimation of the – Z clearance at around 1. The restoring force curve at 1 g also reveals the activation of the + Z stop, beyond a relative displacement of about 1.5. In Section 1.2, the SASSA isolators were also mentioned as possible sources of nonlinear behaviour. Fig. 1.11 (c – e) depicts the nonlinearities across the three SASSA connections in the Z direction at 1 g. As suspected, they exhibit a weak nonlinearity, which is however not further investigated in favour of the much stronger nonlinearities of the WEMS device.

1.4.3 Time-frequency analysis using the wavelet transform

The Fourier transform (FT), which maps a time-domain signal $x(t)$ onto its frequency-domain representation $X(\omega)$, is defined as

$$X(\omega) = \int_{-\infty}^{\infty} x(t)\, e^{-j\omega t}\, dt\,. \tag{1.4}$$

Though it is widely used in structural dynamics for various purposes, the FT fails to capture nonstationary effects. In this regard, an improvement of the classical FT is the short-time Fourier transform (STFT). The signal to be analysed is first multiplied by a window $w(t-\tau)$, which is nonzero for only a short period of time. The FT of the signal is then calculated as the window $w(t-\tau)$ is slid along the time axis, resulting in a more general time-dependent representation $X(\omega,\tau)$ of the spectrum of the signal, that is,

$$X(\omega,\tau) = \int_{-\infty}^{\infty} x(t)\, w(t-\tau)\, e^{-j\omega t}\, dt\,. \tag{1.5}$$

The inherent limitation of the STFT is that the window length is not adjustable, and a wide (narrow) window thus gives good (poor) frequency resolution but poor (good) time resolution. This fixed resolution of the STFT can be addressed using more sophisticated time-frequency analysis methodologies, such as the wavelet transform (WT). Unlike the STFT, the WT involves a windowing strategy with variable-sized regions:

$$X(a,b) = \frac{1}{\sqrt{a}} \int_{-\infty}^{\infty} x(t)\, \psi\left(\frac{t-b}{a}\right)\, dt \tag{1.6}$$

where ψ is referred to as the mother wavelet. Parameter b, similarly to τ, locates the observation window in the time domain, and a contracts or expands the window depending upon the frequency components of $x(t)$. This adaptability makes the WT one of the most suitable tools for interpreting harmonics generated by nonlinear systems in response to swept-sine excitations [110]. The Morlet mother wavelet, which is a Gaussian-windowed complex exponential, is exploited herein for its versatility.

The wavelet amplitudes of the relative displacements of Fig. 1.8 (a – b) are displayed in logarithmic scaling in Fig. 1.12 (a – b), respectively. At 0.6 g, the appearance of wideband

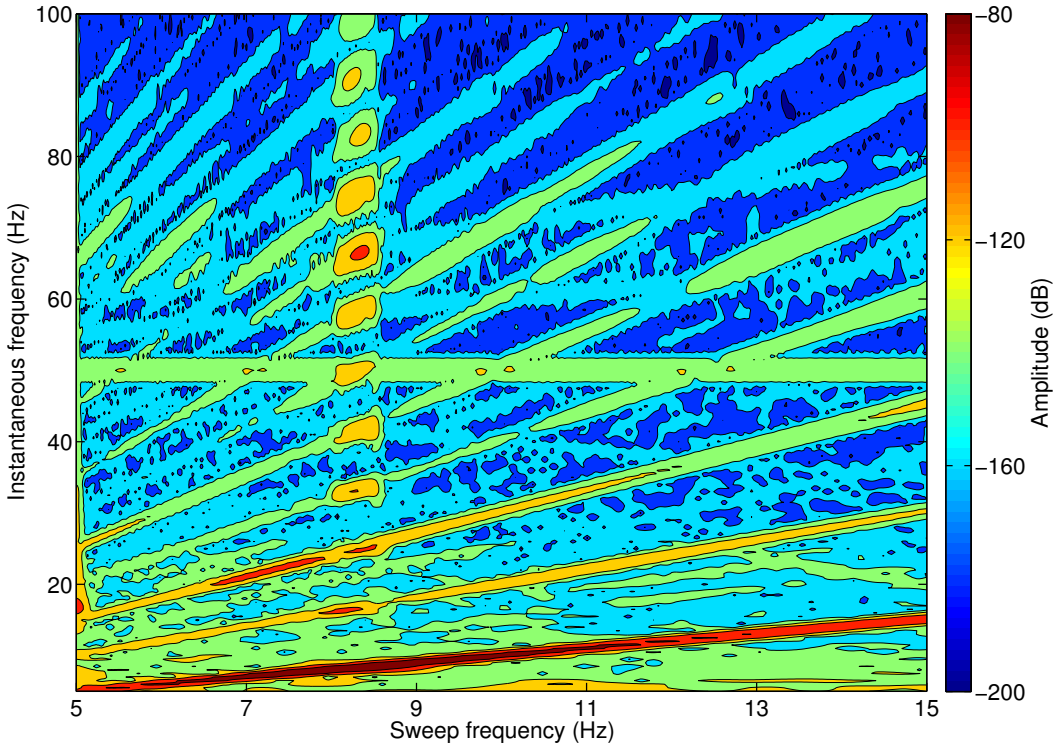

(a)

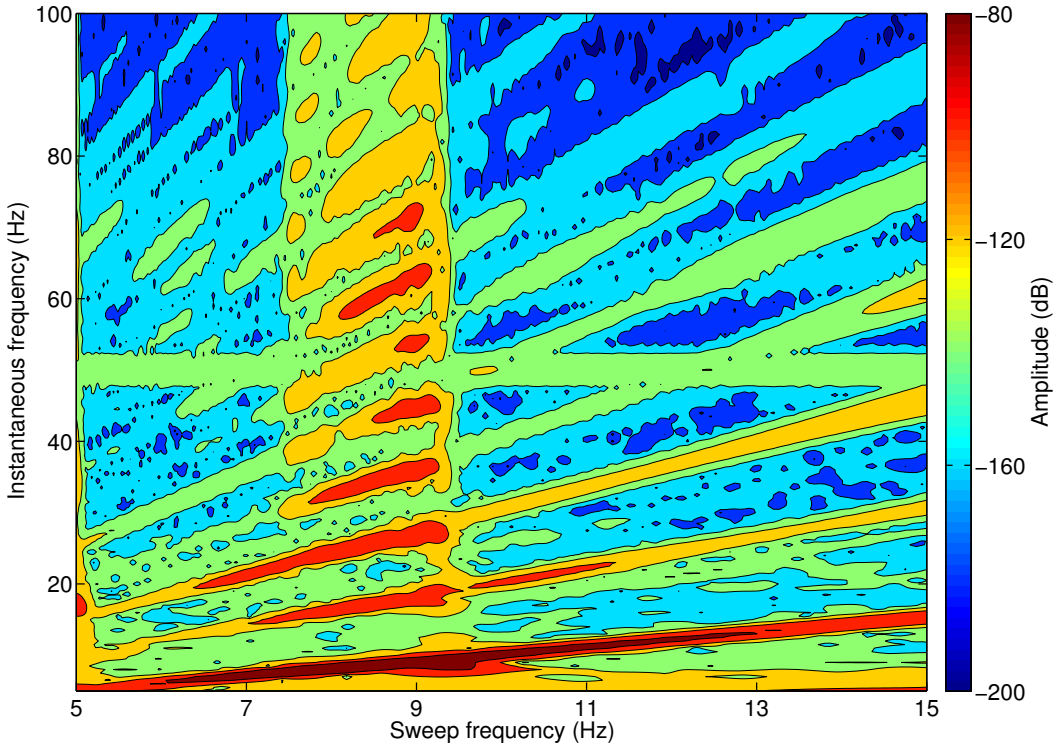

(b)

Figure 1.12: Nonlinearity characterisation through the WT amplitude of the relative displacement measured across NC 1. (a) 0.6 g; (b) 1 g.

frequency components around 8.5 Hz, including even harmonics, confirms the activation of a nonsmooth nonlinearity in the neighbourhood of the resonance and the existence of an asymmetry in the system. Fig. 1.12 (b) shows that, at 1 g, the nonlinearity is activated over a wider sweep frequency interval. Nonsmooth effects are also found to be stronger as indicated by the relative importance of the harmonics in the response. The disappearance of the wideband content at 1 g can be seen to coincide closely with the jump phenomenon observed in Fig. 1.8 (b). One should also point out that impurities in the input sine wave turn into weak harmonics visible throughout the spectra, but hence not attributable to nonlinearity. Similarly, electrical noise is responsible for polluting frequency lines around 50 Hz.

In summary, the nonlinearity characterisation step reveals that an accurate representation of the WEMS nonlinear behaviour should account for combined nonsmooth and asymmetric effects. This leads us to select a trilinear model with dissimilar clearances for the nonlinearity, as presented in Fig. 1.13. No characterisation of damping was attempted in this section as the scope of the chapter is focused on the identification of the nonlinear dynamics introduced by the WEMS mechanical stops. Moreover, the understanding of dissipation mechanisms is particularly challenging, and would certainly require specific test data other than the sine sweeps available herein. One therefore opts for a simple linear damping model for the elastomer components of the WEMS, even if it will be shown in Section 1.5.2 that they may exhibit more complex, time-dependent characteristics.

1.4.4 Evidence of nonlinear modal interactions

The WT can evidence a salient feature of nonlinear systems that has no counterpart in linear theory, namely modal interactions between modes with well-separated frequencies. These interactions were extensively studied in the technical literature [46, 48, 71], but they were so far rarely reported in the case of a real-life structure. To reveal nonlinear modal interactions in the SmallSat dynamics, Fig. 1.14 (a) depicts the wavelet amplitude of the acceleration measured at NC 4 in the Z direction over 5 – 35 Hz. Compared to the two wavelets represented in Fig. 1.12 (a – b), a linear scale is used herein to focus on the most significant frequency components in the time series. The excitation frequency is clearly seen throughout the wavelet, but higher harmonic components of at least comparable amplitude are also visible. In particular, a significant level of response, encircled in Fig. 1.14 (a), is observed around 60 Hz for sweep frequencies just below 30 Hz. This corresponds to a 2:1 interaction between two internally resonant modes of the structure, namely mode 3, which involves an out-of-phase motion of the inertia wheel and the WEMS bracket, and mode 7, which consists in an axial motion of the telescope supporting panel. The existence of a 2:1 interaction between modes 3 and 7 is confirmed in Fig. 1.14 (b), where the raw acceleration signal measured at the centre of the instrument panel is plotted at 0.1 g and 1 g. A high amplitude response at 1 g is observed between 20 and 30 Hz, which can be confidently attributed to a nonlinear resonance as no linear mode of the panel is located in this interval. One also remarks the presence of

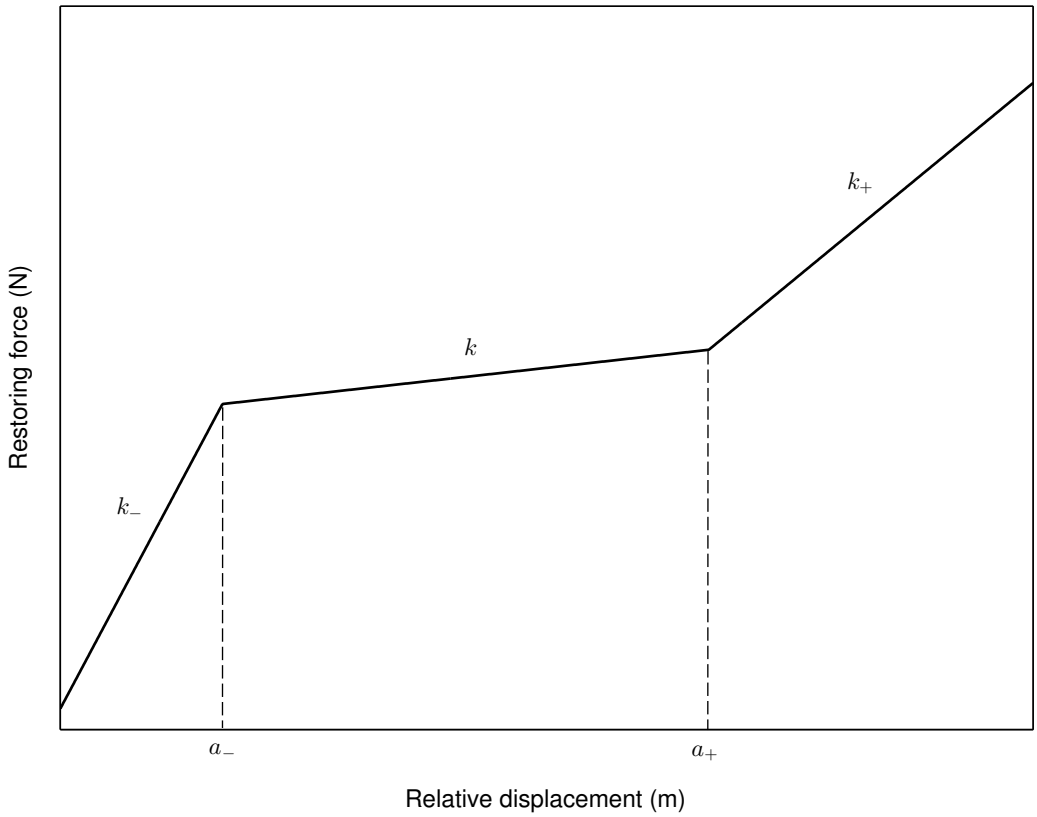

Figure 1.13: Trilinear model with dissimilar clearances selected to represent the WEMS elastic nonlinearities. The negative and positive clearances are denoted a_- and a_+, respectively; the linear and nonlinear stiffness coefficients in negative and positive displacement are denoted k, k_- and k_+, respectively.

two resonances around 46 and 56 Hz, as predicted by the linear modal analysis carried out in Section 1.2. At the 0.1 g excitation level for which the satellite behaves linearly, there is no sign of the 2:1 modal interaction, proving that it is an inherently nonlinear phenomenon activated for sufficiently large energies.

Unlike what is frequently discussed in the literature [71], the ratio of the linear natural frequencies of modes 3 and 7 is not an integer, it is around 2.5 (see Table 1.2). However, the frequency of nonlinear modes may vary according to the excitation level. This is clearly visible in Fig. 1.15 where the acceleration measured at NC 3 is plotted at 0.1 g and 1 g. At 0.1 g, the linear resonance frequencies of modes 2 and 3 identified in Section 1.2 are retrieved around 20.3 and 23 Hz, whereas they are seen to be shifted up to 24 and 29 Hz at 1 g, respectively. This means that a 2:1 ratio between modes 3 and 7 can still be realised due to the energy dependence of nonlinear modes. Indeed, the frequency of mode 3 increases rapidly as soon as nonlinearity is activated, while the frequency

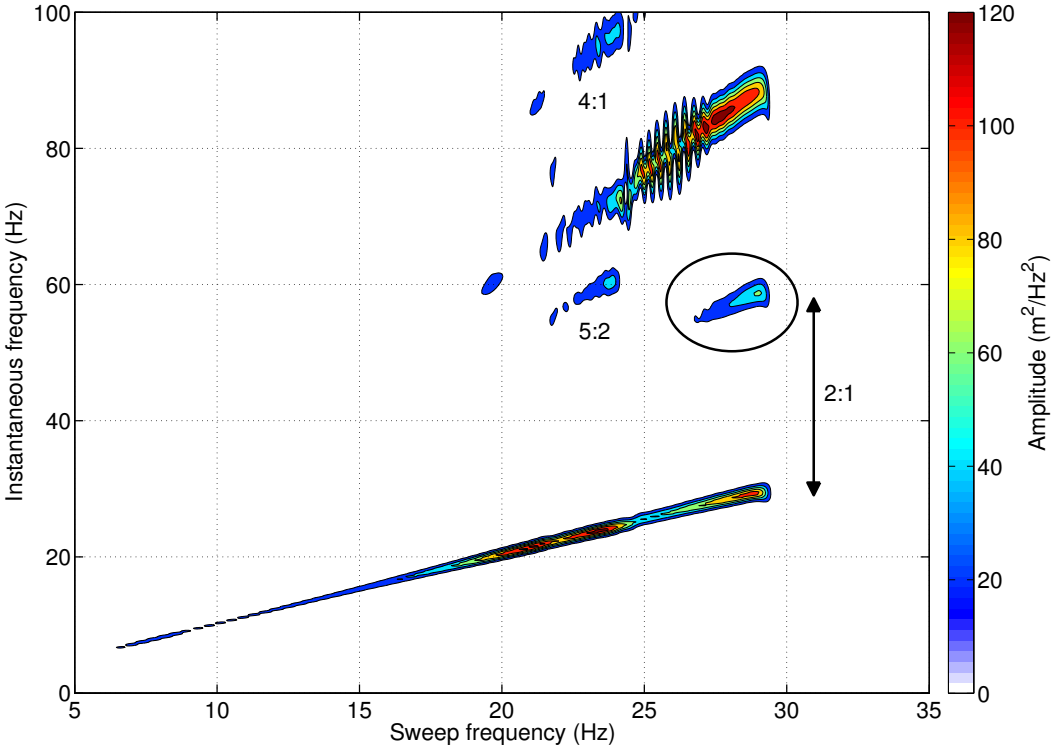

(a)

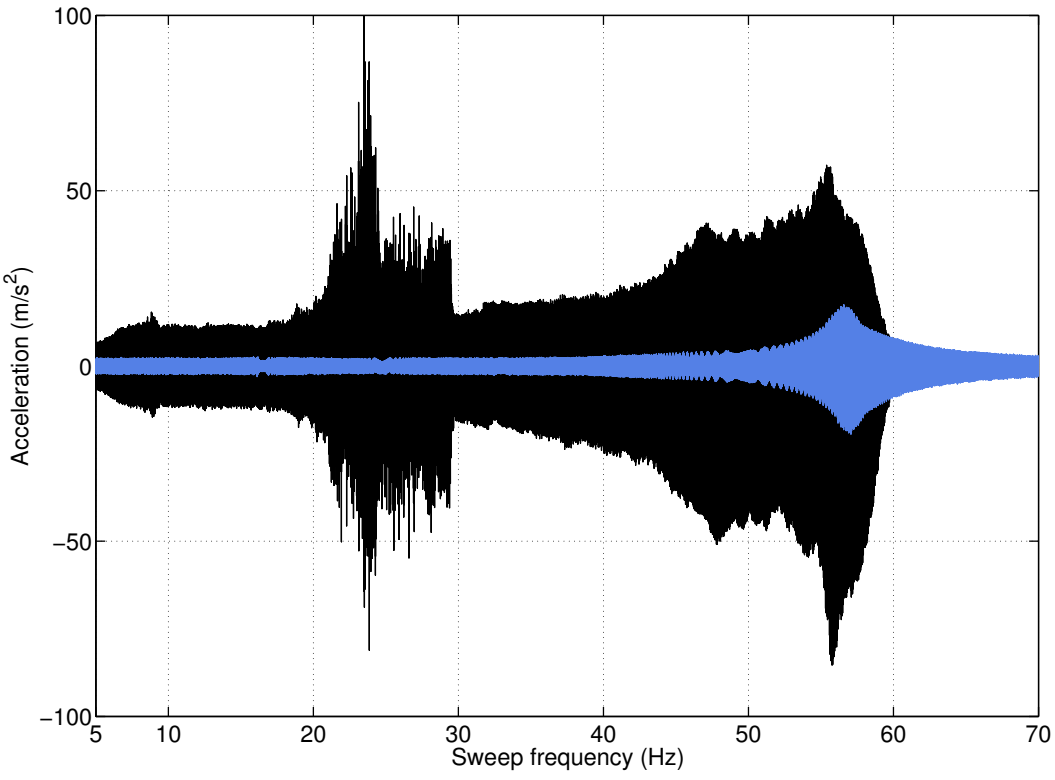

(b)

Figure 1.14: (a) Evidence of nonlinear modal interactions using the WT calculated at NC 4 in the Z direction, and presented in 5 – 35 Hz in linear scaling. A 2:1 modal interaction between modes 3 and 7 is encircled; (b) confirmation of the existence of the 2:1 modal interaction through the raw acceleration measured at the centre of the instrument panel at 0.1 g (in blue) and 1 g (in black).

of mode 7 remains unchanged as it involves no WEMS motion. This is therefore the experimental evidence of an interaction between nonlinear modes with noncommensurate linear frequencies. It should also be stressed that this 2:1 modal interaction may jeopardise the integrity of the structure as it is accompanied by an energy transfer from a local mode of the spacecraft with low effective mass, *i.e.* mode 3, to a global mode with high effective mass, *i.e.* mode 7. In addition, the time series at 1 g in Fig. 1.14 (b) shows that the nonlinear resonance involving the instrument panel is associated with larger accelerations (*i.e.*, 100 m/s^2) than the linear resonance of the panel (*i.e.*, 80 m/s^2). Furthermore, the 2:1 interaction is not an isolated phenomenon as other internal resonances, such as a 5:2 interaction between mode 2 and mode 7 and a 4:1 interaction between modes 2 and 9, can also be noticed in Fig. 1.14 (a). Fig. 1.16 eventually shows that an additional 2:1 experimental modal interaction can be evidenced using the WT, by analysing the acceleration measured at NC 4 in the Y direction. This modal interaction is interesting because, at this sensor, the only visible frequency component is 45 Hz despite the fact that the excitation frequency is 22.5 Hz. The present discussion implies that important, and potentially dangerous, dynamic phenomena can be missed when ignoring nonlinearity.

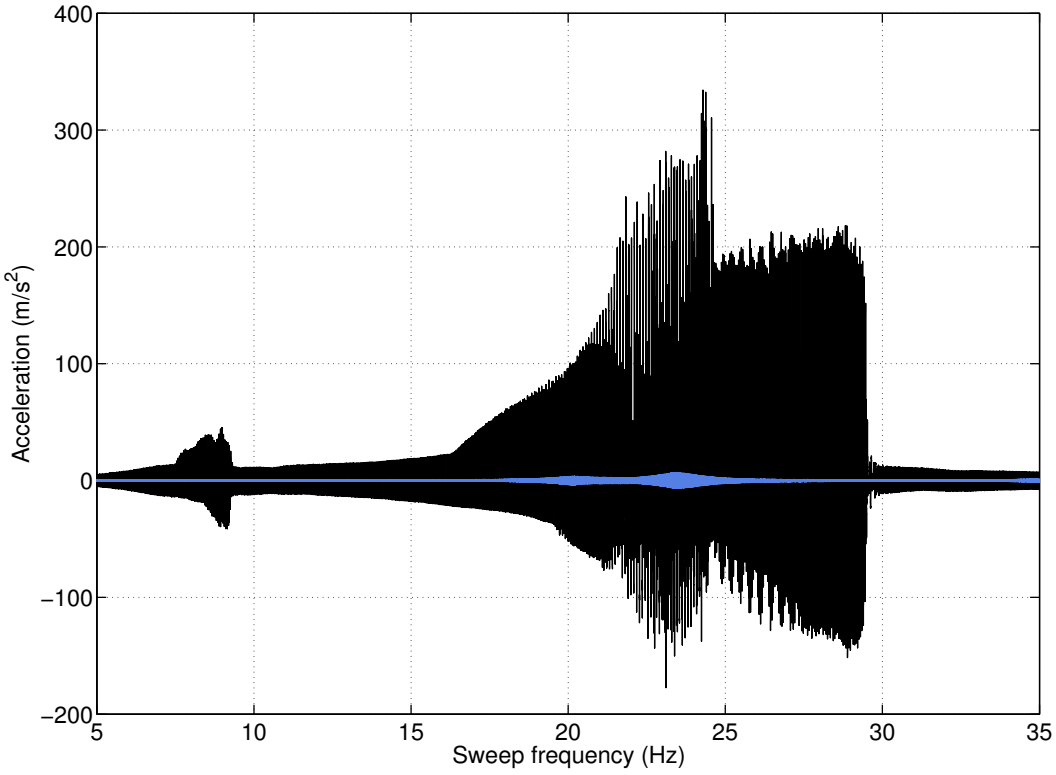

Figure 1.15: Acceleration measured at NC 3 at 0.1 g (in blue) and 1 g (in black).

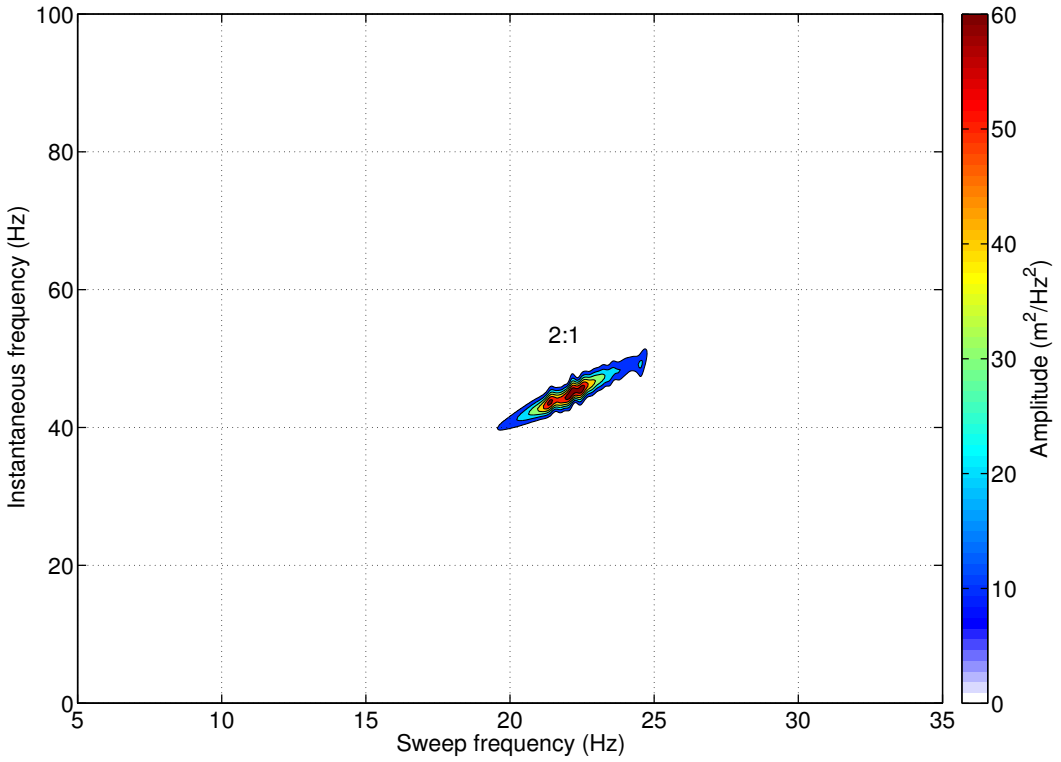

Figure 1.16: Evidence of another nonlinear modal interaction using the WT at NC 4 in the Y direction, presented in 5 – 35 Hz in linear scaling.

1.4.5 Numerical prediction of nonlinear modal interactions

The existence of modal interactions in a nonlinear system can be reliably predicted based on the analysis of its nonlinear normal modes (NNMs). Following Rosenberg's extended definition [46], NNMs are rigorously defined as nonnecessarily synchronous, periodic motions of the unforced, conservative system. In this section, the algorithm proposed in Ref. [90] is exploited to calculate the NNMs of the SmallSat satellite. To this end, a finite element model of the structure was developed. A detailed description of this model is provided in Chapter 3.

The frequencies associated with NNMs may vary with the amplitude of excitation, and for this reason, NNMs are usually depicted in a so-called frequency-energy plot (FEP). A mode in a FEP is represented by a point at a frequency corresponding to the minimal period of the periodic motion, and at an energy equal to the total conserved energy accompanying the motion. A branch in a FEP details the complete frequency-energy dependence of the considered mode.

The FEP of the first NNM of the spacecraft is illustrated in Fig. 1.17 (a). The plot

is formed by a main backbone to which a "tongue" is attached. For low energies, the frequency of the NNM remains constant since no mechanical stop is activated. The corresponding modal shape at point A is identical to the first normal mode of the underlying linear structure. Beyond an energy threshold of about 0.2 J, the relative displacements along X axis at NC 1 and NC 2 exceed the corresponding clearances of the WEMS device. The NNM frequency then rapidly increases because of the important difference between the stiffnesses of the elastomer plots and the mechanical stops.

When progressing along the nonlinear backbone curve, harmonic components of the fundamental frequency are generated. These harmonics may have a frequency close to the oscillation frequency of another NMM of the system. In this situation, a dynamic coupling between the two specific modes is established together with an energy transfer, leading to the appearance of a tongue of internal resonance. This phenomenon precisely results in Fig. 1.17 (a) in a 5:1 interaction. As energy increases along the branch of resonance, the fifth harmonic progressively becomes more important than the fundamental frequency. The modal shape depicted at point B has no linear counterpart, and is a mixing between NNM 1 and NNM 5. At the extremity of the tongue at point C, only the fifth harmonics remains, and the transition to NNM 5 is completed. Interactions between NNMs with similar topologies were previously reported in technical literature, *e.g.*, in Refs. [46, 51]. They were also observed in the case of a two-DOF vibro-impact system in [52], and in a full-scale aircraft in [45].

Fig. 1.17 (b) presents the FEP of the third NNM of the SmallSat. This is an interesting mode because it was shown experimentally to exhibit a 2:1 modal interaction in Section 1.4.4. Similarly to NNM 1 in Fig. 1.17 (a), the frequency of NNM 3 is constant at low energy because of the absence of impacts. Accordingly, the modal shape drawn at point A in Fig. 1.17 (b) is identical to the corresponding linear normal mode of the system. Beyond a certain energy threshold, mechanical stops are activated, and the NNM frequency severely increases due to the nonsmooth nature of the WEMS nonlinearities. Tongues of internal resonances are also created, during which one harmonic component of mode 3 excites another mode of the structure. More specifically, a 2:1 interaction can be distinguished. The modal shape depicted at its right end (point B) shows that a transition from a local mode involving the WEMS device to a more global mode of the instrument panel, located between 57 and 58 Hz, takes place. The excitation of this higher-frequency mode is possible thanks to the second harmonics generated by the nonlinear behaviour of mode 3. This is therefore the clear numerical confirmation of the experimental observation in Fig. 1.14. To the best of the author's knowledge, this is the first time that such an agreement between finite element predictions and experimental observations is reported in the case of an interaction between modes of a real-life structure with noncommensurate linear frequencies. Note that other modal interactions, namely 3:1, 9:1 and 26:1, are predicted by the continuation algorithm but are not further investigated in this thesis. We refer the interested reader to Ref. [95] for a more in-depth analysis. The numerical reproduction of the 2:1 internal resonance briefly described in Fig. 1.16 is also achieved therein.

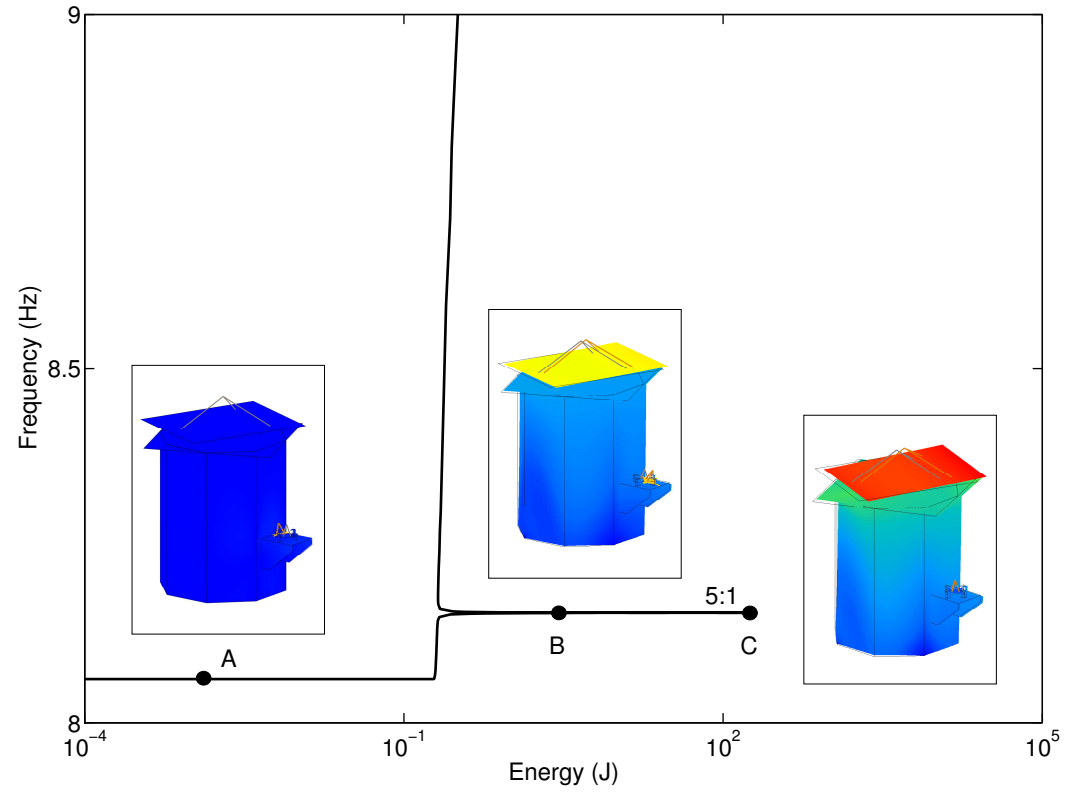

(a)

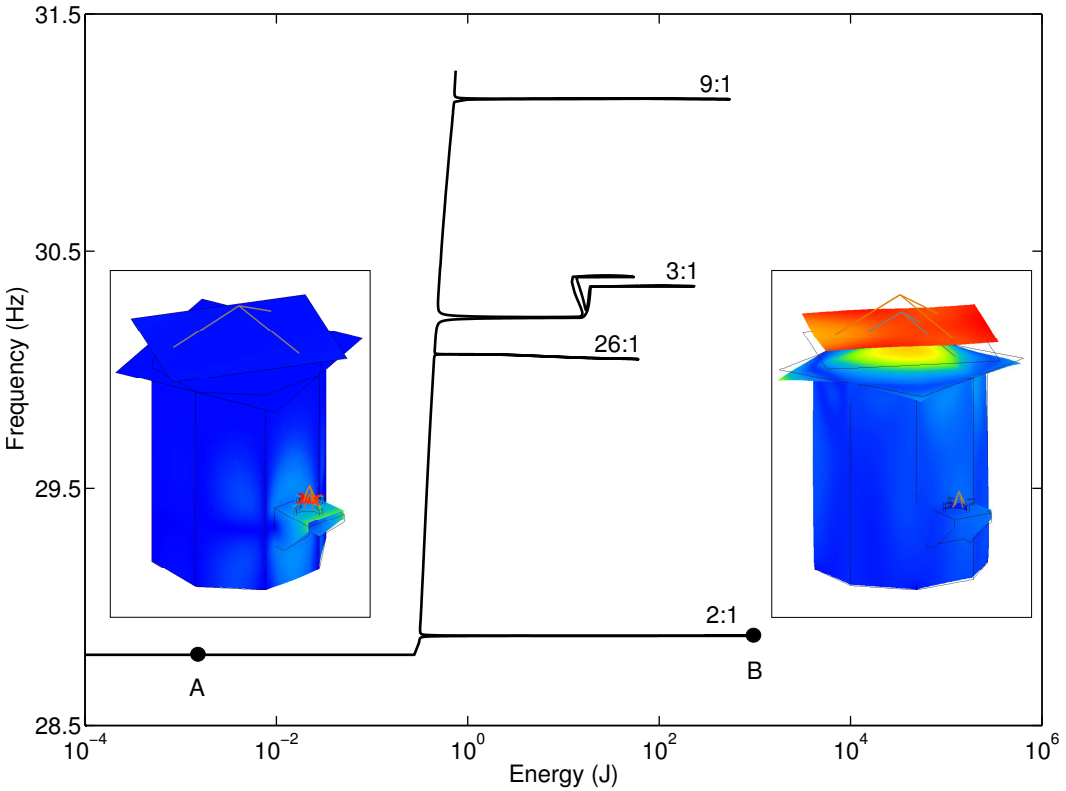

(b)

Figure 1.17: (a) FEP of NNM 1 with different modal shapes illustrating the mechanism of an internal resonance; (b) FEP of NNM 3 showing a 2:1 internal resonance correlating with the experimental observation in Fig. 1.14.

1.5 Parameter estimation in the presence of nonlinearity

Based on the choice made in Section 1.4 to use trilinear functional forms to characterise the WEMS elastic behaviour together with linear damping properties, the last step towards the establishment of a nonlinear model with good predictive capabilities is the estimation of the associated parameters, *i.e.*, the clearances, stiffness and damping coefficients. Quite surprisingly, a review of the technical literature about parameter estimation [47] reveals that base-sine excitations have so far received little attention in the nonlinear system identification community. This is manifestly because a measure of the force is a common requirement of most existing techniques, as is the case, for example, of the feedback-based [3] and reverse path [69, 98] methods. It turns out from this survey that the RFS method is one of the only approaches compatible with unmeasured base-sine excitations.

Though it was shown to extend to multi-DOF systems [62], the utilisation of the RFS method for parameter estimation is in general limited to small-scale structures, since the starting point of the approach is a rigorous writing of Newton's second law as discussed in Section 1.4.2. For instance, an impacting beam, presented in Fig. 1.2 (c), was studied in Ref. [43] as a single-DOF system through a band-limited excitation centred on its first natural frequency. The nonlinear identification of an automotive shock absorber that was constrained to move in only one direction to justify a single-DOF assumption is described in Ref. [124]. Al-Hadid and Wright also addressed a T-beam structure with well-separated bending and torsion modes in Ref. [6].

1.5.1 Multi-degree-of-freedom RFS-based methodology

In this section, it is demonstrated that the equations of motion of the WEMS mobile part, *i.e.* the dummy inertia wheel and its metallic cross-shaped support, can be formulated explicitly by asserting that it behaves as a rigid body. The dynamics of a rigid body is known to obey 6 scalar equations, namely 3 equations describing the translation of its centre of gravity, and 3 equations governing the rotation of the body around the centre of gravity. One herein concentrates on the translation along Z-axis of the centre of gravity of WEMS mobile part. Under the rigidity assumption, its kinetic energy T_z thus writes

$$T_z = \frac{1}{2}\, m\, \dot{z}_{CoG}^{\,2} \tag{1.7}$$

where m is the mass of the WEMS mobile part estimated at 8.75 kg and $\dot{z}_{CoG}$ the Z-velocity of its centre of gravity. This latter quantity can simply be evaluated as the mean of the axial velocities of two opposite NCs, namely

$$\dot{z}_{CoG} = \frac{\dot{z}_1 + \dot{z}_2}{2}. \tag{1.8}$$

The potential energy V_z associated with the trilinear stiffness forces in the system is formed as

$$V_z = V_{NC\,1}(z_1) + V_{NC\,2}(z_2) \tag{1.9}$$

where the contributions related to NC 3 and NC 4 are neglected as they involve considerably lower displacements. This results from the swing motion of the WEMS around Y-axis observed in the frequency band of interest (see Fig. 1.7 in Section 1.2). Similarly, damping forces in NC 3 and NC 4 are neglected in the writing of the dissipation function D_z, *i.e.*,

$$D_z = \frac{1}{2}\, c_{v,1}\, \dot{z}_1^{\,2} + \frac{1}{2}\, c_{v,2}\, \dot{z}_2^{\,2} \tag{1.10}$$

were $c_{v,1}$ and $c_{v,2}$ are the linear viscous damping coefficients of the NC 1 and NC 2 elastomer plots, respectively. Note that in the definition of the potential energy and dissipation function in Eqs. (1.9) and (1.10), respectively, it is assumed that there exists no coupling terms between the restoring forces at NC 1 and NC 2, so that their contributions can be separated. The axial equation of motion of the WEMS mobile part can finally be deduced from Lagrange's equation

$$\frac{d}{dt}\left(\frac{\partial T_z}{\partial \dot{z}}\right) - \frac{\partial T_z}{\partial z} + \frac{\partial V_z}{\partial z} + \frac{\partial D_z}{\partial \dot{z}} = 0. \tag{1.11}$$

Therefore, plugging Eqs. (1.7), (1.8), (1.9) and (1.10) into Eq. (1.11) yields

$$m\,\frac{\ddot{z}_1 + \ddot{z}_2}{2} + f_{NC\,1}(z_1) + c_{v,1}\,\dot{z}_1 + f_{NC\,2}(z_2) + c_{v,2}\,\dot{z}_2 = 0 \tag{1.12}$$

where $f_{NC\,1}$ and $f_{NC\,2}$ are the trilinear stiffness forces.

It is interesting to point out that the rigidity assumption imposes geometrical constraints onto the possible motion of the WEMS. Hence, if we denote by $\mathbf{v}_{12}$ and $\mathbf{v}_{34}$ the vectors joining opposite NCs, we have

$$\begin{cases} d(|\mathbf{v}_{12}|)/dt = d(|\mathbf{v}_{34}|)/dt = 0 \\ \mathbf{v}_{12} \cdot \mathbf{v}_{34} = 0 \\ \mathbf{v}_{12}/2 = \mathbf{v}_{34}/2 \end{cases} \tag{1.13}$$

where the third relationship is vectorial and should be understood as an element-by-element mean. Considering the metallic cross in Fig. 1.4 (b), these constraints express the invariability of the length of its two arms, their orthogonality and their common midpoints, respectively. Beyond this geometrical interpretation, they provide a means of verifying quantitatively the rigidity of the WEMS mobile part. To this end, Fig. 1.18 represents the deviations in percent from these six scalar constraint relationships, observed as the excitation frequency increases at the 1 g level. In general, they are well satisfied, and orthogonality is even found to be exactly verified, as intuitively guessed. The largest errors occur in the X direction, being however limited to less than 5 % at resonance. This confirms that the WEMS motion in the 5 – 15 Hz band is predominantly a swing oscillation entailing impacts onto the NC 1 and NC 2 stops.

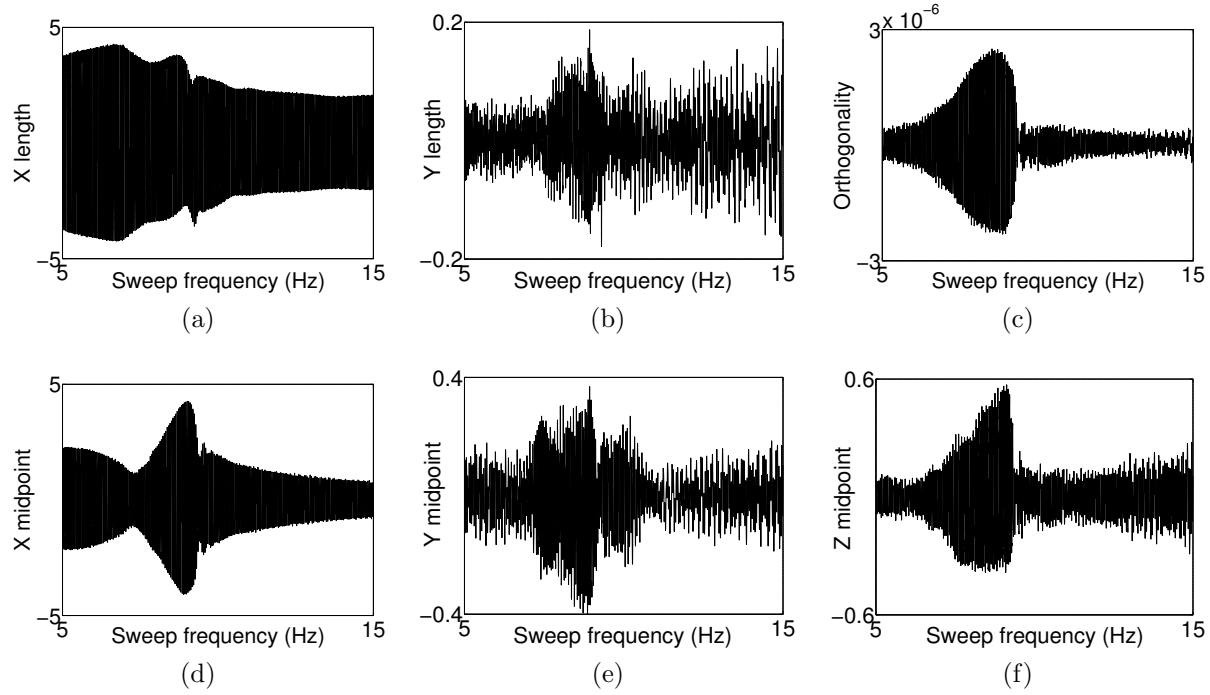

Figure 1.18: Verification of the geometrical conditions of rigidity at 1 g (in %). (a – b) Length invariability; (c) orthogonality; (d – f) midpoint coincidence.

The restoring force surfaces constructed via Eq. (1.12) at NC 1 and NC 2 given the triplets $(z_1,\, \dot{z}_1,\, f_{NC\,1} + c_{v,1}\, \dot{z}_1)$ and $(z_2,\, \dot{z}_2,\, f_{NC\,2} + c_{v,2}\, \dot{z}_2)$, respectively, can now be fitted using a trilinear model in stiffness and a linear model in damping. Curve-fitting results are given in Table 1.3, and were computed in the 8.5 – 9 Hz interval in which the first resonance of the system is located. The damping coefficients of the elastomer plots are found to be much larger than their reference value of 63 Ns/m (see Table 1.1), but are prone to significant uncertainty as they were computed from a limited number of low-displacement samples. The stiffness curves extracted as cross sections of the corresponding restoring force surfaces are plotted in Fig. 1.19 (a – b), together with the fitted trilinear models. The calculated coefficients show that the stiffnesses of the elastomer plots and mechanical stops match well with their reference values of 8 and 100, respectively (see Table 1.1), considering that no asymmetry is present in the reference model. Impacts are also found to be comparatively softer for positive displacements.

Moreover, one observes the existence of an even stiffness contribution in the curve in Fig. 1.19 (a), which is attributed to gravity and is in line with the WEMS asymmetry clearly evidenced in Figs. 1.8 (d), 1.10 (b) and 1.11 (b). This term essentially originates from an initial displacement of the system from its gravity-free equilibrium position [38]. Nevertheless, because of its marginal significance in the characterisation of the nonlinearity, no even term was incorporated in the WEMS stiffness model. It should also be noticed that there appears no gravity-induced trend in Fig. 1.19 (b). This is because

the bracket hardly bends at NC 2 and is thus locally close to its gravity-free equilibrium position.

Finally, a comparison between the measured and reconstructed restoring forces across NC 1 and NC 2 is shown in Fig. 1.20 (a – b), respectively, for sweep frequencies in 8.6 – 8.7 Hz. The agreement between the two curves is satisfactory in view of the complexity of the time series. In particular, the fundamental frequency of vibration is correctly retrieved by the model, and the increase of stiffness for positive displacements in Fig. 1.20 (a) is also well represented. However, for negative displacements, the reconstructed curves fail to capture the complete behaviour of the system during impacts. This discrepancy, which can be attributed to viscoelastic effects introduced by the elastomer components of the WEMS and contact chattering, is further analysed in the next section. One also notes that the identification of the NC 3 and NC 4 parameters could be achieved using a similar procedure, but this would require additional testing of the spacecraft as the corresponding mechanical stops were not activated during the measurement campaign considered herein.

	Reference value	NC 1	NC 2
Linear damping coefficient c_v (Ns/m)	63	218.29	147.75
Linear stiffness coefficient k	8	8.30	9.21
Clearance a_-	1.5	1.01	0.84
Clearance a_+	1.5	1.55	1.62
Nonlinear stiffness coefficient k_-	100	118.07	116.73
Nonlinear stiffness coefficient k_+	100	79.40	88.41

Table 1.3: Damping coefficients, stiffness coefficients and clearances of NC 1 and NC 2 estimated using the RFS method and compared with their reference values.

1.5.2 Internal force relaxation and chattering

The restoring force surface derived at NC 1 from Eq. (1.12) is shown in Fig. 1.21, and exhibits an asymmetry with respect to the zero-velocity axis. Specifically, for negative displacements, the appearance of large force values, signalling impacts on the mechanical stop, dies out as velocity goes from negative to positive values. This suggests a viscoelastic behaviour of the elastomer components in the system, namely internal force relaxation. This phenomenon is better perceived in Fig. 1.22 (a – b) where the relative displacement and restoring force corresponding to Fig. 1.21 are displayed versus sweep frequency. The joint analysis of the two graphs clearly demonstrates the decrease of the internal force for constant negative displacements around -1. This motivated us to construct the stiffness curves in Fig. 1.19 (a – b) as cross sections of the corresponding restoring force surfaces for velocities lower than -0.07 m/s, *i.e.*, prior to the initiation of force relaxation.

Furthermore, it can be estimated that a single relaxation cycle lasts 0.025 s, which can appear to be extremely fast, but may result from the high speed of loading (typically

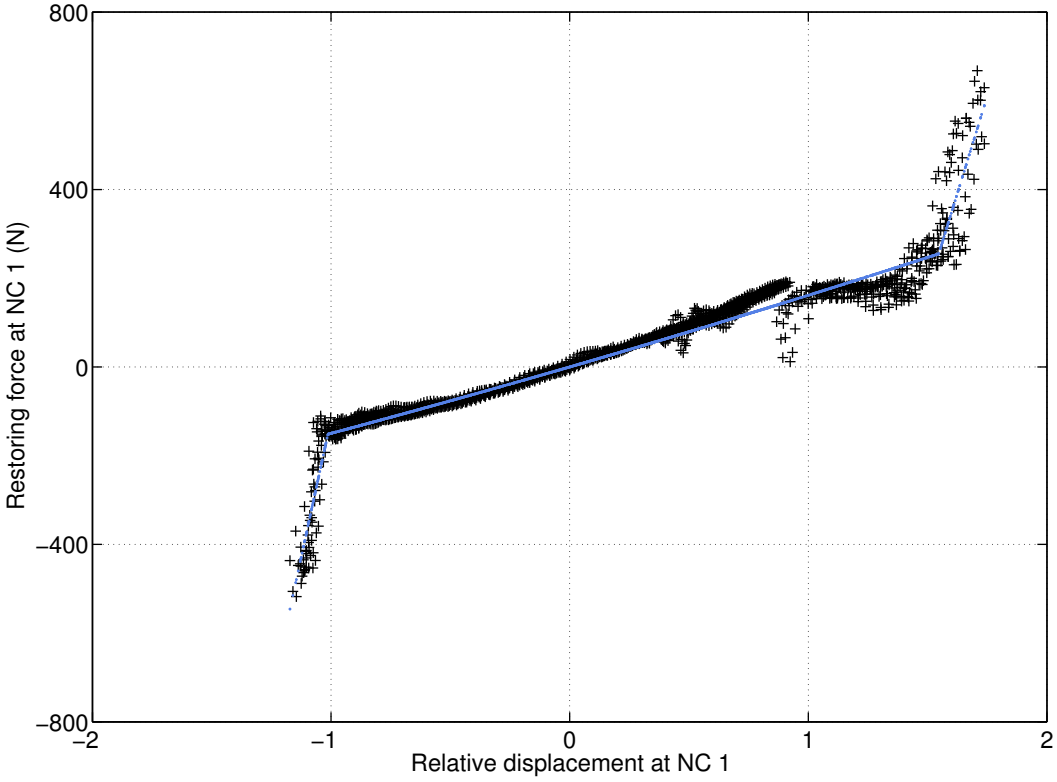

(a)

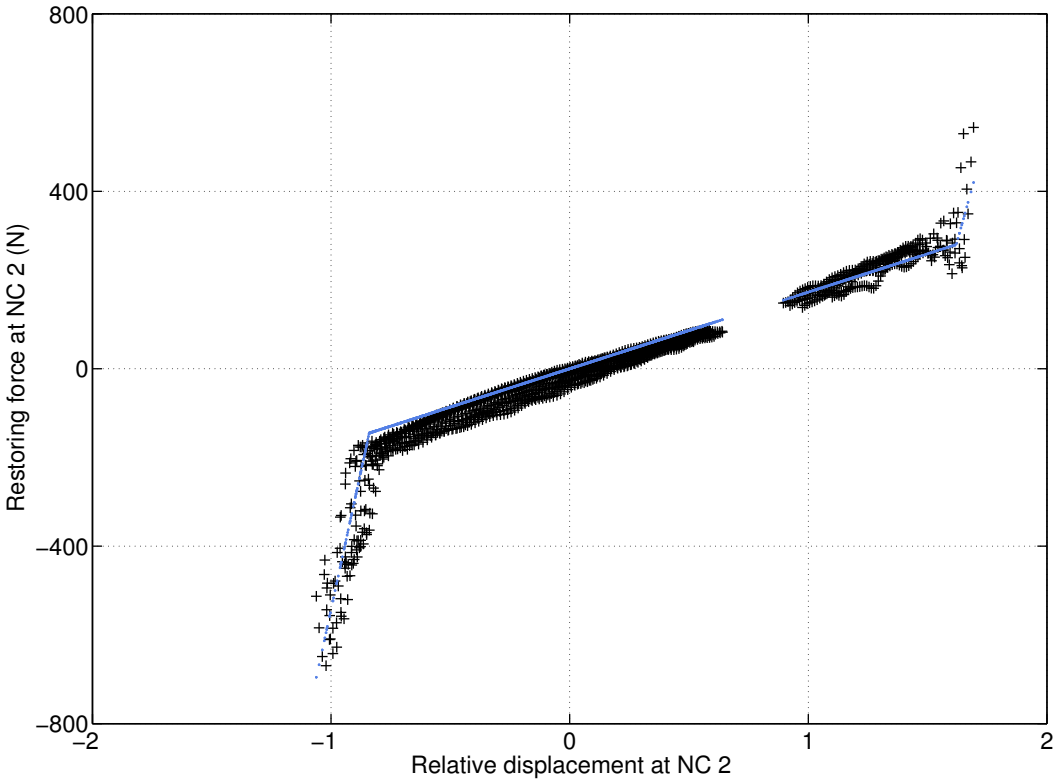

(b)

Figure 1.19: WEMS nonlinear stiffness curves constructed based upon Eq. (1.12) (in black) and compared with the fitted trilinear models (in blue). (a) NC 1; (b) NC 2.

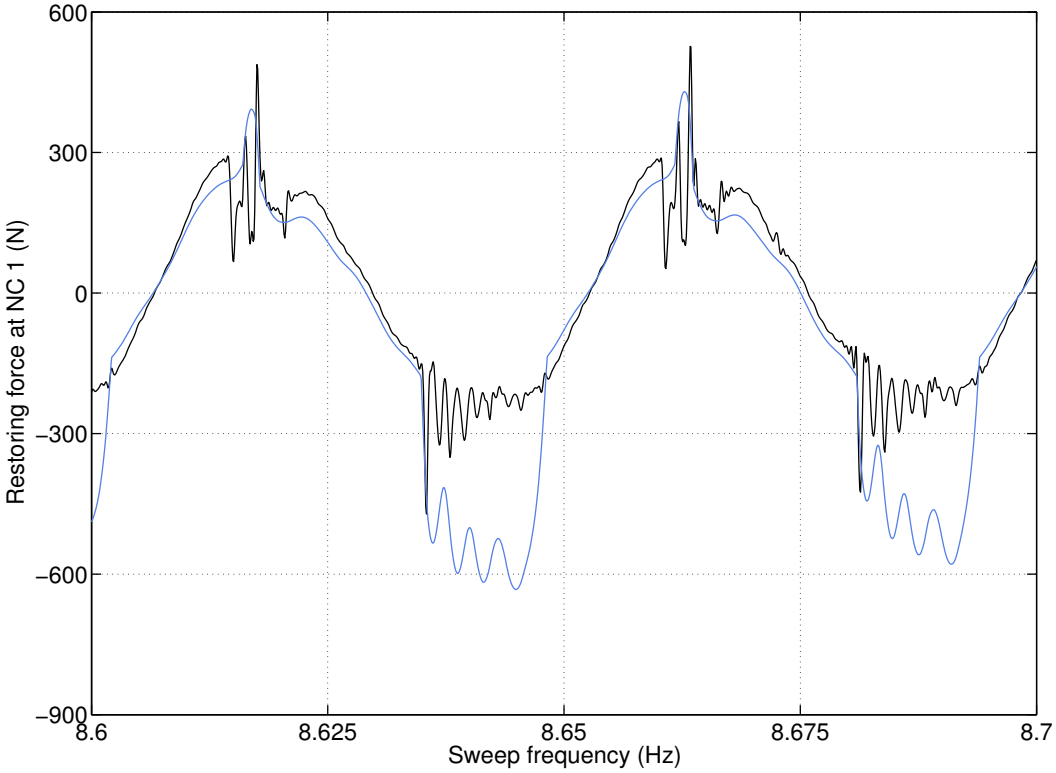

(a)

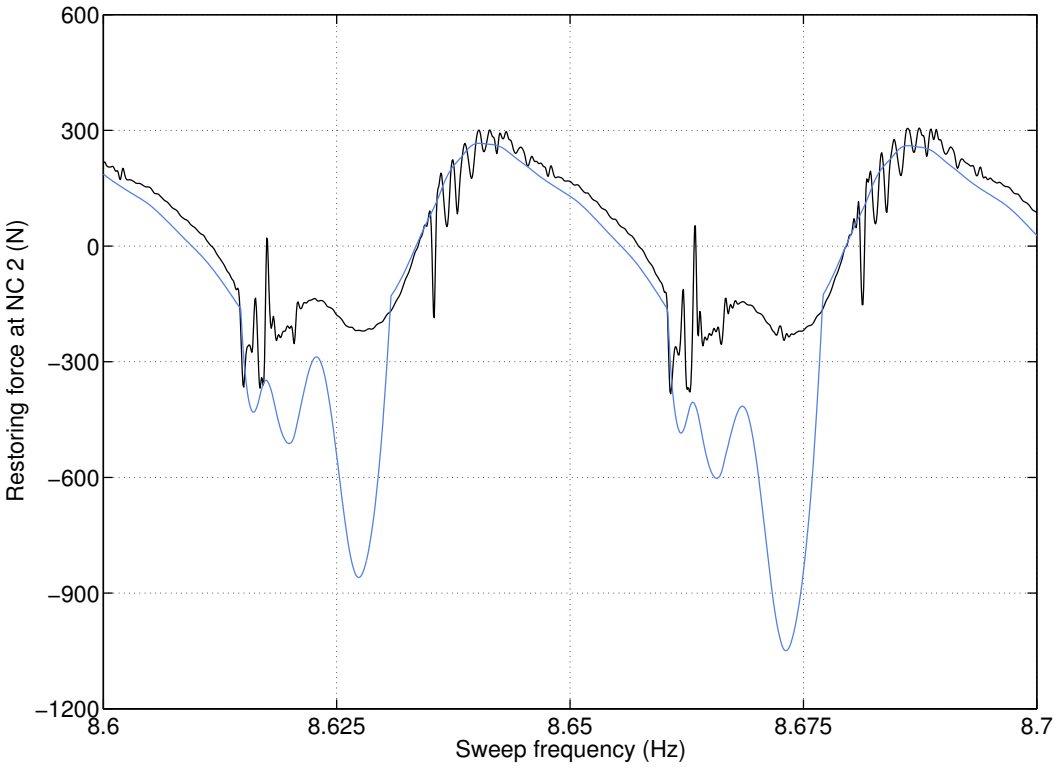

(b)

Figure 1.20: Comparison between the measured (in black) and reconstructed (in blue) restoring forces versus sweep frequency. (a) NC 1; (b) NC 2.

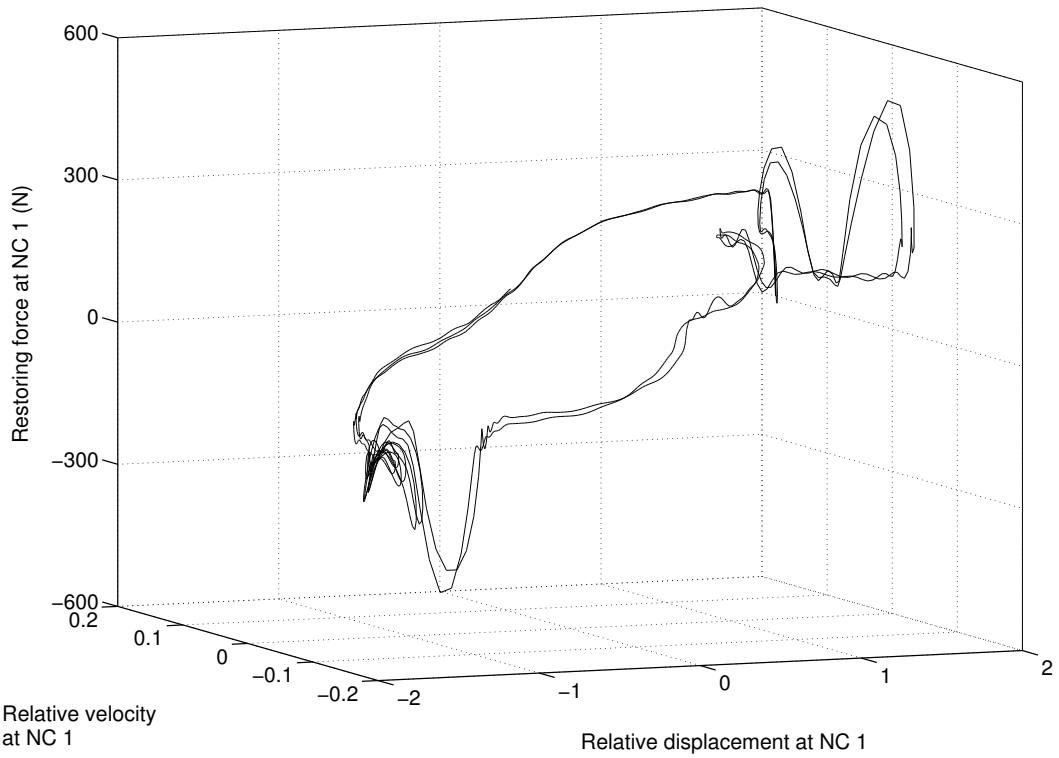

Figure 1.21: Restoring force surface measured at NC 1, and associated with the stiffness curve displayed in Fig. 1.19 (a).

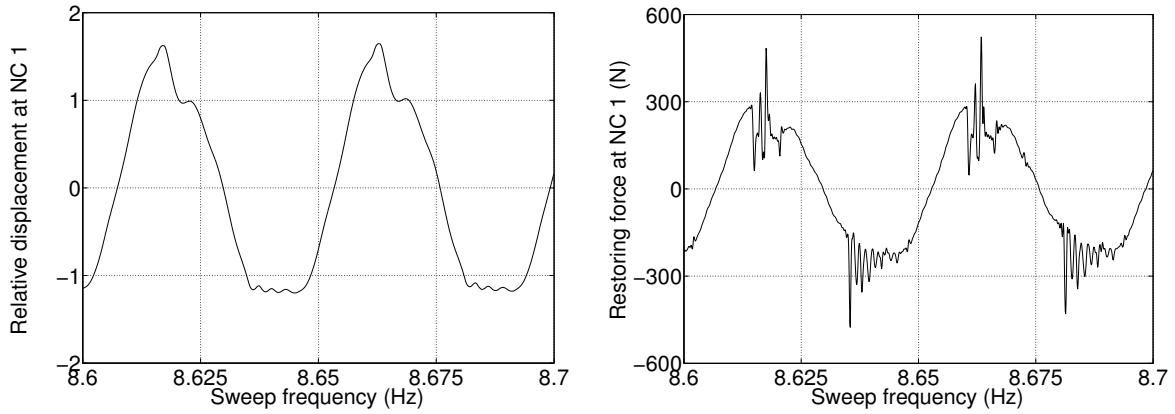

(a) (b)

Figure 1.22: Internal force relaxation and chattering evidenced through the comparison of the (a) relative displacement and (b) restoring force at NC 1 plotted versus sweep frequency.

0.15 m/s and acceleration of about 100 m/s^2), the prestress in the filtering plots and the limited thickness of the elastomer layer hit during impacts. Prestress combined with speed of loading could also explain why relaxation is not manifest for positive velocities. It is also interesting to note that the displacement in Fig. 1.22 (a) is not rigorously constant within the relaxation regions, but exhibits rapid bounces. These bounces are interpreted as a contact chattering phenomenon [55, 121] triggered by the conflict between prestress and restoring forces. Chattering explains why relaxation occurs through oscillations in Fig. 1.22 (b) and not as a monotonic decrease. Moreover, in the simple Maxwell model for viscoelasticity, the stress is found to decrease exponentially with time at constant strain. The decay envelopes in the relaxation regions in the same figure confirm this prediction. One finally presents in Fig. 1.23 the locus of the minima and maxima of the oscillating force decays for 6 successive relaxation regions. Minima and maxima are depicted through squares and circles, respectively, and a typical force relaxation pattern is also superimposed in this figure. The squares and circles are both found to form clusters, which indicates that the relaxation behaviour observed in Fig. 1.22 (b) is in fact generic during impacts on the mechanical stops.

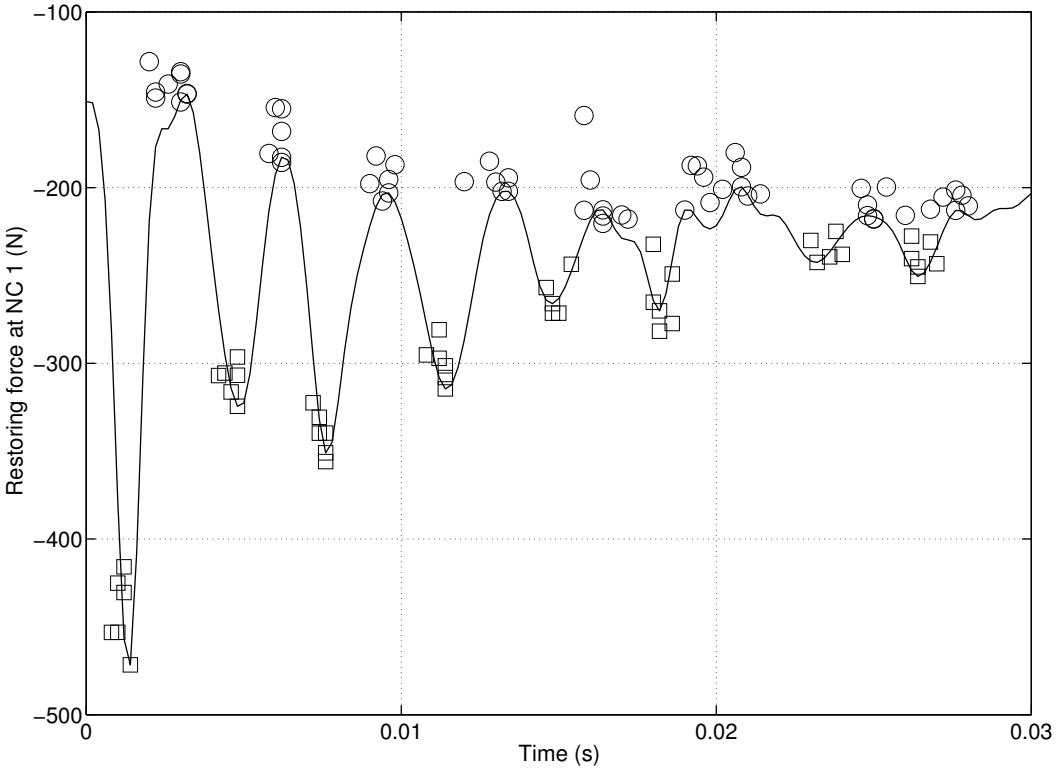

Figure 1.23: Locus of the minima and maxima of the oscillating force decays for 6 successive relaxation regions depicted through squares and circles, respectively. A typical force relaxation pattern is also superimposed to the clusters of minima and maxima.

1.6 Concluding remarks

The first objective of this chapter was to address the experimental identification of the SmallSat spacecraft. For this purpose, no dedicated tests were performed, but rather typical sine-sweep data collected during a qualification campaign were exploited. The complete progression through nonlinearity detection, characterisation and parameter estimation was carried out by means of several existing analysis techniques. Their combined utilisation allowed to achieve an accurate modelling of the nonlinear components, including the estimation of their clearances and stiffness properties.

The second objective of the chapter was to demonstrate that the complex dynamics that can be obtained during numerical simulations of nonlinear systems with low dimensionality can also be observed in experimental conditions commonly endured by engineering structures in industry. This includes intrinsically nonlinear phenomena such as jumps and modal interactions, but also force relaxation and chattering during impacts on the mechanical stops. In particular, the evidence of modal interactions between modes with noncommensurate linear frequencies is interesting, as they were so far rarely reported in the technical literature in the case of real-life, strongly nonlinear systems. They were also successfully correlated with predictions obtain by continuation algorithms applied to a finite element model of the spacecraft.

Chapter 2

Frequency-domain subspace identification for nonlinear systems

Abstract

This second chapter introduces a new subspace identification method dedicated to nonlinear systems by revisiting existing linear frequency-domain subspace algorithms. The proposed frequency-domain nonlinear subspace identification (FNSI) method is applicable to multi-input, multi-output systems with high modal density and nonproportional damping, and makes no assumption as to the importance of nonlinearities in the system dynamics. An identification theorem is stated and proved, and the consistency of the developed algorithm is investigated in the presence of measurement noise. The FNSI method is demonstrated numerically on a Duffing oscillator, and experimentally on an electronic circuit emulating the behaviour of a single-degree-of-freedom mechanical system with one nonlinear spring.

2.1 Introduction

Subspace methods are widely recognised as powerful identification tools for linear systems, arguably because they are applicable in the multi-input, multi-output (MIMO) case, and are noniterative and hence computationally tractable. They were first introduced in the time domain [68, 116] and later revisited to consider frequency response functions (FRFs) [63, 117] and power spectra [119] as input data. Since then, subspace-based algorithms have been successfully applied to a wide variety of real-life systems, *e.g.*, in control [1] or biomedical [81] engineering. In the field of structural dynamics, they are routinely used not only for modal analysis [97], but also for advanced processing such as damage detection and structural health monitoring [65].

However, we stressed in the introductory chapter of the dissertation that there now exists a need for developing effective nonlinear system identification methodologies to meet the ever increasing performance demanded in industry. An important theoretical contribution in this context was introduced by Adams and Allemang. They interpreted the effect of structural nonlinearities as an internal feedback into the underlying linear system [2]. Based on this interpretation, they introduced a MIMO, least-squares parameter estimation method for nonlinear systems, which naturally decouples the linear and nonlinear parameters [3]. The feedback formulation was more recently exploited by Lacy and Bernstein [49] who derived a time-domain subspace identification algorithm for nonlinear feedback systems. A numerically robust implementation of this algorithm was soon proposed by Marchesiello and Garibaldi in Ref. [58], yielding superior accuracy. In view of the efficacy of subspace methods, these nonlinear subspace algorithms opened up new horizons for the identification of nonlinear structural models.

Relying on the feedback interpretation, the present chapter introduces a new subspace identification method dedicated to nonlinear systems by revisiting existing linear frequency-domain subspace algorithms. The proposed frequency-domain nonlinear subspace identification (FNSI) method is applicable to MIMO systems with high modal density and high nonproportional damping, and makes no assumption as to the importance of nonlinearities in the system dynamics. Moreover, the use of frequency-domain data contributes to substantially decreasing the computational burden involved in the identification by focusing on specific frequency ranges of interest. Finally, one of the other important advantages of the FNSI algorithm is that its implementation relies on robust tools from numerical analysis, such as the QR and singular value decompositions.

The chapter is organised as follows. The theoretical background of the FNSI method is introduced in great detail from Section 2.2 to Section 2.8. In particular, an identification theorem is stated and proved in Section 2.5. The consistency of the developed algorithm is also investigated in the presence of measurement noise in Section 2.7. The FNSI method is illustrated numerically on an academic example, namely a Duffing oscillator, in Section 2.9. The experimental identification of an electronic circuit emulating the behaviour of a single-degree-of-freedom mechanical system with one nonlinear spring, referred to as

the Silverbox benchmark, is finally addressed in Section 2.10. Measurements on the Silverbox were acquired at the department ELEC of the Vrije Universiteit Brussel (Brussels, Belgium) in collaboration with Prof. J. Schoukens. The content of the chapter is to a large extent described in Ref. [74].

2.2 Nonlinear model equations in the physical space and problem statement

The FNSI method is dedicated to nonlinear vibrating systems possessing an underlying linear regime of motion in stiffness and damping. The vibrations of such nonlinear systems obey Newton's second law of dynamics

$$\mathbf{M}\,\ddot{\mathbf{q}}(t) + \mathbf{C}_v\,\dot{\mathbf{q}}(t) + \mathbf{K}\,\mathbf{q}(t) + \mathbf{g}(\mathbf{q}(t),\dot{\mathbf{q}}(t)) = \mathbf{p}(t) \tag{2.1}$$

where $\mathbf{M}$, $\mathbf{C}_v$, $\mathbf{K} \in \mathbb{R}^{n_p \times n_p}$ are the mass, linear viscous damping and linear stiffness matrices, respectively; $\mathbf{q}(t)$ and $\mathbf{p}(t) \in \mathbb{R}^{n_p}$ are the generalised displacement and external force vectors, respectively; $\mathbf{g}(t) \in \mathbb{R}^{n_p}$ is the essentially nonlinear, *i.e.* nonlinearisable, restoring force vector comprising elastic and dissipative contributions. In other words, the notation in Eq. (2.1) assumes that all linear components of the restoring forces in the system are included in the matrices $\mathbf{K}$ and $\mathbf{C}_v$. The number of degrees of freedom (DOFs) of the structure obtained after spatial discretisation, which is the dimension of the physical space, is denoted n_p. The amplitude, direction, location and frequency content of the excitation $\mathbf{p}(t)$ determine in which regime, linear or nonlinear, the structure behaves.

The nonlinear restoring force term $\mathbf{g}(\mathbf{q}(t),\dot{\mathbf{q}}(t))$ in Eq. (2.1) is expressed by means of a linear combination of known basis functions $\mathbf{h}_a(\mathbf{q}(t),\dot{\mathbf{q}}(t))$ as

$$\mathbf{g}(\mathbf{q}(t),\dot{\mathbf{q}}(t)) = \sum_{a=1}^{s} c_a\,\mathbf{h}_a(\mathbf{q}(t),\dot{\mathbf{q}}(t)). \tag{2.2}$$

In this sum, the coefficients c_a associated with the nonlinear basis functions $\mathbf{h}_a(\mathbf{q}(t),\dot{\mathbf{q}}(t))$ play a role similar to the linear stiffness and viscous damping coefficients contained in the matrices $\mathbf{K}$ and $\mathbf{C}_v$ in Eq. (2.1), respectively. Note that the total number of basis functions s introduced in the model may be larger than the number of physical nonlinearity sources in the system, as multiple model terms are generally required to capture the behaviour of a single nonlinear component. The motivation for choosing a linear-in-the-parameters representation of nonlinear restoring forces is to not resort to optimisation techniques in the identification process, and avoid issues related to initialisation and convergence thereof. This only excludes from the scope of the FNSI method specific basis functions, for example, rational functions, transcendental functions with unknown coefficients in their arguments, such as the arctangent functions utilised to model softening effects in joints [66], or merely polynomial expansions with unknown exponents. Nonlinearity representations with internal variables, such as the Bouc-Wen model of hysteresis, cannot similarly be addressed in the FNSI framework.

Given measurements of $\mathbf{p}(t)$ and $\mathbf{q}(t)$ or its derivatives, and an appropriate selection of the functionals $\mathbf{h}_a(t)$, the FNSI method aims at computing estimates of (i) the FRF matrix

$$\mathbf{G}_p(\omega) = \left(-\omega^2\,\mathbf{M} + j\,\omega\,\mathbf{C}_v + \mathbf{K}\right)^{-1} \tag{2.3}$$

describing the underlying linear properties of the system in Eq. (2.1), where ω is the pulsation and j the imaginary unit, and (ii) the nonlinear coefficients c_a in Eq. (2.2). This is achieved through the intermediate construction of a state-space model describing the dynamics governed by Eq. (2.1), as detailed from Section 2.3 to Section 2.7. Models in the state space are appealing because of their intrinsic capability to represent systems with multiple inputs and outputs. The conversion from state space to the physical-space parameters $\mathbf{G}_p(\omega)$ and c_a is discussed in Section 2.8.

2.3 Feedback interpretation and state-space model equations

The FNSI approach builds on a block-oriented interpretation of nonlinear structural dynamics, which sees nonlinearities as a feedback into the linear system in the open loop [2, 3], as depicted in Fig. 2.1. This interpretation boils down to moving the nonlinear internal forces in Eq. (2.1) to the right-hand side, and viewing them as additional external forces applied to the underlying linear structure, that is,

$$\mathbf{M}\,\ddot{\mathbf{q}}(t) + \mathbf{C}_v\,\dot{\mathbf{q}}(t) + \mathbf{K}\,\mathbf{q}(t) = \mathbf{p}(t) - \sum_{a=1}^{s} c_a\,\mathbf{h}_a(\mathbf{q}(t), \dot{\mathbf{q}}(t)). \tag{2.4}$$

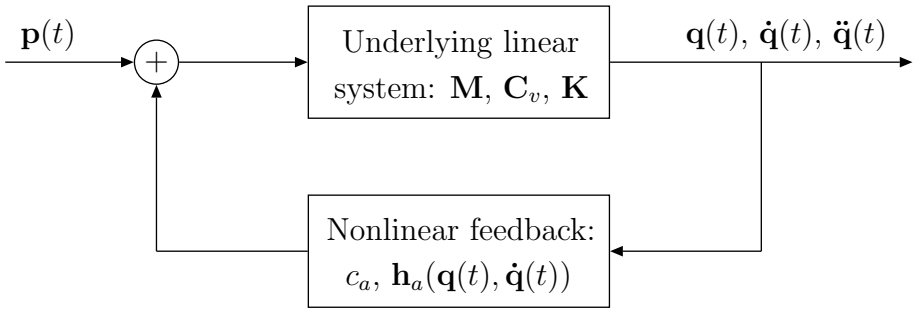

Figure 2.1: Feedback interpretation of nonlinear structural dynamics [2, 3].

Note that the model structure in Fig. 2.1 shares similarities with the class of Hammerstein models for which the input to a linear system is the output of a static nonlinearity. Assuming that displacements are measured and defining the state vector $\mathbf{x} = \begin{pmatrix}\mathbf{q}^T & \dot{\mathbf{q}}^T\end{pmatrix}^T \in \mathbb{R}^{n_s}$,

where T is the matrix transpose, Eq. (2.4) is recast in the state space as the set of first-order equations

$$\left\{ \begin{array}{rcl} \dot{\mathbf{x}}(t) & = & \mathbf{A}\,\mathbf{x}(t) + \mathbf{B}\,\mathbf{e}(t) \\ \mathbf{q}(t) & = & \mathbf{C}\,\mathbf{x}(t) + \mathbf{D}\,\mathbf{e}(t) \end{array} \right. \tag{2.5}$$

where the vector $\mathbf{e} \in \mathbb{R}^{(s+1)\,n_p}$, termed the *extended input vector*, concatenates the external forces $\mathbf{p}(t)$ and the nonlinear basis functions $\mathbf{h}_a(t)$. The matrices $\mathbf{A} \in \mathbb{R}^{n_s \times n_s}$, $\mathbf{B} \in \mathbb{R}^{n_s \times (s+1)\,n_p}$, $\mathbf{C} \in \mathbb{R}^{n_p \times n_s}$ and $\mathbf{D} \in \mathbb{R}^{n_p \times (s+1)\,n_p}$ are the state, extended input, output and direct feedthrough matrices, respectively. The dimension of the state space is $n_s = 2\,n_p$. State-space and physical-space matrices correspond through the relations

$$\mathbf{A} = \begin{pmatrix} \mathbf{0}^{n_p \times n_p} & \mathbf{I}^{n_p \times n_p} \\ -\mathbf{M}^{-1}\,\mathbf{K} & -\mathbf{M}^{-1}\,\mathbf{C}_v \end{pmatrix} \; ; \quad \mathbf{B} = \begin{pmatrix} \mathbf{0}^{n_p \times n_p} & \mathbf{0}^{n_p \times n_p} & \mathbf{0}^{n_p \times n_p} & \dots & \mathbf{0}^{n_p \times n_p} \\ \mathbf{M}^{-1} & -c_1\,\mathbf{M}^{-1} & -c_2\,\mathbf{M}^{-1} & \dots & -c_s\,\mathbf{M}^{-1} \end{pmatrix}$$

$$\mathbf{C} = \begin{pmatrix} \mathbf{I}^{n_p \times n_p} & \mathbf{0}^{n_p \times n_p} \end{pmatrix} \; ; \quad \mathbf{D} = \mathbf{0}^{n_p \times (s+1)\,n_p} \tag{2.6}$$

where $\mathbf{0}$ and $\mathbf{I}$ are the zero and identity matrices, respectively. In a standard measurement setup, only limited sets of DOFs in $\mathbf{p}(t)$ and $\mathbf{q}(t)$ are excited and observed, respectively. The identification problem is therefore preferably stated in terms of m applied forces and l measured displacements collected in the vectors $\mathbf{u}(t) \in \mathbb{R}^{m \leq n_p}$ and $\mathbf{y}(t) \in \mathbb{R}^{l \leq n_p}$, respectively. Accordingly, the nonlinear basis functions vector is formed as $\mathbf{h}_a(\mathbf{y}(t), \dot{\mathbf{y}}(t))$, and the extended input vector is $\mathbf{e}(t) \in \mathbb{R}^{m+sl}$, concatenating $\mathbf{u}(t)$ and $\mathbf{h}_a(\mathbf{y}(t), \dot{\mathbf{y}}(t))$. Eqs. (2.5) become

$$\left\{ \begin{array}{rcl} \dot{\mathbf{x}}(t) & = & \mathbf{A}\,\mathbf{x}(t) + \mathbf{B}\,\mathbf{e}(t) \\ \mathbf{y}(t) & = & \mathbf{C}\,\mathbf{x}(t) + \mathbf{D}\,\mathbf{e}(t) \end{array} \right. \tag{2.7}$$

where $\mathbf{A}$, $\mathbf{B}$, $\mathbf{C}$ and $\mathbf{D}$ are now projections of the original matrices onto the controlled and observed DOFs. Note that no identifiability condition constraints the number of measured displacements, provided that the nonlinear basis functions $\mathbf{h}_a(\mathbf{y}(t), \dot{\mathbf{y}}(t))$ can be formed form the recorded channels. In particular, l can be lower than the model order n_s. In practice, the number of instrumented locations is dictated by the spatial resolution of the structural mode shapes required to limit linear modelling errors, and by the number of available sensors.

Although there is a complete equivalence between time- and frequency-domain system identification [92], differences may arise in the way acquired information is interpreted and exploited in the two domains. In particular, a distinct advantage of frequency-domain data is that they provide intuitive insights into the nature and importance of nonlinearity, for instance by analysing the harmonic components in the response spectra (see Fig. 1.12 in Chapter 1) or the distortions affecting the resonance peaks in FRF plots [103]. By truncating the measured frequency axis, frequency-domain data can also be made more compact than time-domain data, which may therefore substantially decrease the computational burden. The price to pay is that information is discarded outside the band of interest, but the user has full control over the frequencies exploited in the identification process. By contrast, in a time-domain approach, the time series cannot be decimated without affecting the entire frequency spectrum. These arguments motivate the development of a nonlinear subspace identification method in the frequency domain. The discrete

Fourier transform (DFT) is applied to Eqs. (2.7) to write

$$\left\{ \begin{array}{rcl} \xi_k \, \mathbf{X}(k) & = & \mathbf{A} \, \mathbf{X}(k) + \mathbf{B} \, \mathbf{E}(k) \\ \mathbf{Y}(k) & = & \mathbf{C} \, \mathbf{X}(k) + \mathbf{D} \, \mathbf{E}(k) \end{array} \right. \tag{2.8}$$

where $\xi_k = s_k = j\,2\pi\,f_s\,k/N$ is the Laplace transform variable for continuous-time models, and $\xi_k = z_k = e^{\,j\,2\pi\,k/N}$ is the Z-transform variable for discrete-time models; f_s is the sampling frequency, k the frequency line, and N the number of recorded time samples; $\mathbf{X}(k)$, $\mathbf{E}(k)$ and $\mathbf{Y}(k)$ are the DFTs of $\mathbf{x}(t)$, $\mathbf{e}(t)$ and $\mathbf{y}(t)$, respectively.

Provided that the time signal $x(t)$ is periodic and observed over an integer number of periods in steady-state conditions, its DFT $X(k)$ is given by

$$X(k) = \sum_{t=0}^{N-1} x(t) \, e^{-j\,2\pi\,k\,t/N}. \tag{2.9}$$

It is strongly advised to opt for periodic excitations in frequency-domain system identification because the leakage error can be completely avoided in this case. An important exception is the burst signal whose DFT spectrum is also an exact copy of the continuous spectrum at the DFT lines. If it is not possible to enforce periodicity during the experiment, windowing techniques can be employed to mitigate leakage distortions as covered in Ref. [33]. Other advantages of opting for periodic inputs is the improvement of the signal-to-noise ratio (SNR) obtained by averaging over the periods, and the possibility to separate signal from noise in measured data, which leads to nonparametric estimates of the input and output noise covariance matrices [92]. For all these reasons, periodic excitation signals will be considered throughout the present thesis.

2.4 Formulation of an output-state-input model equation

Frequency-domain subspace methods estimate the matrices $\mathbf{A}$, $\mathbf{B}$, $\mathbf{C}$ and $\mathbf{D}$ based on a reformulation of the state-space relations in Eqs. (2.8) in matrix form. For this purpose, the measured output spectra are organised in a complex-valued matrix $\mathbf{Y}_i^c$ defined as

$$\mathbf{Y}_i^c = \left(\begin{array}{cccc} \mathbf{Y}(1) & \mathbf{Y}(2) & \dots & \mathbf{Y}(F) \\ \xi_1 \, \mathbf{Y}(1) & \xi_2 \, \mathbf{Y}(2) & \dots & \xi_F \, \mathbf{Y}(F) \\ \xi_1^2 \, \mathbf{Y}(1) & \xi_2^2 \, \mathbf{Y}(2) & \dots & \xi_F^2 \, \mathbf{Y}(F) \\ \vdots & & & \\ \xi_1^{i-1} \, \mathbf{Y}(1) & \xi_2^{i-1} \, \mathbf{Y}(2) & \dots & \xi_F^{i-1} \, \mathbf{Y}(F) \end{array} \right) \in \mathbb{C}^{\,li \times F} \tag{2.10}$$

where superscript c stands for *complex*, and where i is the user-defined number of block rows in $\mathbf{Y}_i^c$ and F the number of frequency lines exploited in the identification. Defining

$\zeta = \mathrm{diag}\,(\xi_1\, \xi_2\, \ldots\, \xi_F) \in \mathbb{C}^{F\times F}$ and grouping frequencies from lines 1 to F, $\mathbf{Y}_i^c$ is recast into

$$\mathbf{Y}_i^c = \begin{pmatrix} \mathbf{Y} \\ \mathbf{Y}\,\zeta \\ \mathbf{Y}\,\zeta^2 \\ \ldots \\ \mathbf{Y}\,\zeta^{i-1} \end{pmatrix}. \tag{2.11}$$

The matrix of the extended input spectra is similarly formed as

$$\mathbf{E}_i^c = \begin{pmatrix} \mathbf{E} \\ \mathbf{E}\,\zeta \\ \mathbf{E}\,\zeta^2 \\ \ldots \\ \mathbf{E}\,\zeta^{i-1} \end{pmatrix} \in \mathbb{C}^{(m+sl)\,i\times F}. \tag{2.12}$$

It is well-known that, due to the particular structure of the data matrices $\mathbf{Y}_i^c$ and $\mathbf{E}_i^c$, referred to as a block-Vandermonde structure in linear algebra, frequency-domain subspace algorithms formulated in continuous time are badly conditioned and generally lead to poor estimates. Solutions exist to improve the conditioning of the continuous-time subspace inverse problem, such as the use of the Forsythe recursions [117] or the w-operator [128]. Nevertheless, we prefer to guarantee the good conditioning of the proposed approach by fitting a discrete-time model to measured data, and next converting the resulting state-space matrices to the continuous-time domain. This comes down to setting $\xi_k = z_k$ in Eqs. (2.11) and (2.12).

The conversion of the state-space matrices from discrete to continuous time can be achieved through the following relations, considering a sampling frequency f_s,

$$\mathbf{A}_{ct} = \mathrm{logm}(\mathbf{A}_{dt})/f_s\,; \quad \mathbf{B}_{ct} = \mathbf{A}_{ct}(\mathbf{A}_{dt} - \mathbf{I}^{\,n_s\times n_s})^{-1}\mathbf{B}_{dt}$$

$$\mathbf{C}_{ct} = \mathbf{C}_{dt}\,; \quad \mathbf{D}_{ct} = \mathbf{D}_{dt} \tag{2.13}$$

where subscripts *ct* and *dt* stand for *continuous-time* and *discrete-time*, respectively, and where logm is the matrix logarithm. One should stress that Eqs. (2.13) are rigorously valid, *i.e.*, the conversion introduces no systematic error in the continuous-time model, if the elements of the extended input vector $\mathbf{e}(t)$ are piecewise constant between sampling instants, which refers to the zero-order-hold (ZOH) intersample assumption [92]. In general, the applied forces $\mathbf{u}(t)$ in $\mathbf{e}(t)$ cannot be assumed to be ZOH inputs since they are typically passed through antialias filters before acquisition, nor can the nonlinear basis functions $\mathbf{h}_a(\mathbf{y}(t), \dot{\mathbf{y}}(t))$ as they are generated via the feedback loop of the system. However, this violation of the ZOH assumption only affects marginally the continuous-time model provided that a sufficiently large sampling frequency is selected, as is anyhow recommended in nonlinear system identification. If a too low sampling frequency is even so considered, we advise to redo the measurements with a higher sampling rate, or, if this is not possible, to use a continuous-time subspace algorithm with a proper conditioning of the data matrices [117, 128].

Introducing the extended observability matrix

$$\mathbf{\Gamma}_i = \begin{pmatrix} \mathbf{C} \\ \mathbf{CA} \\ \mathbf{CA}^2 \\ \cdots \\ \mathbf{CA}^{i-2} \\ \mathbf{CA}^{i-1} \end{pmatrix} \in \mathbb{R}^{li \times n_s} \tag{2.14}$$

and the lower-block triangular Toeplitz matrix $\mathbf{\Lambda}_i$

$$\mathbf{\Lambda}_i = \begin{pmatrix} \mathbf{D} & \mathbf{0} & \mathbf{0} & \dots & \mathbf{0} \\ \mathbf{CB} & \mathbf{D} & \mathbf{0} & \dots & \mathbf{0} \\ \mathbf{CAB} & \mathbf{CB} & \mathbf{D} & \dots & \mathbf{0} \\ \vdots & \vdots & \vdots & & \vdots \\ \mathbf{CA}^{i-2}\mathbf{B} & \mathbf{CA}^{i-3}\mathbf{B} & \mathbf{CA}^{i-4}\mathbf{B} & \dots & \mathbf{D} \end{pmatrix} \in \mathbb{R}^{li \times (m+sl)\, i}, \tag{2.15}$$

recursive substitution of the second relation into the first relation of Eqs. (2.8) results in the output-state-input relationship

$$\mathbf{Y}_i^c = \mathbf{\Gamma}_i \, \mathbf{X}^c + \mathbf{\Lambda}_i \, \mathbf{E}_i^c \tag{2.16}$$

where $\mathbf{X}^c \in \mathbb{C}^{n_s \times F}$ is the state spectrum, and where the index i is explicitly written to signal the number of block rows in the matrices. To force the identified state-space model $(\mathbf{A}, \mathbf{B}, \mathbf{C}, \mathbf{D})$ to be real-valued, Eq. (2.16) is finally converted into the real equation

$$\mathbf{Y}_i = \mathbf{\Gamma}_i \, \mathbf{X} + \mathbf{\Lambda}_i \, \mathbf{E}_i \tag{2.17}$$

by separating the real and imaginary parts of $\mathbf{Y}_i^c$, $\mathbf{X}^c$ and $\mathbf{E}_i^c$, for instance,

$$\mathbf{Y}_i = [\mathcal{R}(\mathbf{Y}_i^c) \; \mathcal{I}(\mathbf{Y}_i^c)] \in \mathbb{R}^{li \times 2F} \tag{2.18}$$

where $\mathcal{R}$ and $\mathcal{I}$ denote the real and imaginary parts, respectively.

2.5 Identification theorem

This section presents an identification theorem underlying the FNSI method, and which rigorously solves the problem:

Given F measured frequency lines of the extended input and output spectra $\mathbf{E}(k)$ and $\mathbf{Y}(k)$, find an appropriate system order n_s and estimate the extended observability matrix of the system $\mathbf{\Gamma}_i$.

It will be shown that the estimation of $\mathbf{\Gamma}_i$ lies in the elimination of the term depending on the forces and the nonlinearities in Eq. (2.17), namely $\mathbf{\Lambda}_i \, \mathbf{E}_i$, using a geometrical

projection. The two-dimensional interpretation of Eq. (2.17) depicted in Fig. 2.2 shows that a projection onto a vector perpendicular to $\mathbf{E}_i$, denoted $\mathbf{E}_i^\perp$, cancels the extended input term $\mathbf{\Lambda}_i\,\mathbf{E}_i$. Matrix $\widehat{\mathbf{\Gamma}}_i$, where a hat denotes an estimated quantity, can then be obtained by means of a truncated singular value decomposition of the result of the projection. It will also be proved that the number of retained singular values in the truncation yields the system order n_s.

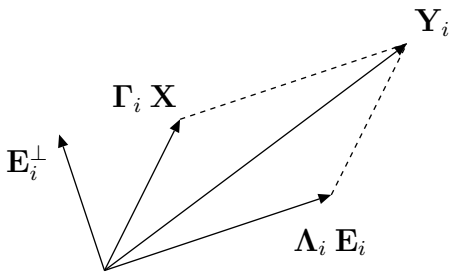

Figure 2.2: Geometrical interpretation of Eq. (2.17) in a two-dimensional space.

2.5.1 Assumptions and claims

To demonstrate the FNSI theorem, it is assumed that the four following conditions hold:

i. all the linear modes of vibration in the frequency band of interest are excited or, alternatively, they are all observable in input-output data. Formally, this requires that the rank of the system states, noted $\text{rank}(\mathbf{X})$, is equal to n_s. Provided that i is chosen greater than or equal to n_s, the observability of the underlying linear system entails the full column-rank property of the extended observability matrix, *i.e.* $\text{rank}(\mathbf{\Gamma}_i) = n_s$, as often assumed in the subspace literature [49, 63, 118];

ii. the row spaces of the states $\mathbf{X}$ and of the extended input spectra matrix $\mathbf{E}_i$ do not share information. Mathematically,

$$\text{span}_{\text{row}}(\mathbf{X}) \cap \text{span}_{\text{row}}(\mathbf{E}_i) = 0 \tag{2.19}$$

where $\text{span}_{\text{row}}(\cdot)$ denotes the subspace spanned by the rows of a given matrix. This implies that the row space of $\mathbf{X}$ adds n_s dimensions to the row space of $\mathbf{E}_i$, or, as in [68],

$$\begin{aligned} \text{rank}(\mathbf{X}/\mathbf{E}_i^\perp) &= \text{rank}(\mathbf{X}) - \dim(\text{span}_{\text{row}}(\mathbf{X}) \cap \text{span}_{\text{col}}(\mathbf{E}_i^\perp)^\perp) \\ &= \text{rank}(\mathbf{X}) = n_s \end{aligned} \tag{2.20}$$

where $\dim(\cdot)$ is the subspace dimension, and $\text{span}_{\text{col}}(\cdot)$ is the subspace spanned by the columns of a given matrix. $\mathbf{a}/\mathbf{b}$ is the orthogonal projection of the row space of

a onto the row space of **b**, and $\mathbf{b}^{\perp}$ is the orthogonal complement of **b**, also termed null space of **b** in linear algebra. Note that the result of the projection **a**/**b** lies in the subspace of **b**;

iii. the extended input spectra matrix $\mathbf{E}_i$ is of full rank, *i.e.*,

$$\text{rank}(\mathbf{E}_i) = (m + sl)\, i. \tag{2.21}$$

In time-domain linear problems, this assumption is often referred to as the persistency of the excitation. Excitations *and* nonlinearities are herein required to be such that the inversion of the problem is well-posed;

iv. $\mathbf{W}_i \in \mathbb{R}^{li \times li}$ is a user-defined weighting matrix of full rank, *i.e.*,

$$\text{rank}(\mathbf{W}_i) = li. \tag{2.22}$$

Introducing the orthogonal projection $\mathbf{O}_i = \mathbf{Y}_i/\mathbf{E}_i^{\perp}$ and its weighted singular value decomposition (SVD) $\mathbf{W}_i\mathbf{O}_i = \mathbf{U}\,\mathbf{S}\,\mathbf{V}^T$, it is claimed that:

1. the orthogonal projection is given by $\mathbf{O}_i = \mathbf{\Gamma}_i\,\mathbf{X}/\mathbf{E}_i^{\perp}$;
2. the system order n_s is equal to the number of nonzero singular values in the weighted SVD of $\mathbf{O}_i$;
3. the extended observability matrix $\mathbf{\Gamma}_i$, computed in a state-space basis different from that of the original model in Eqs. (2.8), is given by $\mathbf{\Gamma}_i = \mathbf{W}_i^{-1}\,\mathbf{U}_1\,\mathbf{S}_1^{1/2}$ where $\mathbf{U}_1$ and $\mathbf{S}_1$ contain the first n_s left singular vectors and singular values of $\mathbf{W}_i\mathbf{O}_i$, respectively.

2.5.2 Proof and remarks

The orthogonal projection of Eq. (2.17) onto the null space of $\mathbf{E}_i$ cancels the term $\mathbf{\Lambda}_i\,\mathbf{E}_i$ containing the applied forces and the nonlinear basis functions as

$$\mathbf{O}_i = \mathbf{Y}_i/\mathbf{E}_i^{\perp} = \mathbf{\Gamma}_i\,\mathbf{X}/\mathbf{E}_i^{\perp}. \tag{2.23}$$

Since, from assumption (iii), the projection operator $/\mathbf{E}_i^{\perp}$ exists, this proves the first claim of the theorem. The efficient computation of orthogonal projections in subspace algorithms is due to Verhaegen and exploits the QR decomposition [120].

The two matrices $\mathbf{W}_i\mathbf{\Gamma}_i$ and $\mathbf{X}/\mathbf{E}_i^{\perp}$ are both of rank n_s due to assumptions (i), (ii) and (iv). Their product $\mathbf{W}_i\mathbf{O}_i$ is thus also of rank n_s, which leads to the second claim.

The weighted SVD of $\mathbf{O}_i$ is therefore conveniently written as

$$\mathbf{W}_i\mathbf{O}_i = \begin{pmatrix}\mathbf{U}_1 & \mathbf{U}_2\end{pmatrix} \begin{pmatrix}\mathbf{S}_1 & 0 \\ 0 & 0\end{pmatrix} \begin{pmatrix}\mathbf{V}_1^T \\ \mathbf{V}_2^T\end{pmatrix} \tag{2.24}$$

where the n_s nonzero singular values of $\mathbf{W}_i\mathbf{O}_i$ fill the diagonal of $\mathbf{S}_1$. Eq. (2.24) can be split into the two relations

$$\begin{cases} \mathbf{W}_i\mathbf{\Gamma}_i = \mathbf{U}_1\,\mathbf{S}_1^{1/2}\,\mathbf{T} \\ \mathbf{X}/\mathbf{E}_i^{\perp} = \mathbf{T}^{-1}\,\mathbf{S}_1^{1/2}\,\mathbf{V}_1^T \end{cases} \tag{2.25}$$

where the arbitrary nonsingular similarity transformation matrix $\mathbf{T}$ is introduced to recover $\mathbf{\Gamma}_i$ and $\mathbf{X}/\mathbf{E}_i^{\perp}$ numberwise. Taking $\mathbf{T}$ as the identity matrix, as discussed in Section 2.8, the final claim of the theorem is demonstrated given assumption (iv).

One formulates the following list of remarks:

I. the choice and interpretation of the weighting matrix $\mathbf{W}_i$ is postponed to Section 2.7, where its effect on the FNSI algorithm in the presence of measurement noise is studied based on stochastic arguments;

II. because the state-space model in Eqs. (2.8) is linear-in-the-states, assumption (i) exclusively impacts the underlying linear properties of the system. This assumption is well known in linear modal analysis and is found to remain applicable in nonlinear system identification. In particular, it is violated if any targeted mode in the identification is excited perpendicularly to its deformed shape;

III. without assumption (ii), it can simply be asserted that

$$\text{rank}(\mathbf{O}_i) \leq \text{rank}(\mathbf{X}) = n_s, \tag{2.26}$$

or, in other words, that the system order can only be underestimated as a result of rank cancellation, but never overestimated since information cannot be created. In linear system identification, few results exist regarding the interpretation of rank cancellation. In Ref. [68], Moonen *et al.* point out that rank cancellation is not generic in practice, and that the probability of such an occurrence decreases for increasing time histories. McKelvey *et al.* also demonstrate in Ref. [63] that assumption (ii) can be omitted under certain conditions. In the presence of nonlinearities, a physical interpretation of this assumption is difficult and practical conditions under which rank cancellation due to nonlinearities may occur remain unclear;

IV. the null space of the linear functional which maps the extended inputs $\mathbf{E}_i$ onto the outputs $\mathbf{Y}_i$ contains more than the zero vector if assumption (iii) is not fulfilled. In this case, this functional is not injective, and the inverse problem is ill-posed. While assumption (i) is a condition on the identifiability of the underlying linear system, assumption (iii) can be viewed as a condition on the selected nonlinear basis functions.

2.6 Estimation of the state-space matrices

From the knowledge of an estimate of the extended observability matrix $\widehat{\mathbf{\Gamma}}_i$ given by the first relation in Eqs. (2.25), the next step in the FNSI algorithm is the computation of the four state-space matrices $(\mathbf{A}, \mathbf{B}, \mathbf{C}, \mathbf{D})$. First, the output matrix $\widehat{\mathbf{C}}$ is merely extracted from $\widehat{\mathbf{\Gamma}}_i$ as its l first rows. The state matrix $\mathbf{A}$ is then estimated by exploiting the shifted structure of $\mathbf{\Gamma}_i$. This shift property writes

$$\underline{\mathbf{\Gamma}_i}\,\mathbf{A} = \overline{\mathbf{\Gamma}_i} \tag{2.27}$$

where $\underline{\mathbf{\Gamma}_i}$ and $\overline{\mathbf{\Gamma}_i}$ are the matrix $\mathbf{\Gamma}_i$ without its last and first l rows. Matrix $\widehat{\mathbf{A}}$ is thus found as the least-squares solution

$$\widehat{\mathbf{A}} = \underline{\widehat{\mathbf{\Gamma}}_i}^{\,\dagger}\,\overline{\widehat{\mathbf{\Gamma}}_i} \tag{2.28}$$

where the symbol † denotes the pseudo-inverse.

Given the estimates $\widehat{\mathbf{A}}$ and $\widehat{\mathbf{C}}$, the extended input and direct feedthrough matrices $\mathbf{B}$ and $\mathbf{D}$ can be calculated by defining the transfer function matrix $\mathbf{G}_s$ associated with the state-space model in Eqs. (2.8) as

$$\mathbf{G}_s(k) = \widehat{\mathbf{C}}\left(z_k\,\mathbf{I}^{\,n_s\times n_s} - \widehat{\mathbf{A}}\right)^{-1}\mathbf{B} + \mathbf{D}, \tag{2.29}$$

and minimising the weighted difference between the measured and modelled output spectra in a linear least-squares sense, *i.e.*,

$$\widehat{\mathbf{B}}, \widehat{\mathbf{D}} = \arg\min_{\mathbf{B},\mathbf{D}} \sum_{k=1}^{F} \mathbf{W}^2(k)\,|\mathbf{Y}(k) - \mathbf{G}_s(k)\mathbf{E}(k)|^2 \tag{2.30}$$

where $\mathbf{W}(k)$ is a real-valued weighting function, related but not identical to matrix $\mathbf{W}_i$, as discussed in next Section.

2.7 Consistency analysis in the presence of measurement noise

The philosophy behind the FNSI method can be summarised as follows. Assuming that noiseless measurements of the applied forces $\mathbf{u}(t)$ and displacements $\mathbf{y}(t)$ acquired on a nonlinear structure obey Newton's second law of dynamics, the parameters of an equivalent state-space model of the structure are extracted by manipulating Eqs. (2.7) using linear algebra. This deterministic approach is attractive because it is noniterative and can be effectively implemented using robust tools from numerical analysis, ensuring the

tractability of the estimation problem even for large systems. However, it offers no guarantee that the model parameters still behave well in the presence of disturbing noise in the measurement of the inputs and outputs of the system.

In the noisy case, model parameters become stochastic variables characterised by probability density functions (PDFs). This means that if different data sets are independently measured on a structure using the same excitation signal, they will result in different estimations of the model parameters due to the random nature of noise corrupting the data. A particularly appropriate tool for quantifying the quality of stochastic parameter estimates is the notion of consistency [92]. Loosely speaking, consistency asserts that the estimates converge to their true values for an infinite number of measured frequencies F. More precisely, the PDFs of consistently estimated parameters contract around their true values as F tends to infinity. Denoting by $\tilde{\theta}$ a consistent estimate of the parameter θ and by θ_0 its true value, the contraction of the PDF of $\tilde{\theta}$ is depicted in Fig. 2.3. For F approaching infinity, the PDF transforms into a Dirac function.

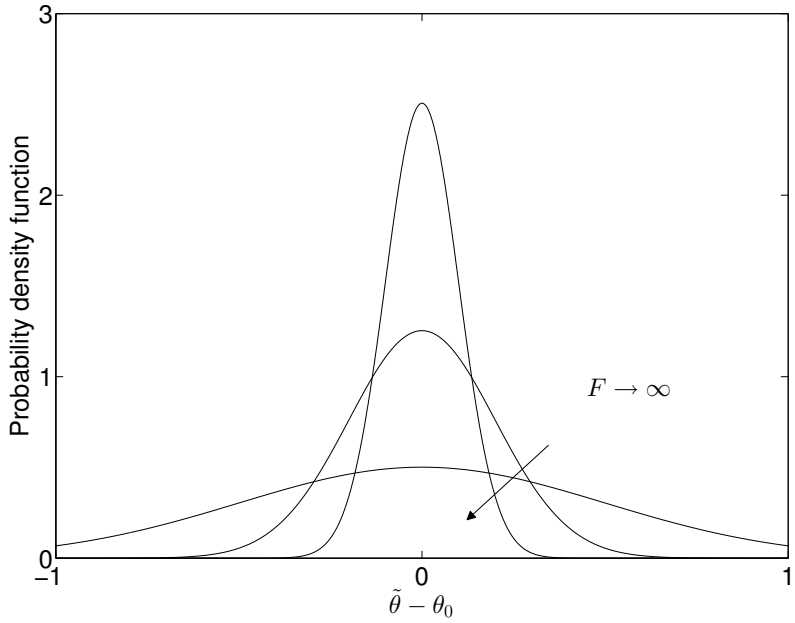

Figure 2.3: Consistent estimate $\tilde{\theta}$ of a model parameter θ. An arrow indicates the contraction of the probability density function of $\tilde{\theta}$ around the true value of the parameter noted θ_0 for an increasing number of measured frequencies F.

In this section, the consistency of the estimates of the state-space matrices $\left(\widehat{\mathbf{A}}, \widehat{\mathbf{B}}, \widehat{\mathbf{C}}, \widehat{\mathbf{D}}\right)$ calculated in Section 2.6 is analysed based on existing results in the technical literature, in particular those derived in Refs. [63, 91]. This analysis is carried out assuming that the extended input spectrum $\mathbf{E}(k)$ is exactly known and that the output spectrum $\mathbf{Y}(k)$

is observed with errors. This noise modelling is illustrated in Fig. 2.4. One writes

$$\left\{ \begin{array}{c} \mathbf{E}(k) = \mathbf{E}_0(k) \\ \mathbf{Y}(k) = \mathbf{Y}_0(k) + \mathbf{N}_Y(k) \end{array} \right. \tag{2.31}$$

where $\mathbf{E}_0(k)$ and $\mathbf{Y}_0(k)$ are the true extended input and output spectra; the disturbing noise term $\mathbf{N}_Y(k)$ has zero mean, *i.e.* $\mathcal{E}\left(\mathbf{N}_Y(k)\right) = 0$ where $\mathcal{E}$ is the expected value, and variance $\boldsymbol{\sigma}_Y^2(k) = \mathcal{E}\left(|\mathbf{N}_Y(k)|^2\right)$.

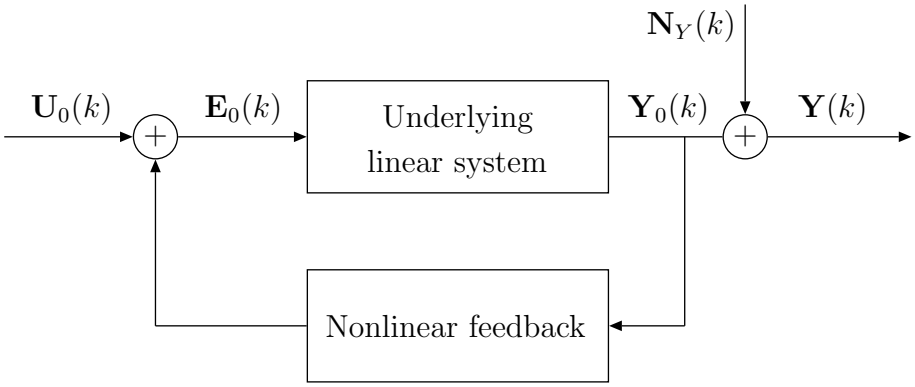

Figure 2.4: Noise modelling in the study of the consistency of the FNSI method.

In Ref. [63], it is demonstrated that $\boldsymbol{\Gamma}_i$ is consistently estimated using the first relation in Eqs. (2.25) if the weighting matrix $\mathbf{W}_i$ is chosen as

$$\mathbf{W}_i = \left[\mathcal{R}\left(\mathbf{C}_i\, \mathbf{C}_i^H\right)\right]^{-1/2} \tag{2.32}$$

where H denotes the matrix Hermitian transpose, and where $\mathbf{C}_i$ is the matrix of the output noise standard deviations arranged in a block-Vandermonde structure, similarly to $\mathbf{Y}_i^c$ in Eq. (2.10), that is

$$\mathbf{C}_i = \begin{pmatrix} \boldsymbol{\sigma}_Y(1) & \boldsymbol{\sigma}_Y(2) & \dots & \boldsymbol{\sigma}_Y(F) \\ z_1\, \boldsymbol{\sigma}_Y(1) & z_2\, \boldsymbol{\sigma}_Y(2) & \dots & z_F\, \boldsymbol{\sigma}_Y(F) \\ z_1^2\, \boldsymbol{\sigma}_Y(1) & z_2^2\, \boldsymbol{\sigma}_Y(2) & \dots & z_F^2\, \boldsymbol{\sigma}_Y(F) \\ \vdots & & & \\ z_1^{i-1}\, \boldsymbol{\sigma}_Y(1) & z_2^{i-1}\, \boldsymbol{\sigma}_Y(2) & \dots & z_F^{i-1}\, \boldsymbol{\sigma}_Y(F) \end{pmatrix} \in \mathbb{C}^{li \times F}. \tag{2.33}$$

The consistency of $\widehat{\boldsymbol{\Gamma}}_i$ implies in a straightforward manner the consistency of $\widehat{\mathbf{C}}$ and, in turn, the consistency of $\widehat{\mathbf{A}}$ calculated by Eq. (2.28). Finally, by setting $\mathbf{W}(k)$ to $\boldsymbol{\sigma}_Y^{-1}(k)$ in Eq. (2.30), consistent estimates of $\widehat{\mathbf{B}}$ and $\widehat{\mathbf{D}}$ are also obtained [63]. Note that the construction of the weighting terms $\mathbf{W}_i$ and $\mathbf{W}(k)$ requires the exact knowledge of the covariance matrix of the output noise. In practice, an estimate of this matrix can be extracted from experimental data by using a periodic excitation signal [92]. In Ref. [91],

it is proved that, if at least 4 successive periods of the response are measured in steady-state conditions, the consistency of the FNSI method is preserved.

It is finally worth stressing that consistency is lost if the extended input spectrum $\mathbf{E}(k)$ is not exactly known, *i.e.* $\mathbf{E}(k) = \mathbf{E}_0(k) + \mathbf{N}_E(k)$. In good approximation, the external forces $\mathbf{U}(k)$ in $\mathbf{E}(k)$ can be assumed to be observed without error, as force sensors typically yield SNRs of about 80 dB. The DFT spectra of the nonlinear basis functions $\mathbf{H}_a(k)$ are, in general, more importantly affected by noise, as they are formed using the displacements and velocities obtained by integrating noisy accelerometer signals, as illustrated in Fig. 2.5. This leads, to the author's experience, to a significant bias in the FNSI estimation of the model parameters for acceleration measurements with a SNR below 40 dB. One exception that should yet be pointed out is the direct measurement of the displacements at the nonlinearity locations, using techniques such as scanning laser Doppler vibrometers [28, 109], which may provide very large SNRs.

The theoretical analysis of the systematic errors associated with the noise modelling in Fig. 2.5 is difficult because the output noise is passed through a nonlinear filter in the feedback loop prior to being applied to the linear system in the open loop. One possible approach to achieve this analysis is the use of the particle filtering theory [37]. In Chapter 5, it will nonetheless be shown that, even in the case of a low SNR at the output, consistency can be retrieved by optimising the FNSI model in the maximum likelihood framework.

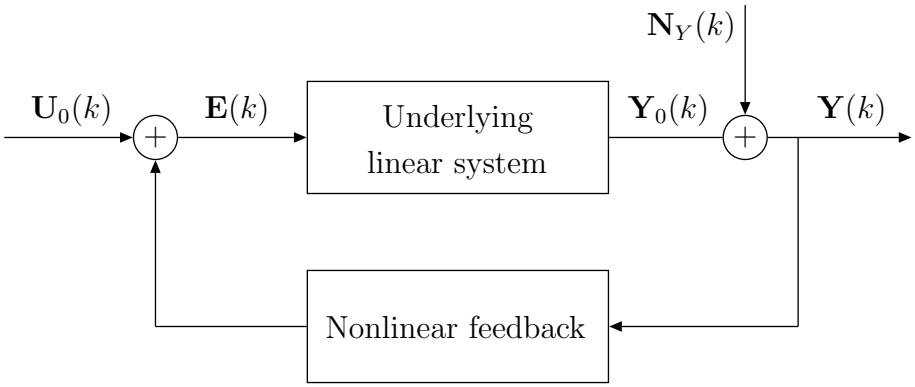

Figure 2.5: More realistic noise modelling where noisy output signals are used to form the nonlinear feedback.

2.8 Conversion from state space to physical space

The final step of the FNSI methodology is the conversion of the estimated state-space model $\left(\widehat{\mathbf{A}}, \widehat{\mathbf{B}}, \widehat{\mathbf{C}}, \widehat{\mathbf{D}}\right)$ into physical-space parameters, namely the FRF matrix of the un-

derlying system $\mathbf{G}_p(\omega)$ defined in Eq. (2.3) and the nonlinear coefficients c_a in Eq. (2.2). The complexity of this conversion stems from the similarity transformation matrix $\mathbf{T}$ introduced in Eqs. (2.25), but omitted afterwards following the choice $\mathbf{T} = \mathbf{I}^{n_s \times n_s}$. This specific choice fixed the state-space basis in which the resulting subspace model is identified. Because the nonlinear coefficients c_a are elements of the matrix $\mathbf{B}$, they vary according to the choice of the basis in which $\mathbf{B}$ is calculated. Therefore, the estimates $\widehat{c_a}$ cannot be obtained from a direct inspection of $\widehat{\mathbf{B}}$.

To achieve the conversion from the state space back to the physical space, the transfer function matrix $\mathbf{G}_s(\omega)$ associated with the state-space model in the continuous-time domain is formed as

$$\mathbf{G}_s(\omega) = \widehat{\mathbf{C}} \left(j\omega \, \mathbf{I}^{n_s \times n_s} - \widehat{\mathbf{A}} \right)^{-1} \widehat{\mathbf{B}} + \widehat{\mathbf{D}} \tag{2.34}$$

where the estimated matrices are converted in continuous time using Eqs. (2.13). Matrix $\mathbf{G}_s(\omega)$ is an invariant system property with respect to any similarity transformation $\mathbf{T}$ [58]. It can be expressed in terms of the physical parameters of the system if one notes that the substitution of Eq. (2.2) into Eq. (2.1) yields, in the frequency domain,

$$\mathbf{G}_p^{-1}(\omega)\mathbf{Q}(\omega) + \sum_{a=1}^{s} c_a \, \mathbf{H}_a(\omega) = \mathbf{P}(\omega) \tag{2.35}$$

where $\mathbf{Q}(\omega)$, $\mathbf{H}_a(\omega)$ and $\mathbf{P}(\omega)$ are the Laplace transforms of $\mathbf{q}(t)$, $\mathbf{h}_a(t)$ and $\mathbf{p}(t)$, respectively. The concatenation of $\mathbf{P}(\omega)$ and $\mathbf{H}_a(\omega)$ into the extended input Laplace spectrum $\mathbf{E}(\omega)$ finally gives

$$\mathbf{Q}(\omega) = \mathbf{G}_p(\omega) \left[\begin{array}{cccc} \mathbf{I}^{n_p \times n_p} & -c_1 \, \mathbf{I}^{n_p \times n_p} & \dots & -c_s \, \mathbf{I}^{n_p \times n_p} \end{array} \right] \mathbf{E}(\omega) = \mathbf{G}_s(\omega) \, \mathbf{E}(\omega). \tag{2.36}$$

Matrix $\mathbf{G}_p(\omega)$ is therefore simply extracted using Eqs. (2.34) and (2.36) as the first n_p columns of matrix $\mathbf{G}_s(\omega)$. Subsequently, the nonlinear coefficients c_a are computed from the other columns of $\mathbf{G}_s(\omega)$ given the knowledge of $\mathbf{G}_p(\omega)$. These coefficients are consequently spectral quantities, *i.e.* they are complex-valued and frequency-dependent. This is an attractive property, because the significance of the frequency variations and imaginary parts of the coefficients is particularly convenient for assessing the quality of the identification results. This possibility relies on the fact that, as a result of the consistency of the FNSI method and in the absence of modelling errors, the real parts of the coefficients converge (for an increasing number of measured frequencies) to their exact values with no frequency dependence, and the imaginary parts accordingly converge to zero. These indications will serve as quality criteria throughout this dissertation.

To summarise, Fig. 2.6 presents an overview of the FNSI algorithm.

1. Select appropriate basis functions $\mathbf{h}_a(\mathbf{q}(t), \dot{\mathbf{q}}(t))$ to represent the nonlinearities.
2. Choose the index i and the number of processed frequency lines F in the measured band.
3. Concatenate the measured forces $\mathbf{u}(t)$ and the nonlinear basis functions $\mathbf{h}_a(t)$ to form the extended input vector $\mathbf{e}(t)$.
4. Form the extended input and output spectra matrices $\mathbf{E}_i$ and $\mathbf{Y}_i$.
5. Compute the orthogonal projection $\mathbf{O}_i = \mathbf{Y}_i/\mathbf{E}_i^{\perp}$ using QR decomposition.
6. Compute the weighted SVD of $\mathbf{O}_i$: $\mathbf{W}_i\mathbf{O}_i = \mathbf{U}\,\mathbf{S}\,\mathbf{V}^T$ considering the weighting matrix defined in Eq. (2.32).
7. Inspect the singular values in $\mathbf{S}$ to determine the model order n_s, and truncate $\mathbf{U}$ and $\mathbf{S}$ accordingly to define $\mathbf{U}_1$ and $\mathbf{S}_1$.
8. Estimate the extended observability matrix $\mathbf{\Gamma}_i$ using the first relation in Eqs. (2.25).
9. Estimate $\mathbf{A}$ using Eq. (2.28) and $\mathbf{C}$ as the first block row of $\widehat{\mathbf{\Gamma}}_i$.
10. Estimate $\mathbf{B}$ and $\mathbf{D}$ using Eq. (2.30) considering $\mathbf{W}(k) = \boldsymbol{\sigma}_Y^{-1}(k)$.
11. Convert the identified state-space model into the continuous-time domain using Eqs. (2.13), and form the transfer function matrix $\mathbf{G}_s(\omega)$ using Eq. (2.34).
12. Estimate the underlying linear FRF matrix $\mathbf{G}_p(\omega)$ and the nonlinear coefficients c_a using Eq. (2.36).

Figure 2.6: Overview of the FNSI methodology.

2.9 Numerical demonstration on a Duffing oscillator

In this section, the FNSI method is demonstrated based on noise-free synthetic data using a single-DOF system with one nonlinearity, namely a Duffing oscillator. The vibrations of a Duffing oscillator are governed by the equation

$$M\,\ddot{q}(t) + C_v\,\dot{q}(t) + K\,q(t) + c_1\,q^3(t) = p(t). \tag{2.37}$$

The linear and nonlinear parameters selected in this analysis are listed in Table 2.1, including the natural frequency ω_0 and damping ratio ϵ. The system was simulated in time using a nonlinear Newmark scheme, with a sampling frequency of 15000 Hz to guarantee the accuracy of the integration. Synthetic time series were then decimated down to 750 Hz for practical use, considering low-pass filtering to avoid aliasing. Throughout this thesis, we opt for sampling frequencies at least 20 times larger than the linear frequencies of interest. This heuristic rule takes account of the existence of harmonics in the response spectrum of nonlinear systems.

M (kg)	C_v (Ns/m)	K (kN/m)	c_1 (MN/m^3)
2	10	100	100
Natural frequency ω_0 (Hz)		Damping ratio ϵ (%)	
35.59		1.12	

Table 2.1: Linear and nonlinear parameters of the Duffing oscillator.

The excitation $p(t)$ was a random phase multisine [92]. A random phase multisine is a periodic random signal with a user-controlled amplitude spectrum, and a random phase spectrum drawn from a uniform distribution. If an integer number of periods is measured, the amplitude spectrum is perfectly realised, unlike classical Gaussian noise. One of the other main advantages of a multisine is that its periodic nature can be utilised to separate signal from noise, which leads to an easy estimation of the output noise covariance matrix required to weight the FNSI algorithm, as described in Section 2.7. A multisine excitation with a flat amplitude spectrum in 5 – 150 Hz was chosen herein to include the third harmonics of the oscillator around 110 Hz. The root-mean-squared (RMS) amplitude of the signal was set to 100 N. The time simulation was conducted over 25 periods of 8192 samples each, and the first 5 periods of measurement were rejected to achieve steady-state oscillations.

The number of block rows i in the construction of the data matrices $\mathbf{E}_i$ and $\mathbf{Y}_i$, as defined in Section 2.4, is chosen equal to 20 . This index i should be adjusted so as to encompass sufficient valuable information to identify the system. From a theoretical point of view, it is sufficient to select i greater than or equal to the model order n_s to ensure asymptotically the consistency of the identification. In the case of finite length measurements, opting for a too low value of i may however lead to poor estimates. A rigorous solution to this problem is to compute the index i which minimises the difference in some metric between model predictions and measured data. This results in general in a tedious optimisation

search, without guarantee of convergence. We thus prefer to seek an acceptable value of i by trial and error, limiting the probing interval to $[1.5\,n_s - 10\,n_s]$.

The frequencies measured in the input band, *i.e.* in 5 – 150 Hz, are exploited in the estimation of the parameters, giving an overall computational time of 0.6 s to process $F = 1585$ frequency lines (considering an AMD Phenom triple-core processor unit at 2.10 GHz with 4 Go RAM). Fig. 2.7 (a – b) displays the complex and frequency-dependent estimation of the cubic stiffness coefficient of the Duffing system. Its real part shows no visible dependence upon frequency, and its imaginary part is 5 orders of magnitude smaller (see Table 2.2). These are clear proofs of an excellent identification.

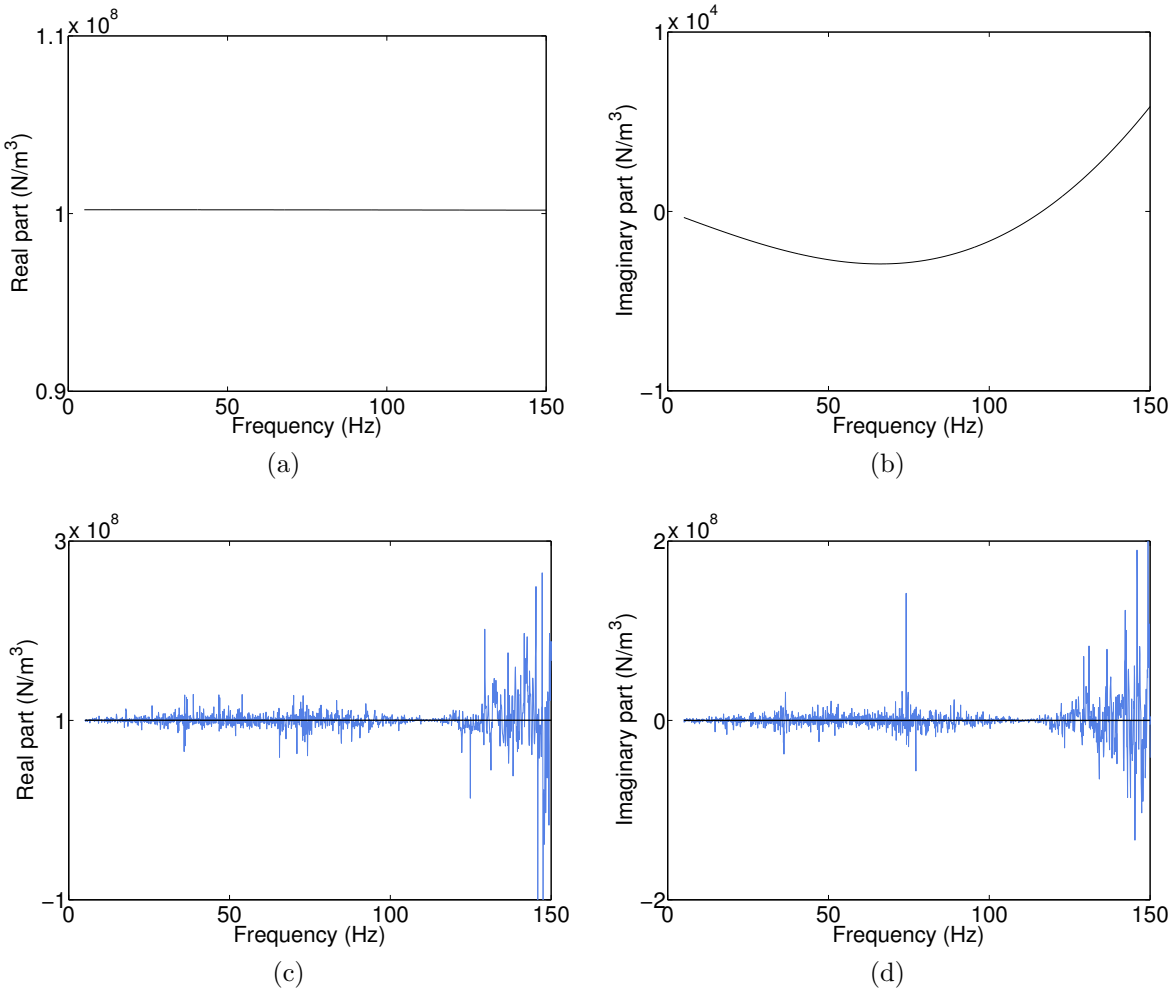

Figure 2.7: (a – b) Complex and frequency-dependent estimation of the nonlinear coefficient c_1; the scaling of the vertical axis of the real part is chosen such that 10 %-error bounds are visible; (c – d) comparison between the FNSI and CRP methods.

In Fig. 2.7 (c – d), the FNSI method is compared to another frequency-domain technique, the conditioned reverse path (CRP) method, introduced by Richards and Singh [98] and recognised as one of the most promising approaches for the identification of nonlinear structures [47]. The results obtained using the CRP method are also reported in the

Method	Real part (MN/m^3)	Error (%)	Log_{10} (real/imag.)
FNSI	10.02	0.21	5.05
CRP	10.03	0.28	2.26

Table 2.2: Estimation of the nonlinear coefficient c_1 of the Duffing using the FNSI (first line) and CRP (second line) methods.

second line of Table 2.2, showing an excellent agreement with the reference value of c_1. One notes that CRP however generates a much less smooth coefficient in Fig. 2.7 (c), with large frequency variations. The ratio between the real and imaginary parts of the coefficient is also lower in the case of the CRP method. Finally, Fig. 2.8 demonstrates the capability of the FNSI method to reconstruct the FRF of the underlying linear system from nonlinear data. The natural frequency and damping ratio of the Duffing oscillator are almost perfectly recovered with relative errors of -1.94 and 2.93 10^{-3} %, respectively. The FRF calculated using the classical H1 estimator [92] is also superposed in this figure to evidence the important nonlinear distortions present in the data at 100 N RMS .

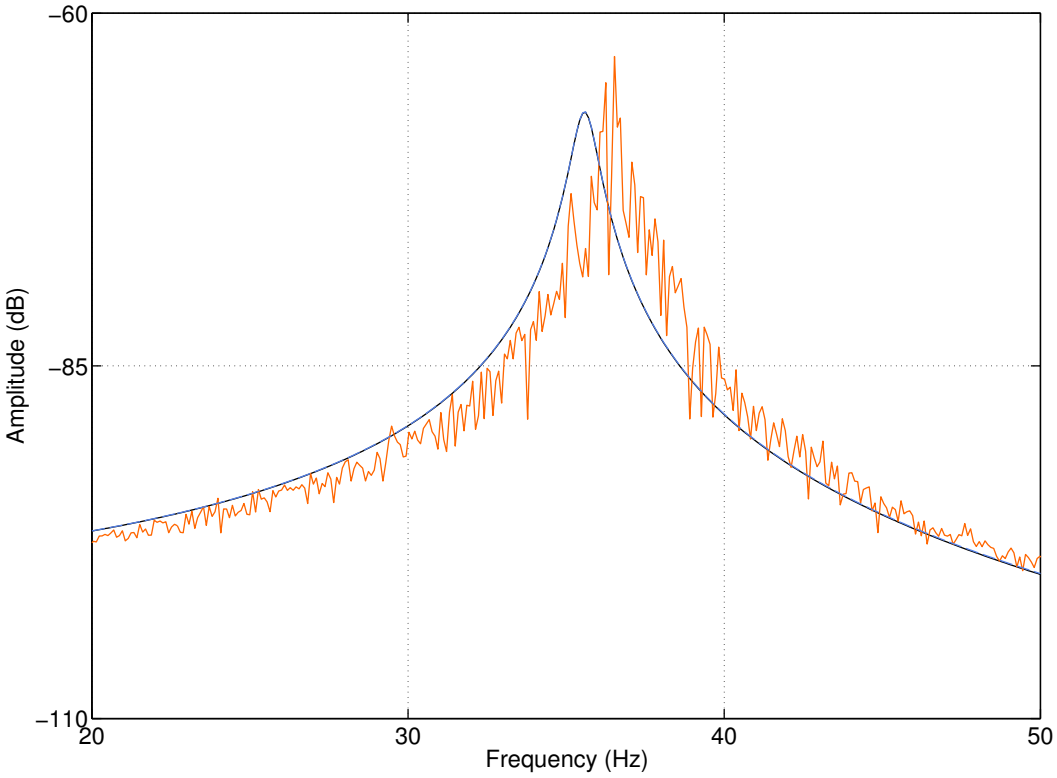

Figure 2.8: Comparison between the FRF of the Duffing oscillator at low level, *i.e.* 1 N RMS, where the system behaves linearly (in black) and the corresponding curve reconstructed using the FNSI method at high level (in blue), *i.e.* 100 N RMS. The FRF calculated using the H1 estimator at high level is also superposed (in orange).

2.10 Experimental identification of the Silverbox benchmark

The Silverbox benchmark shown in Fig. 2.9 is an electronic circuit designed to emulate the behaviour of a single-DOF mechanical system with one nonlinear spring. Measurements on the Silverbox were acquired at the department ELEC of the Vrije Universiteit Brussel (Brussels, Belgium) in collaboration with Prof. J. Schoukens. Ideally, the system should exhibit the dynamics of a Duffing oscillator with cubic nonlinearity, as prescribed by Eq. (2.37). In practice, it is known to be also characterised by a quadratic stiffness term $c_2\, q^2(t)$ [101].

The system was excited using random phase multisines at low and high levels, considering equivalent RMS amplitudes of 5 and 150 mN, respectively. The spectra of the multisine signals were limited to 0 – 300 Hz, excluding the DC component, with a sampling frequency of 2441 Hz. Similarly to the Duffing identification in Section 2.9, 25 periods of 8192 samples were collected, removing the first 5 periods to avoid leakage. A linear FNSI analysis at low level, *i.e.* 5 mN RMS, was carried out to estimate the underlying linear properties of the Silverbox listed in Table 2.3.

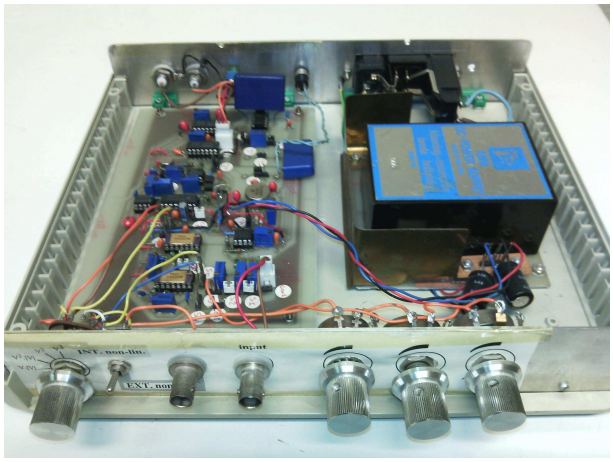

Figure 2.9: Silverbox benchmark.

Natural frequency ω_0 (Hz)	Damping ratio ϵ (%)
68.57	4.68

Table 2.3: Linear natural frequency and damping ratio of the Silverbox benchmark estimated at low level (5 mN RMS).

At high level of excitation, the system vibrates in a strongly nonlinear regime. Fig. 2.10 depicts the comparison between the linear FRF of the Silverbox measured at 5 (in black)

and 150 (in orange) mN RMS, and reveals a shift of more than 13 Hz of its resonance frequency together with severe noisy-like distortions [92]. The identification of the nonlinear coefficients of the system at high level is achieved by setting i to 20 and processing the measured frequency lines exclusively in the input band, giving $F = 1007$. Fig. 2.11 (a – d) presents the estimation of the cubic and quadratic coefficients c_1 and c_2 through their real and imaginary parts versus frequency. The real parts of the coefficients are found to be satisfactorily stable, and their imaginary parts remain more than 2 orders of magnitude smaller (see Table 2.4).

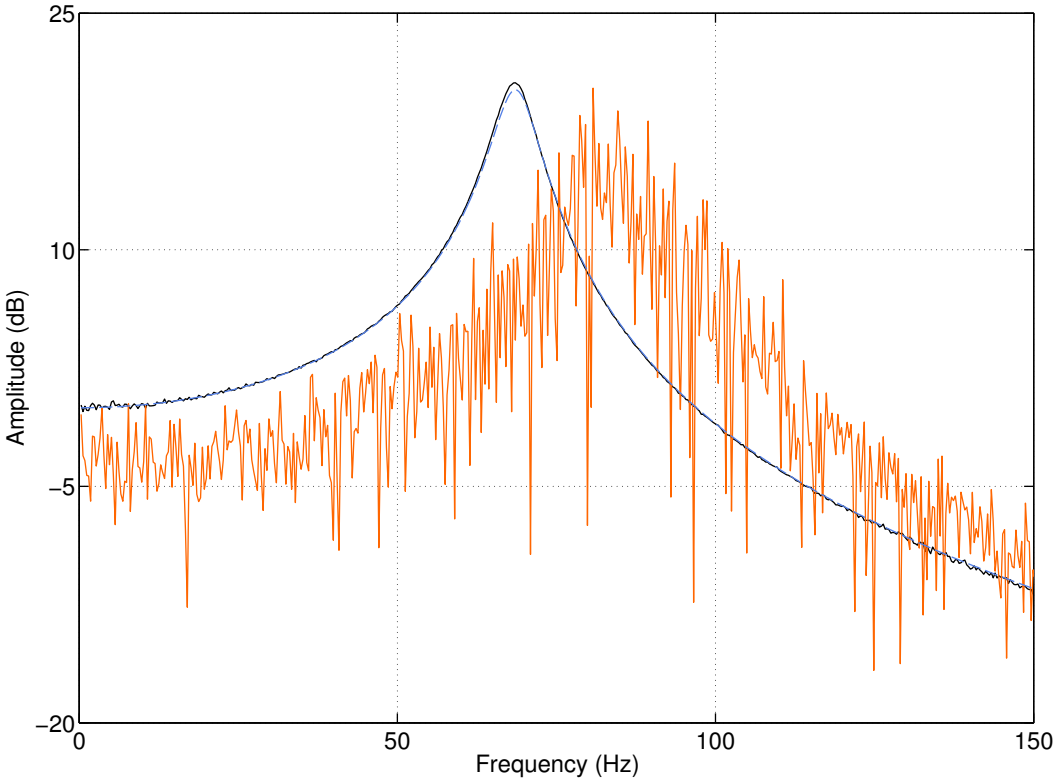

Figure 2.10: Comparison between the FRF of the Silverbox at low level, *i.e.* 5 mN RMS, where the system behaves linearly (in black) and the corresponding curve reconstructed using the FNSI method at high level (in blue), *i.e.* 150 mN RMS. The FRF calculated using the H1 estimator at high level is also superposed (in orange).

The linear FRF of the system computed at high level by FNSI is plotted in Fig. 2.10 in blue. The agreement with the FRF measured at low level is very good. The errors on the estimated frequency and damping are equal to 0.23 and 5.23 %, respectively. The larger error in the damping estimation is visible in Fig. 2.10 through a difference in amplitude between the black and blue curves. This small discrepancy is attributed to modelling errors in the description of the Silverbox nonlinearity, which may require higher-order contributions than quadratic and cubic terms to be fully captured in the model.

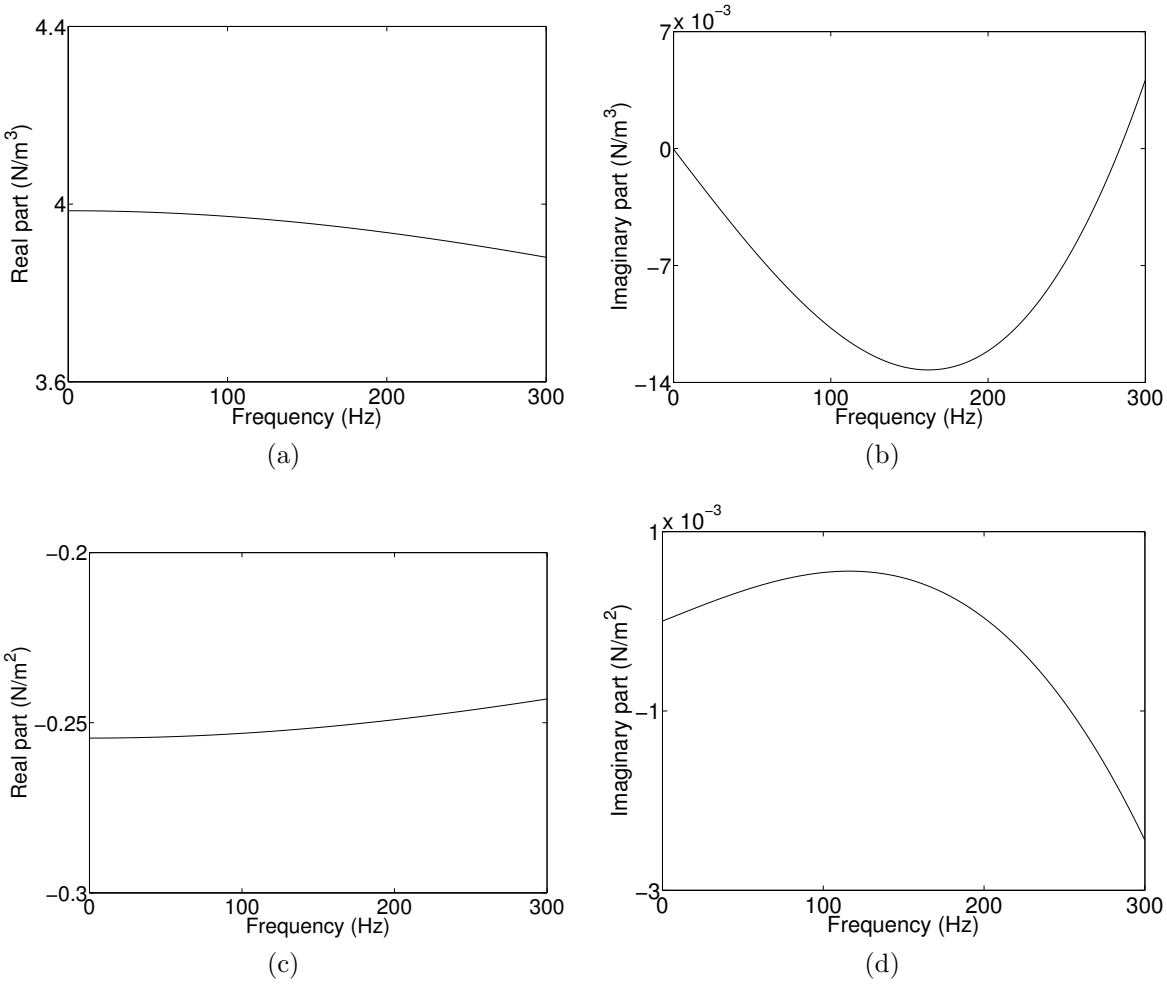

Figure 2.11: Complex and frequency-dependent estimation of the nonlinear coefficients (a – b) c_1 and (c – d) c_2 of the Silverbox using the FNSI method.

Method	Real part c_1 (N/m^3)	Log_{10} (r/i)	Real part c_2 (N/m^2)	Log_{10} (r/i)
FNSI	3.95	2.71	-0.25	3.38
CRP	3.96	2.10	-0.25	1.45
Paduart [84]	3.92	–	-0.26	–

Table 2.4: Estimation of the nonlinear coefficients c_1 and c_2 of the Silverbox using the FNSI and CRP methods, and using the approach proposed in [84].

A comparison with the estimation results obtained using the CRP method is plotted for c_1 in Fig. 2.12 and summarised in the second line of Table 2.4. As in the case of the Duffing identification, the mean values of the real parts of the FNSI and CRP estimates match very well, though the CRP coefficients vary more importantly over the frequency axis and possess larger imaginary parts. Another methodology proposed by Paduart to identify nonlinear feedback systems [84] was applied to the Silverbox benchmark, considering other data sets than those exploited in this section. The approach relies on the nonlinear optimisation of an initial linear approximation of the system. The identification results obtained using this approach are given in Table 2.4, and confirm the accuracy of parameters estimated using the FNSI method.

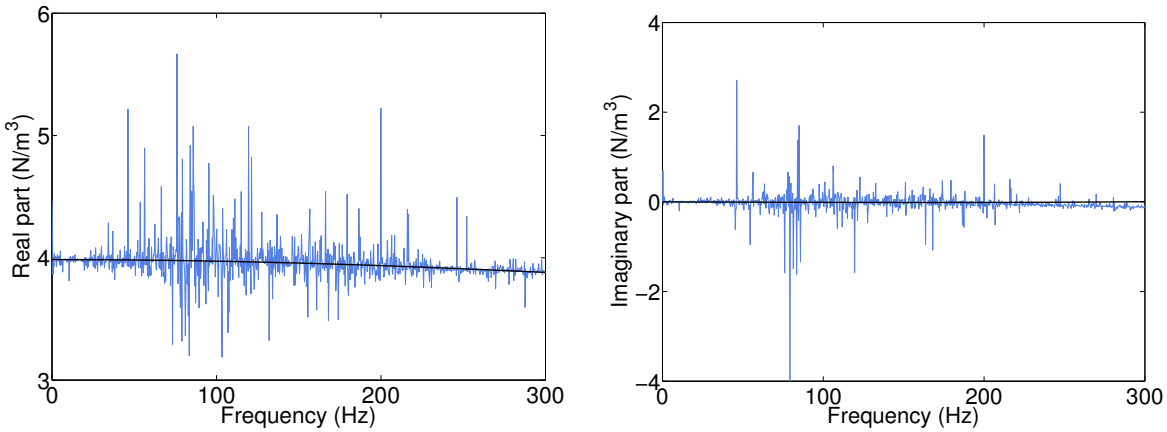

(a) (b)

Figure 2.12: Comparison between the FNSI and CRP methods in the estimation of c_1.

2.11 Concluding remarks

The objective of the present chapter was to revisit the frequency-domain subspace identification algorithms existing in the technical literature to propose a new subspace method dedicated to nonlinear systems. The theoretical background underlying the proposed FNSI method was exposed, culminating in the formulation of an identification theorem. This theorem brought insights into the necessary assumptions and weighting strategies to support the sound identification of nonlinear behaviour in mechanical systems. The FNSI method was also shown to succeed in decoupling the estimation of the linear and nonlinear parameters. This property of the method will lead to the generalisation of the stabilisation diagram in nonlinear system identification in the next chapter.

Moreover, during our theoretical developments, the motivations for working in the discrete-time and frequency domains were substantiated. Discrete-time models offer numerical stability. The use of frequency-domain data allows the user to select frequency intervals of interest where the nonlinearities are known to corrupt severely the dynamics of the system under test. The restriction of the measured frequency axis also results in the decrease of the computational burden involved in the identification. These capabilities pave the way for addressing complex, large-scale structures with multiple inputs, outputs and nonlinearities.

In this chapter, the FNSI method was demonstrated on a Duffing oscillator using noise-free synthetic data. The experimental identification of the Silverbox benchmark was also achieved. In the two cases, very satisfactory results were obtained, specifically in the estimation of the underlying linear properties and nonlinear coefficients of the two systems from strongly nonlinear data.

Chapter 3

Subspace-based identification of the SmallSat spacecraft

Abstract

The objective of the present chapter is to demonstrate the identification capabilities of the FNSI method using the SmallSat spacecraft. To this end, a full-scale finite element model of the structure is built to conduct a series of numerical experiments. The SmallSat identification is challenging for several reasons, including the number and the nonsmoothness of the nonlinearities, the presence of high nonproportional damping and the important overlaps between modal frequencies. The existence of local and global modes of vibration, the great number of instrumented locations, and the selection of the model order are additional difficulties.

3.1 Introduction

In Chapter 2, a frequency-domain generalisation of subspace identification techniques was introduced for nonlinear mechanical systems. The proposed FNSI method yielded very satisfactory results in the identification of two low-dimensional systems comprising a single nonlinearity, namely a Duffing oscillator and the Silverbox benchmark. In the present chapter, the capabilities of the FNSI method are demonstrated using the SmallSat spacecraft. To this end, a full-scale finite element model of the structure is built to conduct a series of numerical experiments. The SmallSat identification is challenging for several reasons, including the number and the nonsmoothness of the nonlinearities, the presence of high nonproportional damping and the important overlaps between modal frequencies. The existence of local and global modes of vibration, the great number of instrumented locations, and the selection of the model order are additional difficulties. In this context, an important contribution of the chapter is the introduction of the use of stabilisation diagrams in nonlinear system identification.

This chapter is structured as follows. The finite element model of the spacecraft structure is described in Section 3.2, implementing the clearances and stiffness coefficients estimated experimentally in Chapter 1. The identification of the SmallSat satellite is addressed in Section 3.3. The five main steps of the FNSI methodology, as reminded in Fig. 3.1, are addressed based on two noise-free synthetic data sets. In the first numerical experiment, the excitation is chosen such that a single axial nonlinear connection is activated. The identification of the nonlinear stiffness coefficients of the connection is discussed according to two sets of processed channels. A second identification case is then analysed involving the activation of the twelve nonlinearities of the WEMS device. Specific attention is devoted to the analysis of the frequency dependence of the nonlinear coefficients as they convey valuable information to assess the quality of the identification. The conclusions of the chapter are drawn in Section 3.4.

1. Select appropriate basis functions $\mathbf{h}_a(\mathbf{q}(t), \dot{\mathbf{q}}(t))$ to represent the nonlinearities in the structure under test.
2. Choose the index i and the number of processed frequency lines F.
3. Determine the order of the model.
4. Convert the state-space model to modal space to estimate the FRF matrix $\mathbf{G}_p(\omega)$ of the underlying linear structure.
5. Convert the state-space model to physical space to estimate the nonlinear coefficients c_a associated with the basis functions.

Figure 3.1: Reminder of the five main steps of the FNSI methodology.

The content of this chapter is reported in Ref. [77], where a comparison between the FNSI method and a counterpart approach in the time domain [58] can also be found.

3.2 Finite element modelling of the spacecraft

A detailed description of the structural components of the SmallSat spacecraft was made in Section 1.2. In particular, the spacecraft was shown to incorporate a mechanical filtering device supporting an inertia wheel, referred to as the WEMS device, and vibration isolators between its main structure and the telescope platform, termed SASSAs. For the purpose of the present chapter, a finite element model (FEM) of the SmallSat structure was developed in the LMS-Samtech Samcef software in order to conduct numerical experiments. The model comprises about 65000 degrees of freedom (DOFs), and consists of (i) shell elements, namely orthotropic elements for the octagon structure and isotropic elements for the top floor, instrument baseplate, bracket and WEMS metallic cross, and (ii) lumped masses for the dummy inertia wheel and telescope. The behaviour of the SASSA isolators is considered as linear in the FEM according to the analysis in Section 1.4.2. Boundary conditions are met with four clamped nodes imposed at the base of the structure. Proportional damping is introduced following the relation

$$\mathbf{C}_v = \alpha\mathbf{M} + \beta\mathbf{K}, \tag{3.1}$$

where the parameters $\alpha = 1.98$ and $\beta = 15.7\ 10^{-5}$ were obtained from EADS-Astrium technical documentation. The high dissipation in the elastomer components of the WEMS device is described using lumped dashpots, hence resulting in a highly nonproportional damping matrix. The coefficients of the dashpots were chosen equal to 63 and 10 Nm/s in the axial and lateral directions, respectively. In comparison with the reference values given in Table 1.1, the lateral coefficient was modified so as to be consistent with the experimental damping ratios listed in Table 1.2.

Table 3.1 gives the natural frequencies and damping ratios of the first 11 modes of the SmallSat FEM up to 50 Hz, together with a brief description of the corresponding deformations of the structure. One notes the very large modal overlap existing between certain modes in this list. For instance, the natural frequencies of modes 6 and 7 are distinct by 0.28 Hz, while they have half-power bandwidths of 3.39 and 1.33 Hz, respectively. One also remarks that the WEMS local modes, which are likely to involve nonlinear dynamics, are clustered in two groups around 9 and 23 Hz. Subsequent resonances involve bracket bending, and axial and lateral motions of the telescope supporting panel. Modes 2, 4, 6 and 8 are depicted in Fig. 3.2 (a – d), respectively, and illustrate well this variety of modal shapes in 0 – 50 Hz. Finally, the natural frequencies and damping ratios of the FEM are compared in Table 3.2 with those identified experimentally in Chapter 1 based on the analysis of transmissibility functions. Bringing the predictions of the linear model in very close quantitative agreement with the experimental observations, *i.e.* carrying out a formal linear model updating process, is not an objective of this chapter. A good

qualitative agreement is however observed in Table 3.2 with the correct mode ordering, proving that the FEM has satisfactory prediction capabilities.

3.2.1 Linear reduced-order modelling

To achieve tractable nonlinear calculations, the linear elements of the FEM were condensed using the Craig-Bampton reduction technique. This linear condensation is effective because the WEMS nonlinearities are spatially localised. The Craig-Bampton approach consists in expressing the system dynamics in terms of some retained DOFs and internal modes of vibration of the structure clamped on the retained nodes [10]. Specifically, the complete FEM of the spacecraft was reduced to 13 nodes (excluding DOFs in rotation), namely nodes on both sides of each NC (8), the inertia wheel lumped mass (1) and the four corners of the instrument baseplate (4), and 100 internal modes. In total, the reduced-order model thus contains 139 DOFs.

The accuracy of this reduced-order model can be assessed by comparing its modal parameters with the predictions of the original FEM. This is achieved in Fig. 3.3 where the deviations between the natural frequencies and mode shapes of the two models are plotted. Deviations between mode shapes are quantified using the modal assurance criterion (MAC). The values of MAC range from 0 in the absence of correlation to 1 in the case of a complete correspondence. One observes an almost perfect agreement for the first 11 modes of the structure covering the frequency interval of interest.

3.2.2 Modelling of the WEMS nonlinearities

Piecewise-linear springs were subsequently introduced within the WEMS module between the NC nodes considering the clearances and stiffness parameters identified experimentally in Chapter 1 (see Table 3.3). The two experimental data sets treated in Chapter 1 were not sufficient to identify all NCs. Some parameters in Table 3.3 were therefore established by copying experimentally known values, *e.g.*, the axial nonlinear stiffness parameters at NC 3 and NC 4. Furthermore, the clearances at NC 3 and NC 4 in the Z direction were chosen as the mean values of those estimated at NC 1 and NC 2, which is coherent with the physics. The clearances and stiffnesses of the mechanical stops in the X and Y directions were obtained from the analysis of additional data sets recorded under lateral swept-sine loadings [73].

Finally, to avoid numerical issues during time integration, the continuity of the first derivative of the WEMS nonlinear restoring forces was enforced using regularisation. To this end, third-order polynomials were implemented in the close vicinity of the clearances, *i.e.* in an interval $[a - \Delta,\ a + \Delta]$, where a is the clearance value and 2Δ the size of the regularisation zone. Throughout the chapter, a ratio a/Δ of about 2 % is considered.

Mode	Natural frequency ω_0 (Hz)	Damping ratio ϵ (%)	Description
1	8.51	4.91	Concave motion of the WEMS mobile part (WMP) along X
2	8.93	4.92	Symmetric to mode 1 along Y
3	18.16	7.95	Rotation of the WMP around Z
4	22.39	6.50	Convex motion of the WMP along X
5	23.25	6.31	Symmetric to mode 4 along Y
6	31.36	5.41	Bracket bending and in-phase motion of the WMP along Z
7	31.64	2.10	Bracket bending and rotation of the instrument panel (IP)
8	32.79	2.57	Bracket bending and rotation of the IP perpendicularly to mode 7
9	37.47	2.27	Rotation of the IP similarly to mode 8 and rotation around Z
10	38.25	2.32	Main structure bending and in-plane motion of the IP in phase
11	43.31	2.51	Rotation of the IP similarly to mode 8

Table 3.1: Natural frequencies ω_0 and damping ratios ϵ of the first 11 modes of the FEM of the SmallSat satellite and description of the corresponding deformations of the structure.

Mode	FEM ω_0 (Hz)	Experimental ω_0 (Hz)	FEM ϵ (%)	Experimental ϵ (%)
1	8.51	8.19	4.91	4.36
2	8.93	–	4.92	–
3	18.16	–	7.95	–
4	22.39	20.18	6.50	5.21
5	23.25	–	6.31	–
6	31.36	22.45	5.41	6.76
7	31.64	–	2.10	–
8	32.79	34.30	2.57	5.03
9	37.47	–	2.27	–
10	38.25	43.16	2.32	2.76
11	43.31	–	2.51	–

Table 3.2: Comparison between the natural frequencies and damping ratios of the FEM and those identified experimentally in Chapter 1 with the correct mode ordering.

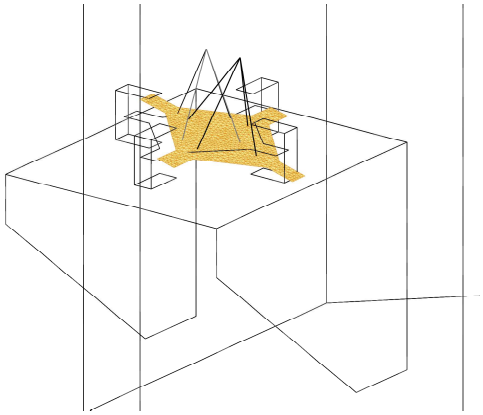

(a) Mode 2: $\omega_0 = 8.93\ Hz$, $\epsilon = 4.92\ \%$.

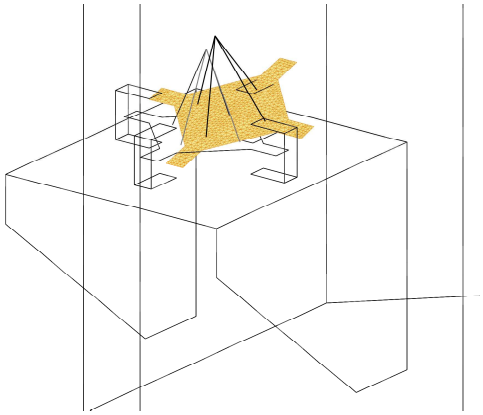

(b) Mode 4: $\omega_0 = 22.39\ Hz$, $\epsilon = 6.50\ \%$.

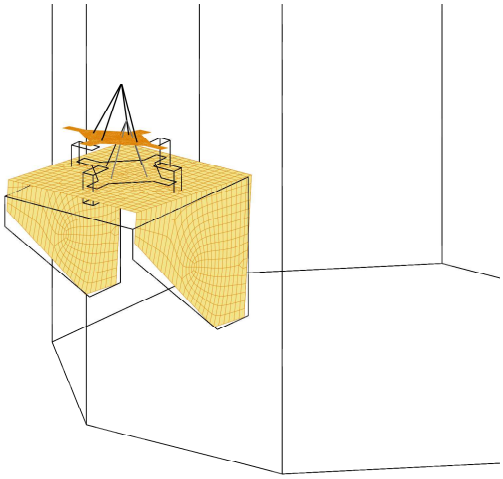

(c) Mode 6: $\omega_0 = 31.36\ Hz$, $\epsilon = 5.41\ \%$.

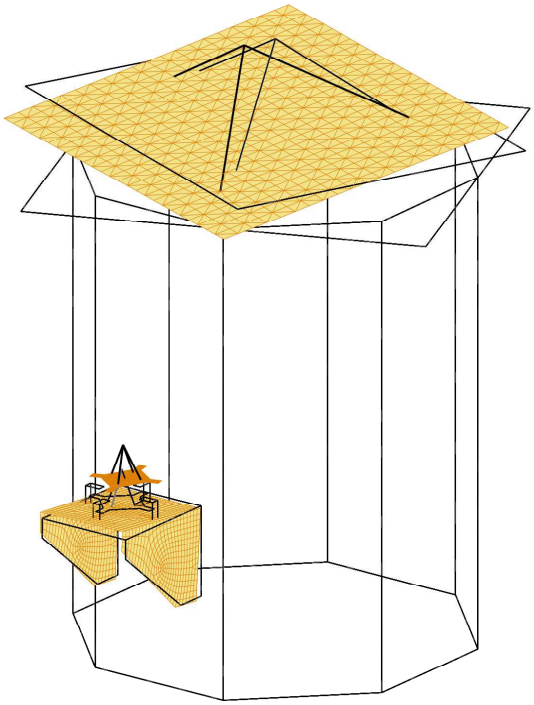

(d) Mode 8: $\omega_0 = 32.79\ Hz$, $\epsilon = 2.57\ \%$.

Figure 3.2: Deformed shapes of the SmallSat satellite for modes 2, 4, 6 and 8. For modes 2, 4 and 6, only a close-up of the WEMS device is shown.

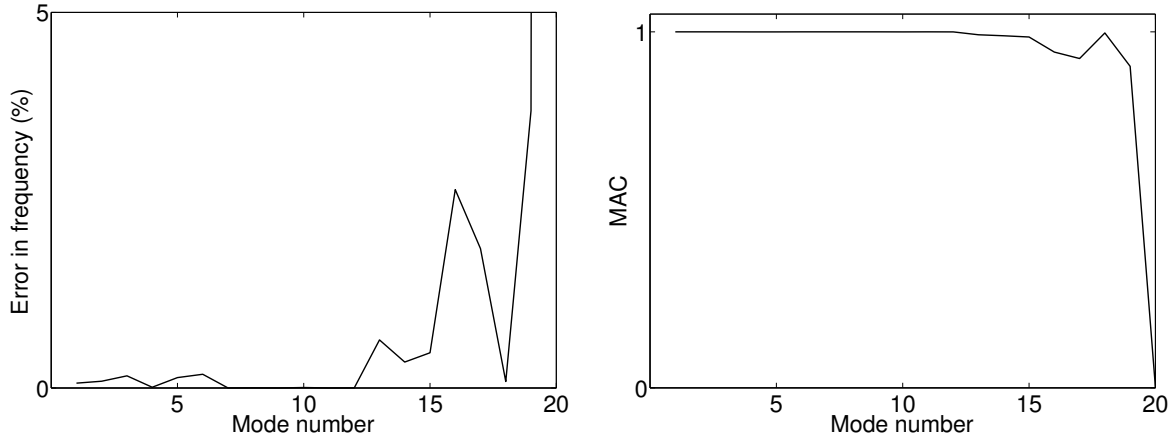

(a) (b)

Figure 3.3: Assessment of the accuracy of the reduced-order model of the SmallSat satellite. (a) Deviations in natural frequencies; (b) deviations between mode shapes quantified using the modal assurance criterion (MAC).

NC	Neg. clearance a_-	Pos. clearance a_+	Neg. nonlinear stiffness k_-	Pos. nonlinear stiffness k_+
1 – X	1.90	—	26.76	—
2 – X	—	1.93	—	46.23
3 – Y	1.90	—	26.76	—
4 – Y	—	1.93	—	46.23
1 – Z	1.01	1.55	118.07	79.40
2 – Z	0.84	1.62	116.73	88.41
3 – Z	0.93	1.59	118.07	79.40
4 – Z	0.93	1.59	116.73	88.41

Table 3.3: Experimental clearances and stiffness parameters of the WEMS piecewise-linear springs given through adimensional values for confidentiality reasons.

3.3 Subspace identification using the FNSI method

This section addresses the identification of the SmallSat structure using the FNSI method based on two noise-free synthetic data sets. The first step in Fig. 3.1 consists in selecting appropriate basis functions for the nonlinearities. For that purpose, it was described in Section 1.4 how sine-sweep data can be exploited to yield accurate estimates of the system clearances using, for example, the restoring force surface method. Two other possible ways are discussed in Ref. [77]. The first one relies on the formulation of a multiple-term nonlinearity model with varying clearances. The coefficients associated with the basis functions are estimated, and the different model terms are discriminated a posteriori based on their contribution in the reconstruction of the measured output. A second approach exploited in [77] is based upon the definition of a subspace identification error criterion, which is minimised to estimate the clearance parameters. In this section, one assumes the exact knowledge of the clearances, and focuses on the estimation of the stiffness coefficients of the WEMS nonlinear components.

3.3.1 Activation of a single nonlinearity of the WEMS device

A multisine excitation with a flat amplitude spectrum and a root-mean-squared (RMS) amplitude of 100 N was applied in the axial direction to NC 2 on the inertia wheel side. The excited band was limited to $5 - 50$ Hz to encompass the linear modes of interest. Time integration was carried out using a nonlinear Newmark algorithm with a sampling rate of 20000 Hz, and the time histories were low-passed filtered prior to being decimated down to 1000 Hz. The SmallSat response was simulated over 6 periods of 8192 samples, 5 periods of which were discarded to achieve steady-state conditions. The choice of a relatively low number of periods is explained by the unnecessary need to average the measurements in the absence of noise. The amplitude and the location of the excitation caused impacts exclusively on the negative and positive mechanical stops of NC 2. In the application of the FNSI method, the number of block rows i is set to 60, and measured frequency lines are processed in $5 - 250$ Hz to capture the contributions appearing outside the input band due to nonlinearities. This completes the second step in Fig. 3.1.

The next step in the FNSI methodology is the determination of an adequate model order, *i.e.* step 3 in Fig. 3.1. In linear system identification, stabilisation diagrams are most frequently utilised as convenient decision-making tools [9, 88]. They have proved successful in numerous industrial applications, as for instance in Ref. [87]. In the presence of nonlinearities, the model order translates the number of excited modes of the underlying linear structure (see Section 2.5). Because the FNSI method succeeds in decoupling the estimation of the linear and nonlinear parameters, the use of stabilisation diagrams is still effective in nonlinear system identification for selecting the model order.

Processing of all measured channels

Fig. 3.4 charts the stabilisation of the natural frequencies, damping ratios and mode shapes of the structure computed at 100 N RMS using FNSI for model orders up to 60. This analysis was conducted using all measured channels, *i.e.* 39 DOFs or 13 nodes, as output data. In the diagram, the MAC for complex-valued mode shapes (MACX), as defined in Ref. [113], is considered as the damping mechanisms in the SmallSat were shown to be highly nonproportional.

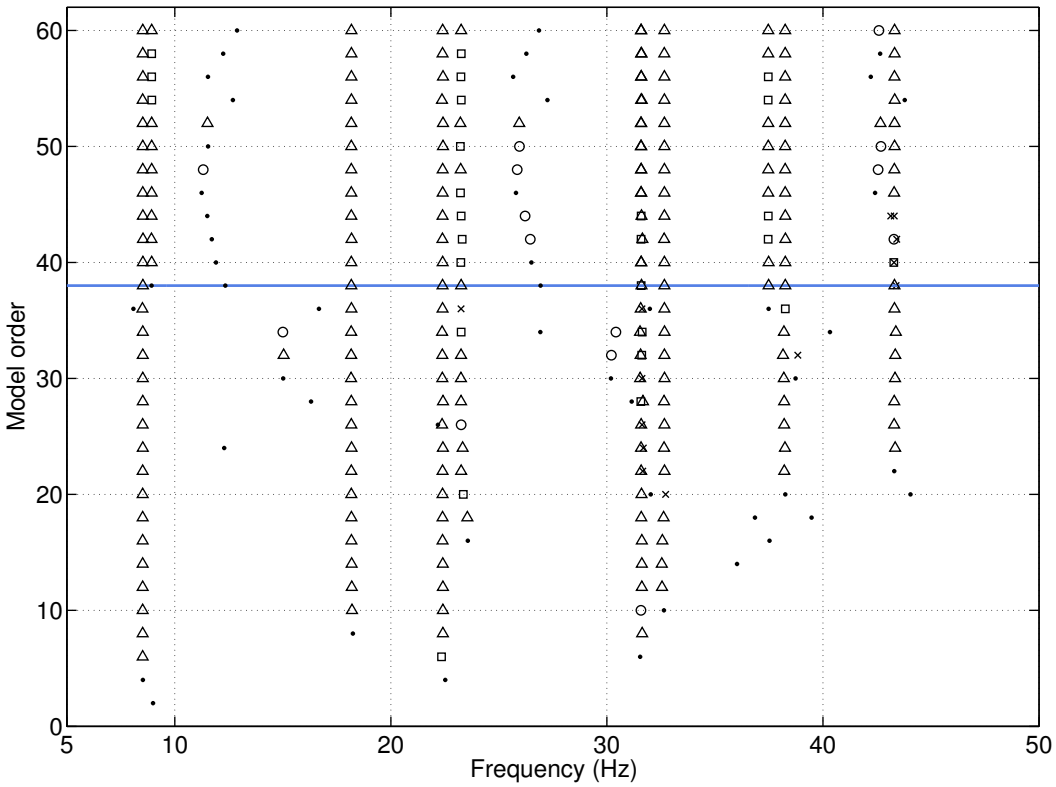

Figure 3.4: Stabilisation diagram computed using all measured channels. Dot: new pole; cross: stabilisation in natural frequency; square: extra stabilisation in damping ratio; circle: extra stabilisation in MACX; triangle: full stabilisation. Stabilisation thresholds in natural frequency, damping ratio and MACX are 1 %, 5 % and 0.98, respectively. Blue lines indicate the selected orders.

Fig. 3.4 shows full stabilisation of 11 modes at order 38. Note that in the case of mode 2 around 9 Hz and mode 6 around 31 Hz, full stabilisation symbols only appear at order 40. However, since this is tested between successive model orders taking as reference the lowest order, equal stabilisation is also achieved at order 38, which is therefore selected to avoid spurious poles. Table 3.4 lists the relative errors on the estimated natural frequencies and damping ratios together with the diagonal MACX values. The results in this table demonstrate the ability of the FNSI method to recover the modal properties of the underlying linear spacecraft from nonlinear data. One notes the very low MACX

value for mode 2 in Table 3.4, which is due to a poor distinction in the model between the deformed shapes of modes 1 and 2. The overall quality of the linear parameter estimates is confirmed in Fig. 3.5, where the driving-point frequency response function (FRF) of the system calculated at 1 N RMS is compared with the corresponding FRF synthesised using the FNSI method at 100 N RMS. The H1 FRF calculated at high level is also visible in this plot and highlights the importance of the nonlinear distortions affecting the SmallSat dynamics.

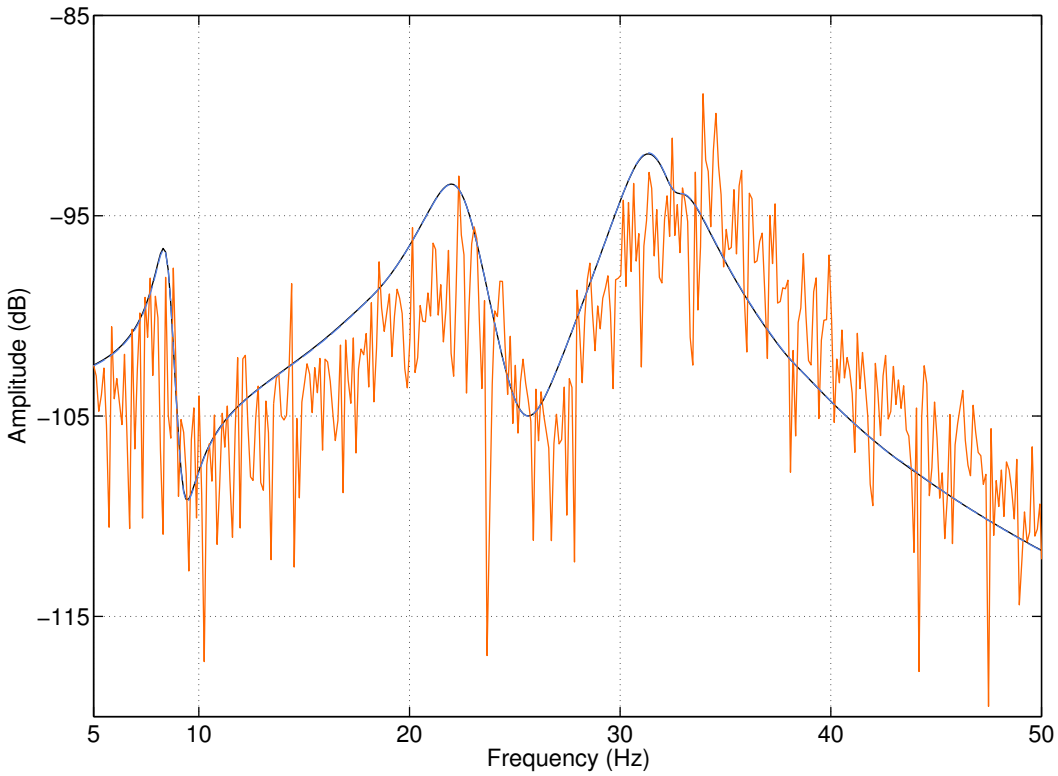

Figure 3.5: Comparison between the driving-point FRF at low level, *i.e.* 1 N RMS, where no nonlinearity is activated (in black) and the corresponding curve synthesised using the FNSI method at high level (in blue), *i.e.* 100 N RMS. The FRF calculated using the H1 estimator at high level is also superposed (in orange).

The complex-valued coefficients of the NC 2 nonlinearities are depicted in Fig. 3.6 (a – b). Their real parts show marginal dependence upon frequency, and their imaginary parts are three orders of magnitude smaller (see Table 3.5). These observations are signs of an accurate estimation. Table 3.5 gives the averaged values of the nonlinear coefficients, the relative errors and the ratios between real and imaginary parts in logarithmic scaling. This table highlights the excellent agreement between the identified and exact coefficients. In this identification case involving a single nonlinear connection, the time needed to solve the parameter estimation problem amounts to 159 s.

Mode	Error on ω_0 (%)	Error on ϵ (%)	MACX
1	0.11	-0.85	1.00
2	-0.08	0.92	0.04
3	0.04	-0.43	1.00
4	0.03	0.27	1.00
5	0.01	0.09	1.00
6	0.06	-0.68	1.00
7	-0.01	0.17	0.99
8	0.00	0.51	1.00
9	0.05	2.20	0.99
10	0.02	0.51	1.00
11	-0.01	0.38	1.00

Table 3.4: Relative errors on the estimated natural frequencies and damping ratios (in %) and diagonal MACX values computed at order 38 using all measured channels.

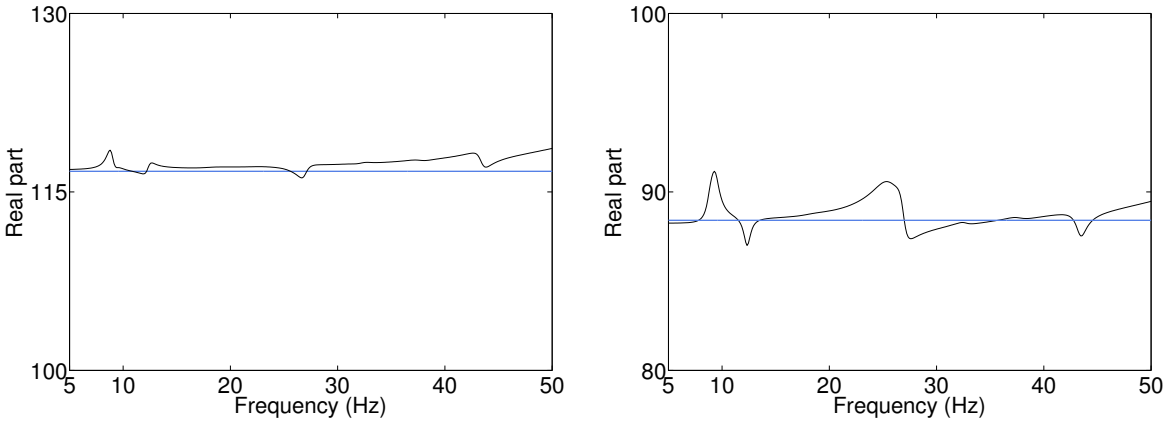

(a) (b)

Figure 3.6: Complex-valued estimates of the NC 2 – Z nonlinear coefficients in (a) negative and (b) positive displacement computed using all measured channels. Blue lines indicate the exact values of the coefficients.

NC	Exact value	Real part	Error (%)	Log_{10} (real/imag.)
2 – Z (neg.)	116.73	117.38	0.56	3.33
2 – Z (pos.)	88.41	88.71	0.34	3.00

Table 3.5: Estimates of the NC 2 – Z nonlinear coefficients computed using all measured channels. Real parts averaged over 5 – 50 Hz, relative errors (in %) and ratios between the real and imaginary parts (in logarithmic scaling).

Processing of three measured channels

A second analysis of the same data set can now be carried out considering only three output sensors, namely the axial DOFs on both nodes of NC 2 and of the inertia wheel node. This corresponds to the more practical situation where the number of available channels is limited, and where the system responses are only recorded close to the nonlinearity. The resulting stabilisation diagram constructed by the FNSI method is depicted in Fig. 3.7 and reveals fewer modes than in Fig. 3.4. Specifically, only modes 1, 4, 6 and 8 are now identifiable as they involve an axial motion of the WEMS device.

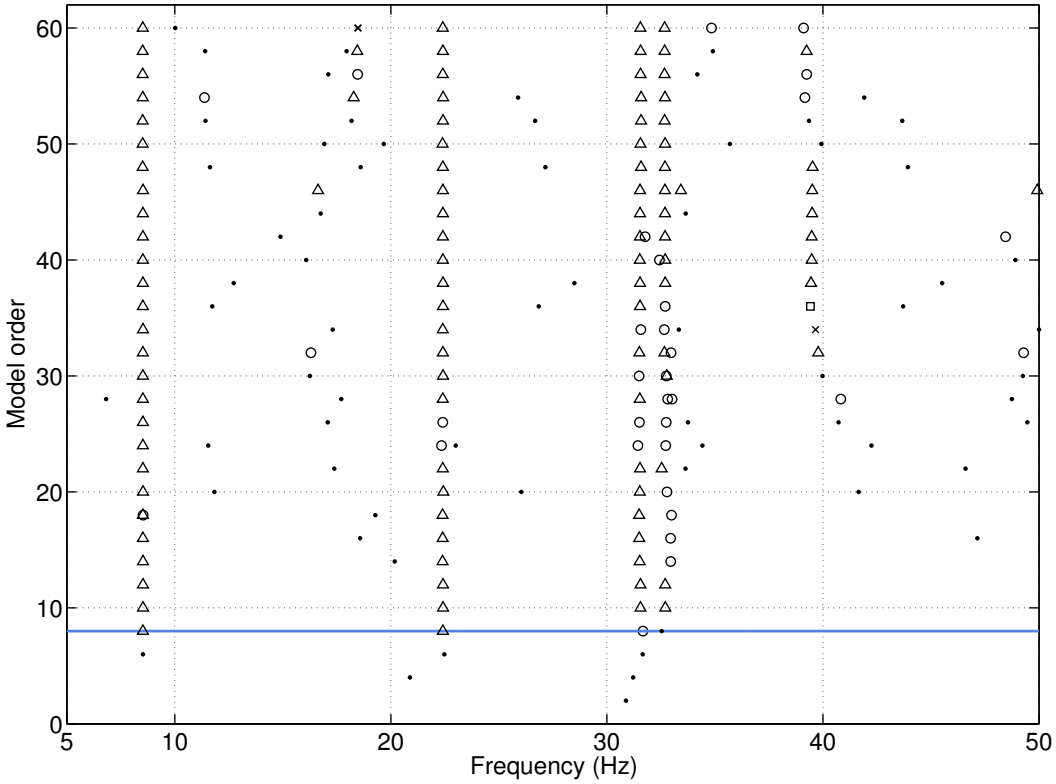

Figure 3.7: Stabilisation diagram computed using three measured channels. Stabilisation thresholds in natural frequency, damping ratio and MACX are 1 %, 5 % and 0.98, respectively.

Full stabilisation is achieved at order 8, and the corresponding modal parameters are given in Table 3.6. One observes very accurate results, except in the case of the damping ratio of mode 8, which nevertheless consists predominantly in a rotation of the instrument panel. The updated FNSI estimates of the nonlinear coefficients are shown in Fig. 3.8 (a – b) and summarised in Table 3.7. The somewhat limited number of analysed sensors is found to yield a significant decrease of the computational burden (10 s), but deteriorates the accuracy of the nonlinear coefficients through the appearance of a drift over the frequency axis of their real and imaginary parts. More important peaks are also visible in their frequency dependence, translating in lower real-to-imaginary ratios in Table 3.7.

Mode	Error on ω_0 (%)	Error on ϵ (%)	MACX
1	0.10	-0.55	1.00
4	0.10	0.51	1.00
6	0.27	2.99	1.00
8	-0.37	-12.52	1.00

Table 3.6: Relative errors on the estimated natural frequencies and damping ratios (in %) and diagonal MACX values computed at order 8 using three measured channels.

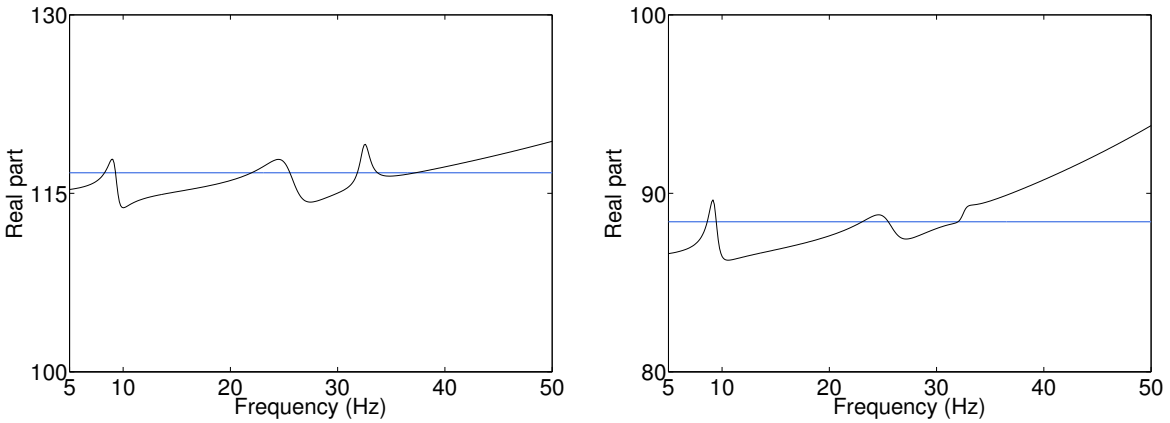

(a) (b)

Figure 3.8: Complex-valued estimates of the NC 2 – Z nonlinear coefficients in (a) negative and (a) positive displacement computed using three measured channels.

NC	Exact value	Real part	Error (%)	Log_{10} (real/imag.)
2 – Z (neg.)	166.73	116.47	-0.22	2.63
2 – Z (pos.)	88.41	88.96	0.63	2.60

Table 3.7: Estimates of the NC 2 – Z nonlinear coefficients computed using three measured channels. Real parts averaged over 5 – 50 Hz, relative errors (in %) and ratios between the real and imaginary parts (in logarithmic scaling).

Fig. 3.8 (a – b) demonstrates that the information contained in the frequency dependence of the nonlinear coefficients is particularly valuable to assess the quality of the identification. Specifically, inaccuracies in the estimation of the linear system parameters generally translate into peaks in the frequency-dependent coefficients. Missing modes and errors in the modelling of the nonlinearities rather affect the entire frequency dependence of the coefficients through the appearance of a drift.

3.3.2 Activation of multiple nonlinearities of the WEMS device

A multisine forcing with a RMS amplitude of 200 N was then applied to the inertia wheel node in the symmetric X – Y direction. It caused the activation of all WEMS nonlinearities. The selected number of excited frequencies, periods and samples per periods are similar to the first identification case in Section 3.3.1. In the present analysis, all measured channels are processed, and the index i is set to 60. It is worth stressing the resulting dimension of the inverse problem, which comprises 13 inputs, *i.e.* 1 external force and 12 nonlinear basis functions, 39 outputs.

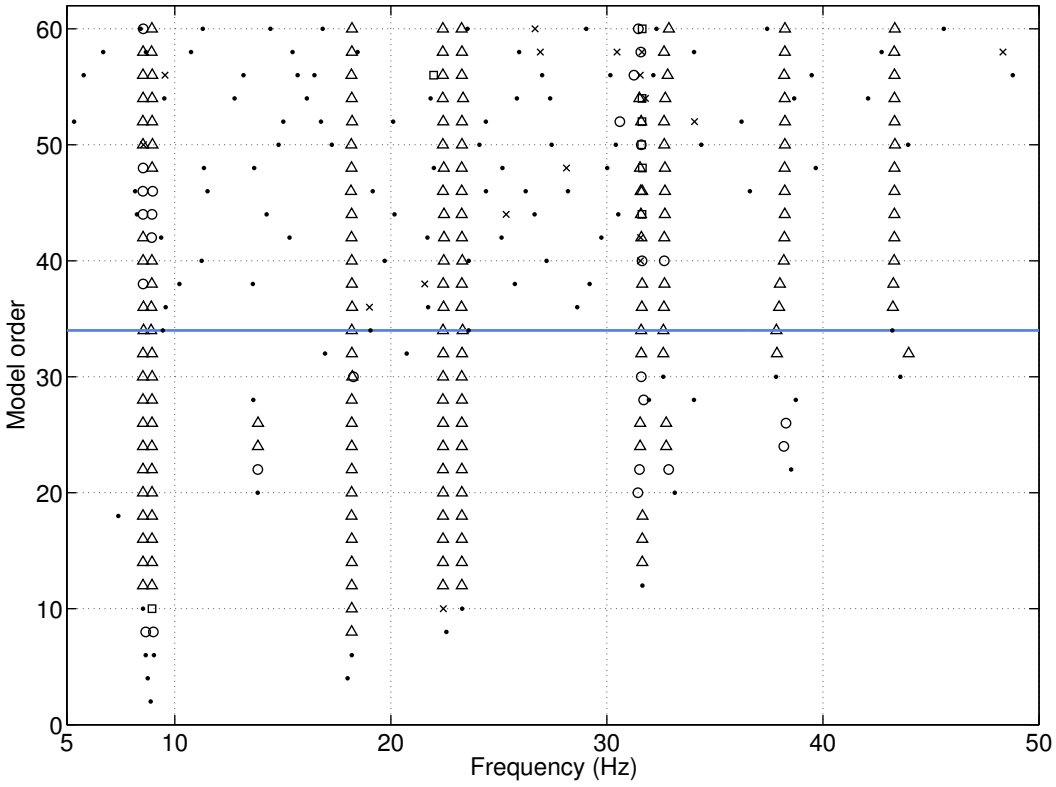

Figure 3.9: Stabilisation diagram computed using all measured channels. Stabilisation thresholds in natural frequency, damping ratio and MACX value are 1 %, 5 % and 0.98, respectively.

The FNSI stabilisation diagram in Fig. 3.9 leads to the selection of the order 34, where 9 modes are captured with full stabilisation features. This implies that the four matrices of the derived state-space model $(\mathbf{A}, \mathbf{B}, \mathbf{C}, \mathbf{D})$ of the structure possess in this case 1156, 442, 1292 and 494 elements, respectively. The results listed in Table 3.8 show that the underlying linear properties of the structure can be identified in the presence of a large number of nonlinearities.

Mode	Error on ω_0 (%)	Error on ϵ (%)	MACX
1	0.24	4.73	1.00
2	-0.07	0.59	1.00
3	0.11	0.44	1.00
4	0.11	0.15	1.00
5	0.32	-0.04	1.00
6	0.04	-4.29	1.00
7	—	—	—
8	-0.12	5.73	0.99
9	1.09	0.20	0.04
10	—	—	—
11	-0.30	2.32	0.99

Table 3.8: Relative errors on the estimated natural frequencies and damping ratios (in %) and diagonal MACX values computed at order 34 using all measured channels.

The lateral nonlinear coefficients identified using FNSI are represented in Fig. 3.10 (a – d). They are seen to remain bounded within 20-% intervals around their exact values. Furthermore, Table 3.9 proves that the imaginary parts of these coefficients are around 2 orders of magnitude smaller than the corresponding real parts.

The axial nonlinear coefficients are depicted in Fig. 3.11 (a – f) and Fig. 3.12 (a – b). They exhibit much larger frequency variations, in particular between 30 and 50 Hz, because of the absence of modes with significant axial components in this interval. One attractive advantage of the FNSI algorithm is the possibility to consider distinct frequency intervals to process measured data and average the real parts of the nonlinear coefficients, respectively. This may be useful if the inspection of the coefficients reveals that the model performs badly for specific frequencies. Table 3.10 compares the real parts and the real-to-imaginary ratios of the axial coefficients averaged over $5 - 50\ Hz$ and $5 - 30\ Hz$. This table clearly shows that limiting the frequency band of averaging improves significantly the identification quality.

It should finally be remarked that spurious poles in the model are usually accompanied by very low damping ratios, and therefore appear as easily detectable, sharp peaks in the real parts of the coefficients. As an example, a spurious pole around 10 Hz was captured at order 34 in Fig. 3.9, and is clearly noticeable in Fig. 3.11 (c) and in Fig. 3.12 (a – b).

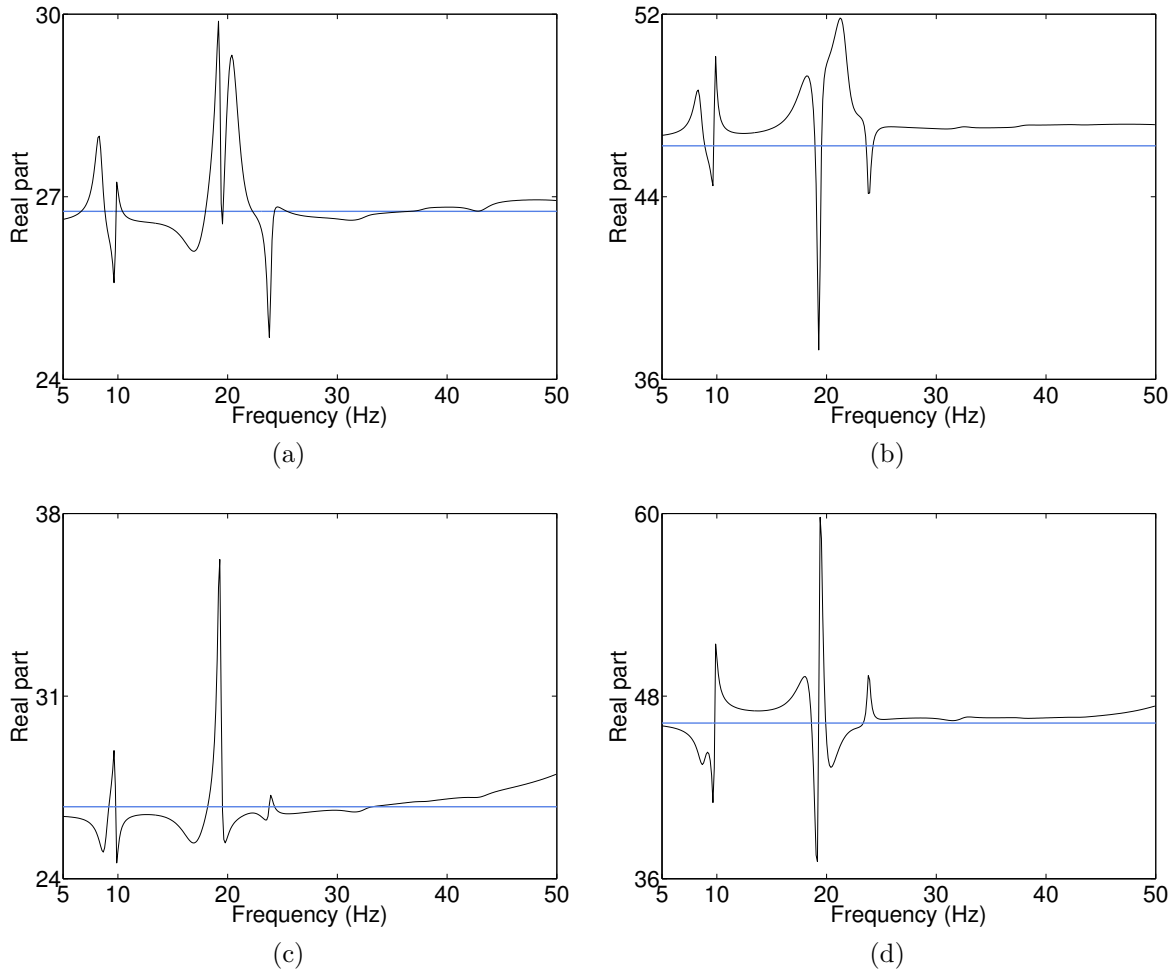

Figure 3.10: Complex-valued estimates of the lateral nonlinear coefficients computed using all measured channels. (a) NC 1 – X; (b) NC 2 – X; (c) NC 3 – Y; (d) NC 4 – Y.

NC	Exact value	Real part	Error (%)	Log_{10} (real/imag.)
1 – X (neg.)	26.76	26.82	0.22	1.70
2 – X (pos.)	46.23	47.27	2.20	2.33
3 – Y (neg.)	26.76	26.78	0.05	2.06
4 – Y (pos.)	46.23	46.58	0.76	2.11

Table 3.9: Estimates of the lateral nonlinear coefficients computed using all measured channels. Real parts averaged over 5 – 50 Hz, relative errors (in %) and ratios between the real and imaginary parts (in logarithmic scaling).

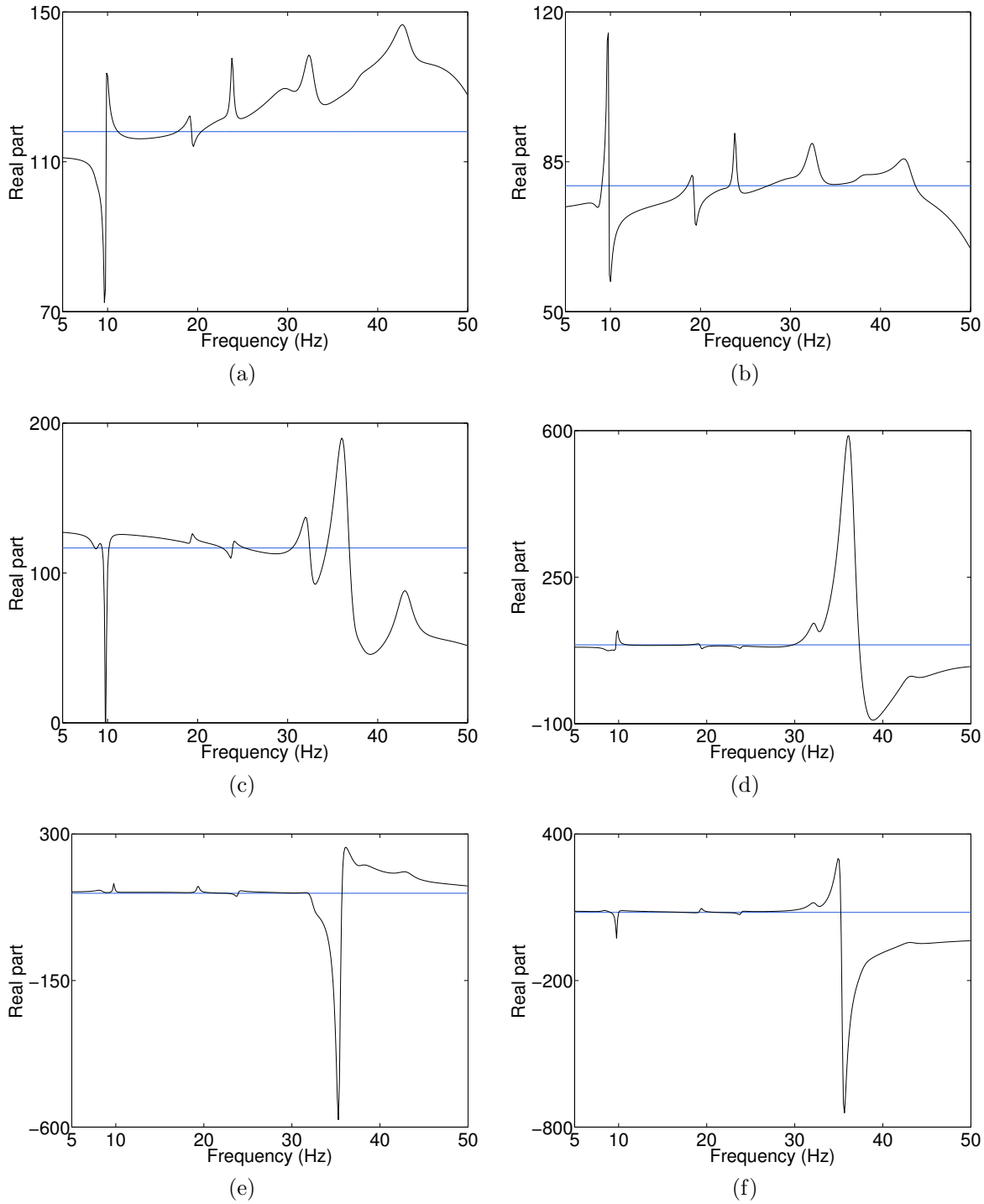

Figure 3.11: Complex-valued estimates of the axial nonlinear coefficients computed using all measured channels. (a) NC 1 –Z (neg.); (b) NC 1 – Z (pos.); (c) NC 2 – Z (neg.); (d) NC 2 – Z (pos.); (e) NC 3 – Z (neg.); (f) NC 3 – Z (pos.).

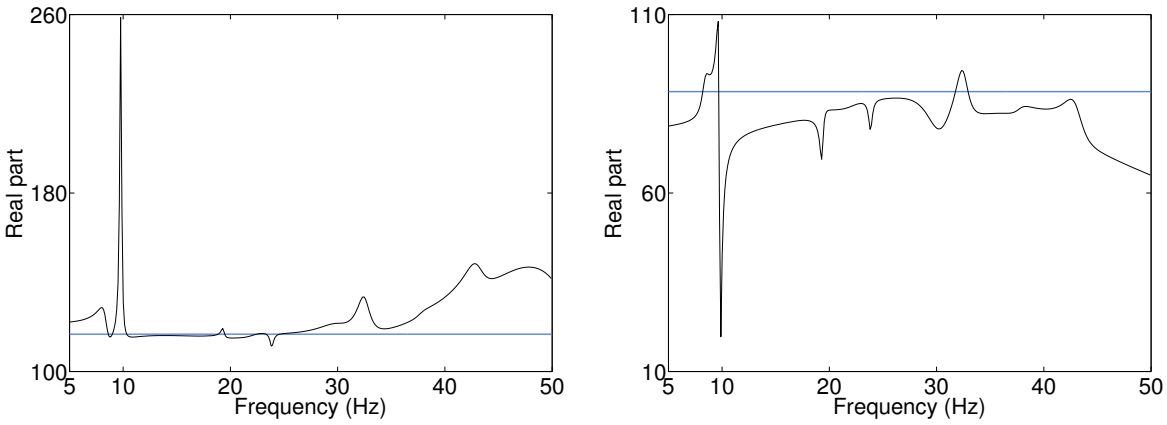

(a) (b)

Figure 3.12: Complex-valued estimates of the axial nonlinear coefficients computed using all measured channels. (a) NC 4–Z (neg.); (b) NC 4 – Z (pos.).

NC	Error (%)		Log_{10} (real/imag.)	
	5 – 50 Hz	5 – 30 Hz	5 – 50 Hz	5 – 30 Hz
1 – Z (neg.)	5.93	-0.12	1.05	1.56
1 – Z (pos.)	-1.77	-3.23	0.84	3.45
2 – Z (neg.)	-11.06	2.13	0.49	1.56
2 – Z (pos.)	-4.54	-3.47	-0.12	1.52
3 – Z (neg.)	40.41	38.52	0.56	1.66
3 – Z (pos.)	-68.24	2.01	0.03	2.41
4 – Z (neg.)	7.84	2.25	0.71	1.49
4 – Z (pos.)	-9.19	-8.40	0.96	2.12

Table 3.10: Comparison between the estimates of the eight axial coefficients averaged over the 5 – 50 Hz and 5 – 30 Hz intervals.

3.4 Concluding remarks

This chapter demonstrated the excellent capabilities of the FNSI method in the identification of the SmallSat spacecraft, a large-scale structure possessing multiple nonsmooth nonlinearities. The important number of measured channels to process in the estimation of parameters, the existence of nonproportional damping and the presence of closely-spaced modes were additional challenges successfully tackled.

It is interesting to note the increased complexity of the nonlinear coefficients presented throughout the chapter with respect to the identification, for example, of the Duffing oscillator in Section 2.9. It was remarked that the analysis the frequency dependence of these coefficients provides a convenient means to assess the quality of the identification. Specifically, important peaks in the frequency variations of the coefficients generally originate from inaccuracies in the linear parameter estimation. The entire frequency dependence may also be affected by a drift in the case of missing modes, or as a result of nonlinear modelling errors. The detection of spurious poles is also possible via the inspection of the nonlinear coefficients.

This discussion stresses that the selection of the model order in complex identification cases remains a distinct challenge. In this context, the possibility to mitigate drifts in the frequency-dependent coefficients using the static contributions of higher-frequency modes is an interesting approach that should deserve more investigation.

Chapter 4

Grey-box identification of a solar array structure using cubic splines

Abstract

As most identification approaches in nonlinear structural dynamics, the FNSI method assumes in advance a mathematical model of the nonlinearities. This is however possible in specific situations only, since nonlinear effects may be caused by numerous phenomena and a priori knowledge may be limited. In this context, the present chapter investigates the usefulness of piecewise third-order polynomials, termed cubic splines, to identify the complex nonlinear dynamics of solar arrays in their stowed configuration. The capability of the FNSI method to calculate accurately a large number of parameters makes tractable the use of splines in real-life systems, as the dimensionality of the inverse problem is known to increase dramatically in this case. The experimental structure of interest consists of two parallel aluminium plates assembled with bolted connections. This application is challenging because of the existence of impacts between the two plates at high excitation amplitude, and because of the activation of complicated stiffness and damping mechanisms within the bolted connections.

4.1 Introduction

In the introduction to Chapter 1, nonlinear system identification in structural dynamics was presented as a three-step process [47]. Starting with the detection of nonlinearity, it is then usually accomplished through the selection of a suitable model class based on available prior knowledge, and the treatment of measured data to estimate model parameters. Different types of models can be distinguished by the amount of prior knowledge they incorporate, namely white-box, grey-box and black-box models [107]. In white-box identification, the overall model structure and the mathematical representation of the nonlinearities are specified in advance based on physics, which precisely refers to the second step in Fig. 1.1. Assuming the functional form of the nonlinearities is however possible in specific situations only. This was, for instance, the case in Section 1.4, where histograms, time-frequency spectra and restoring force plots were exploited to characterise the WEMS nonlinearities in the SmallSat spacecraft. In most circumstances, this is rather a hard requirement to handle, since nonlinear effects may be caused by numerous phenomena and a priori knowledge may be limited. The complexity of nonlinearity characterisation may be bypassed by embracing black-box approaches, where a sufficiently rich and flexible model structure is employed [11, 85, 125] to capture all relevant physics [127]. The major drawback of black-box models is that they make no use of the physical insights the user may possess into the structure under test. They also suffer from a rapid growth of the dimensionality of the inverse problem as the number of degrees of freedom (DOFs) and of nonlinearities increases.

Grey-box modelling is therefore a relevant alternative. In grey-box identification, a known model structure, usually dictated by Newton's second law of dynamics, is complemented with mathematical functionals that may represent a vast variety of nonlinear behaviours. The most standard practice is to resort to high-order polynomial expansions, such as ordinary [93] or Chebyshev polynomials [60]. Some authors utilised neural networks and learning algorithms to approximate nonlinearities and estimate model parameters, respectively [24, 61]. Another approach for handling unknown nonlinearities is proposed in Ref. [70], where nonlinear effects are seen as disturbances to the linear system and model parameters are calculated using the so-called disturbance rejection control theory. Applications of this approach to Coulomb friction identification in an industrial robot and crack detection in turborotors are reported in Refs. [70, 108]. A final example of grey-box modelling is the possibility of using an integral of the first kind to identify a nonlinear force, as investigated in the context of a computer disk drive servo in Ref. [64].

The present chapter adopts a grey-box identification methodology by exploiting cubic splines to represent nonlinearities. A cubic spline is a continuous, piecewise third-order function defined by a series of knot points. Spline-based identification of nonlinear systems has recently attracted some attention [18, 30, 40, 131]. Indeed, splines have the advantage of being as simple as ordinary polynomials, while overcoming some of their drawbacks. In particular, high-degree polynomials used to approximate complex nonlinearities are known to diverge rapidly outside the approximation interval, which generally prevents them from

being utilised for numerical simulations. Furthermore, such high-degree polynomials may exhibit unbounded oscillations near the boundaries of the interval when interpolating equally-spaced knots. This behaviour, referred to as the Runge's phenomenon, indicates that increasing the degree of a polynomial interpolation does not always result in a decrease of the error. Finally, even if splines are naturally geared towards fitting smooth nonlinearities, they may also be reasonably well suited for representing piecewise linear functions [18], unlike polynomials. This latter capability requires nonevenly distributed knots, hence involving a nonlinear-in-the-parameters identification problem.

In this chapter, cubic splines with equally-spaced knots are employed to identify the complex nonlinear dynamics of solar arrays in their stowed configuration. The estimation of the model parameters is achieved using the FNSI method. The capability of the FNSI method to calculate accurately a large number of parameters makes tractable the use of splines in real-life systems, as the dimensionality of the inverse problem is known to increase dramatically in this case. The experimental structure of interest consists of two parallel aluminium plates assembled with bolted connections. This application is challenging because of the existence of impacts between the two plates at high excitation amplitude, and because of the activation of complicated stiffness and damping mechanisms within the bolted connections.

The chapter begins with a detailed description of the solar array setup in Section 4.2. Low-level data are also exploited to derive a linear model of the structure. Three data sets collected for increasing force levels are analysed in Section 4.3 to detect nonlinearity based on distortions in frequency response function (FRF) measurements. The nonlinear identification of the structure based on cubic splines is finally addressed in Section 4.4 using high-level data. This final section is structured according to the five main steps of the FNSI methodology, as reminded in Fig. 4.1. The conclusions of the chapter are summarised in Section 4.5. Experimental data exploited in this chapter were collected during a stay at the FEMTO-ST Institute (Besançon, France), with the support of Prof. E. Foltête and Dr. S. Cogan. The analysis carried out herein is reported in Refs. [75, 76].

1. Select appropriate basis functions $\mathbf{h}_a(\mathbf{q}(t), \dot{\mathbf{q}}(t))$ to represent the nonlinearities in the structure under test.
2. Choose the index i and the number of processed frequency lines F.
3. Determine the order of the model using a stabilisation diagram.
4. Convert the state-space model to modal space to estimate the FRF matrix $\mathbf{G}_p(\omega)$ of the underlying linear structure.
5. Convert the state-space model to physical space to estimate the nonlinear coefficients c_a associated with the basis functions.

Figure 4.1: Reminder of the five main steps of the FNSI methodology.

4.2 Linear analysis of a simplified solar array structure at low level

As emphasised in the introductory chapter of the thesis, nonlinear phenomena are frequently evidenced in dynamic testing of aerospace systems. In the case of space structures, nonlinearity commonly results from imperfect mounting interfaces between subsystems, as in the examples of the Cassini spacecraft [14] and of the International Space Station [50]. Another specific difficulty encountered in spacecraft testing is the behaviour of solar arrays in their stowed configuration. In fact, solar panels are folded in the launch vehicle fairing not only to save volume, but also to better withstand dynamic loads. When folded, they are assembled with bolts introduced at specific points, termed stacking points. Impact snubbers are also inserted between adjacent panels to maintain contact and absorb vibration. Some of the many phenomena that may lead to nonlinear effects are the loss of contact at high excitation amplitude, and the complicated stiffness and damping mechanisms activated within the stacking points.

To investigate these phenomena, a simplified test rig that mimics the complex dynamics of folded solar generators was built at the FEMTO-ST Institute (Besançon, France). It consists of two $77 \times 44 \times 0.5\ cm^3$ parallel aluminium plates mounted in free-free configuration, as pictured in Fig. 4.2 (a). They are clamped together at the top edge and connected through three stacking points (see Fig. 4.2 (a – b)). Two solithane snubbers were mounted on steel supports at both corners of the bottom free edge, as shown in Fig. 4.2 (c). As pointed out in Ref. [36], the small contact areas between the stacking points and the plates are an additional possible source of nonlinear behaviour, as they may induce large, localised bending deformations.

The structure was instrumented with 10 accelerometers positioned on both sides of each suspected nonlinearity (see Fig. 4.2 (c)), *i.e.* the three stacking points and the two snubbers. These five potentially nonlinear connections are denoted NL 1 – 5 in Fig. 4.2 (a). Excitation signals were applied to the front panel by means of a 10-N shaker, visible in Fig. 4.2 (a). Force and acceleration time histories were recorded at the excitation point through an impedance head. In this study, gaps of less than a millimetre were introduced between the two snubbers and the opposite plate such that there is no contact at rest (see Fig. 4.2 (c – d)). However, the relatively small size of the sought gaps complicated the mounting of the two snubbers. This resulted in dissimilar gap sizes, and in an imperfect alignment of the snubber and the rear panel at NL 5, as noticeable in Fig. 4.2 (d).

Since a gap exists at rest between the two impact snubbers and the rear panel, a linear analysis of the structure can safely be achieved at very low level. To this end, a periodic noise forcing with a root-mean-squared (RMS) amplitude of 0.16 N was applied to the front panel, considering a sampling frequency of 6400 Hz. A periodic noise consists in the repetition of a band-limited, random time series. A white amplitude spectrum in 5 – 350 Hz was chosen herein, as depicted in Fig. 4.3. The experiment was conducted over 28 periods of 4 seconds each, providing a frequency resolution of 0.25 Hz. As achieved

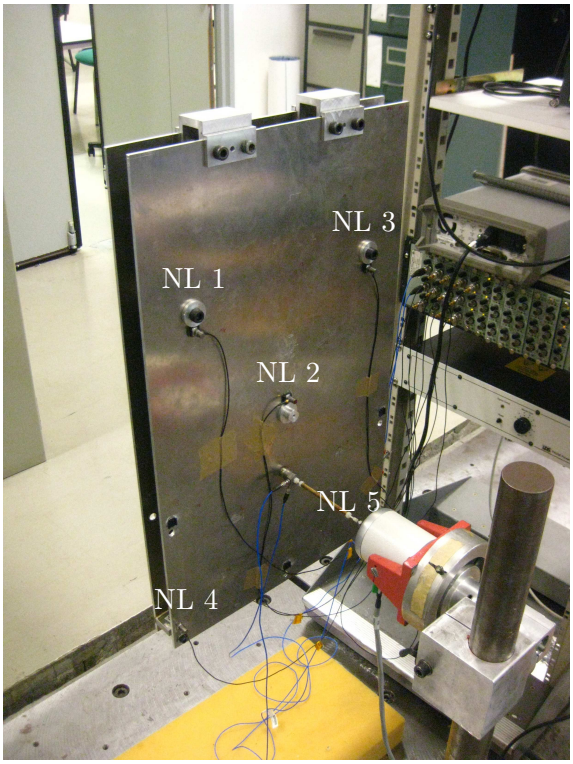

(a) Overall view of the two aluminium plates clamped together at the top edge, and mounted in free-free configuration.

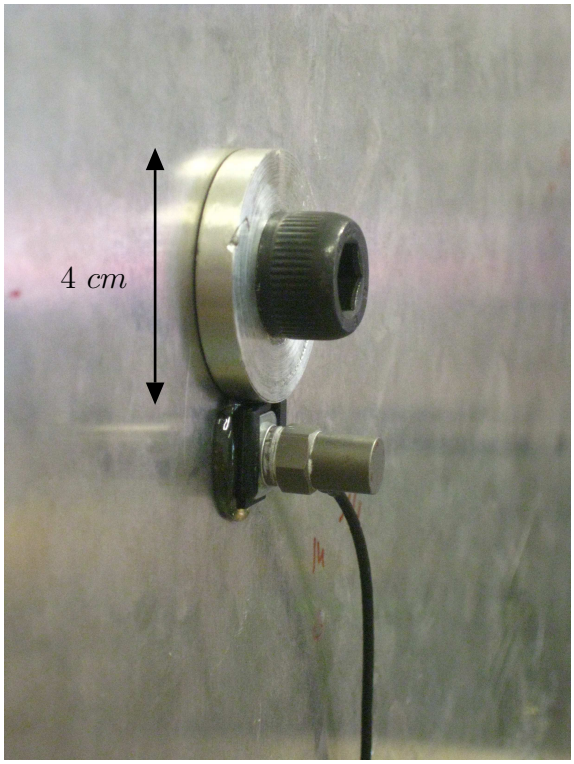

(b) Close-up of the stacking point at NL 1.

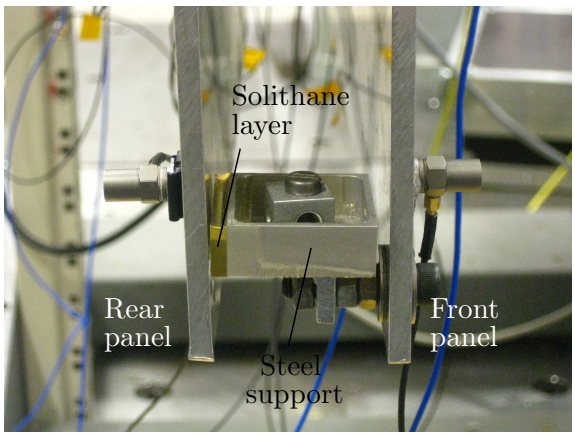

(c) Close-up of the impact snubber at NL 4 instrumented with one accelerometer on both sides.

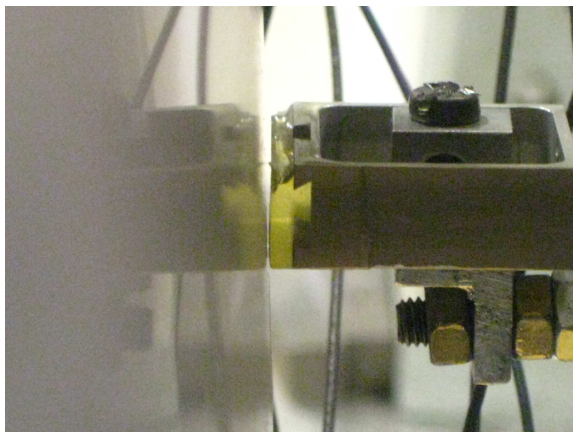

(d) Close-up at NL 5 showing the imperfect alignment between the snubber and the rear panel.

Figure 4.2: Simplified experimental solar array structure in stowed configuration.

throughout the thesis, the first 10 periods were rejected to settle the transients, and thus to avoid leakage distortions in the frequency domain. Output measurements were averaged over the remaining 18 periods to mitigate noise and obtain a sample estimate of its covariance matrix, as required for the FNSI method. Note that the acquisition software utilised during the test campaign did not allow the possibility of applying multisine excitations. The difference between a multisine and a periodic noise is that the amplitude and phase spectra of the latter are randomly distributed, as opposed to the flat amplitude spectrum of the multisine signal.

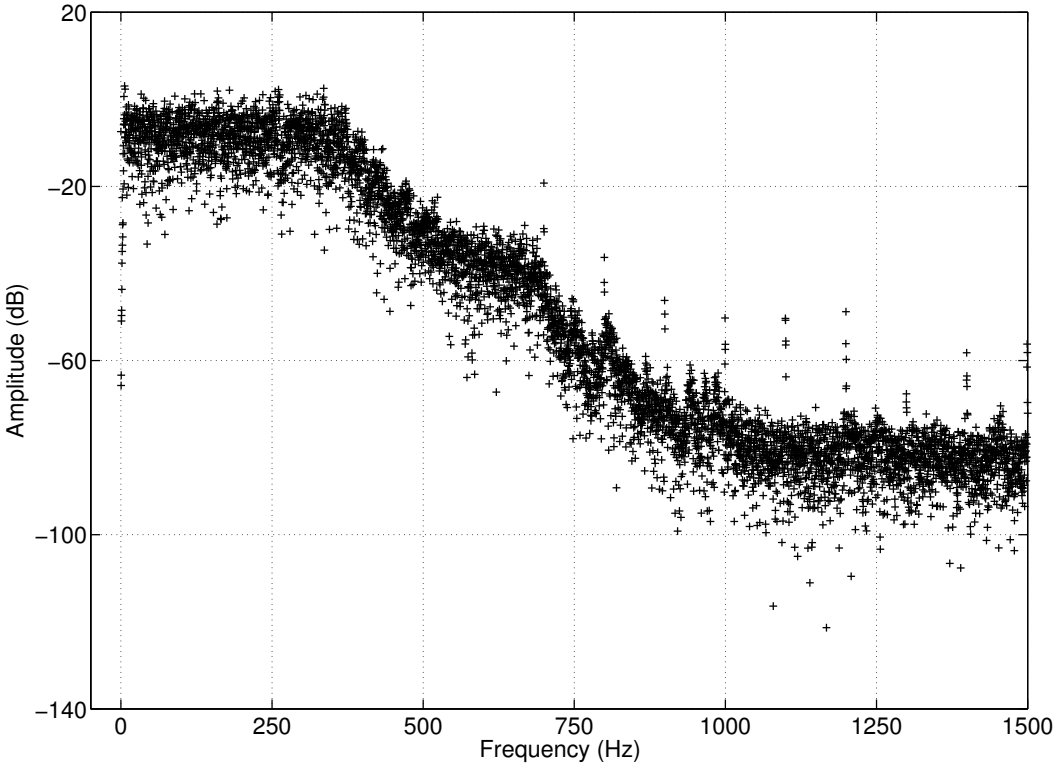

Figure 4.3: Amplitude spectrum over 0 – 1500 Hz of a single period of the noise forcing at 0.16 N RMS.

The linear analysis of the structure is conducted using a stabilisation diagram, as proposed in Fig. 4.4 (a) up to the order 150. This diagram was constructed using the FNSI algorithm considering no nonlinear basis functions in input, nor noise weighting. The stabilisation thresholds in natural frequency, damping ratios and MAC value were set to 2 %, 10 % and 0.95, respectively. These tolerances were loosened with respect to the SmallSat identification in Chapter 3 because of the presence of noise in the data. The knowledge of the output noise covariance matrix gained via the periodicity of the excitation can be incorporated in the stabilisation diagram, as illustrated in Fig. 4.4 (b). This latter figure demonstrates that introducing a noise weighting into the FNSI algorithm helps identify noisy modes, as particularly visible below 100 Hz where the signal-to-noise ratio (SNR) is low.

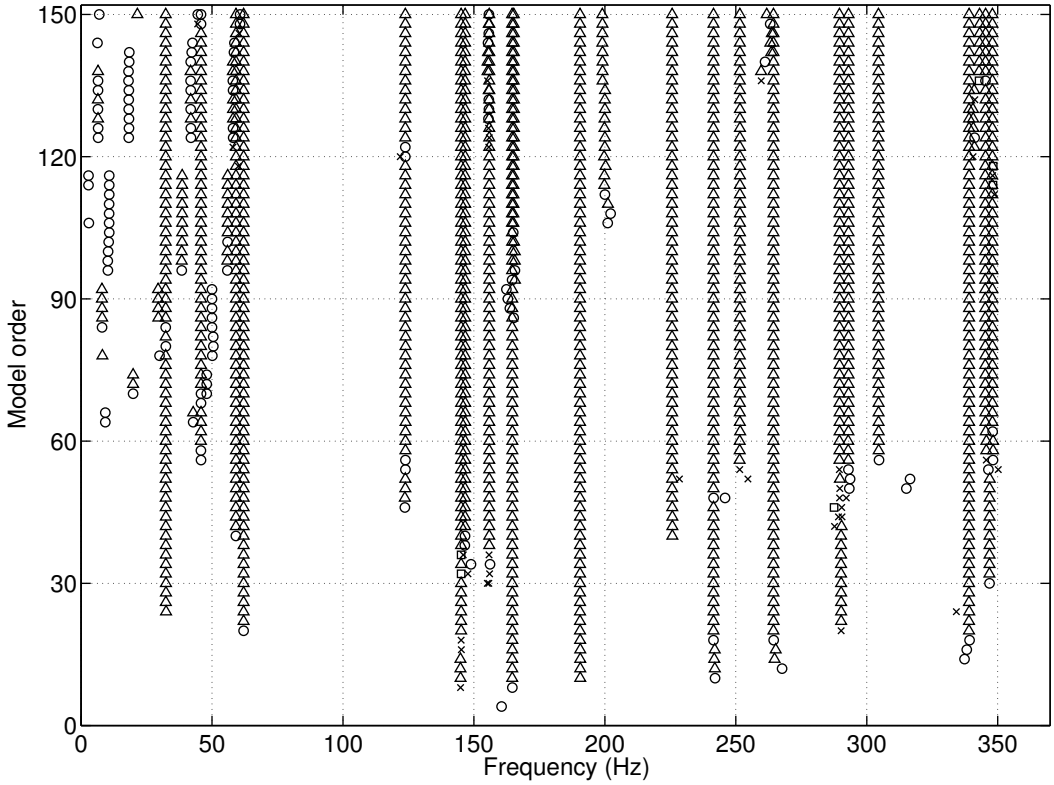

(a)

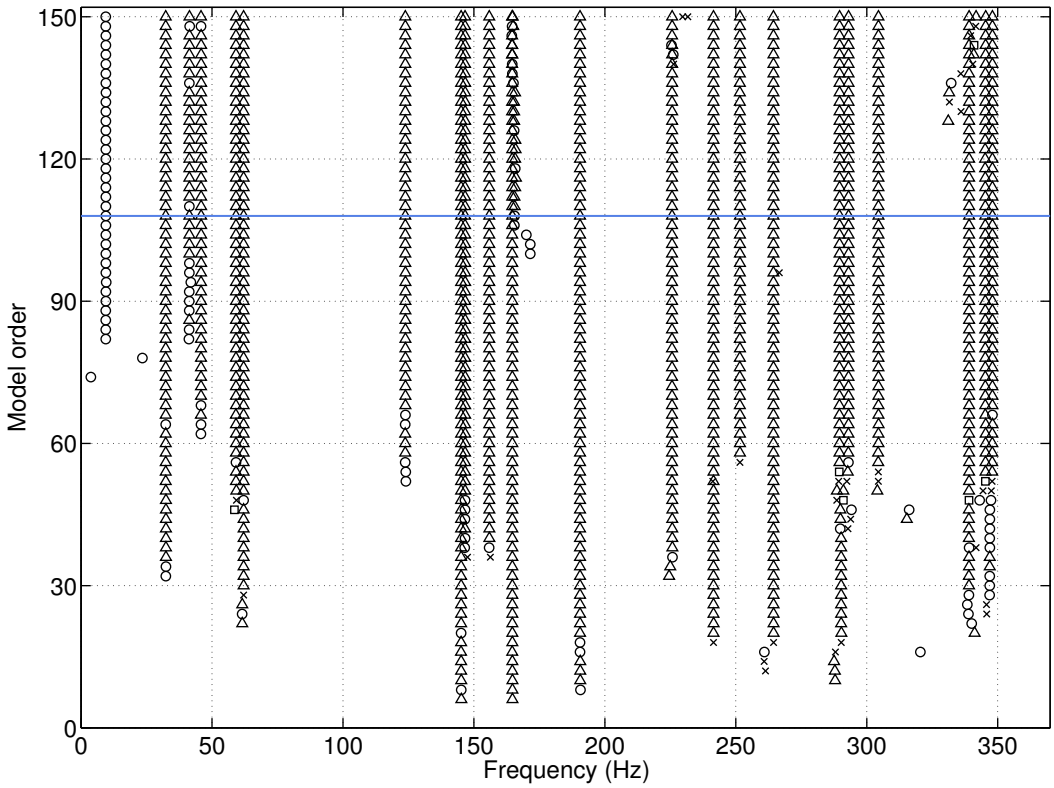

(b)

Figure 4.4: Stabilisation diagram computed at low level (0.16 N RMS) (a) without and (b) with noise weighting. Stabilisation thresholds in natural frequency, damping ratio and MAC value are 2 %, 10 % and 0.95, respectively.

The noise-weighted diagram in Fig. 4.4 (b) leads to the selection of the order 108, for which 21 physical modes are captured in the 5 – 350 Hz band. Table 4.1 lists their natural frequencies and damping ratios. Damping ratios are all found to be lower than 1 %, as expected for an aluminium structure. Fig. 4.5 (a – f) depicts the deformed shapes of modes 1, 3, 7, 11, 12 and 15, respectively. Modes 1, 3 and 11 are likely to involve impacts between the two panels as they correspond to out-of-phase motions of their bottom free edges. One points out an asymmetry around a vertical axis at mid-width of each panel for mode 1, entailing larger displacements at NL 1 and NL 4. A similar asymmetry is also observed in Fig. 4.5 (c), where mode 7 is moreover seen to be an in-phase motion. Higher-frequency modes, such as modes 12 and 15, are associated with in-plane deformations of the panels, causing large relative displacements at the stacking points, but no potential impact.

Mode	Natural frequency ω_0 (Hz)	Damping ratio ϵ (%)
1	32.32	0.64
2	41.36	0.80
3	45.83	0.31
4	59.14	0.27
5	62.07	0.16
6	123.82	0.14
7	145.13	0.08
8	146.64	0.22
9	155.87	0.39
10	164.62	0.14
11	190.52	0.14
12	225.68	0.32
13	241.50	0.20
14	251.56	0.36
15	264.37	0.17
16	289.60	0.43
17	293.05	0.31
18	304.48	0.15
19	339.08	0.36
20	345.24	0.38
21	347.96	0.18

Table 4.1: Natural frequencies and damping ratios of the 21 modes identified at low-level (0.16 N RMS) in the 5 – 350 Hz band.

The choice of the order 108 in the diagram of Fig. 4.4 (b) is based on an individual analysis of its stabilisation columns. This is illustrated in Fig. 4.6 (a – d) where the frequency and damping ratio of modes 1 and 7 are depicted for increasing model orders. In general, the four graphs show important variations below the order 70, translating the successive

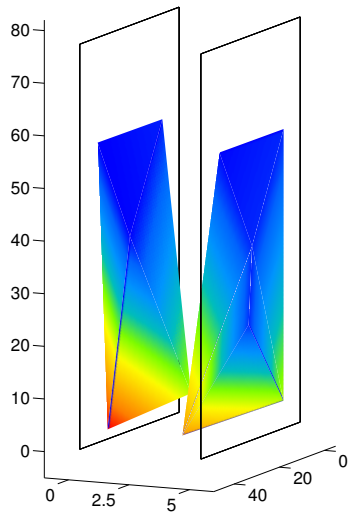

(a) Mode 1 (32.32 Hz)

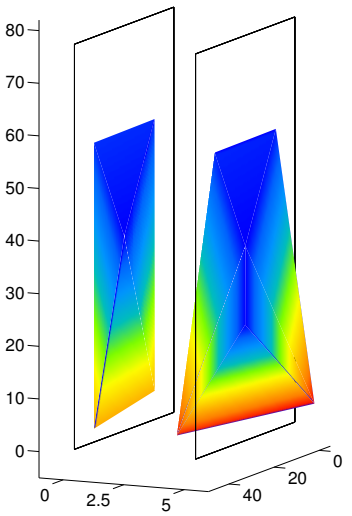

(b) Mode 3 (45.83 Hz)

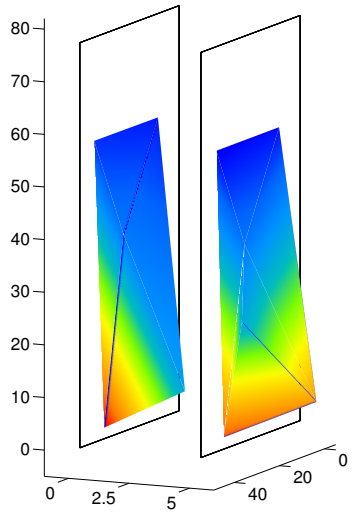

(c) Mode 7 (145.13 Hz)

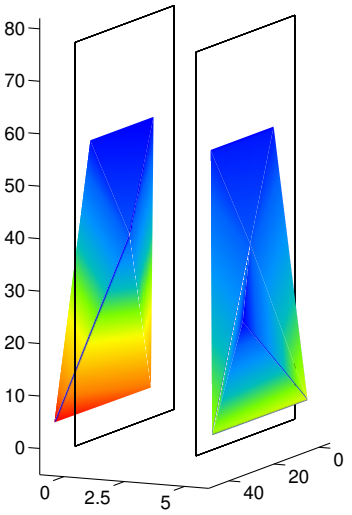

(d) Mode 11 (190.52 Hz)

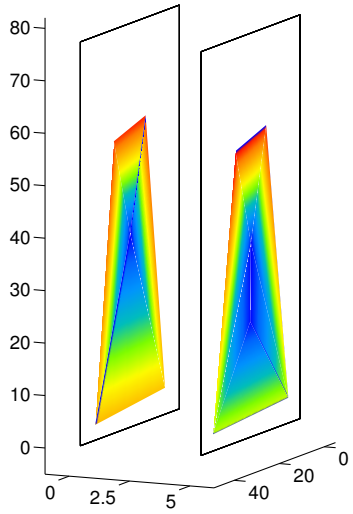

(e) Mode 12 (225.68 Hz)

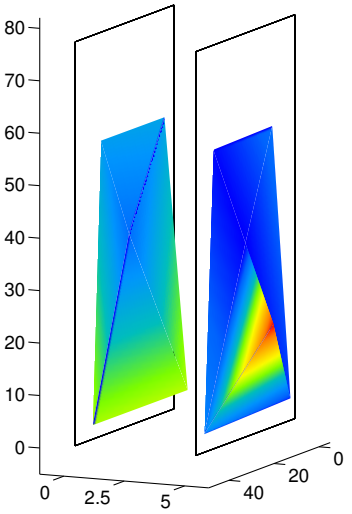

(f) Mode 15 (264.37 Hz)

Figure 4.5: Deformed shapes corresponding to modes 1, 3, 7, 11, 12 and 15 identified at low level (0.16 N RMS). Geometrical dimensions are given in centimetres.

appearance of stable modes in Fig. 4.4 (b). In the present section, the index i was chosen equal to 200. Moreover, in Chapter 2, it was noted that poor parameter estimates may be obtained for values of i lower than 1.5 n_s. This implies that the high-order poles in Fig. 4.4 (a – d) should also be assessed with care, as the accuracy of the subspace model is expected to decrease beyond the order 134. The motivation for selecting the order 108 is primarily due to the behaviour of the frequency and damping ratio of mode 1 in Fig. 4.6 (a –b). Indeed, they both exhibit a significant variability at lower orders, attributed to the reduced value of the SNR in the corresponding frequency interval. The complete stabilisation of mode 7 also requires the order 108 as the damping ratio in Fig. 4.6 (d) suddenly varies at orders 96 and 104, as a result of the late stabilisation of mode 2 in Fig. 4.4 (b).

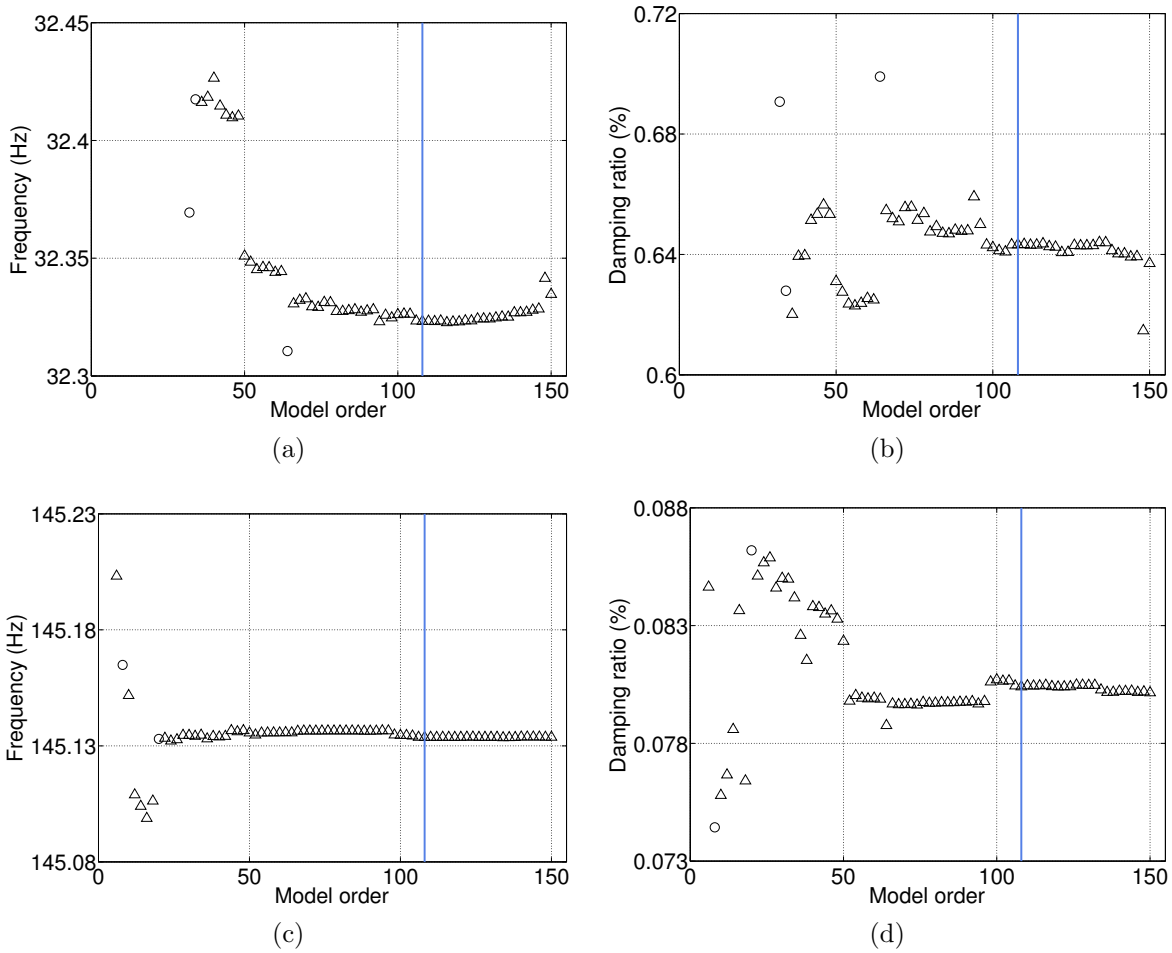

Figure 4.6: Frequency and damping ratio of (a – b) mode 1 and (c – d) mode 7 calculated at low level (0.16 N RMS) for increasing model orders.

Fig. 4.7 finally shows the comparison between the FRF measured at NL 4 on the front panel (in black) and the corresponding FRF synthesised by the linear subspace model (in

dashed blue). In what follows, the difference between two frequency-dependent quantities should be understood as the difference of their magnitudes taken in dB. The difference between the noise variance and the measured FRF is plotted in Fig. 4.7 (in grey). This grey curve yields a convenient visualisation of the SNR with a negative sign. One notes that the SNR is around 40 dB inside the 100 – 350 Hz band, and reaches 60 dB at the resonance locations. The low frequencies below 100 Hz are more importantly affected by noise as the SNR drops to 30 dB. One also observes a very good agreement between measured and reconstructed FRFs. This is confirmed by the difference between the modelling error and the measured FRF depicted in Fig. 4.7 (in orange), showing a signal-to-modelling-error ratio of about 20 dB throughout the 100 – 350 Hz interval. Greater errors are noticed where the relative importance of noise is larger, in particular in the vicinity of anti-resonances and below 100 Hz.

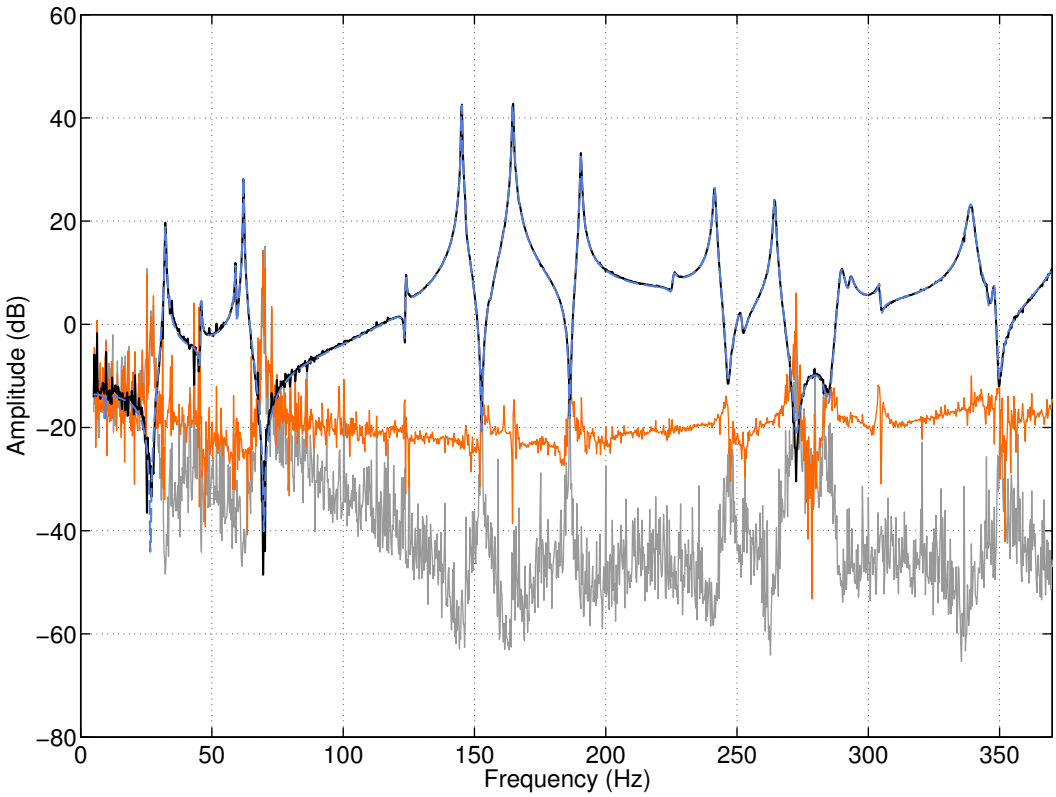

Figure 4.7: FRF measured at low level (0.16 N RMS) at NL 4 on the front panel (in black) and corresponding FRF synthesised by the linear subspace model (in dashed blue) over 5 – 350 Hz; difference between the noise variance and the measured FRF (in grey); difference between the modelling error and the measured FRF (in orange).

4.3 Nonlinearity detection based on distortions in FRF measurements

The comparison of FRF measurements at different input levels is an interesting intermediate step in the nonlinear identification process. Since FRFs are required to be independent of the force amplitude spectrum if the system under test is linear [47], this comparison provides a reliable indicator of the presence of nonlinear behaviour in specific frequency bands. An additional interest in FRF measurements at multiple levels is that the complexity of the nonlinear modelling problem can be assessed prior to estimating parameters, by inspecting the global hardening or softening trend of the resonance peaks and the importance of their noisy-like distortions [92].

Fig. 4.8 (a) depicts the FRFs measured at NL 4 on the front panel for input levels of 0.16 N (in black), 1.91 N (in orange) and 3.79 N (in blue) RMS. The parameters of the excitation signals at 1.91 and 3.79 N RMS are identical to those selected at low level and discussed in Section 4.2. The analysis of Fig. 4.8 (a) reveals substantial nonlinear effects throughout the excitation band. A close-up of the 5 – 100 Hz interval is proposed in Fig. 4.8 (b). Modes 1 and 3 around 32 and 46 Hz are seen to be subjected to severe hardening distortions. This is confidently attributed to the activation of the impact snubbers, as Fig. 4.5 (a – b) showed that both modes involve out-of-phase motions of the two panels. The existence of impacts in the dynamics shifts the resonance frequencies of modes 1 and 3 of about 2 and 3 Hz, respectively. The more significant distortions affecting mode 3 are most probably due to a nonlinear geometrical effect originating from large, local deformations in the stacking points areas, as anticipated in Ref. [36]. This is coherent with the important torsion of the front panel visible in the deformed shape of mode 3 in Fig. 4.5 (b). One finally notes in Fig. 4.8 (b) that mode 5 at 62 Hz, which is an in-phase motion of the assembly, remains unaffected by an increase of the input level.

A second close-up in Fig. 4.9 (a) displays the superposition of FRFs from 100 to 200 Hz. Similarly to mode 5, mode 7 at 145 Hz is invariant with respect to the force amplitude, in agreement with its deformed shape in Fig. 4.5 (c). Mode 10 at 165 Hz, involving tensile deformations of the stacking connection at NL 2, manifests a decrease of the resonance frequency. This phenomenon, *i.e.* the softening due to micro-impacts of a bolted connection undergoing normal loadings, has often been reported in the technical literature [5, 22, 34]. The deformed shape of mode 11 at 191 Hz, presented in Fig. 4.5 (d), combines an out-of-phase motion of the panels, and hence impacts, and tensile deformations at NL 2. This hardening-softening combination results in nonlinear distortions in Fig. 4.9 (a), but without apparent modification of the resonance frequency.

A final close-up of the FRFs is plotted in 200 – 350 Hz in Fig. 4.9 (b). In this interval, modal motions essentially consist of large relative displacements at the stacking points, as depicted in Fig. 4.5 (f) for mode 15. This translates into softening distortions of most resonance peaks in this band, associated with significant frequency shifts. For instance, the frequency of mode 19 decreases from 339 Hz at low level to 335 Hz at 3.79 N

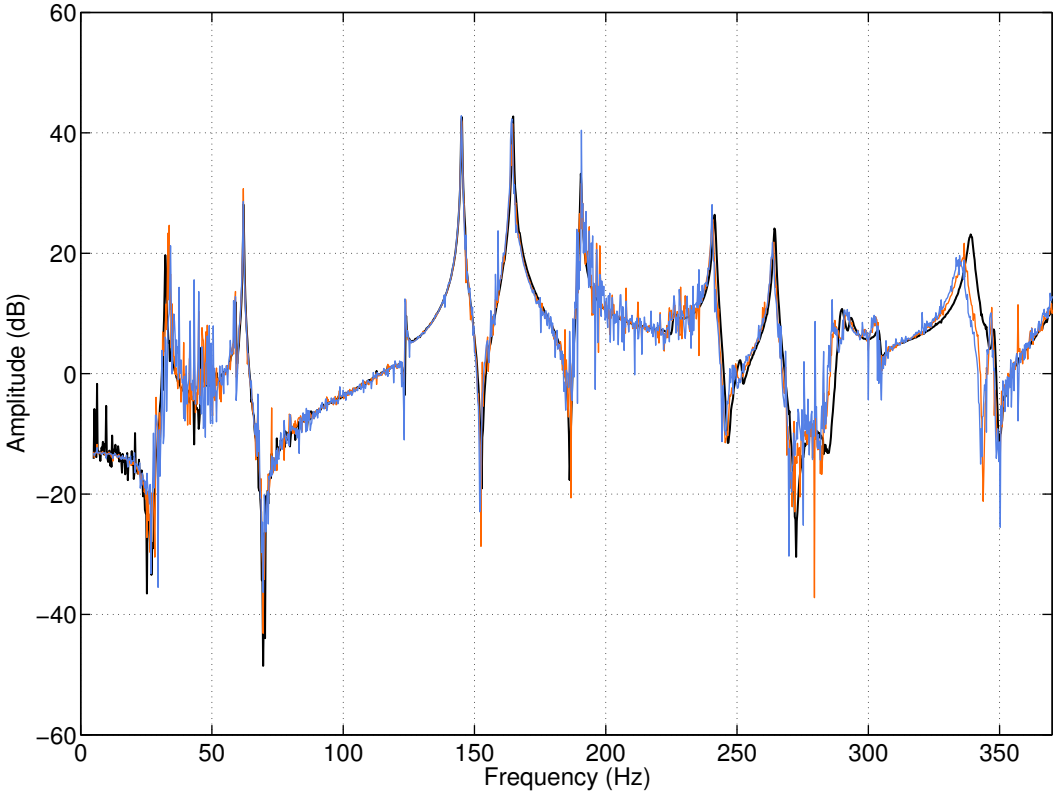

(a)

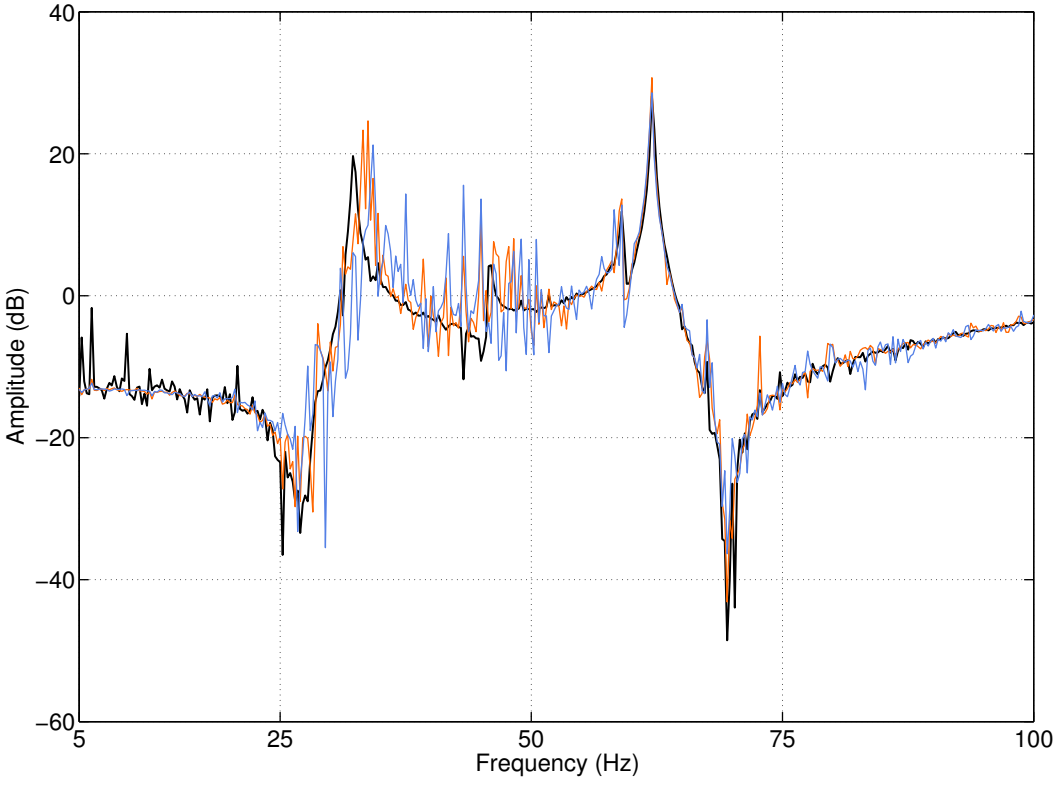

(b)

Figure 4.8: FRFs measured at NL 4 on the front panel at 0.16 N (in black), 1.91 N (in orange) and 3.79 N (in blue) RMS. (a) Full band over 5 – 350 Hz; (b) close-up in the 5 – 100 Hz band.

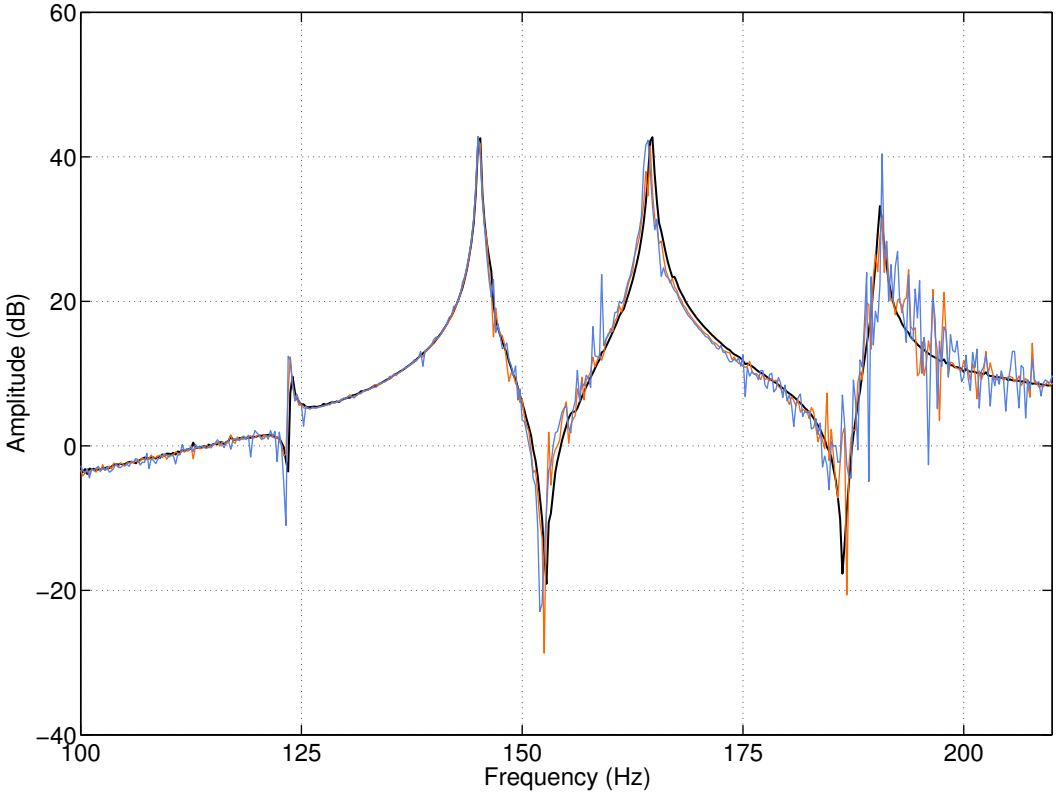

(a)

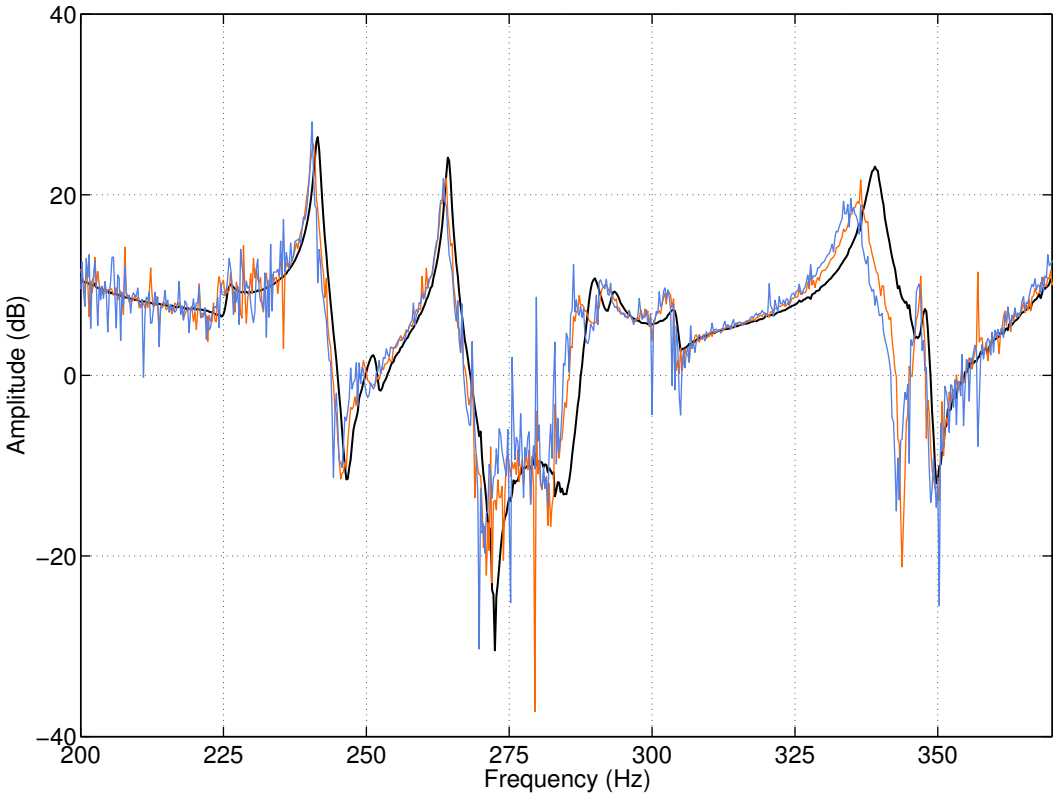

(b)

Figure 4.9: FRFs measured at NL 4 on the front panel at 0.16 N (in black), 1.91 N (in orange) and 3.79 N (in blue) RMS. (a) Close-up in the 100 – 200 Hz band; (b) close-up in the 200 – 350 Hz band.

RMS. This may be explained by the opening of the bolted connections at high frequency, implying an important loss of stiffness due to macro-impacts.

In summary, the analysis of the distortions affecting FRF measurements at multiple force levels highlighted very rich nonlinear dynamics. Impacts were first attested for modes entailing out-of-phase motions of the panels, *e.g.* modes 1 and 11, resulting in hardening behaviour. Large bending deformations localised in the stacking points areas were reported for mode 3 as an additional hardening phenomenon of geometrical nature. Softening effects due to tensile loadings of the bolted connections were finally evidenced, and attributed to micro-impacts in the case of mode 10 and gapping for high-frequency modes beyond 200 Hz.

4.4 Nonlinearity identification at high level using cubic splines

According to the FNSI methodology summarised in Fig. 4.1, the construction of a nonlinear subspace model of the solar array dynamics at 3.79 N RMS requires in practice the completion of five successive steps. The first step is an appropriate selection of the nonlinear basis functions $\mathbf{h}_a(\mathbf{q}(t), \dot{\mathbf{q}}(t))$ defined in Eq. (2.2). In this context, the following section introduces an approximation strategy of nonlinear restoring forces relying on cubic splines, and alleviating the need for selecting the functional forms based on physics.

4.4.1 Cubic spline representation of the solar array nonlinearities

For the sake of simplicity and without loss of generality, the scope of this section is restricted to an elastic nonlinear restoring force $g(q(t))$ in the single-DOF case. Let q be divided into R segments of arbitrary length and defined by their abscissas, denoted by q_r for $r = 1, \ldots, R+1$. Each abscissa is associated with an ordinate g_r, together defining a knot (q_r,g_r) of the spline. Thus, if q is a displacement value in between knots r and $r+1$, the corresponding point of a cubic-spline-based approximation of $g(q(t))$ is given by [16]

$$g(q(t)) = (2d^3-3d^2+1)g_r+(-2d^3+3d^2)g_{r+1}+(d^3-2d^2+d)(q_{r+1}-q_r)g'_r+(d^3-d^2)(q_{r+1}-q_r)g'_{r+1} \tag{4.1}$$

where d is the normalised displacement $\frac{q-q_r}{q_{r+1}-q_r}$. The computation of the first derivatives $g'_r = \partial g_r/\partial q$ can be achieved by forcing the cubic spline and its first two derivatives to be continuous across each of the interior knots. This results in $R-1$ linear constraint equations

$$\frac{g'_{r-1}}{q_r - q_{r-1}} + 2\left(\frac{1}{q_r - q_{r-1}} + \frac{1}{q_{r+1} - q_r}\right) g'_r + \frac{g'_{r+1}}{q_{r+1} - q_r} = 3\left(\frac{g_r - g_{r-1}}{(q_r - q_{r-1})^2} + \frac{g_{r+1} - g_r}{(q_{r+1} - q_r)^2}\right). \tag{4.2}$$

Since the essentially nonlinear restoring force $g(q(t))$ is zero and has zero slope at equilibrium, one should also enforce, in the segment containing the abscissa of the equilibrium point, that

$$(d_0^3-2d_0^2+d_0)(q_{r+1}-q_r)\,g'_r+(d_0^3-d_0^2)(q_{r+1}-q_r)\,g'_{r+1} = -(2d_0^3-3d_0^2+1)\,g_r-(-2d_0^3+3d_0^2)\,g_{k+1} \tag{4.3}$$

and

$$(3d_0^2-4d_0+1)(q_{r+1}-q_r)\,g'_r+(3d_0^2-2d_0)(q_{r+1}-q_r)\,g'_{r+1} = 6(d_0-d_0^2)(g_r-g_{r+1}) \tag{4.4}$$

where $d_0 = \frac{-q_r}{q_{r+1}-q_r}$. Eqs (4.2), (4.3) and (4.4) constitute $R+1$ relations that uniquely define the $R+1$ parameters $g'_1,\ldots,g'_{R+1}$ as functions of the ordinates of the knots $g_1,\ldots,g_{R+1}$. The first derivatives can thus be substituted in Eq. (4.1) to compute the basis functions associated with the ordinates. These basis functions correspond to the terms $\mathbf{h}_a(\mathbf{q}(t),\dot{\mathbf{q}}(t))$ introduced as additional external forces in the FNSI algorithm, as described in Chapter 2. Note finally that the constraint relation in Eq. (4.3) is a manifestation of the necessity in the FNSI approach to ensure that the row space of the states $\mathbf{X}$ and of the extended input spectra matrix $\mathbf{E}_i$ do not share information, as formally stated through the assumption (ii) in Section 2.5.1.

In the solar array identification, splines in displacement and velocity are implemented at NL 4 and NL 5. No nonlinearity is considered at NL 1, NL 2 and NL 3, since the relative displacements and velocities measured at these three connections are of comparable amplitude to the noise level. This is illustrated in Fig. 4.10 (a – b) where the relative displacements at NL 1 and NL 4 are plotted versus time and compared to the noise signal. The SNR in RMS value is equal to 11.65 at NL 4, while it drops to 1.51 at NL 1 because of the position of the shaker and of the stiffness distribution of the assembly. Note that implementing splines exclusively at NL 4 and NL 5 prevents the nonlinear effects due to the stacking points and the impact snubbers from being distinguished in the identified force curves.

The optimal number of knots in the definition of the splines should be sought by minimising the difference in some metric between the predictions of the nonlinear model and measured data, similarly to the rigorous determination of the index i. One nevertheless opt again for a practical approach where an acceptable number of knots is found by trial and error, maximising the accuracy of the underlying linear properties of the system estimated from nonlinear data. Splines with 5 and 3 knots are therefore chosen to model stiffness and damping nonlinearities, respectively, because the agreement between the properties listed in Table 4.1 and the corresponding estimates computed at 3.79 N RMS was found to degrade for larger numbers of knots. It is worth stressing the high dimensionality of the consequent inverse problem, which encompasses 17 inputs, *i.e.* 1 external force and 16 nonlinear basis functions, and 11 outputs. Few identification methods in the technical literature are capable of reliably handling such a large amount of nonlinear coefficients. For instance, the well-established CRP method [47, 98] estimates the coefficients sequentially, *i.e.* errors are accumulated throughout the identification process, and would probably lead to very large errors in the present case study.

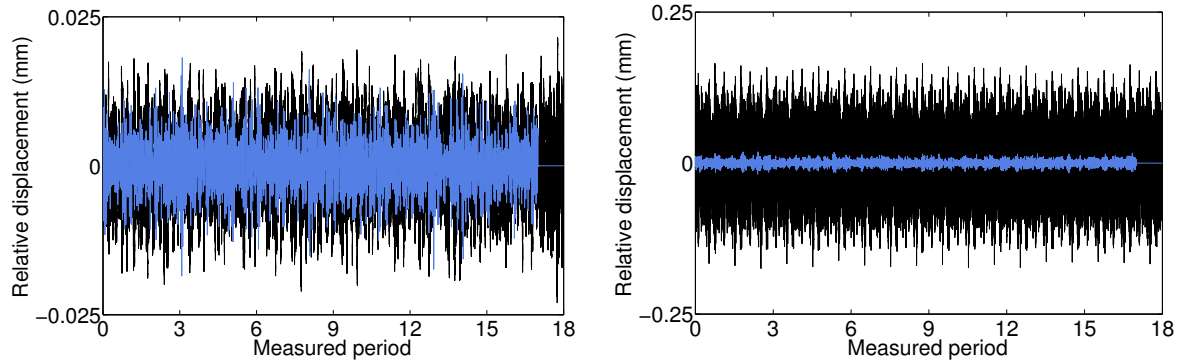

(a) (b)

Figure 4.10: Relative displacement (in black) at (a) NL 1 and (b) NL 4 plotted versus time and compared to the noise signal (in blue).

4.4.2 Choice of the processed bandwidth

The FRF calculated at NL 4 on the front panel is depicted in Fig. 4.11 (a) (in black), together with the difference between the noise variance and the FRF (in grey). The SNR inside the input band reaches 70 to 80 dB at the resonance locations, compared to 60 dB at 0.16 N RMS (see Fig. 4.7). The frequencies below 100 Hz still suffer from larger noise distortions with a SNR around 50 dB. The bandwidth processed in the identification is restricted to 1500 Hz where the SNR is close to 0 dB. This choice completes the second step of the FNSI methodology in Fig. 4.1. The restriction of the bandwidth helps avoid computational memory issues that may arise due to the aforementioned dimensionality of the inverse problem, while preserving the nonlinear distortions appearing outside the input band in the estimation of model parameters.

4.4.3 Determination of the model order

The next step in Fig. 4.1 is the determination of the model order. The stabilisation diagram plotted in Fig. 4.11 (b) indicates that 20 physical modes of the structure can be incorporated in a model of order 130. The choice of the order 130 is motivated by the study of the natural frequency and damping ratio of modes 1 and 3, represented in Fig. 4.12 (a – d) for increasing model orders. One observes that their estimates calculated at low level in Section 4.2 cannot be accurately recovered with acceptable stabilisation features at lower orders. Note that mode 2 identified at low level is not recovered at 3.79 N RMS, most probably because it hardly participates in the response and is dominated by the nonlinear distortions affecting modes 1 and 3 (see Fig. 4.8 (b)).

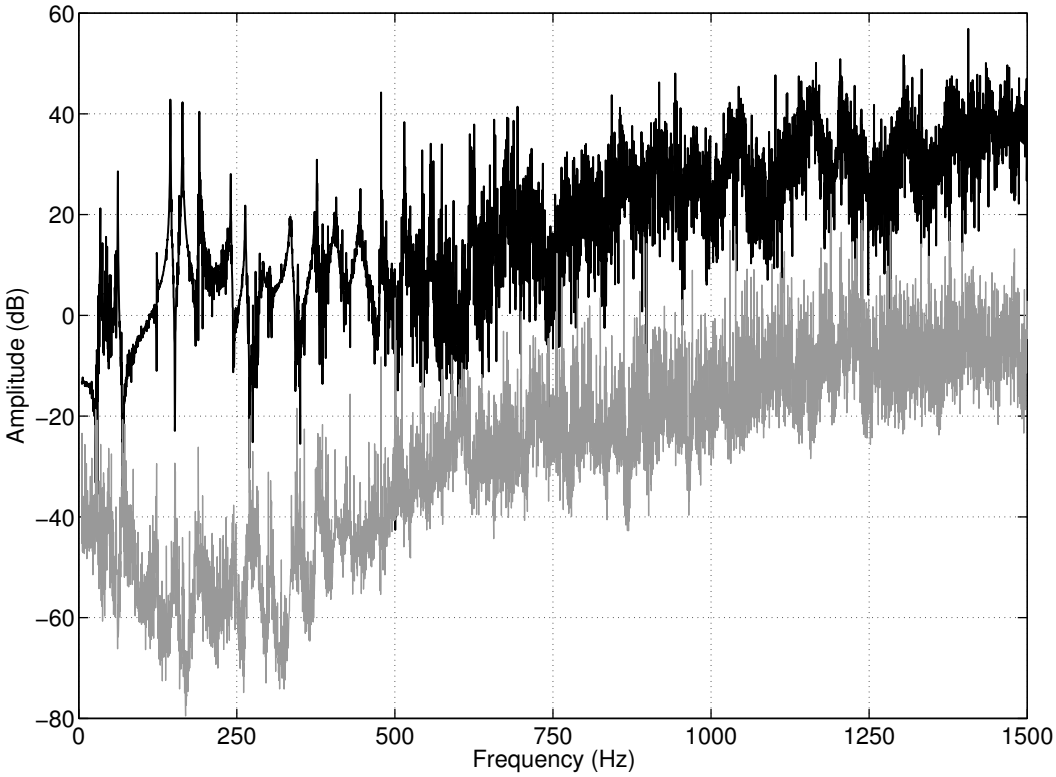

(a)

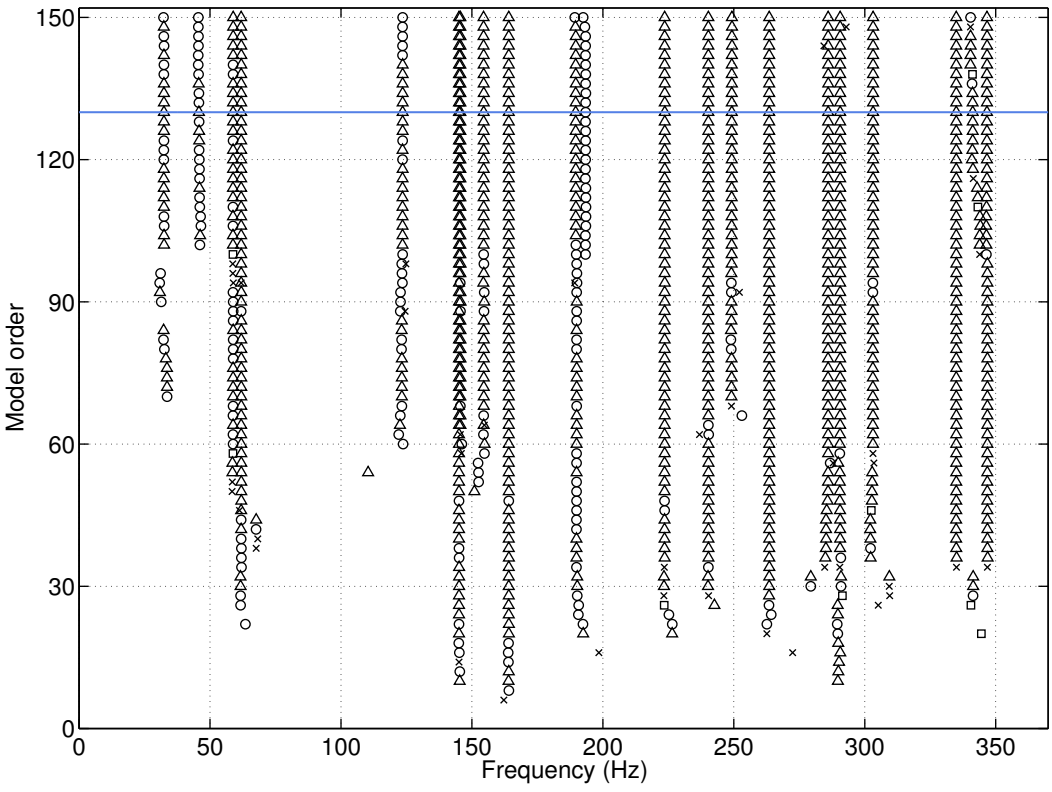

(b)

Figure 4.11: (a) FRF calculated at high level (3.79 N RMS) at NL 4 on the front panel over 0 – 1500 Hz (in black), and difference between the noise variance and the FRF (in grey); (b) stabilisation diagram computed at high level (3.79 N RMS) with noise weighting. Stabilisation thresholds in natural frequency, damping ratio and MAC value are 2 %, 10 % and 0.95, respectively.

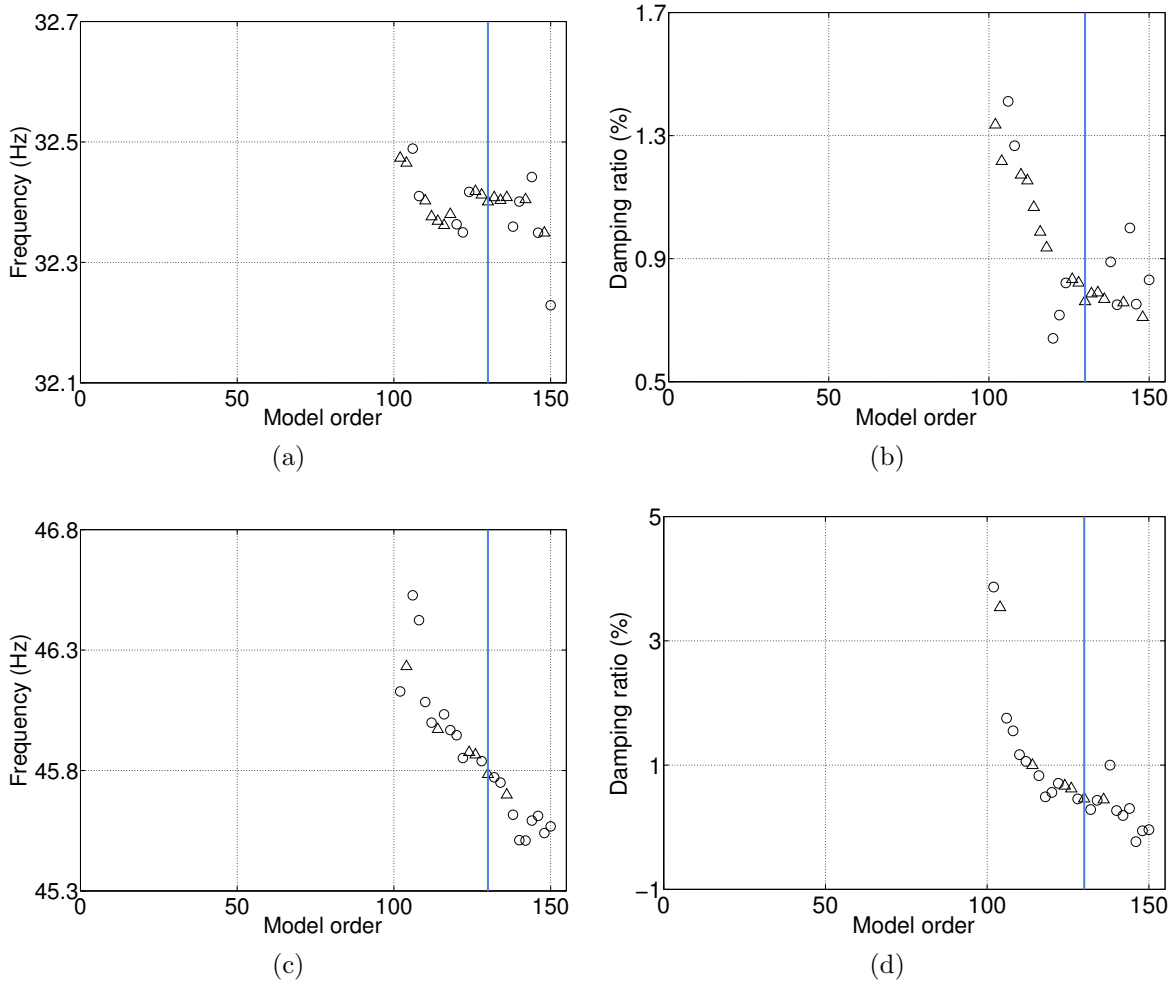

Figure 4.12: Linear frequency and damping ratio of modes 1 (a – b) and 3 (c – d) calculated at high level (3.79 N RMS) for increasing model orders.

4.4.4 Estimation of the underlying linear properties

Table 4.2 lists the linear frequencies of the structure identified at low level for a restricted number of representative modes (second column), together with the associated frequencies estimated at high level using splines (third column). A good agreement is noted for modes below 200 Hz. In particular, the frequencies of modes 1 and 3 are correctly predicted, while they were shown to suffer from the most significant nonlinear distortions in Section 4.3. This is confirmed in Fig. 4.13 (a) where a comparison between the FRF measured at low level at NL 4 on the front panel and the FRF reconstructed using FNSI at high level is plotted. Table 4.2 and Fig. 4.13 (a) prove that the impacts at the snubber connections and the large bending deformations at the stacking points are correctly represented in the nonlinear model.

Mode	Linear model at low level	Spline model at high level	Linear model at high level	Polynomial model at high level
1	32.32	32.39	34.12	31.98
3	45.83	45.80	48.53	46.21
7	145.13	145.08	145.09	145.08
10	164.62	164.07	164.15	164.07
11	190.52	189.64	190.86	189.88
15	264.37	263.53	263.52	263.53
16	289.60	286.04	286.09	286.01
19	339.08	334.95	334.97	334.95

Table 4.2: Natural frequencies (in Hz) of a selection of modes estimated at low level (second column), using a spline model at high level (third column), using a linear model at high level (fourth column) and using a polynomial model with the same number of parameters as the spline model at high level (fifth column).

By contrast, the frequencies of the modes between 200 and 350 Hz are not correctly identified, meaning that the softening effects affecting high-frequency modes are not captured. This is illustrated in Fig. 4.13 (b), where the linear FRF calculated at NL 4 on the front panel (in black) is compared to the FRF reconstructed at high level by the FNSI algorithm (in dashed blue) over 200 – 350 Hz. The FRF measured at high level is also plotted (in orange). One observes that the subspace model linearises the high-frequency dynamics by fitting the distorted resonance peaks. This is also evidenced in the fourth column of Table 4.2 where the frequencies estimated using a linear model fitted to nonlinear data are given.

Mode	Linear model at low level	Spline model at high level	Polynomial model at high level
1	0.64	0.77	0.83
3	0.31	0.49	1.29
7	0.08	0.09	0.09
10	0.14	0.14	0.15
11	0.14	0.37	0.46
15	0.17	0.21	0.21
16	0.43	0.46	0.46
19	0.36	0.53	0.54

Table 4.3: Damping ratios (in %) of a selection of modes estimated at low level (second column), using a spline model at high level (third column) and using a polynomial model with the same number of parameters as the spline model at high level (fourth column).

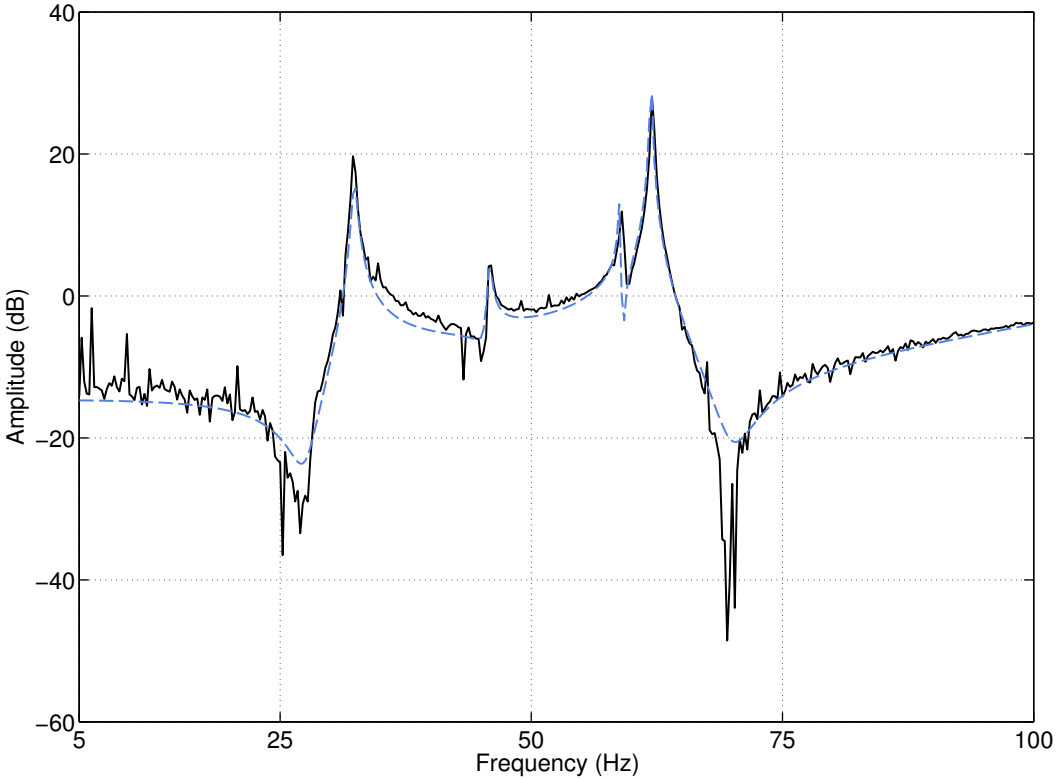

(a)

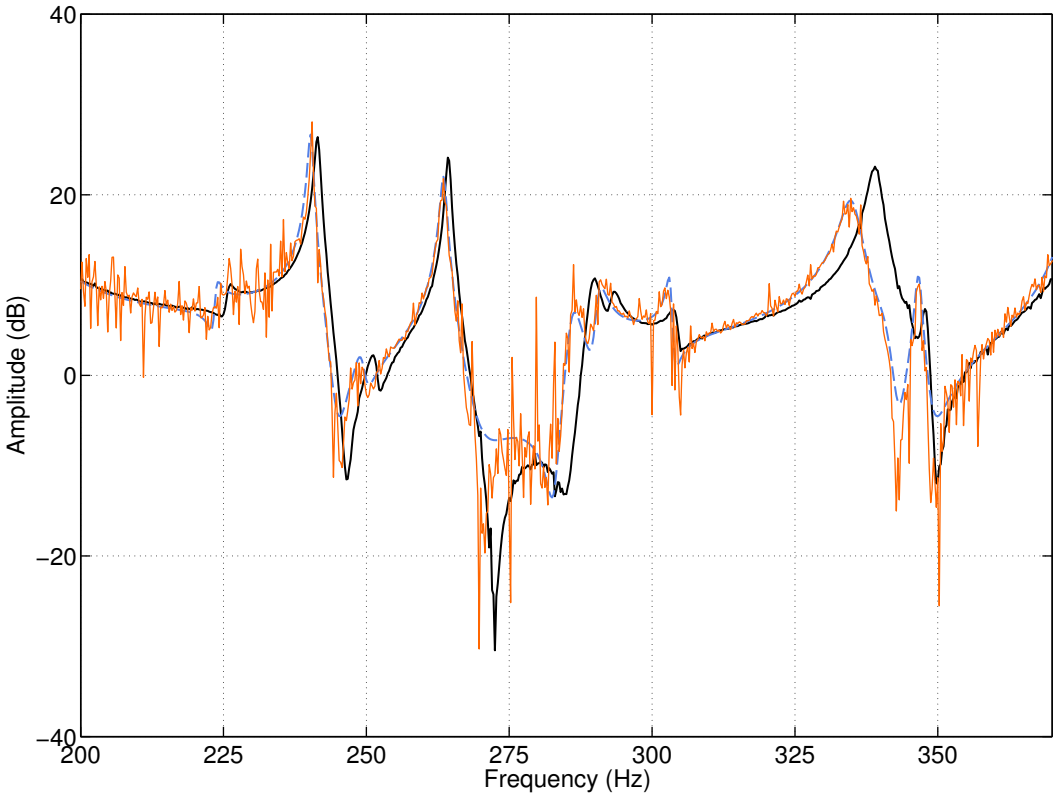

(b)

Figure 4.13: Comparison between the FRF measured at low level (0.16 N RMS) at NL 4 on the front panel (in black) and the FRF reconstructed at high level (3.79 N RMS) by the FNSI algorithm (in dashed blue). (a) Close-up in 5 – 100 Hz; (b) close-up in 200 – 350 Hz, where the FRF measured at high level (3.79 N RMS) is also plotted (in orange).

The fifth column of Table 4.2 finally lists the frequencies estimated using ordinary polynomials possessing the same number of parameters as the cubic splines defined in Section 4.4.1. Specifically, essentially nonlinear polynomials of order 6 were chosen for stiffness nonlinearities, and fourth-order polynomials for damping nonlinearities. In the 200 – 350 Hz band, the polynomial model brings no improvement with respect to the spline model, as it also yields linearised frequencies. This shows that the underestimation of the frequencies beyond 200 Hz is not to be attributed to inaccuracies in the estimation of parameters, but to the inability of continuous functions like splines and polynomials to capture micro-impacts and gapping, most likely associated with discontinuous restoring forces. Moreover, modes 1 and 3 are less accurately retrieved by the polynomials, proving that splines offer additional flexibility in the representation of complex nonlinearities. This is also clearly demonstrated in Table 4.3 where the estimation of the linear damping ratios is assessed using the spline and polynomial models. In particular, the estimates obtained for modes 1 and 3 using polynomials are greatly improved by exploiting splines.

4.4.5 Estimation of the nonlinear restoring force curves

The last step in Fig. 4.1 is the conversion of the state-space model to the physical space in order to visualise the restoring forces fitted using cubic splines and polynomials. To this end, the conversion scheme detailed in Section 2.8 is utilised, limiting the frequency interval of conversion to 200 Hz since the two models do not perform well for higher frequencies. The elastic force curves at NL 4 and NL 5 are proposed in Fig. 4.14 (a – b). One first notes that the spline- and polynomial-based curves give rise to similar dynamics. They exhibit a significant, yet smooth, increase in stiffness for negative displacements, translating impacts on the snubbers. Two variations of slope in the impact region are seen in Fig. 4.14 (b) due to the misalignment between the snubber at NL 5 and the rear panel, pointed out in Fig. 4.2 (d). Moreover, the curves present an increase in stiffness in positive displacement caused by the geometrically nonlinear deformations in the stacking points areas. The associated nonlinear coefficient is found to be larger at NL 5. A similar asymmetry, but in terms of linear stiffness coefficients, was also remarked in the deformed shapes of modes 1 and 7 in Fig. 4.5 (a, c). Finally, the dissipative force curves at NL 4 and NL 5 are depicted in Fig. 4.15 (a – b). Nonlinear damping mainly affects NL 4 through positive even and odd terms. The corresponding spline curve at NL 5 shows an even contribution of marginal amplitude.

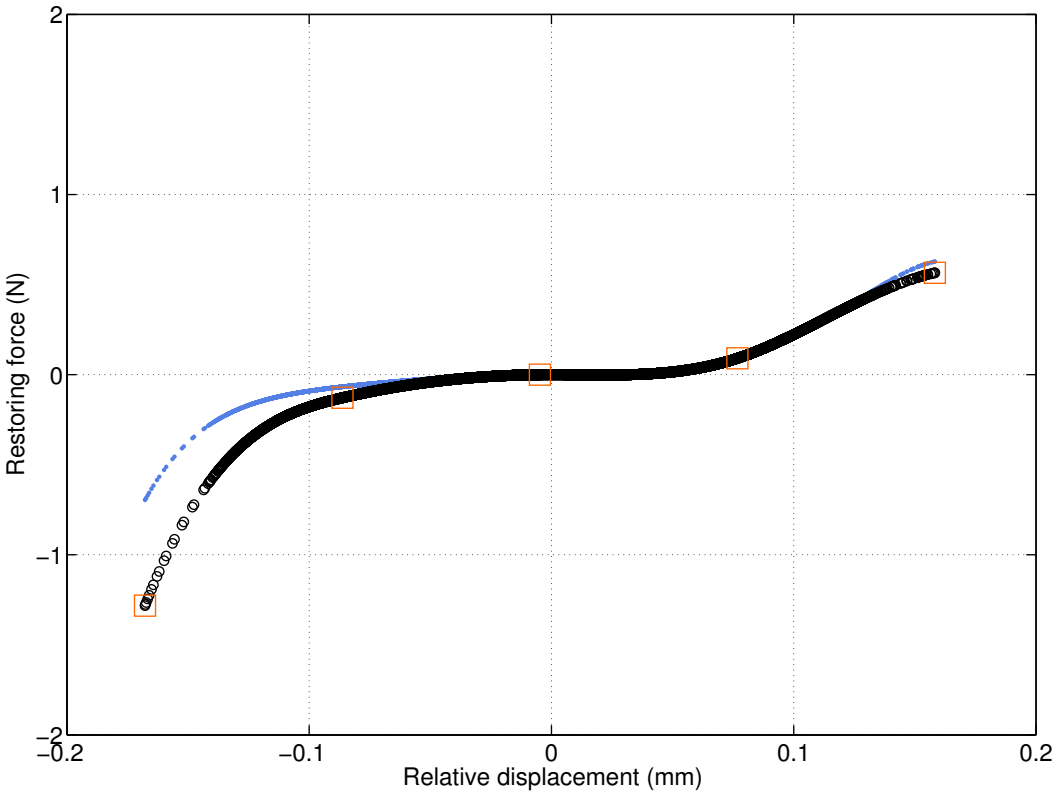

(a)

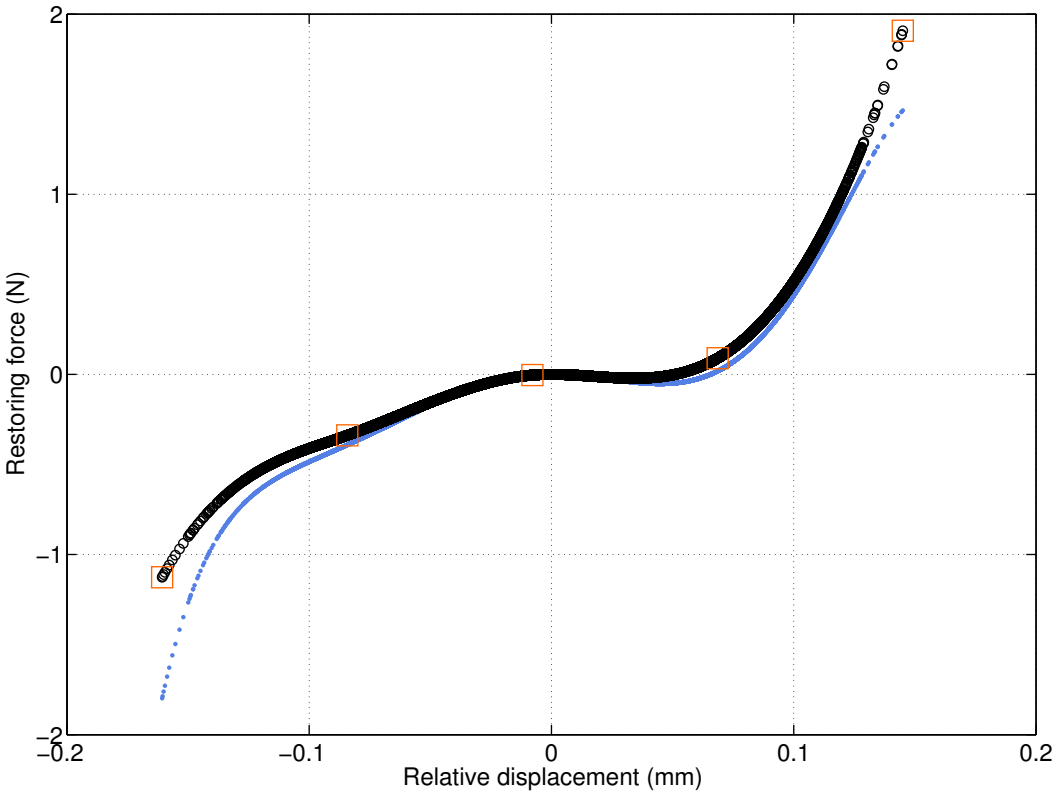

(b)

Figure 4.14: Nonlinear stiffness curve constructed at high level (3.79 N RMS) using cubic splines (black circles) and sixth-order polynomials (blue dots): (a) NL 4; (b) NL 5. Orange squares localise the 5 chosen knots of the splines.

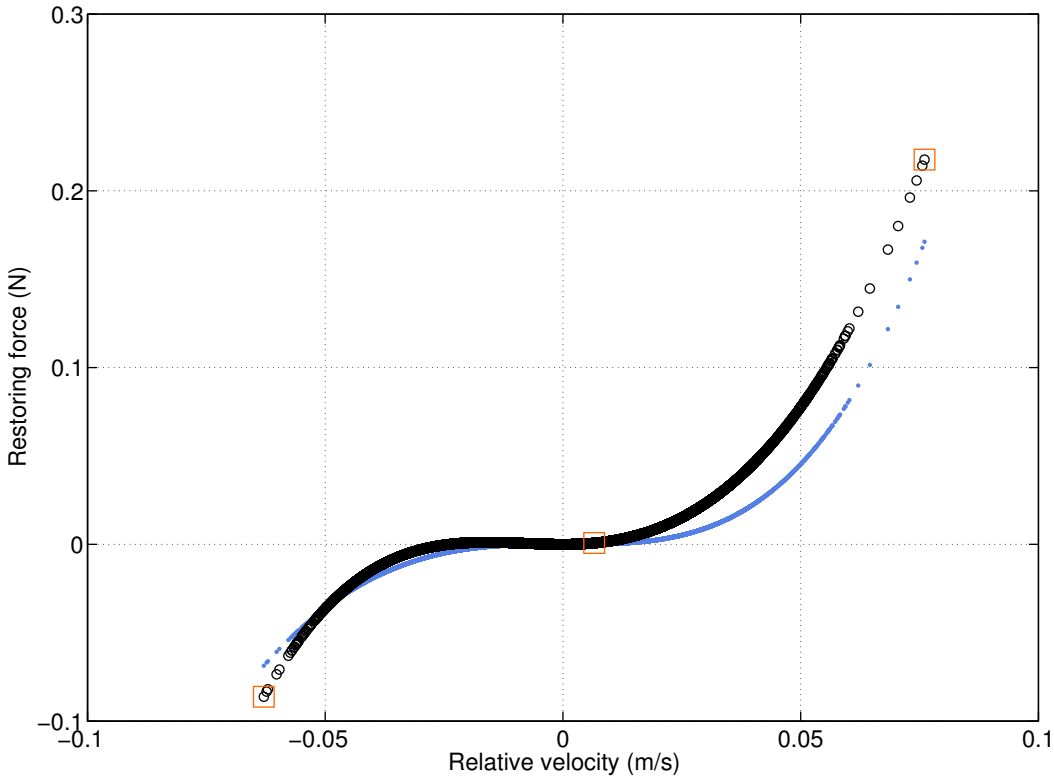

(a)

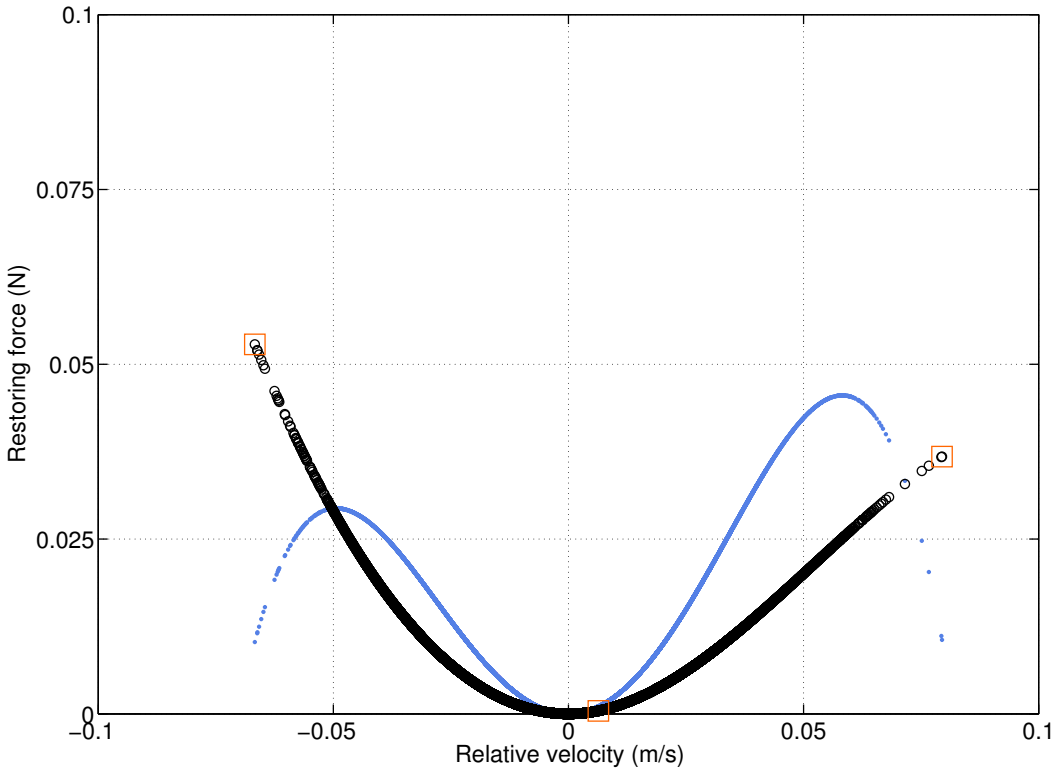

(b)

Figure 4.15: Nonlinear damping curve constructed at high level (3.79 N RMS) using cubic splines (black circles) and fourth-order polynomials (blue dots): (a) NL 4; (b) NL 5. Orange squares localise the 3 chosen knots of the splines.

4.5 Concluding remarks

The objective of the present chapter was to investigate the usefulness of cubic splines to represent complex stiffness and damping nonlinearities. For that purpose, splines were embedded in the FNSI algorithm, which proved to be capable of handling high-dimensional inverse problems. Splines were also shown to bring superior accuracy with respect to ordinary polynomials in the identification of the linear and nonlinear properties of a space solar array structure in stowed configuration. In particular, nonlinear effects due to unilateral impacts and geometrically nonlinear deformations were successfully captured in the nonlinear model. This chapter indicates that the joint utilisation of splines and FNSI opens a promising way for addressing structures exhibiting nonintuitive nonlinearities.

Other nonlinear phenomena were detected in the solar array dynamics, namely micro-impacts and gapping in the bolted connections leading to softening distortions. They could not be correctly incorporated in the nonlinear FNSI model, partly because they are suspected to be associated with discontinuous restoring forces. They are also likely to require more sophisticated phenomenological models. An appropriate representation of systems with discontinuities using splines requires nonequally-spaced knots, and hence solutions for solving nonlinear-in-the-parameters identification problem. Further work focusing on these aspects should lead to the development of automatic schemes for selecting the number of knots and iterative approximations considering adaptive refinement strategies [25].

To conclude the chapter, we revisit the identification of the Silverbox benchmark addressed in Section 2.10. In this section, a difference in amplitude between the measured and synthesised FRFs of the underlying linear system was attributed to an incomplete description of the Silverbox nonlinearity. Fig. 4.16 shows that the use of cubic splines succeeds in achieving an almost perfect agreement between the two FRFs. The errors calculated on the estimates of the linear natural frequency and damping ratio of the Silverbox for an increasing number of knots are also given in Table 4.4. A substantial improvement in the estimation of the damping ratio is observed, compared to the error of 5.23 % obtained in Section 2.10.

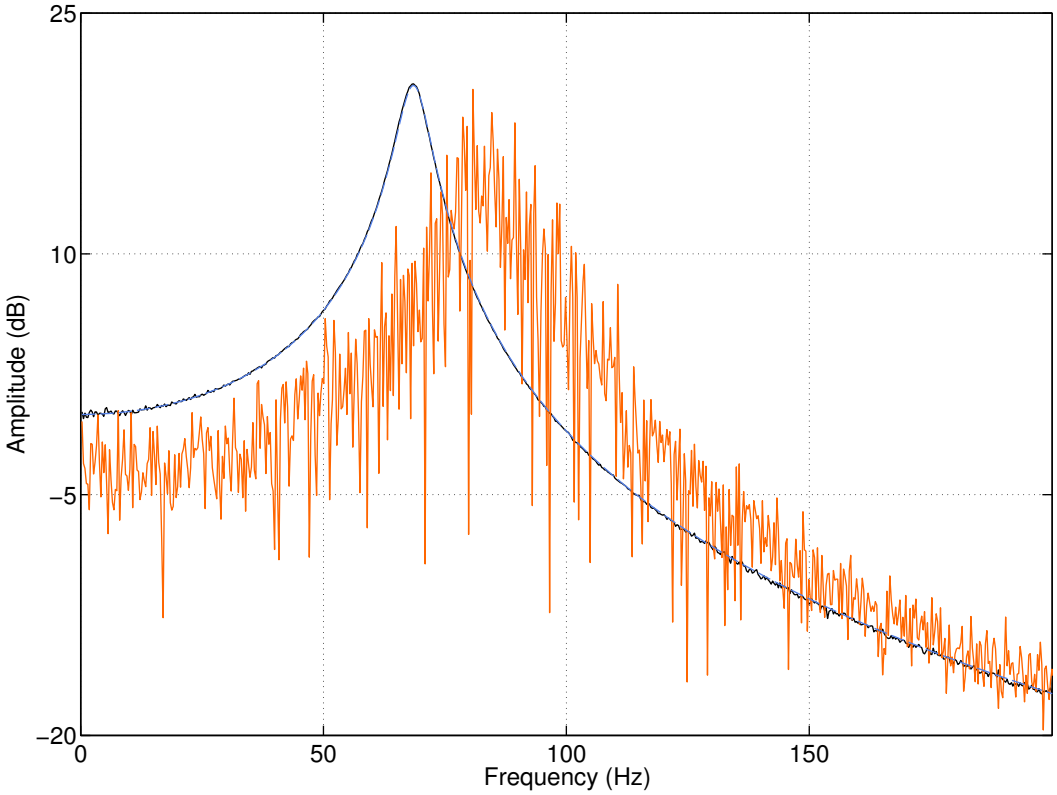

Figure 4.16: Comparison between the FRF of the Silverbox at low level, *i.e.* 5 mN RMS, where the system behaves linearly (in black) and the corresponding curve reconstructed using the FNSI method combined with cubic splines at high level (in blue), *i.e.* 150 mN RMS. The FRF calculated using the H1 estimator at high level is also superposed (in orange).

Number of knots	Error on ω_0 (%)	Error on ϵ (%)
5	0.26	4.98
10	0.24	4.53
15	0.20	2.85
20	0.13	2.26
25	0.16	1.26

Table 4.4: Errors (in %) on the linear natural frequency and damping ratio of the Silverbox benchmark estimated using the FNSI method combined with cubic splines at high level, *i.e.* 150 mN RMS, for an increasing number of knots.

Chapter 5

A stochastic framework for subspace identification of nonlinear systems

Abstract

The present chapter investigates the possibility of embedding the FNSI method into the maximum likelihood framework to derive statistically-optimal models in the presence of noise. The identification problem is formulated in the frequency domain, where it is shown to simplify to the minimisation of a weighted least-squares cost function. The use of a FNSI model to initialise the minimisation is proved to alleviate issues typically encountered in maximum likelihood identification. The Duffing oscillator and the Silverbox benchmark studied in Chapter 2 are revisited to demonstrate the complete methodology.

5.1 Introduction

The behaviour of the FNSI method in the presence of noise was studied in Chapter 2. It was demonstrated that, if the applied forces $\mathbf{u}(t)$ and the nonlinear basis functions $\mathbf{h}_a(\mathbf{y}(t), \dot{\mathbf{y}}(t))$ are observed without error, the method calculates consistent parameter estimates. Consistency is an appealing property, because the probability density function (PDF) of a consistent estimate converges to a Dirac function centred on the true value of the parameter for a sufficiently large number of processed frequencies F, as shown in Fig. 5.1. The basis functions $\mathbf{h}_a(\mathbf{y}(t), \dot{\mathbf{y}}(t))$ are however prone to noise distortions when they are formed using the displacements and velocities obtained by integrating accelerometer signals. This results in the loss of consistency and in a significant bias in the parameter estimation for low output signal-to-noise ratios (SNRs).

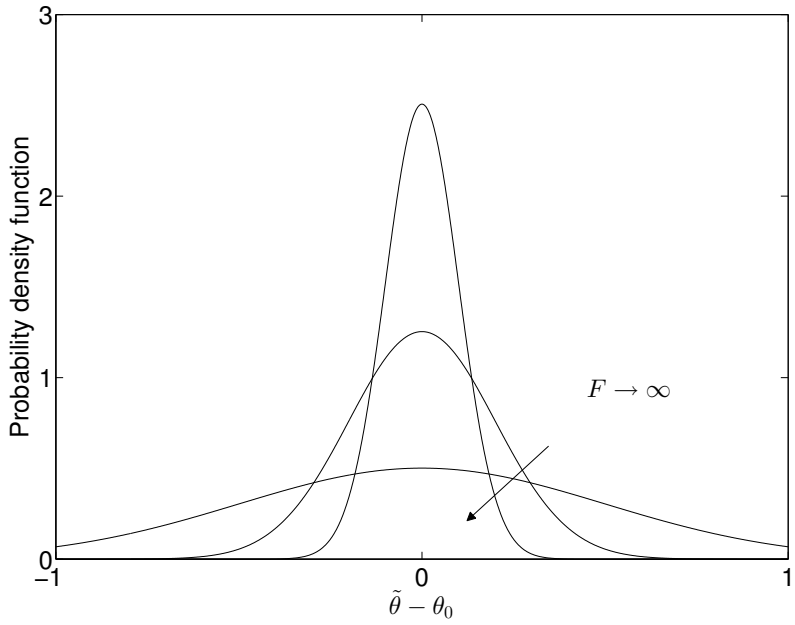

Figure 5.1: Convergence of a consistent estimate $\tilde{\theta}$ of a parameter θ to a Dirac function.

A systematic approach to derive estimators with enhanced noise properties is to embed the identification problem in a stochastic framework. This may be achieved through the minimisation of a well-chosen cost function incorporating noise information. The cost function expresses the distance between model predictions and measured data, and reaches its minimum for the estimated parameters. Classical cost function-based estimators include the least-squares, maximum likelihood and Bayes estimators [92]. The maximum likelihood estimator (MLE) is particularly attractive because it not only preserves the consistency of the parameters for low SNRs, but it also yields estimates with the lowest uncertainty possible. For these two reasons, MLE is referred to as a consistent and efficient estimator. The efficiency property is illustrated in Fig. 5.2, where three different estimates of a parameter θ are compared for a fixed number of measured frequencies F. The PDF of the MLE estimate is found to be more concentrated around the true value

of the parameter θ_0 than any other possible estimates.

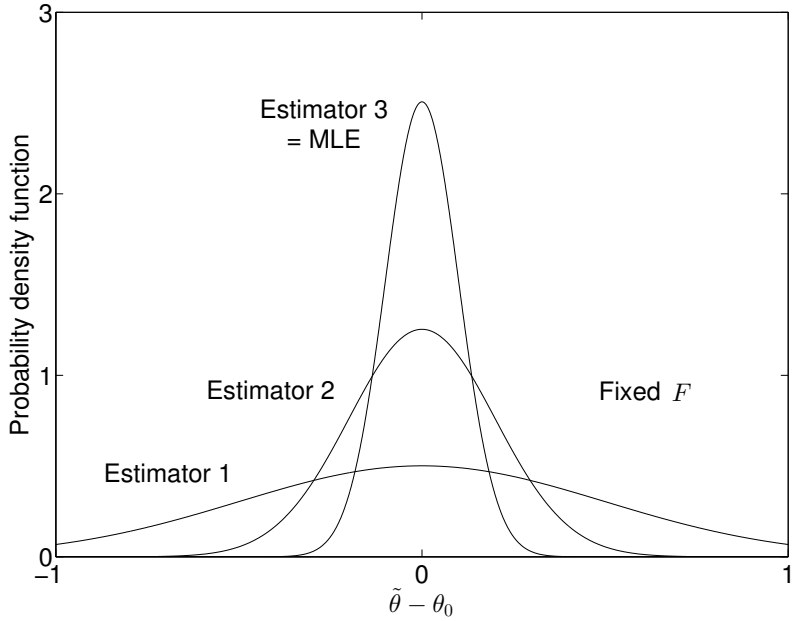

Figure 5.2: Efficient estimate $\tilde{\theta}$ of a parameter θ exhibiting the lowest possible uncertainty.

It is interesting to note that the use of the maximum likelihood is not widespread in structural dynamics. The majority of the contributions in the technical literature addressed experimental and operational modal analysis problems [21, 32, 122, 130]. Nonstationary mechanical systems were also studied [83, 86]. The identification of fluid line networks was reported in Ref. [129], and of a control valve and heat exchanger system in Ref. [35]. This limited number of publications is arguably due to the iterative nature of MLE, while many noniterative identification methods were developed based on Newton's second law of motion [3, 60]. Issues typically encountered in the minimisation of iterative estimators are related to initialisation and convergence to suboptimal solutions. In this context, the contribution of the present chapter is exploit the parameter estimates generated by the FNSI method to serve as starting values for the minimisation of the maximum likelihood cost function. Classical approaches in control and electrical engineering rather use linear approximate models as starting point [85, 115], which are more likely to be trapped into local minima. The combination of MLE with FNSI alleviates this eventuality, and therefore opens new possibilities for the use of maximum likelihood identification in nonlinear structural dynamics.

An introduction to the maximum likelihood estimator is provided in Section 5.2, emphasising that it simplifies to a weighted least-squares cost function in the frequency domain. Analytical expressions for the elements of the Jacobian matrix associated with the cost function are derived in Section 5.3. The Duffing oscillator and the Silverbox benchmark studied in Chapter 2 are revisited to demonstrate the complete methodology in Section 5.4 and Section 5.5, respectively. Concluding remarks are discussed in Section 5.6. The material of this chapter is the result of a collaboration with Prof. J. Schoukens [80].

5.2 Maximum likelihood identification in the frequency domain

The construction of the maximum likelihood cost function requires the knowledge of the PDF of the output noise. This is a particularly demanding requirement because the complete distribution of noise is virtually never measured. However, by applying the discrete Fourier transform (DFT) to measured data, the distribution of frequency-domain noise can be proved to be Gaussian, with a predominantly-diagonal covariance matrix, regardless its time-domain distribution [104]. The noise modelling corresponding to the maximum likelihood estimator described in this section is presented in Fig. 5.3. The input spectrum is assumed to be measured without error, *i.e.* $\mathbf{E}(k) = \mathbf{E}_0(k)$. The disturbing noise term $\mathbf{N}_Y(k)$ is Gaussian distributed, has zero mean $\mathcal{E}\left(\mathbf{N}_Y(k)\right) = 0$, and a covariance matrix with only non-zero diagonal elements equal to $\boldsymbol{\sigma}_Y^2(k) = \mathcal{E}\left(|\mathbf{N}_Y(k)|^2\right)$. The absence of noise in the feedback loop in Fig. 5.3, which guarantees the consistency and the efficiency of MLE, is not an approximation but is gained from the iterative nature of estimator. More specifically, noise-free nonlinear basis functions can be formed, at each iteration, using the modelled output of the system evaluated given $\mathbf{U}_0(k)$ and the parameters of the model estimated at the previous iteration.

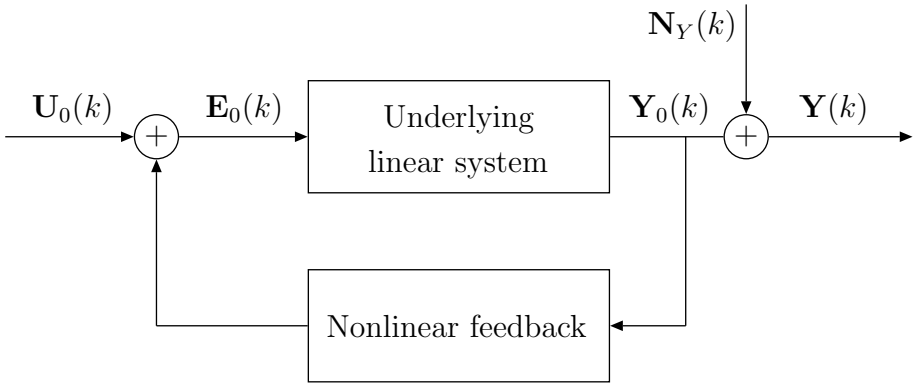

Figure 5.3: Noise modelling in the maximum likelihood framework.

The Gaussianity of the output noise implies that MLE simplifies to a weighted least-squares estimator in the frequency domain [92]. Introducing the vector of model parameters θ as

$$\theta = \left[vec\left(\mathbf{A}\right)\ ;\ vec\left(\mathbf{B}\right)\ ;\ vec\left(\mathbf{C}\right)\ ;\ vec\left(\mathbf{D}\right)\right], \tag{5.1}$$

where the operation denoted *vec* stacks the columns of a matrix on top of each other, the cost function to minimise hence writes

$$\mathbf{V}(\theta) = \sum_{k=1}^{F} \boldsymbol{\epsilon}^H(k,\theta)\, \mathbf{W}^2(k)\, \boldsymbol{\epsilon}(k,\theta) \tag{5.2}$$

where $\mathbf{W}(k)$ is a weighting function chosen equal to $\boldsymbol{\sigma}_Y^{-1}(k)$, similarly to the calculation of $\widehat{\mathbf{B}}$ and $\widehat{\mathbf{D}}$ in Eq. (2.30). The model error vector $\boldsymbol{\epsilon} \in \mathbb{R}^l$ is defined as the complex-valued difference

$$\boldsymbol{\epsilon}(k,\theta) = \mathbf{Y}_m(k,\theta) - \mathbf{Y}(k) \tag{5.3}$$

where $\mathbf{Y}_m(k,\theta)$ and $\mathbf{Y}(k)$ are the DFTs of the modelled and measured outputs, respectively.

5.3 Analytical calculation of the Jacobian matrix

In practice, we minimise the nonlinear least-squares cost function in Eq. (5.2) using a Levenberg-Marquardt optimisation algorithm, which combines the large convergence region of the gradient descent method with the fast convergence of the Gauss-Newton method [54, 59]. This algorithm requires the calculation of the Jacobian matrix $\mathbf{J}(k,\theta)$ associated with the cost function or, equivalently, with the error function in Eq. (5.3), *i.e.*,

$$\mathbf{J}(k,\theta) = \frac{\partial \boldsymbol{\epsilon}(k,\theta)}{\partial \theta} = \frac{\partial \mathbf{Y}_m(k,\theta)}{\partial \theta}. \tag{5.4}$$

Given the nonlinear relationship which exists between $\mathbf{Y}(k)$ and $\mathbf{E}(k)$ in Eq. (2.8), it is not practical to compute the elements of $\mathbf{J}(k,\theta)$ directly in the frequency domain. A convenient approach consists in carrying out the computation of the Jacobian matrix in the time domain, and then in applying the DFT. One first focuses on the determination of the element $J_{A_{ij}}(t) \in \mathbb{R}^l$ of the time-domain Jacobian defined as

$$J_{A_{ij}}(t) = \frac{\partial \mathbf{y}(t)}{\partial A_{i\,j}}. \tag{5.5}$$

The derivative of the output relation in Eqs. (2.7) with respect to $A_{i\,j}$ is given by

$$\begin{aligned} \frac{\partial \mathbf{y}(t)}{\partial A_{i\,j}} &= \frac{\partial}{\partial A_{i\,j}} \left(\mathbf{C}\,\mathbf{x}(t) + \mathbf{D}\,\mathbf{e}(t) \right) \\ &= \mathbf{C}\,\frac{\partial \mathbf{x}(t)}{\partial A_{i\,j}} + \mathbf{D}\,\frac{\partial \mathbf{e}(t)}{\partial A_{i\,j}} \\ &= \mathbf{C}\,\frac{\partial \mathbf{x}(t)}{\partial A_{i\,j}} + \mathbf{D}\,\frac{\partial \mathbf{e}(t)}{\partial \mathbf{y}(t)}\frac{\partial \mathbf{y}(t)}{\partial A_{i\,j}}. \end{aligned} \tag{5.6}$$

The first term in the right-hand side of Eq. (5.6) is obtained by taking the derivative of the state relation in Eqs. (2.7) with respect to $A_{i\,j}$, that is

$$\begin{aligned} \frac{\partial \dot{\mathbf{x}}(t)}{\partial A_{i\,j}} &= \frac{\partial}{\partial A_{i\,j}} \left(\mathbf{A}\,\mathbf{x}(t) + \mathbf{B}\,\mathbf{e}(t) \right) \\ &= \mathbf{A}\,\frac{\partial \mathbf{x}(t)}{\partial A_{i\,j}} + \mathbf{I}_{i\,j}^{n_s \times n_s}\,\mathbf{x}(t) + \mathbf{B}\,\frac{\partial \mathbf{e}(t)}{\partial A_{i\,j}} \\ &= \mathbf{A}\,\frac{\partial \mathbf{x}(t)}{\partial A_{i\,j}} + \mathbf{I}_{i\,j}^{n_s \times n_s}\,\mathbf{x}(t) + \mathbf{B}\,\frac{\partial \mathbf{e}(t)}{\partial \mathbf{y}(t)}\frac{\partial \mathbf{y}(t)}{\partial A_{i\,j}} \end{aligned} \tag{5.7}$$

where $\mathbf{I}_{i\,j}^{n_s \times n_s}$ is a zero matrix with a single element equal to one at entry (i, j).

The element $J_{A_{ij}}(t)$ is therefore given by the solution of the two equations

$$\left\{ \begin{array}{rcl} \dfrac{\partial \dot{\mathbf{x}}(t)}{\partial A_{i\,j}} & = & \mathbf{A}\, \dfrac{\partial \mathbf{x}(t)}{\partial A_{i\,j}} + \mathbf{I}_{i\,j}^{n_s \times n_s}\, \mathbf{x}(t) + \mathbf{B}\, \dfrac{\partial \mathbf{e}(t)}{\partial \mathbf{y}(t)} \dfrac{\partial \mathbf{y}(t)}{\partial A_{i\,j}} \\ \dfrac{\partial \mathbf{y}(t)}{\partial A_{i\,j}} & = & \mathbf{C}\, \dfrac{\partial \mathbf{x}(t)}{\partial A_{i\,j}} + \mathbf{D}\, \dfrac{\partial \mathbf{e}(t)}{\partial \mathbf{y}(t)} \dfrac{\partial \mathbf{y}(t)}{\partial A_{i\,j}}. \end{array} \right. \tag{5.8}$$

Introducing the notations

$$\mathbf{x}^*(t) = \frac{\partial \mathbf{x}(t)}{\partial A_{i\,j}}\,; \quad \mathbf{y}^*(t) = \frac{\partial \mathbf{y}(t)}{\partial A_{i\,j}}\,; \quad \mathbf{e}^*(t) = \left(\begin{array}{cc} \mathbf{x}(t) & \dfrac{\partial \mathbf{e}(t)}{\partial \mathbf{y}(t)} \dfrac{\partial \mathbf{y}(t)}{\partial A_{i\,j}} \end{array} \right) \tag{5.9}$$

and

$$\mathbf{A}^* = \mathbf{A}\,; \quad \mathbf{B}^* = \left(\begin{array}{cc} \mathbf{I}_{i\,j}^{n_s \times n_s} & \mathbf{B} \end{array} \right); \quad \mathbf{C}^* = \mathbf{C}\,; \quad \mathbf{D}^* = \left(\begin{array}{cc} \mathbf{0}^{\,l \times n_s} & \mathbf{D} \end{array} \right), \tag{5.10}$$

Eqs. (5.8) can be recast in the form

$$\left\{ \begin{array}{rcl} \dot{\mathbf{x}}^*(t) & = & \mathbf{A}^*\, \mathbf{x}^*(t) + \mathbf{B}^*\, \mathbf{e}^*(t) \\ \mathbf{y}^*(t) & = & \mathbf{C}^*\, \mathbf{x}^*(t) + \mathbf{D}^*\, \mathbf{e}^*(t). \end{array} \right. \tag{5.11}$$

Eqs. (5.11) reveal that the elements of the Jacobian matrix associated with the parameters in $\mathbf{A}$ are solutions of an auxiliary state-space model defined by the four matrices $(\mathbf{A}^*, \mathbf{B}^*, \mathbf{C}^*, \mathbf{D}^*)$. The first term in the auxiliary extended input $\mathbf{e}^*(t)$ in Eq. (5.9) is the state vector $\mathbf{x}(t)$. It is obtained by simulating in time the original model in Eqs. (2.7) with the estimated parameters of the previous Levenberg-Marquardt iteration. The second term in $\mathbf{e}^*(t)$ depends on $\partial \mathbf{e}(t)/\partial \mathbf{y}(t)$, which is formed using the derivatives of the nonlinear basis functions $\mathbf{h}_a(\mathbf{y}(t), \dot{\mathbf{y}}(t))$ with respect to $\mathbf{y}(t)$.

The determination of the element $J_{B_{ij}}(t) \in \mathbb{R}^{\,l}$ is conducted similarly to $J_{A_{ij}}(t)$. The result is given in Eqs. (5.12), where $J_{B_{ij}}(t)$ is seen to be the solution of another auxiliary state-space model,

$$\left\{ \begin{array}{rcl} \dfrac{\partial \dot{\mathbf{x}}(t)}{\partial B_{i\,j}} & = & \mathbf{A}\, \dfrac{\partial \mathbf{x}(t)}{\partial B_{i\,j}} + \mathbf{I}_{i\,j}^{n_s \times (m+sl)}\, \mathbf{e}(t) + \mathbf{B}\, \dfrac{\partial \mathbf{e}(t)}{\partial \mathbf{y}(t)} \dfrac{\partial \mathbf{y}(t)}{\partial B_{i\,j}} \\ \dfrac{\partial \mathbf{y}(t)}{\partial B_{i\,j}} & = & \mathbf{C}\, \dfrac{\partial \mathbf{x}(t)}{\partial B_{i\,j}} + \mathbf{D}\, \dfrac{\partial \mathbf{e}(t)}{\partial \mathbf{y}(t)} \dfrac{\partial \mathbf{y}(t)}{\partial B_{i\,j}}. \end{array} \right. \tag{5.12}$$

The computation of $J_{C_{ij}}(t) \in \mathbb{R}^{\,l}$ and $J_{D_{ij}}(t) \in \mathbb{R}^{\,l}$ is easier because they do not involve time integration, as shown in Eq. (5.13) and Eq. (5.14), respectively.

$$\frac{\partial \mathbf{y}(t)}{\partial C_{i\,j}} = \mathbf{I}_{i\,j}^{l \times n_s}\, \mathbf{x}(t) + \mathbf{D}\, \frac{\partial \mathbf{e}(t)}{\partial \mathbf{y}(t)} \frac{\partial \mathbf{y}(t)}{\partial C_{i\,j}}. \tag{5.13}$$

$$\frac{\partial \mathbf{y}(t)}{\partial D_{i\,j}} = \mathbf{I}_{i\,j}^{l \times (m+sl)}\, \mathbf{e}(t) + \mathbf{D}\, \frac{\partial \mathbf{e}(t)}{\partial \mathbf{y}(t)} \frac{\partial \mathbf{y}(t)}{\partial D_{i\,j}}. \tag{5.14}$$

5.4 Numerical demonstration on a Duffing oscillator

In this section, the identification of the Duffing oscillator presented in Section 2.9 is revisited in the presence of output noise. The linear and nonlinear parameters of the system are reminded in Table 5.1. The excited frequencies span the 5 – 150 Hz interval, and the simulated response in steady-state conditions consists of 20 periods of 8192 samples each. The time histories were corrupted by Gaussian noise, considering a root-mean-squared (RMS) level equal to 2 % of the response amplitude, or a SNR of about 34 dB. The 20 measured periods were averaged to obtain a sample estimate of the covariance matrix necessary to weight the FNSI algorithm in Eqs. (2.25) and (2.30), and the MLE cost function in Eq. (5.2). In the case of the Duffing oscillator, the parameter vector θ contains 12 elements, given 1 input, 1 nonlinear basis function, 1 output and 2 states.

M (kg)	C_v (Ns/m)	K (kN/m)	c_1 (MN/m^3)
2	10	100	100
Natural frequency ω_0 (Hz)		Damping ratio ϵ (%)	
35.59		1.12	

Table 5.1: Linear and nonlinear parameters of the Duffing oscillator.

Fig. 5.4 (a) proposes a direct comparison between the measured and reconstructed spectra of the Duffing system. This figure reveals that the FNSI model suffers from estimation errors due to noise, mostly visible in the vicinity of resonance. A similar conclusion is drawn from the analysis of the associated time series in Fig. 5.4 (b). In this latter graph, the RMS amplitude of the FNSI error is equal to 1.68 mm, compared to the RMS amplitude of the response equal to 4.25 mm. The subspace errors are drastically reduced using the maximum likelihood. The MLE error on the prediction of the output spectrum is displayed in Fig. 5.4 (a) using blue circles. Estimation errors now have an amplitude comparable to the noise level. The error of the maximum likelihood model is also plotted in the time domain in Fig. 5.4 (b), and corresponds to a RMS value of 0.02 mm.

Fig. 5.5 (a – b) depicts the estimation of the cubic stiffness coefficient of the oscillator calculated by the FNSI method and by the maximum likelihood estimator. The identification result obtained in the noise-free case in Chapter 2 is also plotted. The real parts of the noisy estimates exhibit a substantial drift along the frequency axis. Their averaged values in 5 – 150 Hz, listed in Table 5.2, show comparable errors with respect to the exact value of the coefficient. Moreover, the ratio between the real and imaginary parts of the MLE coefficient is one order of magnitude larger than the corresponding ratio provided by the FNSI method. This is confirmed in Fig. 5.5 (b) where the MLE is found to decrease significantly the initial imaginary part generated by the subspace estimator. Table 5.3 gives the relative errors on the identified linear modal properties of the system. The presence of noise in the data translates into an increase of the error in the damping ratio estimates. An substantial improvement is however brought by the MLE with respect to the FNSI method, which is important in the prediction of the system resonance.

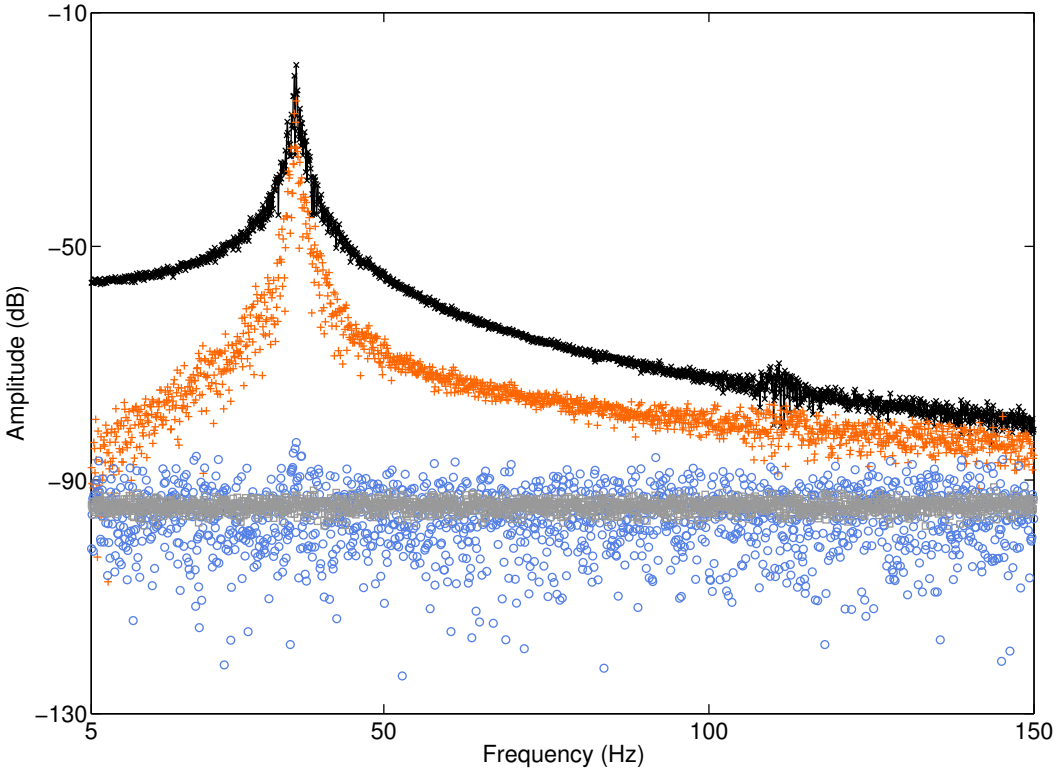

(a)

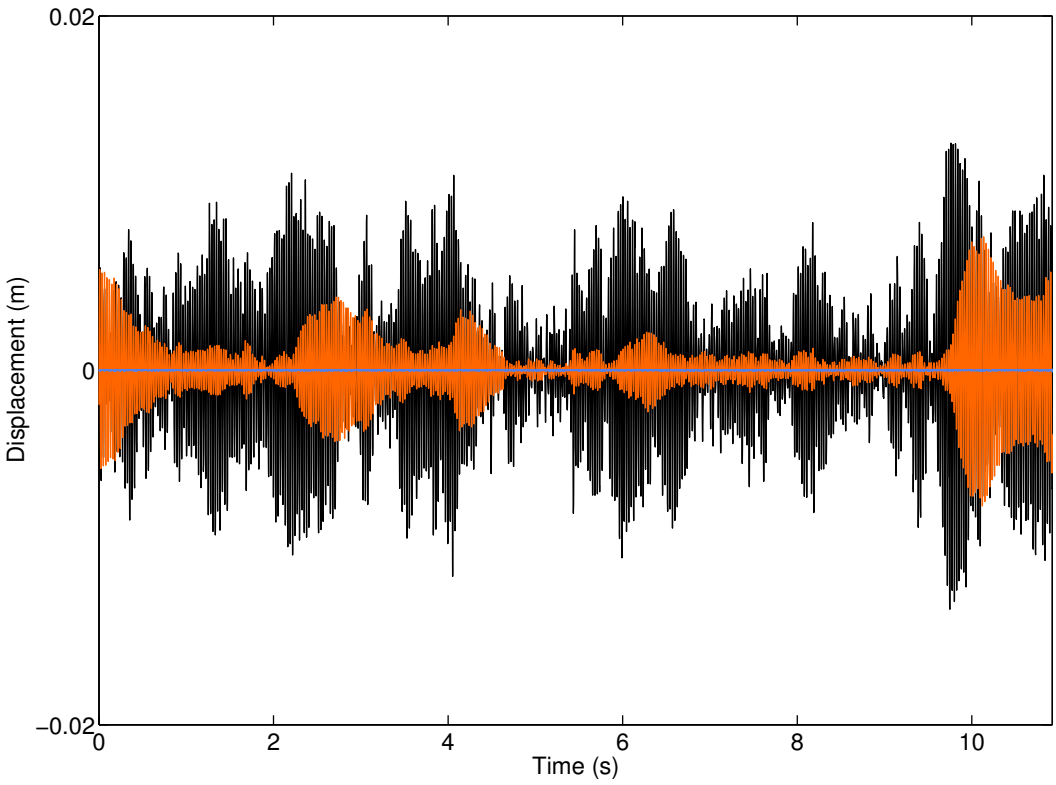

(b)

Figure 5.4: (a) Output spectrum of the Duffing oscillator. Black cross: measured spectrum averaged over 20 periods; red plus: error of the FNSI model; blue circle: error of the MLE model; grey square: noise level. (b) Time response. Black: measured response averaged over 20 periods; red: error of the FNSI model; blue: error of the MLE model.

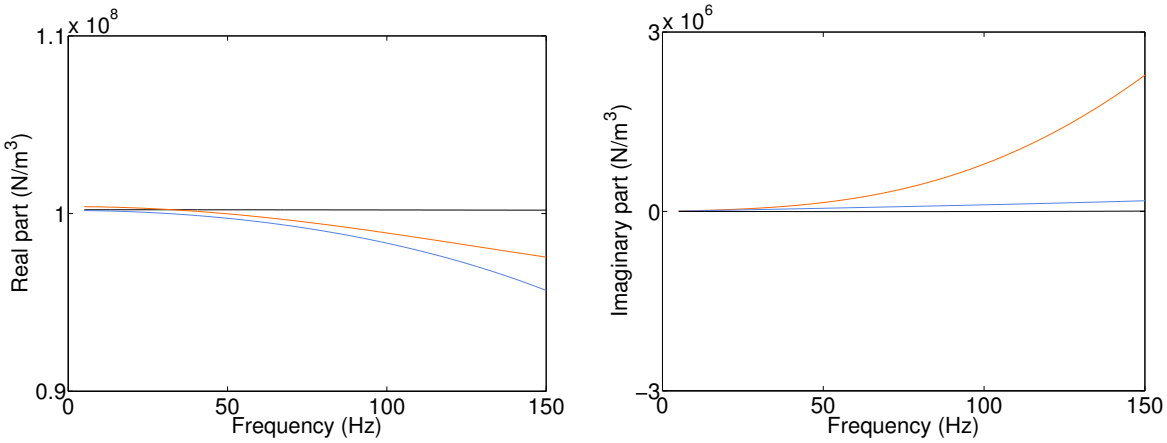

(a) (b)

Figure 5.5: Complex and frequency-dependent estimation of the nonlinear coefficient c_1 of the Duffing oscillator computed using the FNSI method without noise (in black, see Fig 2.7) and with 2 % noise (in orange), and using the MLE with 2 % noise (in blue).

Method	Real part (MN/m^3)	Error (%)	Log_{10} (real/imag.)
FNSI (noise-free)	10.02	0.21	5.05
FNSI	9.93	-0.72	2.18
MLE	9.87	-1.31	3.06

Table 5.2: Estimation of the nonlinear coefficient c_1 of the Duffing oscillator using the FNSI method in the noise-free case (see Table 2.2) and with 2 % noise, and using the MLE with 2 % noise.

Method	Error on ω_0 (%)	Error on ϵ (%)
FNSI (noise-free)	-1.94 10^{-3}	2.93 10^{-3}
FNSI	-1.02 10^{-3}	-0.13
MLE	0.38 10^{-3}	-0.02

Table 5.3: Relative errors on the estimated natural frequency and damping ratio of the Duffing oscillator computed using the FNSI method in the noise-free case (see Section 2.9) and with 2 % noise, and using the MLE with 2 % noise.

5.5 Experimental identification of the Silverbox benchmark

The identification of the Silverbox benchmark studied in Chapter 2 is also revisited in this section using the maximum likelihood estimator. Similarly to the identification of the Duffing oscillator, 20 leakage-free periods of measurement were considered to derive an initial subspace model. In particular, at low level of excitation, the linear properties of the system listed in Table 5.4 were identified. In the high-level identification at 150 mN RMS, the vector θ now consists of 15 parameters, considering two basis functions corresponding to quadratic and cubic stiffness terms.

Natural frequency ω_0 (Hz)	Damping ratio ϵ (%)
68.57	4.68

Table 5.4: Linear natural frequency and damping ratio of the Silverbox benchmark estimated at low level (5 mN RMS).

The improvement brought by using the MLE to optimise the initial FNSI model is clearly visible in Fig. 5.6 (a – b). In the time domain in Fig. 5.6 (b), the RMS amplitude of the FNSI error is equal to 6.24 10^{-7} m compared to the signal RMS value of 10.54 10^{-7} m. The error is decreased down to 0.40 10^{-7} m in the MLE model. The analysis of the reconstructed spectra in Fig. 5.6 (a) is also interesting. The error in the MLE model is generally 20 dB lower than in the subspace model but, unlike the Duffing identification in Section 5.4, this error does not reach the noise level. This is due to an imperfect representation of the nonlinearity in the system, as already mentioned in the analysis of the damping ratio estimate in Section 2.10. This error is particularly visible in Fig. 5.6 (a) at the resonance location around 83 Hz, and close to third harmonics of the system around 250 Hz, proving that it is related to the modelling of the nonlinearity.

The complex and frequency-dependent estimates of the nonlinear coefficients c_1 and c_2 are plotted versus frequency in Fig. 5.7 (a – d). The identification results provided by the two approaches show no significant difference. Their averaged real parts listed in Table 5.6 are almost equal. The underlying linear properties estimated at high level are also very similar (see Table 5.5).

Method	Error on ω_0 (%)	Error on ϵ (%)
FNSI	0.23	5.23
MLE	0.44	4.97

Table 5.5: Relative errors on the estimated natural frequency and damping ratio of the Silverbox computed using the FNSI method and the MLE.

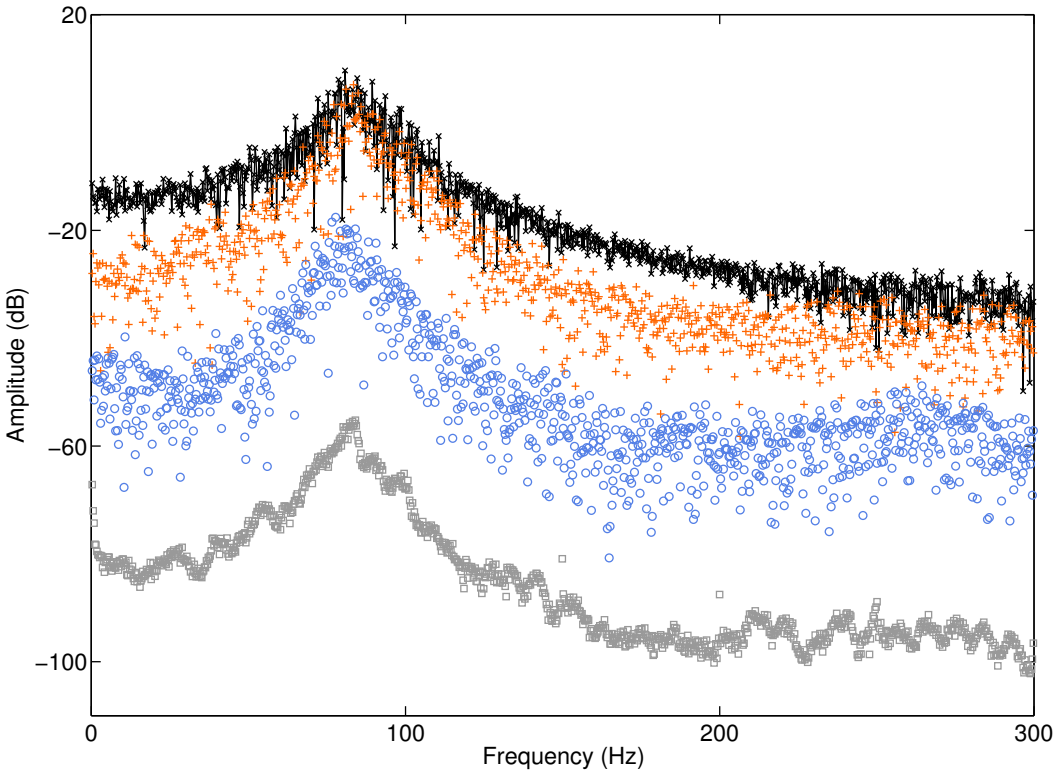

(a)

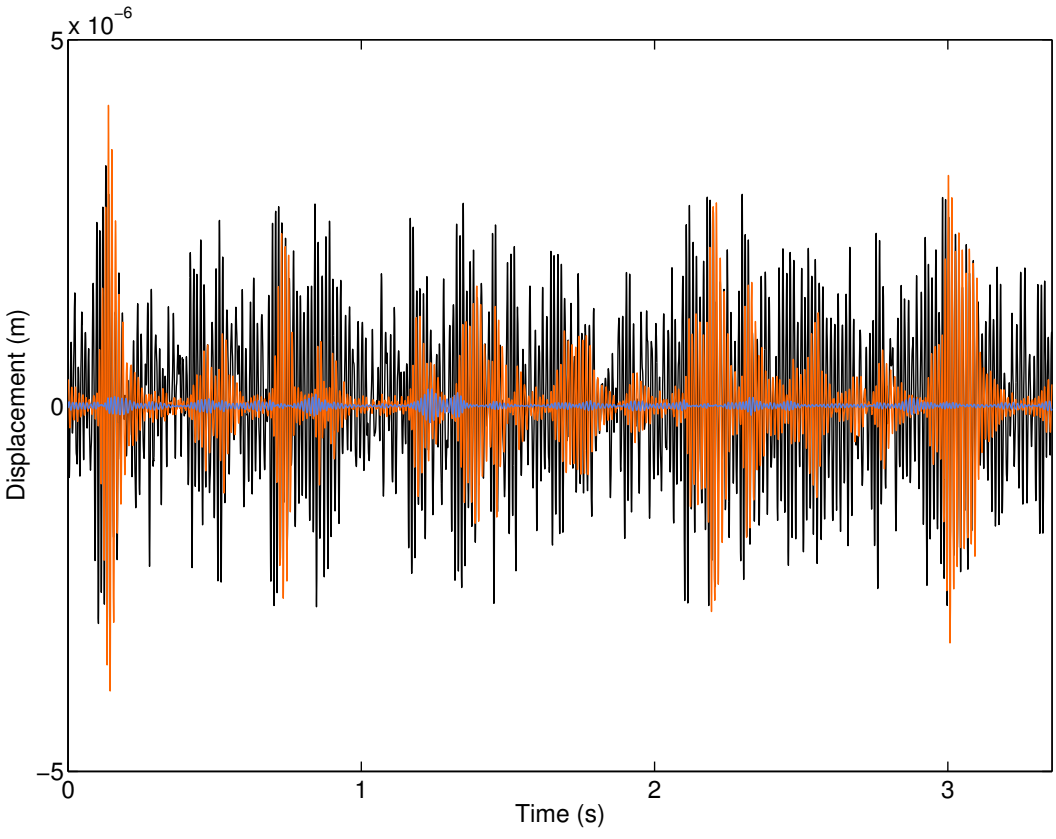

(b)

Figure 5.6: (a) Output spectrum of the Silverbox benchmark. Black cross: measured spectrum averaged over 20 periods; red plus: error of the FNSI model; blue circle: error of the MLE model; grey square: noise level. (b) Time response. Black: measured response averaged over 20 periods; red: error of the FNSI model; blue: error of the MLE model.

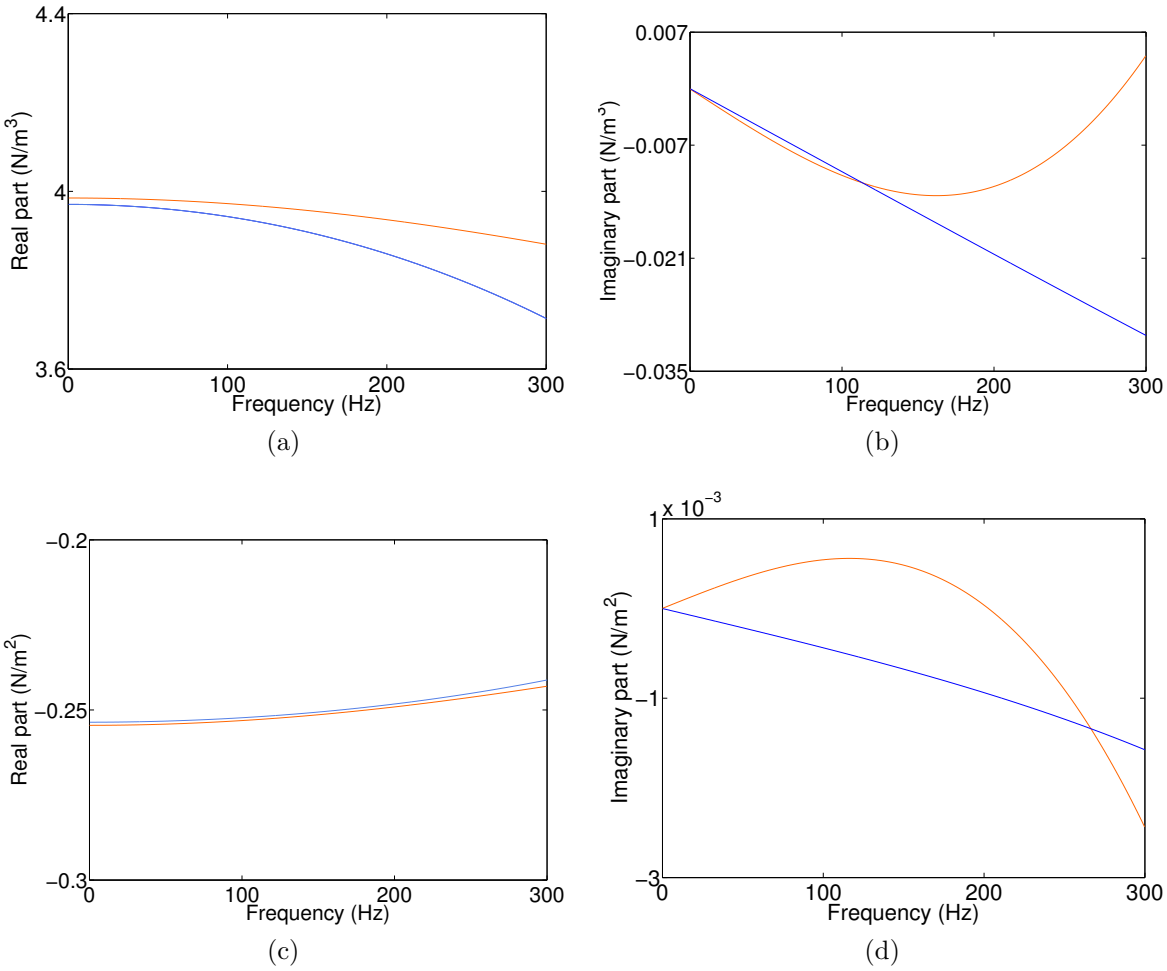

Figure 5.7: Complex and frequency-dependent estimation of the nonlinear coefficients (a – b) c_1 and (c – d) c_2 of the Silverbox computed using the FNSI method (in orange) and the MLE (in blue).

Method	Real part c_1 (N/m^3)	Log_{10} (r/i)	Real part c_2 (N/m^2)	Log_{10} (r/i)
FNSI	3.95	2.71	-0.25	3.38
MLE	3.93	2.41	-0.25	2.54

Table 5.6: Estimation of the nonlinear coefficients c_1 and c_2 of the Silverbox using the FNSI method and the MLE.

5.6 Concluding remarks

This chapter intended to derive nonlinear models with optimal statistical properties in the presence of measurement noise. This was achieved by embedding the FNSI method into the maximum likelihood identification framework. The formulation of a maximum likelihood estimator in nonlinear structural dynamics was facilitated in the frequency domain, where it simplifies to a weighted least-squares cost function. Specific attention was devoted to the analytical calculation of the Jacobian matrix associated with the minimisation of this cost function. The use of the maximum likelihood contributed to significantly decreasing the identification error of the FNSI models in the case of a Duffing oscillator and of the Silverbox benchmark. However, the decrease of this identification error did not always translate into noticeably improved estimates of the natural frequencies, damping ratios and nonlinear coefficients of the two systems. This observation deserves more investigation to precisely understand the relations between the quality of physical- and modal-space parameters and the overall quality of the state-space model.

The combined use of the maximum likelihood and FNSI estimators discussed in the present chapter should be viewed as a more exploratory research topic than the content of the first four chapters of the thesis. Additional work is therefore needed to further assess the capabilities of the proposed methodology. For instance, the sensitivity of the final parameter estimates to the amplitude of excitation and to the quality of the initial model provided by the FNSI method should be carefully studied. The convergence of the parameters throughout the maximum likelihood iterations should also be analysed in more details. Moreover, the Duffing oscillator and the Silverbox benchmark addressed in the chapter possess a single degree of freedom. In the multi-degree-of-freedom case, additional challenges are expected to be encountered, especially related to the dimensionality of the optimisation problem, the selection of the model order, and the sensitivity to spurious poles. In this context, the possibility offered by the FNSI method to exploit stabilisation diagrams to choose the model order is anticipated to be a distinct advantage.

Finally, it is worth stressing that, in addition to the consistency and efficiency properties introduced in this chapter, confidence bounds for the model parameters can also be obtained, in principle, using the maximum likelihood estimator. The accuracy of these bounds is conditional upon the absence of linear and nonlinear modelling errors. If modelling errors cannot be completely eliminated, the confidence intervals are underestimated. Future research in this area should hence focus on possible ways to reduce modelling errors, such as the utilisation of splines initiated in Chapter 4, and on the derivation of upper bounds on the covariance of the parameter estimates in the presence of unmodelled nonlinear effects.

Conclusion

This doctoral thesis constitutes an attempt to progress towards the development of a practical system identification methodology dedicated to real-life nonlinear mechanical systems. To reach this objective, a list of three key needs was established to delineate our research. This list was formulated as follows in the introduction of the dissertation:

i. an effective nonlinear system identification methodology of practical utility should be applicable to structures with multiple inputs and outputs, strong nonlinearities, high modal density and high nonproportional damping;

ii. it should also be sufficiently flexible to represent various types of stiffness and damping nonlinearities, while preserving physical insights into the structural behaviour;

iii. it should finally accommodate the presence of noise in the measurement of the inputs and outputs of the structure to guarantee the accuracy of the identified model in experimental conditions.

The identification of a full-scale aerospace structure achieved in Chapter 1 using existing analysis techniques confirmed these needs and highlighted the necessary introduction of more advanced methodologies. In this context, the thesis subsequently addressed specific facets of nonlinear system identification and brought original contributions to the field. The first contribution described in Chapter 2 was the introduction of the FNSI method. Numerical and experimental systems of low dimensionality, namely a Duffing oscillator and the Silverbox benchmark, were successfully identified and illustrated the capabilities of the approach. The demonstration of the FNSI method culminated in the identification of the SmallSat spacecraft in Chapter 3. Amongst the different advantages of the method, the possibility to calculate accurately a large number of parameters was stressed, and opened the way in Chapter 4 to the use of cubic splines to characterise the nonlinearities of a solar array structure. The proper treatment of measurement noise was finally achieved in Chapter 5, where the FNSI method was embedded into the maximum likelihood framework to attain models with optimal statistical properties. A complete summary of the identification and modelling capabilities of the different tools developed in this thesis is proposed in Table 6.1, together with the analytical and computational means they build on. The price to pay for these capabilities is a number of requirements listed in Table 6.2. We also formulate in this table a series of recommendations to fulfil these requirements and exploit the complete potential of the different tools.

Capability	Means
Applicability	
Multi-input, multi-output systems	State-space model
High non-proportional damping	State-space model
High modal density and large modal overlap	Stabilisation diagram
Nonlinear modelling	
Representation of various types of complex nonlinearities	Cubic splines
Physical insight into the estimated parameters	White- or grey-box model with conversion to the physical space
Averaging of the nonlinear coefficients over specific intervals	Frequency domain
Qualitative detection of modelling errors, missing modes, inaccuracies in linear parameters and spurious poles	Inspection of the frequency dependence of the nonlinear coefficients
Numerical performance	
Data reduction and limitation of the computational burden	Frequency domain
Decoupling between linear nonlinear parameter estimation	Orthogonal decomposition
Good numerical conditioning	Discrete-time model
Numerical robustness in high-dimensional estimation problem	QR and singular value decompositions
Statistical properties	
Consistency with noise-free inputs	Weighting strategies
Consistency with noisy basis functions	MLE
Statistical efficiency	MLE
Calculation of confidence bounds	Possible in the MLE framework in the absence of modelling errors

Table 6.1: Summary of the capabilities of the identification tools developed in the thesis.

Requirement	**Recommendation**
	Measurement
Force measurement	Use an impedance head or instrument the shaker-to-structure interface
Construction of the nonlinear basis functions	Instrument the nonlinearity locations
Data processing using the DFT	Opt for periodic excitations to avoid leakage
Estimation of noise weighting matrices	Opt for periodic excitations
	Signal processing
Exploitation of harmonics / integration of accelerations signals / fulfilment of the ZOH assumption	Consider a sufficiently high sampling frequency
Mitigation of output noise to ensure the consistency of FNSI	Measure a sufficiently large number of periods
Good frequency resolution of the resonance peaks	Consider a sufficiently high number of samples per period
Choice of the number of processed frequency lines	Balance the presence of nonlinear distortions outside the input band, the signal-to-noise ratio and the computational burden
Choice of the value of i	Consider a trial-and-error approach in the interval $[1.5\,n_s - 10\,n_s]$
	Linear and nonlinear estimation
Selection of the nonlinear basis functions	Utilise splines and the techniques described in Chapter 1 if sine-sweep data are available
Selection of the number of knots in splines	Consider a trial-and-error approach maximising the linear parameter accuracy
Selection of the model order in a stabilisation diagram	Track the frequency and damping ratio of the poles, and balance the stability of the nonlinear coefficients, the presence of spurious poles and the computational burden
Selection of the averaging interval of the nonlinear coefficients	Inspect the frequency dependence of the coefficients

Table 6.2: Requirements of the identification tools and recommendations to fulfil them.

Perspectives for future research

In this final section, we briefly describe two specific directions for future research. In this thesis, localised nonlinearities were exclusively addressed. Distributed nonlinearities in mechanical systems have so far received very little attention since most identification methods introduced in structural dynamics assume lumped nonlinear components, which is the case for the FNSI method. Recently developed approaches originating from the systems and control community, in particular the works in [27, 85, 102], yet offer new identification routes compatible with distributed nonlinearities by virtue of their great flexibility. More particularly, the proposed research focuses on the development of a system identification methodology based on the class of nonlinear state-space models [85]. A nonlinear state-space representation is a very flexible model structure that is, in principle, applicable to distributed nonlinearities, without restriction as to their importance in the system dynamics. However, the flexibility of such models prevents them from conveying any physical interpretation of the tested system. For this reason, they are referred to as unstructured models. The main contribution of the research would be to structure nonlinear state-space models, so as to reveal their physical insights. In a first step, a specific effort should be accomplished to incorporate in the model all prior knowledge the experimentalist may possess. Additionally, in a second step, algebraic and optimisation techniques should be applied to further decrease the complexity of the model and retrieve as much structure as possible [114]. Potential applications of this research project include highly flexible structures exhibiting geometrical nonlinearity, and new materials with intrinsically nonlinear dynamics [56].

A second perspective of research we envisage is the development of a generalisation of phase separation techniques to nonlinear systems. Phase separation testing is routinely exploited for experimental modal analysis of linear structures. It consists in exciting several modes of interest at once using either broadband or swept-sine excitations. Considering a randomly-excited nonlinear system where several nonlinear normal modes participate in the response, the objective of this research would be to identify the individual normal modes of the system directly from the measured data. The proposed methodology would combine the FNSI method and numerical continuation tools. More specifically, nonlinear normal modes would be computed using continuation algorithms directly based on the state-space model derived by the FNSI method, and possibly optimised in the maximum likelihood framework. This research project should pave the way for what is arguably the first nonlinear phase separation method.

Bibliography

[1] S. Adachi, I. Yamaguchi, T. Kid, T. Sekiguchi, K. Yamada, and Y. Chida. On-orbit system identification experiments on Engineering Test Satellite-VI. *Control Engineering Practice*, 7:831–841, 1999.

[2] D.E. Adams and R.J. Allemang. A new derivation of the frequency response function matrix for vibrating non-linear systems. *Journal of Sound and Vibration*, 227:1083–1108, 1999.

[3] D.E. Adams and R.J. Allemang. A frequency domain method for estimating the parameters of a non-linear structural dynamic model through feedback. *Mechanical Systems and Signal Processing*, 14:637–656, 2000.

[4] J.R. Ahlquist, J.M. Carreño, H. Climent, R. de Diego, and J. de Alba. Assessment of nonlinear structural response in A400M GVT. In *Proceedings of the 28th International Modal Analysis Conference (IMAC)*, Jacksonville, FL, 2010.

[5] H. Ahmadian and H. Jalali. Identification of bolted lap joints parameters in assembled structures. *Mechanical Systems and Signal Processing*, 21:1041–1050, 2007.

[6] M.A. Al-Hadid and J.R. Wright. Application of the force-state mapping approach to the identification of non-linear systems. *Mechanical Systems and Signal Processing*, 4:463–482, 1990.

[7] R.J. Allemang and D.L. Brown. A unified matrix polynomial approach to modal identification. *Journal of Sound and Vibration*, 221:301–322, 1998.

[8] P. Argoul and T. Le. Instantaneous indicators of structural behaviour based on the continuous Cauchy wavelet analysis. *Mechanical Systems and Signal Processing*, 17(1):243–250, 2003.

[9] P.G. Bakir. Automation of the stabilization diagrams for subspace based system identification. *Expert Systems with Applications*, 38:14390–14397, 2011.

[10] M.C.C. Bampton and J.R.R. Craig. Coupling of substructures for dynamic analyses. *AIAA Journal*, 6(7):1313–1319, 1968.

[11] S.A. Billings. *Nonlinear System Identification: NARMAX Methods in the Time, Frequency, and Spatio-Temporal Domains*. John Wiley & Sons, Chichester, United Kingdom, 2013.

[12] A. Calvi and N. Roy. *Spacecraft Mechanical Loads Analysis Handbook*. ESA Requirements and Standards Division, Noordwijk, The Netherlands, 2013.

[13] P. Camarasa and S. Kiryenko. Shock attenuation system for spacecraft and adaptor (SASSA). In *Proceedings of the European Conference on Spacecraft Structures, Materials and Mechanical Testing*, Toulouse, France, 2009.

[14] K. Carney, I. Yunis, K. Smith, and C.Y. Peng. Nonlinear dynamic behavior in the Cassini spacecraft modal survey. In *Proceedings of the 15th International Modal Analysis Conference (IMAC)*, Orlando, FL, 1997.

[15] A. Carrella and D.J. Ewins. Identifying and quantifying structural nonlinearities in engineering applications from measured frequency response functions. *Mechanical Systems and Signal Processing*, 25:1011–1027, 2011.

[16] C. De Boor. *A Practical Guide to Splines*. Springer-Verlag, New York, NY, 1978.

[17] T. De Troyer, P. Guillaume, R. Pintelon, and S. Vanlanduit. Fast calculation of confidence intervals on parameter estimates of least-squares frequency-domain estimators. *Mechanical Systems and Signal Processing*, 23:261–273, 2009.

[18] E.J. Dempsey and D.T. Westwick. Identification of Hammerstein models with cubic spline nonlinearities. *IEEE Transactions on Biomedical Engineering*, 51(2):237–245, 2004.

[19] G. Dimitriadis. Experimental validation of the constant level method for the identification of non-linear multi-degree-of-freedom systems. *Journal of Sound and Vibration*, 258(2):829–845, 2002.

[20] G. Duffing. *Erzwungene Schwingungen bei Veranderlicher Eigenfrequenz (Forced Oscillations in the Presence of Variable Eigenfrequencies)*. Vieweg & Sohn, Braunschweig, 1918.

[21] M. El-Kafafy, T. De Troyer, B. Peeters, and P. Guillaume. Fast maximum likelihood identification of modal parameters with uncertainty intervals: A modal model-based formulation. *Mechanical Systems and Signal Processing*, 37(1-2):422–439, 2013.

[22] M. Eriten, M. Kurt, G. Luo, D.M. McFarland, L.A. Bergman, and A.F. Vakakis. Nonlinear system identification of frictional effects in a beam with a bolted joint connection. *Mechanical Systems and Signal Processing*, 39:245–264, 2013.

[23] D.J. Ewins. *Modal Testing: Theory, Practice and Application*. Research Studies Press, Baldock, United Kingdom, 2000.

[24] Y. Fan and C.J. Li. Non-linear system identification using lumped parameter models with embedded feedforward neural networks. *Mechanical Systems and Signal Processing*, 16(2-3):357–372, 2002.

[25] J.H. Friedman. Multivariate adaptive regression splines. *The Annals of Statistics*, 19(1):1–67, 1991.

[26] U. Fuellekrug and D. Goege. Identification of weak non-linearities within complex aerospace structures. *Aerospace Science and Technology*, 23(1):53–62, 2012.

[27] F. Giri and E.W. Bai. *Block-oriented Nonlinear System Identification*. Springer, Heidelberg, Germany, 2010.

[28] P. Giuliani, D. Di Maio, C.W. Schwingshackl, M. Martarelli, and D.J. Ewins. Six degrees of freedom measurement with continuous scanning laser doppler vibrometer. *Mechanical Systems and Signal Processing*, 38(2):367–383, 2013.

[29] J.C. Golinval, G. Kerschen, V. Lenaerts, F. Thouverez, and P. Argoul. European COST action F3 on structural dynamics. Working group 3: Identification of nonlinear systems; Introduction and conclusions. *Mechanical Systems and Signal Processing*, 17:177–178, 251–254, 2003.

[30] S. Guarnieri, F. Piazza, and A. Uncini. Multilayer feedforward networks with adaptive spline activation function. *IEEE Transactions on Neural Networks*, 10:672–683, 1999.

[31] J. Guckenheimer and P. Holmes. *Nonlinear Oscillations, Dynamical Systems and Bifurcation of Vector Fields*. Springer, New-York, NY, 1983.

[32] P. Guillaume, R. Pintelon, and J. Schoukens. Description of a parametric maximum likelihood estimator in the frequency domain for multi-input, multi-output systems and its application to flight flutter analysis. *Mechanical Systems and Signal Processing*, 4(5):405–416, 1990.

[33] F. Harris. On the use of windows for harmonic analysis with discrete Fourier transform. *Proceedings of the IEEE*, 66:51–83, 1978.

[34] C.J. Hartwigsen, Y. Song, D.M. McFarland, L.A. Bergman, and A.F. Vakakis. Experimental study of non-linear effects in a typical shear lap joint configuration. *Journal of Sound and Vibration*, 277:327–351, 2004.

[35] A. Haryanto and K. Hong. Maximum likelihood identification of wiener-hammerstein models. *Mechanical Systems and Signal Processing*, 41:54–70, 2013.

[36] A. Hot, G. Kerschen, E. Foltête, and S. Cogan. Detection and quantification of nonlinear structural behaviour using principal component analysis. *Mechanical Systems and Signal Processing*, 26:104–116, 2012.

[37] X. Hu, T.B. Schon, and L. Ljung. A general convergence result for particle filtering. *IEEE Transactions on Signal Processing*, 59(7):3424–3429, 2011.

[38] J.L. Huang, R.K.L. Su, Y.Y. Lee, and S.H. Chen. Nonlinear vibration of a curved beam under uniform base harmonic excitation with quadratic and cubic nonlinearities. *Journal of Sound and Vibration*, 330:5151–5164, 2011.

[39] S.R. Ibrahim and E.C. Mikulcik. A time domain modal vibration test technique. *Shock and Vibration Bulletin*, 43:21–37, 1973.

[40] K. Jalaleddini, D.T. Westwick, and R.E. Kearney. Subspace identification of Hammerstein systems using B-splines. In *Proceedings of the 34th Annual International Conference of the IEEE EMBS*, San Diego, CA, 2012.

[41] J.S. Juang and R.S. Pappa. An eigensystem realization algorithm for modal parameter identification and model reduction. *AIAA Journal of Guidance, Control and Dynamics*, 12:620–627, 1985.

[42] M. Juntunen and J. Linjama. Presentation of the VTT benchmark. *Mechanical Systems and Signal Processing*, 17(1):179–182, 2003.

[43] G. Kerschen, J.C. Golinval, and K. Worden. Theoretical and experimental identification of a non-linear beam. *Journal of Sound and Vibration*, 244(4):597–613, 2001.

[44] G. Kerschen, V. Lenaerts, and J.C. Golinval. Identification of a continuous structure with a geometrical non-linearity. Part I: Conditioned reverse path method. *Journal of Sound and Vibration*, 262:889–906, 2003.

[45] G. Kerschen, M. Peeters, J.C. Golinval, and C. Stephan. Nonlinear modal analysis of a full-scale aircraft. *Journal of Aircraft*, 50(5):1409–1419, 2013.

[46] G. Kerschen, M. Peeters, J.C. Golinval, and A.F. Vakakis. Nonlinear normal modes. Part I: A useful framework for the structural dynamicist. *Mechanical Systems and Signal Processing*, 23(1):170–194, 2009.

[47] G. Kerschen, K. Worden, A.F. Vakakis, and J.C. Golinval. Past, present and future of nonlinear system identification in structural dynamics. *Mechanical Systems and Signal Processing*, 20:505–592, 2006.

[48] M.E. King and A.F. Vakakis. An energy-based approach to computing resonant nonlinear normal modes. *Journal of Applied Mechanics*, 63:810–819, 1995.

[49] S.L. Lacy and D.S. Bernstein. Subspace identification for non-linear systems with measured-input non-linearities. *International Journal of Control*, 78:906–926, 2005.

[50] M. Laible, K. Fitzpatrick, and M. Grygier. International Space Station 2A array modal analysis. In *Proceedings of the 31st International Modal Analysis Conference (IMAC)*, Garden Grove, CA, 2013.

[51] Y.S. Lee, G. Kerschen, A.F. Vakakis, P. Panagopoulos, L.A. Bergman, and D.M. McFarland. Complicated dynamics of a linear oscillator with a light, essentially nonlinear attachment. *Physica D: Nonlinear Phenomena*, 204(1-2):41–69, 2005.

[52] Y.S. Lee, F. Nucera, A.F. Vakakis, D.M. McFarland, and L.A. Bergman. Periodic orbits, damped transitions and targeted energy transfers in oscillators with vibro-impact attachments. *Physica D: Nonlinear Phenomena*, 238(18):1868–1896, 2009.

[53] V. Lenaerts, G. Kerschen, and J.C. Golinval. Identification of a continuous structure with a geometrical non-linearity. Part II: Proper orthogonal decomposition. *Journal of Sound and Vibration*, 262:907–919, 2003.

[54] K. Levenberg. A method for the solution of certain problems in least squares. *Quarterly of Applied Mathematics*, 2:164–168, 1944.

[55] C.C. Lo. A cantilever beam chattering against a stop. *Journal of Sound and Vibration*, 69(2):245–255, 1980.

[56] J. Lydon, K.R. Jayaprakash, D. Ngo, Y. Starosvetsky, A.F. Vakakis, and C. Daraio. Frequency bands of strongly nonlinear homogeneous granular systems. *Physical Review E*, 88:012206, 2013.

[57] N.M.M. Maia and J.M.M. Silva. *Theoretical and Experimental Modal Analysis*. Research Studies Press, Baldock, United Kingdom, 1997.

[58] S. Marchesiello and L. Garibaldi. A time domain approach for identifying nonlinear vibrating structures by subspace methods. *Mechanical Systems and Signal Processing*, 22:81–101, 2008.

[59] D.W. Marquardt. An algorithm for least-squares estimation of nonlinear parameters. *Journal of the Society for Industrial and Applied Mathematics*, 11(2):431–441, 1963.

[60] S.F. Masri and T.K. Caughey. A nonparametric identification technique for nonlinear dynamic problems. *Journal of Applied Mechanics*, 46:433–447, 1979.

[61] S.F. Masri, A.G. Chassiakos, and T.K. Caughey. Structure-unknown non-linear dynamic systems: Identification through neural networks. *Smart Materials and Structures*, 1:45–56, 1992.

[62] S.F. Masri, H. Sassi, and T.K. Caughey. A nonparametric identification of nearly arbitrary nonlinear systems. *Journal of Applied Mechanics*, 49:619–628, 1982.

[63] T. McKelvey, H. Akçay, and L. Ljung. Subspace-based multivariable system identification from frequency response data. *IEEE Transactions on Automatic Control*, 41(7):960–979, 1996.

[64] W. Messner and R. Horowitz. Identification of a nonlinear function in a dynamical system. *ASME Journal of Dynamic Systems, Measurement, and Control*, 115(4):587–591, 1993.

[65] L. Mevel, L. Hermans, and H. Van Der Auweraer. Application of a subspace-based fault detection method to industrial structures. *Mechanical Systems and Signal Processing*, 13:823–838, 1999.

[66] S. Meyer and M. Link. Local non-linear softening behaviour: Modelling approach and updating of linear and non-linear parameters using frequency response residuals. In *Proceedings of the 21st International Modal Analysis Conference (IMAC)*, Kissimmee, FL, 2003.

[67] S. Meyer and M. Link. Modelling and updating of local non-linearities using frequency response residuals. *Mechanical Systems and Signal Processing*, 17(1):219–226, 2003.

[68] M. Moonen, B. De Moor, L. Vandenberghe, and J. Vandewalle. On- and off-line identification of linear state-space models. *International Journal of Control*, 49:219–232, 1989.

[69] P. Muhamad, N.D. Sims, and K. Worden. On the orthogonalised reverse path method for nonlinear system identification. *Journal of Sound and Vibration*, 331(20):4488–4503, 2012.

[70] P.C. Müller. Indirect measurements of nonlinear effects by state observers. In *Proceedings of the IUTAM Symposium on Nonlinear Dynamics in Engineering Systems*, Stuttgart, Germany, 1989.

[71] A.H. Nayfeh. *Nonlinear Interactions: Analytical, Computational and Experimental Methods*. John Wiley & Sons, New-York, NY, 2000.

[72] A.H. Nayfeh and D.T. Mook. *Nonlinear Oscillations*. Wiley-Interscience, New-York, NY, 1979.

[73] J.P. Noël and G. Kerschen. ESA Contract 21539/08/NL/SFe – Advancement of mechanical verification methods for non-linear spacecraft. WP4260: exploitation of test data. Technical report, University of Liège, Liège, Belgium, 2012.

[74] J.P. Noël and G. Kerschen. Frequency-domain subspace identification for nonlinear mechanical systems. *Mechanical Systems and Signal Processing*, 40:701–717, 2013.

[75] J.P. Noël, G. Kerschen, E. Foltête, and S. Cogan. Frequency-domain subspace identification of nonlinear mechanical systems - application to a solar array structure. In *Proceedings of the 31st International Modal Analysis Conference (IMAC)*, Garden Grove, CA, 2013.

[76] J.P. Noël, G. Kerschen, E. Foltête, and S. Cogan. Grey-box identification of a nonlinear solar array structure using cubic splines. *International Journal of Nonlinear Mechanics*, in review, 2014.

[77] J.P. Noël, S. Marchesiello, and G. Kerschen. Subspace-based identification of a nonlinear spacecraft in the time and frequency domains. *Mechanical Systems and Signal Processing*, 43:217–236, 2014.

[78] J.P. Noël, L. Renson, and G. Kerschen. Complex dynamics of a nonlinear aerospace structure: Experimental identification and modal interactions. *Journal of Sound and Vibration*, in press, 2014.

[79] J.P. Noël, L. Renson, G. Kerschen, B. Peeters, S. Manzato, and J. Debille. Nonlinear dynamic analysis of an F-16 aircraft using GVT data. In *Proceedings of the International Forum on Aeroelasticity and Structural Dynamics (IFASD)*, Bristol, UK, 2013.

[80] J.P. Noël, J. Schoukens, and G. Kerschen. A stochastic framework for subspace identification of a strongly nonlinear aerospace structure. In *Proceedings of the 32nd International Modal Analysis Conference (IMAC)*, Orlando, FL, 2014.

[81] J. Nováková, M. Hromčík, and R. Jech. Dynamic causal modeling and subspace identification methods. *Biomedical Signal Processing and Control*, 7:365–370, 2012.

[82] M.B. Özer, H.N. Özgüven, and T.J. Royston. Identification of structural nonlinearities using describing functions and the Sherman-Morrison method. *Mechanical Systems and Signal Processing*, 23:30–44, 2009.

[83] L.R. Padovese. Hybrid time-frequency methods for non-stationary mechanical signal analysis. *Mechanical Systems and Signal Processing*, 18(5):1047–1064, 2004.

[84] J. Paduart. *Identification of Nonlinear Systems using Polynomial Nonlinear State Space Models*. PhD thesis, Vrije Universiteit Brussel, Brussels, Belgium, 2007.

[85] J. Paduart, L. Lauwers, J. Swevers, K. Smolders, and J. Schoukens. Identification of nonlinear systems using Polynomial Nonlinear State Space models. *Automatica*, 46:647–656, 2010.

[86] E. Parloo, P. Guillaume, and B. Cauberghe. Maximum likelihood identification of non-stationary operational data. *Journal of Sound and Vibration*, 268(5):971–991, 2003.

[87] B. Peeters, H. Climent, R. de Diego, J. de Alba, J.R. Ahlquist, J.M. Carreño, W. Hendricx, A. Rega, G. Garcia, J. Deweer, and J. Debille. Modern solutions for Ground Vibration Testing of large aircraft. In *Proceedings of the 26th International Modal Analysis Conference (IMAC)*, Orlando, FL, 2008.

[88] B. Peeters and G. de Roeck. Reference-based stochastic subspace identification for output-only modal analysis. *Mechanical Systems and Signal Processing*, 13(6):855–878, 1999.

[89] B. Peeters, H. Van der Auweraer, P. Guillaume, and J. Leuridan. The PolyMAX frequency-domain method: A new standard for modal parameter estimation? *Shock and Vibration*, 11(3-4):395–409, 2004.

[90] M. Peeters, R. Viguié, G. Sérandour, G. Kerschen, and J.C. Golinval. Nonlinear normal modes. Part II: Toward a practical computation using numerical continuation techniques. *Mechanical Systems and Signal Processing*, 23(1):195–216, 2009.

[91] R. Pintelon. Frequency-domain subspace system identification using non-parametric noise models. *Automatica*, 38:1295–1311, 2002.

[92] R. Pintelon and J. Schoukens. *System Identification: A Frequency Domain Approach*. IEEE Press, Piscataway, NJ, 2001.

[93] M.F. Platten, J.R. Wright, J.E. Cooper, and G. Dimitriadis. Identification of a nonlinear wing structure using an extended modal model. *Journal of Aircraft*, 46(5):1614–1626, 2009.

[94] M.F. Platten, J.R. Wright, G. Dimitriadis, and J.E. Cooper. Identification of multi-degree of freedom non-linear systems using an extended modal space model. *Mechanical Systems and Signal Processing*, 23(1):8–29, 2009.

[95] L. Renson, J.P. Noël, and G. Kerschen. Complex dynamics of a nonlinear aerospace structure: Numerical continuation and normal modes. *Nonlinear Dynamics*, in review, 2014.

[96] E. Reynders, R. Pintelon, and G. De Roeck. Uncertainty bounds on modal parameters obtained from stochastic subspace identification. *Mechanical Systems and Signal Processing*, 22:948–969, 2008.

[97] E. Reynders and G. De Roeck. Reference-based combined deterministic-stochastic subspace identification for experimental and operational modal analysis. *Mechanical Systems and Signal Processing*, 22:617–637, 2008.

[98] C.M. Richards and R. Singh. Identification of multi-degree-of-freedom non-linear systems under random excitations by the "reverse path" spectral method. *Journal of Sound and Vibration*, 213:673–708, 1998.

[99] C.M. Richards and R. Singh. Characterization of rubber isolator nonlinearities in the context of single- and multi-degree-of-freedom experimental systems. *Journal of Sound and Vibration*, 247:807–834, 2001.

[100] A.G. Russell. Thick skin, faceted, CFRP, monocoque tube structure for smallsats. In *Proceedings of the European Conference on Spacecraft Structures, Materials and Mechanical Testing*, Noordwijk, The Netherlands, 2000.

[101] J. Schoukens, J.G. Nemeth, P. Crama, Y. Rolain, and R. Pintelon. Fast approximate identification of nonlinear systems. *Automatica*, 39:1267–1274, 2003.

[102] J. Schoukens, R. Pintelon, T. Dobrowiecki, and Y. Rolain. Identification of linear systems with nonlinear distortions. *Automatica*, 41:491–504, 2005.

[103] J. Schoukens, R. Pintelon, Y. Rolain, and T. Dobrowiecki. Frequency response function measurements in the presence of nonlinear distortions. *Automatica*, 37:939–946, 2001.

[104] J. Schoukens and J. Renneboog. Modeling the noise influence of the Fourier coefficients after a discrete Fourier transform. *IEEE Transactions on Instrumentation and Measurement*, 35(3):279–286, 1986.

[105] M. Simon and G.R. Tomlinson. Use of the Hilbert transform in modal analysis of linear and non-linear structures. *Journal of Sound and Vibration*, 96:421–436, 1984.

[106] R. Singh, P. Davies, and A.K. Bajaj. Identification of nonlinear and viscoelastic properties of flexible polyurethane foam. *Nonlinear Dynamics*, 34:319–346, 2003.

[107] J. Sjöberg, Q. Zhang, L. Ljung, A. Benveniste, B. Delyon, P.Y. Glorennec, H. Hjalmarsson, and A. Juditsky. Nonlinear black-box modeling in system identification: A unified overview. *Automatica*, 31(12):1691–1724, 1995.

[108] D. Söffker, J. Bajkowski, and P.C. Müller. Detection of cracks in turborotors - a new observer based method. *ASME Journal of Dynamic Systems, Measurement, and Control*, 115(3):518–524, 1993.

[109] M.W. Sracic, M.S. Allen, and H. Sumali. Identifying the modal properties of nonlinear structures using measured free response time histories from a scanning laser Doppler vibrometer. In *Proceedings of the 29th International Modal Analysis Conference (IMAC)*, Jacksonville, FL, 2012.

[110] W.J. Staszewski. Analysis of non-linear systems using wavelets. *Proceedings of the Institution of Mechanical Engineers Part C – Journal of Mechanical Engineering Science*, 214(11):1339–1353, 2000.

[111] S.H. Strogatz. *Nonlinear Dynamics and Chaos: With Applications to Physics, Biology, Chemistry, and Engineering.* Addison-Wesley, Reading, MA, 1994.

[112] S.T. Trickey, L.N. Virgin, and E.H. Dowell. The stability of limit-cycle oscillations in a nonlinear aeroelastic system. *Proceedings of the Royal Society of London Series A*, 458:2203–2226, 2002.

[113] P. Vacher, B. Jacquier, and A. Bucharles. Extensions of the MAC criterion to complex modes. In *Proceedings of the ISMA International Conference on Noise and Vibration Engineering 2010*, Leuven, Belgium, 2010.

[114] A. Van Mulders, J. Schoukens, and L. Vanbeylen. Identification of systems with localised nonlinearity: From state-space to block-oriented models. *Automatica*, 49:1392–1396, 2013.

[115] A. Van Mulders and L. Vanbeylen. Comparison of some initialisation methods for the identification of nonlinear state-space models. In *Proceedings of the IEEE International Instrumentation and Measurement Technology Conference (I2MTC)*, Minneapolis, MN, 2013.

[116] P. Van Overschee and B. De Moor. N4SID: Subspace algorithms for the identification of combined deterministic-stochastic systems. *Automatica*, 30:75–93, 1994.

[117] P. Van Overschee and B. De Moor. Continuous-time frequency domain subspace system identification. *Signal Processing*, 52:179–194, 1996.

[118] P. Van Overschee and B. De Moor. *Subspace Identification for Linear Systems: Theory, Implementation and Applications*. Kluwer Academic Publishers, Dordrecht, The Netherlands, 1996.

[119] P. Van Overschee, B. De Moor, W. Dehandschutter, and J. Swevers. A subspace algorithm for the identification of discrete time frequency domain power spectra. *Automatica*, 33(12):2147–2157, 1997.

[120] M. Verhaegen. Identification of the deterministic part of MIMO state space models given in innovations form from input-output data. *Automatica*, 30(1):61–74, 1994.

[121] D.J. Wagg. Periodic sticking motion in a two-degree-of-freedom impact oscillator. *International Journal of Non-linear Mechanics*, 40:1076–1087, 2005.

[122] P.R. White, M.H. Tan, and J.K. Hammond. Analysis of the maximum likelihood, total least squares and principal component approaches for frequency response function estimation. *Journal of Sound and Vibration*, 290:676–689, 2006.

[123] K. Worden. Data processing and experiment design for the restoring force surface method. Part I: Integration and differentiation of measured time data. *Mechanical Systems and Signal Processing*, 4:295–319, 1990.

[124] K. Worden, D. Hickey, M. Haroon, and D. E. Adams. Nonlinear system identification of automotive dampers: A time and frequency-domain analysis. *Mechanical Systems and Signal Processing*, 23:104–126, 2009.

[125] K. Worden, W.J. Staszewski, and J.J. Hensman. Natural computing for mechanical systems research: A tutorial overview. *Mechanical Systems and Signal Processing*, 25:4–111, 2011.

[126] K. Worden and G.R. Tomlinson. *Nonlinearity in Structural Dynamics: Detection, Identification and Modelling*. Institute of Physics Publishing, Bristol, UK, 2001.

[127] K. Worden, C.X. Wong, U. Parlitz, A. Hornstein, D. Engster, T. Tjahjowidodo, F. Al-Bender, D.D. Rizos, and S.D. Fassois. Identification of pre-sliding and sliding friction dynamics: Grey box and black-box models. *Mechanical Systems and Signal Processing*, 21:514–534, 2007.

[128] Z.J. Yang and S. Sanada. Frequency domain subspace identification with the aid of the w-operator. *Electrical Engineering in Japan*, 132(1):46–56, 2000.

[129] A.C. Zecchin, L.B. White, M.F. Lambert, and A.R. Simpson. Parameter identification of fluid line networks by frequency-domain maximum likelihood estimation. *Mechanical Systems and Signal Processing*, 37(1-2):370–387, 2013.

[130] S. Zhou, W. Heylen, P. Sas, and L. Liu. Maximum likelihood estimator of operational modal analysis for linear time-varying structures in time-frequency domain. *Journal of Sound and Vibration*, in press, 2014.

[131] Y.C. Zhu. Parametric Wiener model identification for control. In *Proceedings of IFAC World Congress*, Beijing, China, 1999.

List of Journal Publications

1. J.P. Noël and G. Kerschen. Frequency-domain subspace identification for nonlinear mechanical systems. *Mechanical Systems and Signal Processing*, 40:701-717, 2013.

2. J.P. Noël, S. Marchesiello, and G. Kerschen. Subspace-based identification of a nonlinear spacecraft in the time and frequency domains. *Mechanical Systems and Signal Processing*, 43:217-236, 2014.

3. J.P. Noël, L. Renson, and G. Kerschen. Complex dynamics of a nonlinear aerospace structure: Experimental identification and modal interactions. *Journal of Sound and Vibration*, in press, 2014.

4. J.P. Noël, G. Kerschen, E. Foltête, and S. Cogan. Grey-box identification of a nonlinear solar array structure using cubic splines. *International Journal of Nonlinear Mechanics*, in review, 2014.

5. L. Renson, J.P. Noël, and G. Kerschen. Complex dynamics of a nonlinear aerospace structure: Numerical continuation and normal modes. *Nonlinear Dynamics*, in review, 2014.

6. S.B. Shiki, S. da Silva, J.P. Noël, and G. Kerschen. Identification of a geometrically nonlinear beam using Volterra series. *Mechanics Research Communications*, in review, 2014.

List of Conference Publications

1. J.P. Noël, J. Schoukens, and G. Kerschen. A stochastic framework for subspace identification of a strongly nonlinear aerospace structure. In *Proceedings of the 32nd International Modal Analysis Conference (IMAC)*, Orlando, FL, 2014.

2. C. Grappasonni, J.P. Noël, and G. Kerschen. Subspace and nonlinear-normal-modes-based identification of a beam with softening-hardening behaviour. In *Proceedings of the 32nd International Modal Analysis Conference (IMAC)*, Orlando, FL, 2014.

3. J.P. Noël, L. Renson, and G. Kerschen. Experimental identification of the complex dynamics of a strongly nonlinear spacecraft structure. In *Proceedings of the ASME 2013 International Design Engineering Technical Conferences (IDETC)*, Portland, OR, 2013.

4. S.B. Shiki, J.P. Noël, G. Kerschen, V. Lopes Junior, and S. da Silva. Identification of mechanical systems with local nonlinearities through discrete-time Volterra series and Kautz functions. In *Proceedings of the 11th International Conference on Recent Advances in Structural Dynamics (RASD)*, Pisa, Italy, 2013.

5. J.P. Noël, L. Renson, G. Kerschen, B. Peeters, S. Manzato, and J. Debille. Nonlinear dynamic analysis of an F-16 aircraft using GVT data. In *Proceedings of the International Forum on Aeroelasticity and Structural Dynamics (IFASD)*, Bristol, UK, 2013.

6. J.P. Noël and G. Kerschen. Frequency-domain subspace identification of nonlinear mechanical systems. In *Proceedings of the 5th International Operational Modal Analysis Conference (IOMAC)*, Guimarães, Portugal, 2013.

7. J.P. Noël and G. Kerschen. Nonparametric subspace identification of nonlinear structures - Application to a spacecraft. In *Proceedings of the 54th AIAA Structures, Structural Dynamics and Materials Conference*, Boston, MA, 2013.

8. J.P. Noël, G. Kerschen, E. Foltête, and S. Cogan. Frequency-domain subspace identification of nonlinear mechanical systems - Application to a solar array structure. In *Proceedings of the 31st International Modal Analysis Conference (IMAC)*, Garden Grove, CA, 2013.

9. J.P. Noël, S. Marchesiello, and G. Kerschen. Time- and frequency-domain subspace identification of a nonlinear spacecraft. In *Proceedings of the ISMA International Conference on Noise and Vibration Engineering 2012*, Leuven, Belgium, 2012.

10. J.P. Noël and G. Kerschen. A new subspace-based approach to identify nonlinear mechanical structures in the frequency domain. In *Proceedings of the 16th IFAC Symposium on System Identification*, Brussels, Belgium, 2012.

11. J.P. Noël and G. Kerschen. Low-order local modelling of structural nonlinearities. In *Proceedings of the 18th Symposium on Vibrations, Shocks and Noise (VCB)*, Paris, France, 2012.

12. J.P. Noël, L. Renson, and G. Kerschen. Experimental identification of a nonlinear space structure. In *Proceedings of the 12th European Conference on Spacecraft Structures, Materials and Environmental Testing*, Noordwijk, The Netherlands, 2012.

13. L. Renson, J.P. Noël, and G. Kerschen. Nonlinear modal analysis of the SmallSat spacecraft. In *Proceedings of the 12th European Conference on Spacecraft Structures, Materials and Environmental Testing*, Noordwijk, The Netherlands, 2012.

14. J.P. Noël, G. Kerschen, and A. Newerla. Application of the restoring force surface method to a real-life spacecraft structure. In *Proceedings of the 30th International Modal Analysis Conference (IMAC)*, Jacksonville, FL, 2012.